UNIVERSITY OF SOUTHAMPTON

FACULTY OF PHYSICAL SCIENCE AND ENGINEERING

Electronics and Computer Science

High-Performance Amorphous Silicon Solar Cells with Plasmonic Light Scattering

by

Lee Crudgington

Thesis for the degree of Doctor of Philosophy

December 2015

UNIVERSITY OF SOUTHAMPTON

ABSTRACT

FACULTY OF PHYSICAL SCIENCE AND ENGINEERING
Electronics and Computer Science

Doctor of Philosophy

HIGH-PERFORMANCE AMORPHOUS SILICON SOLAR CELLS WITH PLASMONIC LIGHT SCATTERING

by Lee Crudgington

This research project is focused on the process optimisation and optical enhancement of the hydrogenated amorphous silicon solar cell design, achieved by the incorporation of light scattering plasmonic nano-particles. These treatments consist of a very thin layer of finely tuned silver metal-island films, which preferentially scatter light within a wavelength range tailored to the device absorption characteristic. This serves to increase the optical path length without the need for surface texturing of the semiconductor material. Within this study, the PECVD process is used to explore the parameter space and fabricate silicon thin films with excellent optical and electrical performance, and a P-I-N amorphous silicon device structure is fabricated with a high performance of 6.5% conversion efficiency, 14.04mA/cm^2 current density and 0.82V open circuit voltage.

The effects of metallic nano-particle arrays is demonstrated by numerical simulation, showing that variations in particle size, shape, position within the structure and surrounding material greatly influence the enhancement of the nano-particles on silicon absorber layers, and that particles positioned at the rear of the device structure adjacent to a back reflector avoid absorption losses which occur below the particle resonance frequency when such structures are positioned at the front surface. It is shown than an improvement in optical absorption of just over 1% is possible using this method.

Silicon thin films are fabricated with self-organised nano-particle arrays via means of annealed metal films, positioned at the front or back adjacent to a metallic reflector, and measurements of optical transmittance, reflectance and absorption are taken. The optimum annealing temperature and duration is identified, and it is shown that these variables can greatly affect the absorption of the device stack. To conclude the study, an amorphous silicon P-I-N photovoltaic device is fabricated featuring self-organised nano-particle arrays within the back reflector, and a modest improvement of energy conversion efficiency is observed with scope for further optimisation and enhancement.

Contents

List of Figures

List of Tables

Declaration of Authorship

I, Lee Crudgington , declare that the thesis entitled *High-Performance Amorphous Silicon Solar Cells with Plasmonic Light Scattering*, and the work presented in the thesis are both my own, and have been generated by me as the result of my own original research. I confirm that:

- This work was done wholly or mainly while in candidature for a research degree at this University;
- Where any part of this thesis has previously been submitted for a degree or any other qualification at this University or any other institution, this has been clearly stated;
- Where I have consulted the published work of others, this is always clearly attributed;
- Where I have quoted from the work of others, the source is always given. With the exception of such quotations, this thesis is entirely my own work;
- I have acknowledged all main sources of help;
- Where the thesis is based on work done by myself jointly with others, I have made clear exactly what was done by others and what I have contributed myself;
- Parts of this work have been published as:
  - L. J. Crudgington, M. A. Rind, D. N. R. Payne, and D. M. Bagnall. The Effects of Varied Deposition Conditions, Including the Use of Argon, on Thin-Film Silicon Solar Cells Prepared Using PECVD. Molecular Crystals and Liquid Crystals, (April 15), 2014. [1]

Signed:.....

Date:.....

Nomenclature

PECVD	Plasma - Enhanced Chemical Vapour Deposition
HWCVD	Hot - Wire Chemical Vapour Deposition
TCO	Transparent Conduction Oxide
ITO	Indium Tin Oxide
ESH	Equivalent Sun Hours
kWh	Kilowatt Hours
V_{oc}	Open circuit voltage
I_{sc}	Short circuit current
V_{mp}	Voltage at MPP
I_{sc}	Current at MPP
P_{in}	Power
n	Ideality factor
k	Boltzmann's constant
T	Absolute temperature
q	Elementary charge
V	Voltage applied
I_0	Reverse saturation current
I_L	Photo-generated current
N_A	Doping concentration
Δn	Excess carrier concentration
n_i	Intrinsic carrier concentration
G	Generation rate (assumed uniform)
L_n	Electron diffusion length
L_p	Hole diffusion length
n_1	Refractive index of first material
n_2	Refractive index of second material
θ_i	Angle of incidence
θ_r	Angle of reflection
α	Absorption coefficient
t	Depth in to absorber

Chapter 1

Introduction

1.1 The Energy Supply Problem

Energy is of fundamental importance to the global population. Humans consume energy in almost every aspect of life, including heating our homes, working, cooking food, transporting us to different locations and entertaining ourselves using games, televisions and computers. The most developed countries in the world are those that enjoy the highest living standards and consequently are those which have the highest energy consumption per capita. It would be difficult to imagine modern life without the availability of energy in its various forms. A number of issues exist with the supply and extraction of the energy which we use on such an enormous scale. Five main concerns are shared by governments, industry and the population regarding this energy supply:

1. **Increase in Population**
   The World's population currently stands at around 7.4 billion, having exceeded the 7 billion mark in March 2012 [2]. A period of continuous population growth has been observed throughout the last century, and it is widely predicted that the population will stand at between 8 and 10 billion by the year 2050 should these trends continue. From a perspective of energy demand, this means that a significant increase in supply is required to ensure that this larger population enjoy comparable living standards to those we are familiar with in the developed world.

2. **Rising Living Standards**
   While the population of the Earth is set to increase, it is also true that around one fifth of the current population lacks access to the benefits given by access to reliable energy supplies, such as pumped filtered water, heat, light and shelter. [3] The average annual energy consumption per capita in the USA is around 12,000kWh, while for an individual living in Pakistan this value is around twenty times less at 520kWh [4]. International efforts to balance this disparity in living standards have been ongoing for many years, and this will require an increase in the supply of energy to these regions to meet the demand.

3. **Supply of Energy**

   Current supplies of electrical energy are met largely by the burning of fossil fuels such as oil, coal and gas. These fossil fuels are removed from deposits within the Earth and their stored chemical energy is converted to electrical energy via a number of mechanical processes, all of which are only around 50 - 60% efficient depending on the technology [5]. While recent estimates have predicted that these supplies of fossil fuels are sufficient to last approximately 40 years at the current rate of consumption, the complexity involved in extracting such fuels is increasing [6]. This has resulted in several well-publicised issues regarding failure of the technology, such as the deep-water horizon oil catastrophe [7], and a heavy reliance on imported fuels from Middle Eastern regions. While due to a number of economic and political causes the cost of crude oil per barrel has decreased in recent months in comparison to the preceding five years, the Brent Crude classification (shown in figure 1.1) remains higher than the average before the last decade, and market analysts widely predict that the price will once again begin to increase over the coming years. Renewable energy sources are ideally suited to meet these energy needs, with a number of developed regions claiming to have been powered entirely by renewable energy sources for a number of months [8], and peer-reviewed studies predicting that renewable energy will become one of the cheapest forms of energy production available within ten years [9]. Further infrastructure improvements are in development, such as flywheel and battery storage solutions which store surplus energy during peak generation periods and therefore help negate the intermittent nature of this type of energy supply allowing it to be be delivered as required [10].

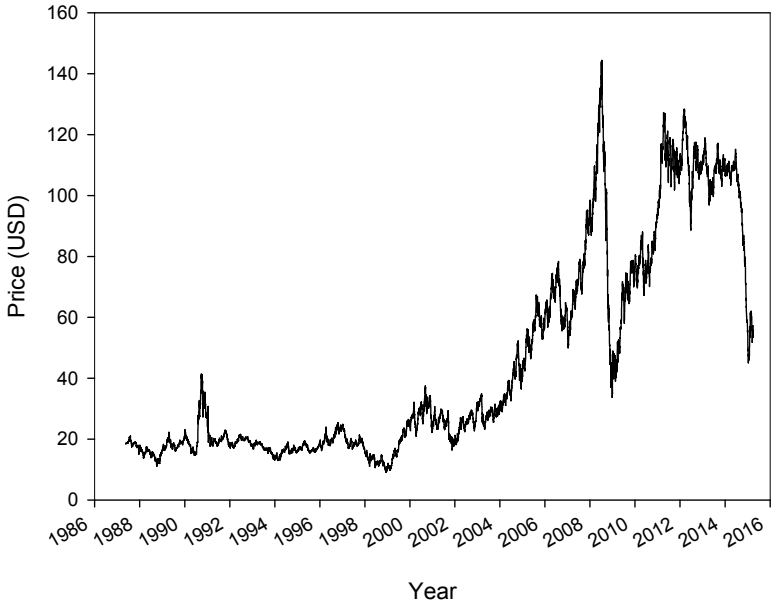

Figure 1.1: Crude Oil Price (USD) Per Barrel 1986 - 2015 [11]

4. **Greenhouse Gas Emissions**
   In addition to the supply and extraction issues of fossil fuels, the combustion of such fuel generates large volumes of CO_2, NO_x and other greenhouse gases. These combustion-product gases and particulates are vented from furnaces, boilers, vehicles and steam-generators and are widely believed to be partly responsible for the worldwide increase of CO_2 in the atmosphere. In most geographic regions, coal-fired power stations are the biggest contributor to electrical power generation, while additionally this type of fuel produces twice the amount of CO_2 compared to oil or gas, further compounding the problem of harmful emissions. In May 2013 it was reported that the atmospheric concentration of CO_2 reached the 400ppm milestone for the first time [12] and is steadily increasing each year. This trend is shown in figure 1.2. The increase in greenhouse gas is known to be damaging to the environment and believed to be responsible for rising sea levels, increasing global temperatures and unpredictable weather patterns.

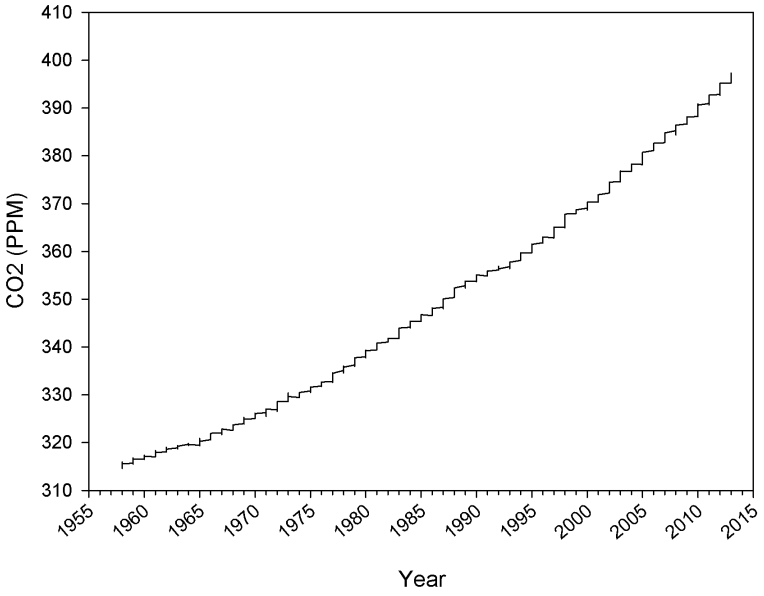

Figure 1.2: Atmospheric CO_2 1959- 2013 [13]

5. **The use of Kerosene Fuel in the Developing World**
   Rural communities in regions such as Madagascar, Kenya and Uganda heavily rely on the use of kerosene to fuel portable house lamps and run electrical generators for facilities such as water pumping and filtration systems. The disastrous results of the use of kerosene in these communities result in house fires which devastate lives and the production of toxic fumes which cause the deaths of up to 4000 children per year [14]. More women die annually as a result of respiratory illness caused by toxic kerosene fumes than they do of malaria and tuberculosis. This reality can be easily changed by the use of inexpensive solar lamps and community based solar generation grids to power basic utilities.

1.2 Introduction to Solar Energy Technologies

Governments and energy suppliers are increasingly aware of these concerns, and have laid down several green initiatives including investing in renewable energy sources. Renewable energy supplies are those which are not consumed at a faster rate than they are created, and encompass sunlight, wind, rain, tidal, waves, geothermal heat and correctly-managed biomass. Experts in the field suggest that the only way to prevent further CO_2 increases is to reduce the burning of fossil fuel by around 60%, [15] which will require an enormous investment in non-polluting forms of energy such as renewables.

Of these renewable energy sources, solar energy is a very promising solution due to the amount of energy which is supplied to the earth every day via solar irradiance. The total amount of energy available from sunlight incident on the Earth is 10,000 times larger than the current energy consumption [16], and therefore the ability to harness this power to generate energy is highly desirable. Other forms of energy are all indirectly powered by solar irradiance, and are therefore secondary forms of solar energy. For example, hydro-electricity is caused by evaporation and precipitation of water; wind turbines are powered by solar induced temperature differences; while fossil fuels are the product of millions of years of organic matter created by means of photo-synthesis decomposing under pressure.

A variety of technologies are available which serve to harness this solar energy. As far back as the 10th century, the power of the Sun has been harnessed using magnifying lenses, focussing mirrors and hot-boxes in order to boil water and cook food, while in the 19th century a solar method of heating water to run steam engines was devised, eliminating the need to burn coal [17]. These solar thermal methods are still in use today in the form of solar thermal hot water heating systems, and many large scale solar collection farms use the solar heat to boil water which power steam turbines and generate electricity. In this thesis, the investigation is focussed on the photovoltaic (PV) method, in which a semiconductor material is used to directly convert the solar light into electricity.

Figure 1.3: A photovoltaic power station [18]

A significant increase in the number of photovoltaic power stations installed can be observed worldwide, which are large-scale photovoltaic systems installed in areas of high solar insolation and output in excess of 4MWp directly into the energy grid. These installations have seen a far more widespread use in the field compared to the solar concentrator systems by a ratio of approximately 40 to 1. Often installed in otherwise low-value agricultural land, these installations supplement the conventional energy supply methods, and are often owned by the electricity utility suppliers or independent power operations taking advantage of feed-in-tariff incentives implemented worldwide.

Cost-per-watt and energy conversion efficiency are two essential factors to consider when designing a photovoltaic energy solution. An increase in the efficiency of a solar cell results in a higher power yield per unit area within the installation, reducing the number of devices needed to meet a given application and also reducing installation costs. A reduction in manufacturing costs, brought about by new methods of cell processing will additionally decrease the cost-per-watt, and open the market to new applications which until now have not been economically viable.

1.2.1 First Generation Solar Cells

The first generation of solar devices are those based on crystalline wafer technologies, including silicon, germanium and GaAs. Silicon-based solar cells represent 90% of the overall market share of solar cell production, [19] and are currently the best compromise between efficiency, performance, longevity and cost of all available photovoltaic technologies. The technology is similar to that of the micro-electronics industry, and therefore aspects of the supply chain and fabrication methods are shared between the two fields. Wafer based devices fall into two categories; mono-crystalline and multi-crystalline, both of which exhibit similar characteristics of high performance and excellent longevity.

Nonetheless, the majority of solar cells produced are of conventional diffused-emitter design, and therefore do not produce the optimal electrical power and cost-per watt economy for a given area. The mono-crystalline silicon wafers which the majority of solar cells are based on are time-consuming and expensive to fabricate, and therefore represent around half of the total module cost of the finished device. The conventional designs also suffer from a reduction in performance with increasing operating temperature, which serves to reduce the power output within a typical installation [20]. Device packaging further reduces the potential performance of this technology, with panels consisting of several cells positioned in a grid-like arrangement with a certain amount of wasted area per panel. Interconnects and device encapsulation pose reliability concerns and this serves to keep the cost per module at a premium despite falling cell prices [21].

1.2.2 Second Generation Solar Cells

The second generation of solar devices are those based on thin-film technologies, such as hydrogenated amorphous silicon (a-Si:H), cadmium telluride / cadmium sulfide (CdTe/CdS), and copper indium gallium selenide (CIGS). Devices based on these thin-film technologies do not feature a thick absorber layer as in the first-generation devices, and instead rely on a substrate material such as glass or plastic, on which the active layers are deposited. Devices such as these can be deposited on large areas, almost $6m^2$ in some cases [22]. Thin-film solar cells fabricated using amorphous silicon films are an alternative technology to crystalline silicon, with many potential advantages over the wafer-based first generation devices. Due to the substantial reduction in silicon material required for their manufacture and greatly enhanced scalability, thin-film devices cost significantly less than first generation wafer-based solar cells. Nonetheless, due to the optical and electrical properties of the amorphous material, these thin-film solar cells have lower energy conversion efficiencies than crystalline devices. They are therefore commonly for used in low-energy systems or indoor applications such as calculators and watches, although a modest number of large-scale amorphous solar installations do exist and can easily be combined with window glass and architectural building features. Nonetheless, optical enhancements to this design are possible, and this investigation proposes a revised device design which can potentially increase the power density whilst keeping the manufacturing costs of the devices low.

1.2.3 Third Generation Solar Cells

The third generation of solar devices are those which aim to exceed the conventional limits of the previous two generations of designs, by using innovative materials and/or using multiple junctions within the same device. Tandem or multi-junction devices which feature multiple semiconducting materials such as amorphous silicon, gallium arsenide or germanium absorber layers can be made to absorb a greater region of the electromagnetic spectrum and therefore improve the energy conversion efficiency [23]. Such devices are able to exceed the fundamental limits imposed by the use of a single semiconductor junction and achieve conversion efficiencies well in excess of those reported by conventional designs, however increased device complexity and associated manufacturing costs presently limit these devices to specialist applications. New and theoretical prototype developments include perovskite solar cells [24], dye-sensitised devices with no conventional p-n junction [25] and polymer solar cells [26], which fall into the category of third generation devices. While some of these technologies only have a limited commercial application due to the very high production cost, others are already being commercialised and are taking market share from the more established technologies.

1.3 The Importance of Energy Conversion Efficiency

The importance of the stabilised energy conversion efficiency, together with the final cost of the photovoltaic module cannot be overstated. Table 1.1 below details a selection of common photovoltaic device products, and their specified conversion efficiencies. The prospect of a roof-mounted residential photovoltaic system is analysed, while the argument is equally relevant when applied to larger scale systems. A case study of a typical scenario, a household with five or more occupants can be assumed to consume on average 6,000kWh of electrical energy per year [27], a daily usage of 16.5kWh.

Solar radiation is often diffuse due to cloud obstruction and reflection, and the energy is only available within daylight hours. The solar insolation environment in a particular region is usually described using the Typical Meteorological Year data (TMY), however for system analysis the average solar radiation can be described using the peak sun hours or equivalent sun hours (ESH) metric. This describes to the equivalent solar insolation which a particular location would receive if the sun were to be shining at its maximum value for a certain number of hours.

Manufacturer	**Model**	**Conversion Efficiency**
SunPower	X-300	21.5%
Sanyo Panasonic	HIT-N245	19.4%
Samsung	LPC241SM-08	15.1%
Sharp	NU-U230F3	14.1%

Table 1.1: Specification of commercially available solar modules

For this estimation, the United States can be considered to have an equivalent sun hours value of 4 hours [28], such that over the course of one day, the amount of solar light in this area is equivalent to the irradiance of 1kW/m^2 for a duration of 4 hours. For an installation using the Sharp NU-U230F3 panels with a rated efficiency of 14.1%, the energy generated per square metre over the course of one day is 0.56 kWh / m^2. With the use of an advanced design solar cell, for example the SunPower Corporation X-Series device with a rated module efficiency of 21.5%, the energy generated over the day is 0.86kWh / m^2, a significantly higher power per square metre. Assuming the use of the Sharp solar device, the family of three would require 30m^2 of photovoltaic devices for their requirements of 16.5 kWh per day to be met. This would necessitate a roof area of around 5m x 6m covered with photovoltaic modules. The advanced SunPower solar device with 21.5% efficiency would only require 19m^2, which requires a roof area of less than 4m x 5m to be covered by photovoltaic modules, nearly 40% less area. This type of installation could be achieved on a residential roof easily, or even on a garage or outbuilding. Assuming the standard module packaging size of approximately 1.6m x 1m, the high-efficiency SunPower solution would require 12 units, whilst the Sharp system would require 19 units.

It is possible to predict the number of panels which would be required to address the total energy consumption of a particular country. Table 1.2 details the equivalent sun hours (ESH) of a series of countries, the approximate area of the country in km^2, together with their total energy consumption per annum. In the following example, the United States is highlighted due to its large per-capita energy consumption.

Country	**ESH**	**Area (km^2)**	**Energy Consumption**
United States	4	9,826,675	3,886,400,000 MWh
United Kingdom	2.5	243,610	344,700,000 MWh
India	5	3,287,263	959,070,000 MWh
Brazil	4.5	8,515,767	455,700,000 MWh
Spain	4.5	505,992	267,500,000 MWh

Table 1.2: Regional energy requirements

In the United States, assuming the use of the 300W SunPower modules described, one panel will generate:

$300W \times 4h \times 365days = 438,000 \, or \, 438 \, kWh/year.$

The total energy consumption of the United States is 3.89x10^9 MWh / year, and so the number of 300W panels required is:

$3.89 \times 10^9 / 0.438 = 8.881 \times 10^9 \, units.$

This can be further broken down into the percentage of the total area of the country. The 300W SunPower module has an area of 1.5m^2, and so the required area of panels to meet the total energy consumption is:

$8.881 \times 10^9 \times 1.5m^2 = 13.32 \times 10^3 \, km^2.$

The United States covers 9.826x10^6 km^2, and so the total percentage of solar panels required to power the entire country is:

$13.32 \times 10^3 / 9.826 \times 10^6 = 0.13\%$ of the total land area.

An alternative method of quantifying the costs and potential acceptance of solar photovoltaic energy as a primary source of energy in the wholesale market is to compare it to wind-generated electricity. In areas of high wind collection potential, on-shore turbine generators have advantages over solar in that the installed costs fall below $1/Watt and require less land area, however the installation of such turbines is often problematic as nearby residents object to their appearance, noise and potential maintenance issues. These issues together with the inherent variable output dynamics which are shared with solar energy means that wind energy in the UK is rarely embraced on a large scale by the mainstream energy suppliers.

1.4 Objectives

This work aims to address the following research objectives:

- The optimisation of deposition parameters which can affect or enhance the performance of amorphous silicon photovoltaic devices, including evaluation of the use of argon gas within the deposition apparatus.
- The performance enhancement of such devices, by means of effective optical path-length increases achieved by the incorporation of optical plasmonic light scattering nano-particles.

The *high-performance* metric is satisfied by means of reporting appreciable electrical performance from the silicon thin films, as described in the literature; and a performance enhancement has been proven by means of incorporating light scattering nano-particles.
Within this report:

- **Chapter 1** introduced the political and economic rationale for renewable energy and explains the metric of energy conversion efficiency and its requirement in modern solar devices.
- **Chapter 2** presents a summary of the existing *silicon* solar cell technologies, together with the current industry records and major academic and industrial researchers. The principles of photovoltaic cell operation are explained, including the optical designs central to this thesis.
- **Chapter 3** describes the design and fabrication methods in detail, together with potential advantages or each technique. The simulation tools are introduced with justification for their applications.
- **Chapter 4** presents a summary of the practical work undertaken on amorphous P-I-N devices and the optimisations performed to achieve the completed devices.
- **Chapter 5** details the optical simulations performed using the numerical finite-difference time-domain (FDTD) method, to enhance the performance of the photovoltaic devices. The development of the optimum topography and dielectric environment is shown together with the simulated results.
- **Chapter 6** describes the practical fabrication of nano-particle arrays on various substrates and the measured optical characteristics, and details the resultant enhancement of the silicon photovoltaic device. Comparisons are made to the simulated results in the previous chapter.
- **Chapter 7** concludes this study with an overview of what is achieved, and a discussion of the important contributions of this work. A view towards applying these techniques using electron-beam lithography is considered as future extensions to this work. Further optimisation techniques are additionally described.

Chapter 2

Literature Review

2.1 The Birth of Photovoltaics

The photovoltaic effect was first observed by A. E. Becquerel in 1839, using coated platinum electrodes immersed in an acidic solution. This arrangement was originally used for measuring light intensity of heated bodies, although no discussion of the generation of electricity was suggested [29]. Many years later in 1873, photo-conductivity was observed in the semiconductor material selenium by W. Smith [30], which was soon followed in 1877 by the first observation of electrical current by W. Adams and R. Day [31]. The first practical photovoltaic cell was demonstrated later in 1883 by C. Fritts [32], with a device based on selenium coated with gold to induce charge carrier separation and collection. This resulted in a device which would produce an energy conversion efficiency of around 1%. These phenomena were explained by Einstein in 1905 [33] for which he received the Nobel Prize for scientific breakthroughs and was a major contributor to the upcoming quantum revolution.

Concurrently, the semiconductor material silicon was under intensive research in the field of rectifiers, for use within crystal radio sets. In 1918 Jan Czochralski was working on the crystallization of silicon material, and devised the Czochralski process of growing single-crystal silicon wafers [34]. This discovery was not only essential for the proliferation of the modern silicon p-n junction diode, but laid the foundation for the design of solar cells made from single crystal silicon. It was noted in 1941 by R.S. Ohl [35] that a well-defined barrier exists within cooled crystal ingots of silicon material, which could be used to generate electrical current from light irradiance. The first modern device using silicon material, with a diffused p-n junction was demonstrated in 1954 by engineers D. Chapin, C.S. Fuller and G. Pearson at the Bell Telephone Laboratories (USA) [36], which exhibited a 6% energy conversion efficiency. Gradually these conversion efficiencies were increased with refinements and optimisations to an efficiency of 11%.

2.2 Operation of a Photovoltaic Cell

The basis of operation of a photovoltaic device is that of photon absorption and charge carrier collection. This is best achieved by the use of semiconductor material with an optical band-gap matched to that of the optical emission peak of the solar spectrum. This arrangement causes a large number of optically-excited free charge carriers to appear within the material under irradiance, and can be observed by an increase in the conductivity of the material under these conditions. The second step is the collection of the charge carriers within the device; this is achieved by the use of doped regions within the material which serve to separate the positive *p-type* and negative *n-type* charge carriers into these regions. These charge carriers are the optically excited holes and electrons, respectively, and sustained irradiance of the photovoltaic device will cause these charges to accumulate. Electrical connection to these regions will result in a current flow proportional to the rate of optical excitation, which can depend on many factors relating to the design and manufacture of the photovoltaic device [37].

2.2.1 I-V Characteristics

The structure of the silicon photovoltaic cell is similar to that of a standard silicon junction diode. Therefore under dark conditions, a photovoltaic cell will behave as a silicon diode when voltage bias is applied to the terminals. This diode will allow conventional current to flow in one direction, from the anode to the cathode, but not in the opposite direction. As can be seen from the I-V characteristic in figure 2.1, as voltage is applied in the forward-bias direction very little current flows until the built-in potential of 0.7 V is overcome, at which point the current can flow unimpeded.

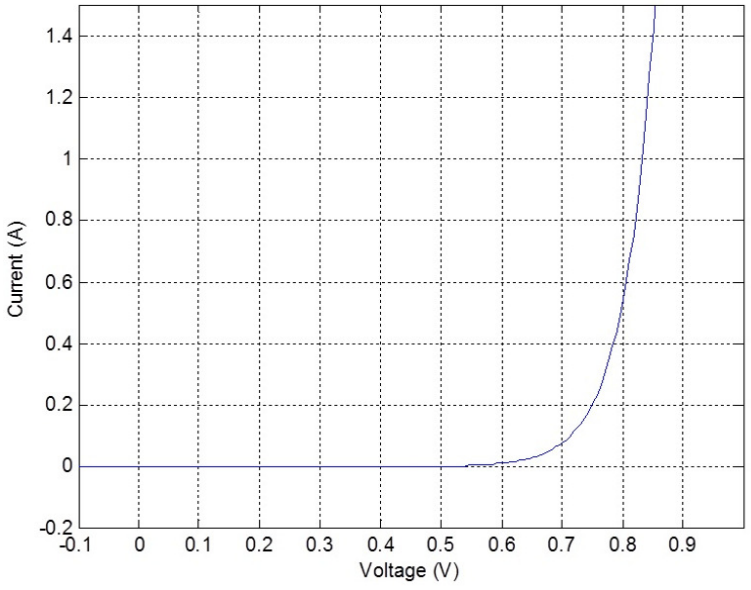

Figure 2.1: Simulated I-V characteristics of a silicon diode

However if the voltage is applied in the reverse-biased direction, the only current which can flow is the very small reverse saturation current, due to the leakage of minority charge carriers, until the point at which the breakdown voltage of the diode is reached. The current flow characteristics can be modelled by the Shockley diode equation 2.1: [38]

$$I = I_0 \left(e^{\frac{qV}{nkT}} - 1 \right) \tag{2.1}$$

Where:
n = Ideality factor
k = Boltzmann's constant
T = Absolute temperature
q = Elementary charge
V = Voltage applied
I_0 = Reverse saturation current

Within a photovoltaic device, this diode response is supplemented by the light-generated current I_L, caused by the absorption of photons. This has the effect of shifting the curve in to the forth quadrant of the I-V axis, which augments the existing *dark* current within the diode. The diode current equation therefore becomes equation 2.2:

$$I = I_0 \left(e^{\frac{qV}{nkT}} - 1 \right) - I_L \tag{2.2}$$

This equation is often re-written to show the increase in light-generated current in the first quadrant, while the -1 term can be neglected in most calculations due to the comparative sizes of the exponential term. The I-V curve equation therefore becomes as per equation 2.3:

$$I = I_L - I_0 \left(e^{\frac{qV}{nkT}} \right) \tag{2.3}$$

The short-circuit current I_{sc} of a photovoltaic device is an important measure of cell performance, and in most configurations is equal to the light-generated current I_L. The value is dependent on the intensity and spectrum of the light source, the optical generation rate of the solar cell, and the electronic properties of the bulk material.

The performance of photovoltaic devices of the same material type and a constant generation rate can be compared by means of the electron and hole diffusion lengths, and therefore an approximation of the short-circuit current or light-generated current is per equation 2.4:

$$I_L = qG(L_n + L_p) \tag{2.4}$$

Where:
G = Generation rate (assumed uniform)
L_n = Electron diffusion length L_p = Hole diffusion length

The open-circuit voltage of a photovoltaic device is determined by the energy difference between the quasi-Fermi levels for electrons and for holes under open-circuit conditions, and therefore the use of a wider band gap material generally results in a larger V_{oc}. The use of wide band-gap materials, however, will result in a reduction in the density of photons absorbed by the material, particularly within the long-wavelength range such as red and near infra-red, and therefore an impaired I_{sc}.

In addition to the band-gap, the extent to which the quasi-Fermi levels are able to split is determined by the density of dopant atoms within the material, and therefore the V_{oc} in a given material is primarily determined by the doping levels in each region of the device. The V_{oc} of a semiconductor material can be determined by equation 2.5 [37] :

$$V_{oc} = \frac{nkT}{q} ln \left(\frac{I_L}{I_o} + 1 \right) \tag{2.5}$$

This can also be expressed in terms of the carrier concentration, giving the *implied* V_{oc} in equation 2.6 [39]:

$$V_{oc} = \frac{kT}{q} ln \left(\frac{(N_A + \Delta n)\Delta n}{n_i^2} \right) \tag{2.6}$$

Where:

k = Boltzmann's constant

T = Absolute temperature

q = Elementary charge

I_L = Photo-generated current

I_o = Reverse saturation current

N_A = Doping concentration

Δn =Excess carrier concentration

n_i = Intrinsic carrier concentration

From these formulas it can be determined that the V_{oc} is dependent on the light-generated current of the solar cell, therefore under standard conditions if charge carrier lifetime is increased, then the quasi-fermi levels are able to split to a greater extent and the V_{oc} will be increased. The charge carrier lifetime is proportional to the defect density of the material which is itself dependant on the device material quality, manufacturing techniques and device design. Similarly, an increase in the reverse saturation current, dependent on the recombination rate within the device, serves to reduce the V_{oc} and is therefore a useful measure of device quality.

The implied V_{oc} shows that as the intrinsic carrier concentration n_i is increased, due to an increase in device temperature, a reduction in V_{oc} will be observed; while an increase in excess carriers Δn due to increased device quality or an increase in I_L, or to a lesser extent an increase in doping N_A, the device performance and correspondingly V_{oc} will increase [40].

The diode-like characteristics of the photovoltaic module when voltage is applied in the forward biased direction are simulated in the Mathworks Matlab software package in figure 2.1. Very little current is observed to flow until the built in potential voltage at 0.7 V is reached at which point an exponential increase is observed.

The characteristic observed in figure 2.1 changes significantly when light is supplied to the active area of the device. Current will be generated and flow from the electrical contacts, which causes the curve to drop below the x-axis into the forth quadrant, continuing on to a peak current as more charge carriers are absorbed. For simplicity, it is conventional to invert the I-V characteristic of the device about the y-axis, as in figure 2.2, so that the photo-generated current is indicated in the positive y-direction.

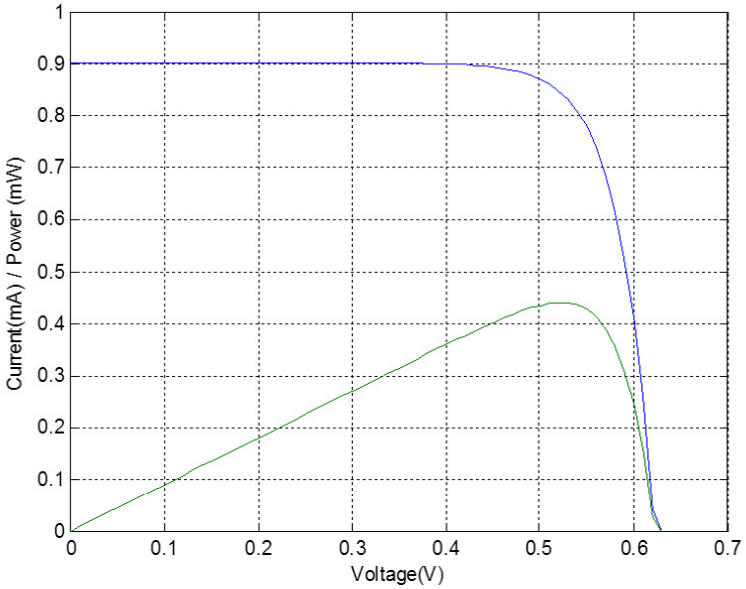

Figure 2.2: Simulated I-V characteristics of a silicon photovoltaic cell

Figure 2.2 shows this characteristic of a typical small crystalline silicon photovoltaic device (blue) under standard test conditions, with a short circuit current of 0.9 mA and an open circuit voltage of 0.62 V. The power output is also depicted on this graph (green), showing a peak of 0.44 mW at the maximum power point. At this point the characteristic resistance of the cell is equal to the resistance of the load, and therefore maximum power is transferred. The cell should always be operated under these conditions when connected within a photovoltaic system in order to obtain the peak power from the device [38].

The fill-factor is an important measure of how much usable power can be extracted from the cell across its range of operation. It is most strongly affected by the parasitic resistances within the cell, such as the contact grid. It is defined as the ratio of the area encompassed by the voltage and current at the maximum power point, and by the area encompassed by the I_{sc} and V_{oc} points. The maximum cell output power in Watts can be obtained by multiplying the product of V_{oc} and I_{sc} by the fill factor ratio. The efficiency of the cell can be obtained by dividing this maximum output power by the light power supplied to the cell in Watts. Once the fill factor is known, the maximum

power point, and overall efficiency of the device can be obtained. It is also possible to derive estimated values for the non-ideal component values in this circuit from the collected results. The R_{sh} and R_s values, the series and shunt resistances can be read from the I-V characteristic graphs from the observed results.

Variables are determined using the following formulae 2.7 - 2.11:

$$Fill\ Factor = \frac{V_{mp}I_{mp}}{V_{oc}I_{sc}} \tag{2.7}$$

$$Maximum\ Power\ Point = V_{oc}I_{sc}FF \tag{2.8}$$

$$Efficiency\ (\%) = 100\frac{V_{oc}I_{sc}FF}{P_{in}} \tag{2.9}$$

$$R_{sh} \approx \frac{V_{mp}}{I_{sc} - I_{mp}} \tag{2.10}$$

$$R_s \approx \frac{V_{oc} - V_{mp}}{I_{mp}} \tag{2.11}$$

Where:
V_{oc} = Open circuit voltage,
I_{sc} = Short circuit current,
V_{mp} = Voltage at MPP,
I_{mp} = Current at MPP,
P_{in} = Power (W/m^2).

2.2.2 Solar Cell Equivalent Circuit

To analyse a photovoltaic device within a circuit, it is useful to consider the cell as a collection of well-understood electrical components. Under dark conditions the photovoltaic device behaves as a silicon p-n junction diode. There will be no optically generated current under these conditions, electrical current will only be produced when the device is irradiated. As this current remains relatively stable for various output loads, an ideal current source is used to model its behaviour. This current source is connected in parallel with silicon junction diodes to model the diode behaviour of the solar device. Series and shunt parallel resistances are connected to complete equivalent circuit, to represent the resistive contacting and non-ideal electrical isolation between the top and bottom surfaces of the device, respectively. This configuration is depicted in figure 2.3. In ideal circumstances, the series resistance R_s would be zero, offering no resistive losses and no reduction in the output of the cell, while the shunt resistance R_{sh} would be an infinite value offering ideal insulation between cell regions and no short-circuit route for current to flow. The total current produced by the device is the current generated by the current source, minus the current flowing through the two diodes and through the shunt resistor. The characteristic formula of the solar cell is therefore as per equation 2.12:

$$I = I_L - I_0 \left[exp \left\{ \frac{q(V + IR)}{nkT} \right\} - 1 \right] - \frac{V + IR_s}{R_{sh}} \tag{2.12}$$

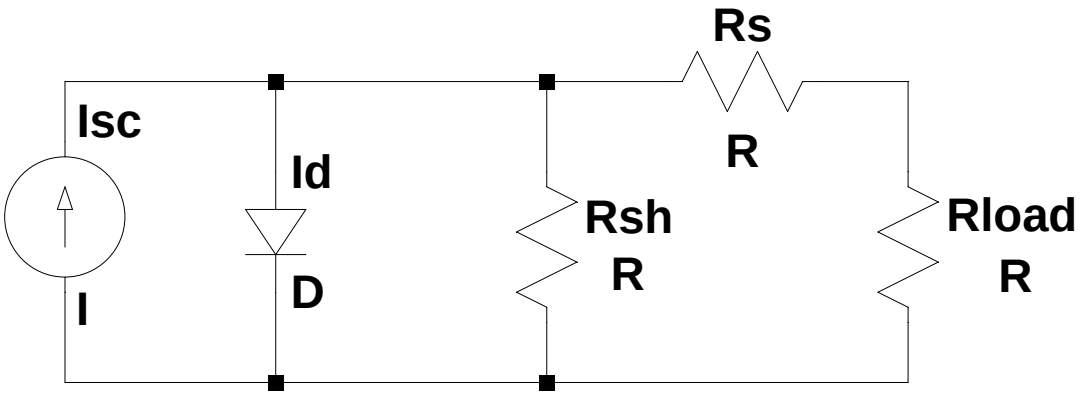

Figure 2.3: Equivalent circuit of a photovoltaic device

2.3 Properties of Silicon

Despite the first investigations with selenium and platinum, the most common material for solar cell production is crystalline silicon. Silicon wafers have been in use for many years as one of the base materials for solar cell manufacturing, and as a mature technology with many suppliers offering 20+ year guarantees on their cells. Silicon is a very abundant element, constituting approximately 28% of the Earth's crust and is very cheap to process into its raw elemental form. It possesses well-known physical, electronic and chemical attributes, and is one of the most researched elements in the world and so many of the required facilities for processing silicon wafers already exist [41].

Silicon atoms possess four valence outer electrons, and therefore exhibit a partially filled 3s/3p electron shell. This outer electron shell creates an SP3 hybridized symmetrical arrangement at 109.5 ° and is the cause of the diamond cubic crystalline lattice of crystalline silicon. When a number of silicon atoms are brought together, the SP3 orbitals merge in accordance with the Pauli Exclusion Principle and form one singular bonding orbital at a lower potential energy than the individual atoms. It is therefore energetically favourable for single-crystal silicon material to form tetrahedral covalent bonds, arranged into a diamond crystal lattice. Additionally, an anti-bonding orbital is formed at a higher potential energy level than the individual SP3 orbitals, but due to the energy required few electrons normally occupy this energy level at thermal equilibrium [42] .

Due to the arrangement of silicon atoms within a crystal structure, very few defects exist within the bulk material. Defects are defined as an unsatisfied covalent bond, stressed or stretched bond length or an impurity atom within the lattice. This lack of defects or grain boundaries ensures that the resulting material has the longest possible charge carrier lifetime, and it is this that allows single-crystal silicon to attain the highest energy-conversion efficiency of all the various types of silicon-based photovoltaic devices available. The full *bonding* electron shell corresponds to the valence band within the semiconductor material and the *anti-bonding* orbital corresponds to the conduction band. At a temperature of absolute zero, silicon material does not pass any current as there are no free charge carriers available. The conduction band is free of electrons and the valence band is entirely full. This condition forbids any electrical current from flowing through the material as no electrons can move freely. An increase in temperature causes electrons from the valence band to be thermally excited, break their bond with their host atom, and move to the conduction band overcoming the forbidden energy gap.

This condition occurs at room temperature for a semiconductor such as silicon, which allows it to become a poor electrical conductor (typically $1x10^5$ Ωcm), rather than an insulator. Limited electron movement through the crystal lattice is now possible due to the free electrons in the conduction band, and the vacant electron state which remains in the valence band. This vacant state (or *hole*) can be filled by the electron from a neighbouring atom, which itself then possesses the vacant state. By this method the *hole* can move throughout the lattice as a positive charge carrier. Bi-polar conduction can

therefore take place using the mechanism of electron and hole movement. For silicon, the mobility of an electron is significantly higher than that of a hole, and therefore it is easier to conduct current through the movement of electrons than through the movement of holes [43].

The absorption of photons by means of optical irradiance will provide significant energy to the silicon crystal lattice, and will promote many valence band electrons into the conduction band. These electrons and their associated holes in the valence band are now also available for electrical conduction, and therefore the conductivity of the silicon material increases. The number of electrons which are promoted is dependent on the generation rate, depicted in equation 2.13, which is defined by the absorption coefficient of the material. This absorption coefficient, α, varies in accordance with the wavelength of the light used to irradiate the material, and is depicted in figure 2.4 for crystalline silicon.

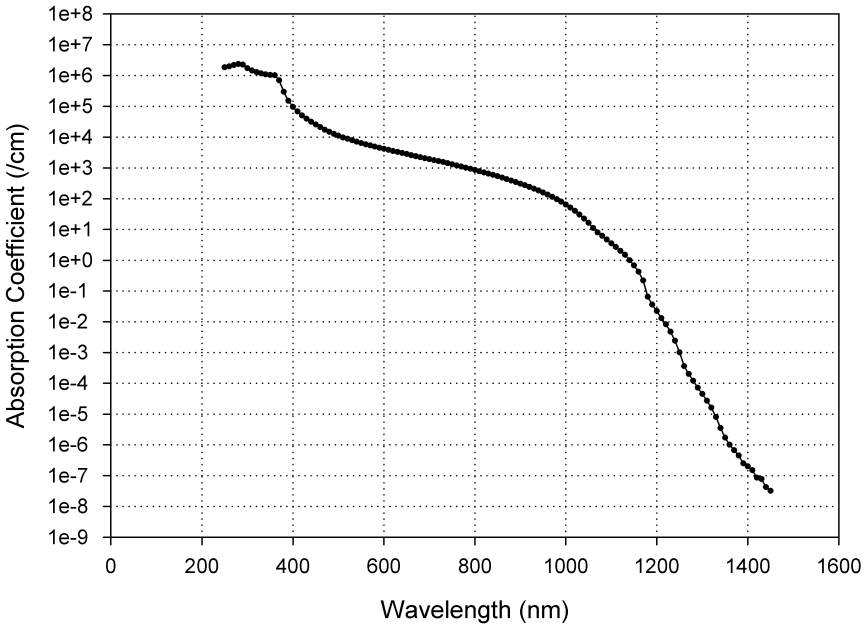

Figure 2.4: Absorption coefficient of silicon [44]

The wavelength-dependant generation rate of free charge carriers when illuminated with a monochromatic light source is therefore given by equation 2.13:

$$G_L(\lambda) = \alpha(\lambda) N_0 e^{-\alpha(\lambda)x} \tag{2.13}$$

Where:
α = Absorption coefficient,
N_0 = Photon flux (photon/area/sec),
x = Distance into the material

The region of energy within the solar spectrum which can be collected using a single-junction photovoltaic device is limited. The *band-gap* of a particular material defines which portion of the solar spectrum the material is sensitive to and can collect photons from. Crystalline silicon, with a band-gap of 1.12eV, is sensitive to the region of wavelengths shorter than 1107nm, and photons with a longer wavelength than this value are not absorbed and transmitted through the device. Amorphous silicon features a larger band gap of around 1.8eV, which further limits the wavelength region to shorter than 680nm. Photons with energies in excess of this value are absorbed and cause the electrons to be temporarily promoted to higher energy states, however this excess energy is subsequently lost as the electron thermalises back down to the conduction band edge. The external quantum efficiency (EQE) is a measure of ratio of the number of optically generated charge carriers, to the number of photons of that wavelength incident on the solar device. The quantum efficiency curve illustrates the effect of the band-gap energies, where no photon energy is absorbed and the EQE is zero, while the effects of other performance-reducing attributes can also be observed such as photon reflection and transmission, insufficient device thickness and rear, bulk and surface recombination.

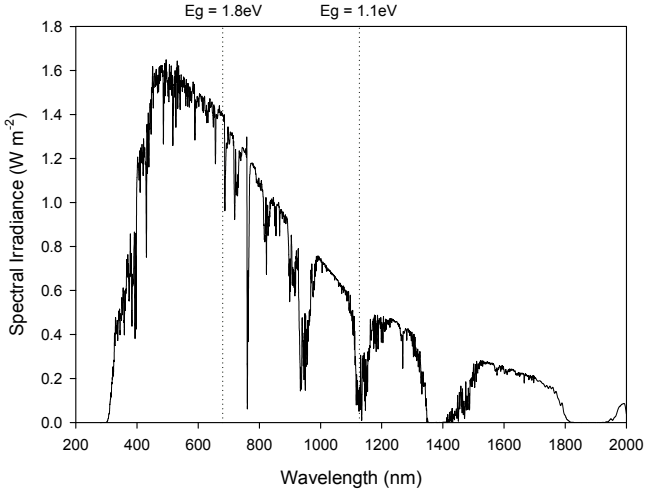

Figure 2.5: AM1.5 (Direct) solar spectrum [45]

The AM1.5 solar spectrum illustrates the density of photons which can be collected from the Sun's rays in each wavelength region. The *ASTM G-173-03* international standard was introduced to standardise the reference spectra used to compare photovoltaic device performance, and is generated using the SMARTS software package (Simple Model of the Atmospheric Radiative Transfer of Sunshine) [45]. The AM1.5 Global spectrum has an integrated power of 1000 W/m^2 (100 mW/cm^2) and is shown in figure 2.5. Concentrator solar cells require an alternative model, the *AM1.5 Direct (+circumsolar)* spectrum to account for the light within 2.5 degrees around the sun. The integration of the wavelength-dependant spectral photon flux results in the photon flux, which reaches a total of $4.3 \times 10^{21} m^{-2} s^{-1}$ up to a wavelength of 4,000nm. The photon flux absorbed by a particular semiconductor material is limited to the band-gap energy wavelength.

For crystalline silicon, for the wavelength region of 300-1100nm and an ideal EQE of 100% under AM1.5 conditions, the maximum theoretical I_{sc} is calculated to be $43.7mA/cm^2$ For a realistic photovoltaic device with an EQE of 90% under AM1.5 conditions, the maximum possible J_{sc} is calculated to be $39.4mA/cm^2$, which is in agreement with measurements from the best laboratory cells described in section 2.3.

The band gap of a semiconductor material can be defined as either *direct* or *indirect*, depending on a number of factors. If the band gap is considered as direct, than the lowest point of the conduction band and the highest point of the valence band are aligned with respect to charge carrier momentum (k), and electrons are able to move freely between bands with only photon energy being required. If the bands are not aligned, such as in the case of crystalline silicon, then a change in charge carrier momentum k (wave-vector) is required in addition to photon energy to move between the two bands. This transition requires the electron interaction with a *phonon* which, upon radiative recombination, causes the generation of heat within the active region. These materials are therefore significantly less effective at absorbing light energy than direct band-gap materials, and require much greater device thicknesses to adequately absorb the incident photon flux.

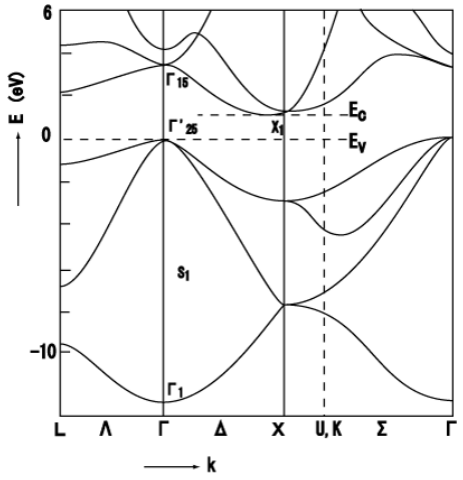

Figure 2.6: E-K diagram of crystalline silicon [46]

As can be seen in the energy-momentum diagram for crystalline silicon presented in figure 2.6, the material requires a change in crystal momentum in order for valence band electrons to be excited to the conduction band. The magnitude of this band gap is 1.12eV, and therefore the material is able to absorb only wavelengths shorter than 1107nm. Indirect band-gap materials such as silicon have direct transitions at certain momentum-space directions. These transitions occur at higher photon energies than the indirect transition, and therefore a significant increase in the absorption coefficient occurs at energies higher than this level. Crystalline silicon has a direct transition at 3.4 eV, which produces a peak in the absorption coefficient for wavelengths shorter than 360 nm as can be observed on the absorption coefficient graph in figure 2.4.

Many different semiconductor materials, however, possess the necessary characteristics to be used in solar cells. The neighbours to silicon in the periodic table are routinely used in alternative designs of solar devices, the requirements are a crystallographic structure with few defects, a band gap which is suited to visible light, and the ability to form a junction for charge carrier separation. The electronic band gap is a measure of electron-lattice interaction, specifically the extent to which the bonding and anti-bonding states split which is dependant on the atomic spacing within the lattice. Close bonds between atoms with few electrons exhibit a wide energy gap between bonding and anti-bonding states. The band gap is therefore a function of the quantization of the electron energy states within a material. Crystalline silicon has an electronic configuration of $[Ne]3s^2 3p^2$, a lattice constant of 0.54nm and an electronic band gap of 1.1eV, while other materials with a similar electronic configuration in group IV of the periodic table also possess semiconductor properties, such as crystalline germanium with a lattice constant of 0.57nm and band gap of 0.66eV. Crystalline carbon (diamond) has an electronic configuration of $[He]2s^2 2p^2$, a much smaller lattice constant of 0.35nm and therefore features a wide band gap of 5.5eV. This material is therefore a strong insulator and unsuitable for semiconductor applications [47]. Compounds of materials within different groups of the periodic table also exhibit semiconducting behaviour, such as gallium phosphide and gallium arsenide from groups III and V; and cadmium telluride from groups II and VI. Figure 2.7 details some of the available semiconductor materials, together with their lattice constants and band gaps.

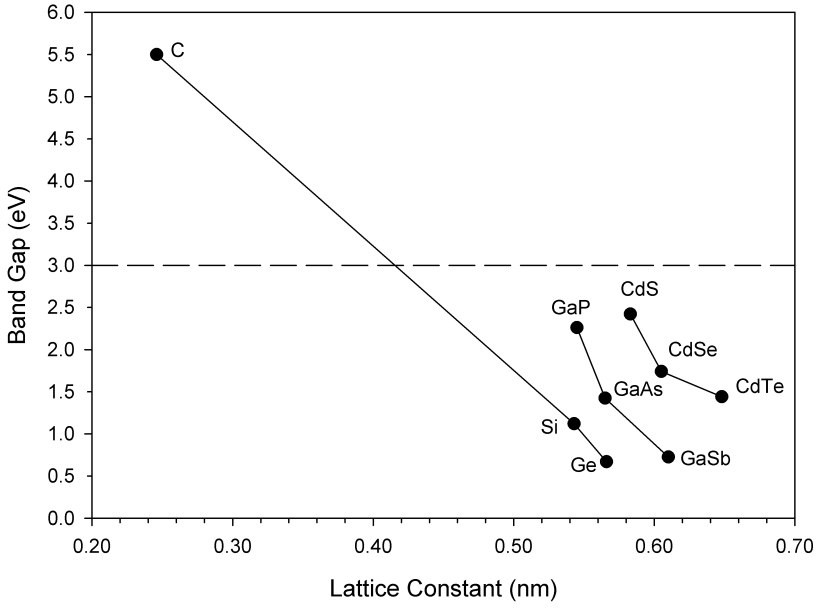

Figure 2.7: Semiconductor materials and their lattice characteristics

2.3.1 Doping and the Operation of the P-N Junction

In addition to the generation of optically excited charge carriers, the ability to separate these charge carriers for collection is fundamental to the operation of the photovoltaic device. This is achieved in silicon solar cells using doped regions of semiconductor material, which draw the charge carriers away from the depletion region and towards the electrical contacts. Doping is achieved either during manufacture or using high temperature diffusion techniques, and significantly changes the density of free electrons or holes within a material. This increases the conductivity of the material by several orders of magnitude, and makes it possible to pass current through the semiconductor. The levels of doping within the semiconductor, and the corresponding change in resistivity are detailed in table 2.2.

Doping	**Dopant Type**	**Atoms cm^{-3}**	**Resistivity (Ωcm)**
Undoped	Intrinsic	0	≥ 1000
Lightly	n- / p-	$10^{13} - 10^{15}$	10 - 1000
Moderately	n / p	$10^{15} - 10^{18}$	0.1 - 10
Highly	n+ / p+	$10^{18} - 10^{20}$	0.001 - 0.1
Very Highly	n++ / p++	$\geq 10^{20}$	≤ 0.001

Table 2.1: Doping levels in crystalline silicon

Doping can be achieved by substituting silicon with trace amounts of impurities with a different electronic configuration. Mixing the silicon with an element from group III of the periodic table, for example boron, will result in a number of the silicon atoms becoming substituted. As boron has three electrons in its outer valence shell it can only form covalent bonds with three surrounding silicon atoms, therefore a vacant electron state remains within the crystalline matrix. The surrounding silicon atoms require this missing electron in order to achieve octet stability and a lower energy state, and so a free electron from a nearby Si-Si bond quickly fills this position. This leaves another vacant electron state elsewhere which results in a localised positive charge in the matrix. It is by this method the vacant state and therefore positive charge can be considered mobile and propagate through the matrix. The original boron atom has now become ionized with the accepted electron, and therefore a fixed negative charge now exists within the crystal. This is regarded as a p-type doped semiconductor. Similarly, n-type doping can be achieved by using an element from group V of the periodic table, for example phosphorus or arsenic. As phosphorus has five electrons in its outer valence shell, this fifth electron does not participate in covalent bonding and is easily lost, providing a free mobile charge carrier. The original phosphorus atom is also now ionized as it has lost an electron, and so a fixed positive charge now exists within the crystal. A junction can be formed by creating both n-type and p-type regions within a single piece of silicon material. This results in a p-n junction which forms the basis of the operation of silicon junction diodes and photovoltaic cells. At the interface between the two regions, the

concentration gradient causes the mobile charge carriers in each region to diffuse into the opposing area where their density is much lower. The fixed charges within the lattice in each region cannot diffuse, and begin to create an opposing electric field as the mobile charge carriers diffuse away, which attracts them back into their native region. This mechanism is known as the drift potential, or built-in electric field, and these two mechanisms form an equilibrium at the point where the drift and diffusion forces are equal. Nonetheless, a number of charge carriers near the interface do diffuse across and will recombine due to the high density of opposite charges in this region. This creates an area which is depleted of all mobile charge carriers, and contains the fixed positive charges in the n-type region and fixed negative charges in the p-type region. This is is the *space charge* or depletion region, depicted in figure 2.8.

Charge carrier pairs which are created using thermal or optical means within this space charge region are immediately separated and drawn into their native region by the fixed charges. Charge carrier pairs generated within the doped regions only supplement the number of minority carriers (electrons in the p-type and holes in the n-type region) as the number of majority carriers introduced by the doping mechanism always far exceed those generated by optical excitation. Provided the minority charge carriers do not encounter a recombination centre, drift currents will cause them to move across the junction into their native region in which they become majority carriers. This causes a semiconductor under illuminated conditions to generate a large number of free charges, which accumulate at the doped regions, until the built-in electric field is reduced. An open-circuit voltage can be observed between these areas due to these accumulations, and if an electrical circuit is connected between the n-type and p-type regions, the accumulating charges will flow through the circuit and recombine at the opposing side. It is by this method that electrical current can flow and net power is produced by the photovoltaic device [38].

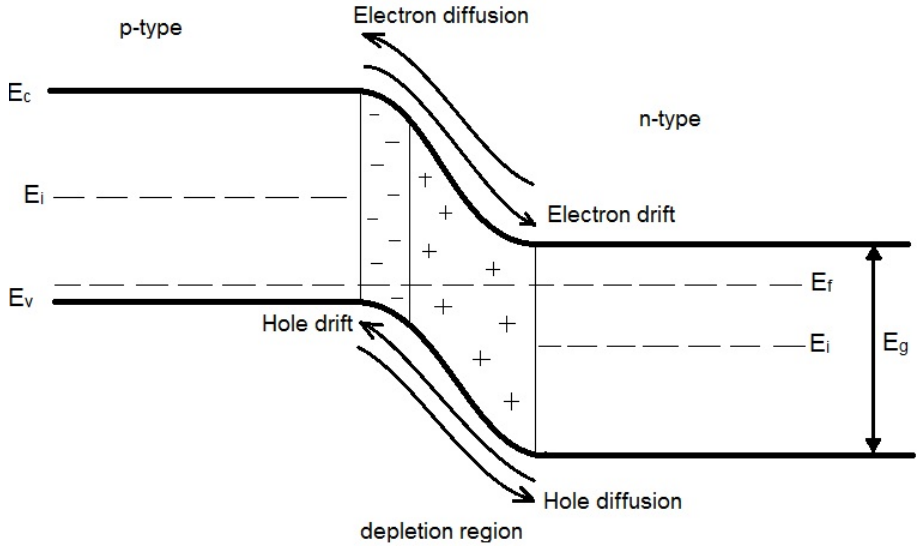

Figure 2.8: Electronic band structure of a P-N junction at equilibrium

2.3.2 Conventional Silicon Solar Cells

By the 1980s, the cost of silicon solar cells had fallen by a factor of 10, and due to intensive research and investment by major energy corporations, energy conversion efficiencies had reached in excess of 14%. [48] During the next decade, the crystalline silicon wafer designs continuously evolved and optimised since the early devices, and significant efforts were directed to development of lab-scale high efficiency devices. The efficiency record for many years was held by the University of New South Wales' *PERL* device (Passivated Emitter Rear Locally-diffused), at 25.0%. [49] The record efficiency was achieved through several optimisations, including the passivation of cell surface areas, significantly reducing surface recombination rates and therefore enhancing the charge carrier lifetime. Surface recombination velocity is by far the most significant loss mechanism, and effective passivation is therefore essential. The wafers are 450μm in thickness, and manufactured using the float-zone technique which ensures the lowest possible concentration of oxygen and boron contamination. The cell surface passivation is performed using trichloroethane oxidation, which has then been treated with an aluminium 'alneal' and 400 °C sintering process; which further reduces recombination losses at the surface regions. An inverted pyramid structure is formed on the front surface using anisotropic KOH etching, which maximizes optical absorption and internal reflection, while the top surface layer is treated with an MgF_2/ZnS anti-reflection coating. Contact regions are heavily doped to reduce charge carrier concentrations in these areas, and the metallization regions are defined as thin as possible through $10\mu m$ holes in the oxide at the rear and a $2\mu m$ strip on the front surface.

A variation of this design is the *PERT* cell, which is designed to be used on lower quality Czochralski silicon wafers. The rear surface of the cell is lightly diffused with boron across its entire surface in addition to in localised areas as in the PERL device, which helps to reduce the current crowding effects of very small dimension contact regions on high resistivity wafers, and further helps to prevent rear surface recombination. All other processing steps follow that of the PERL design [50].

Lab-scale photovoltaic devices serve to illustrate what is possible with extensive optimisation, however the cost of such devices is often prohibitive for commercial applications. Lower efficiency and cost-reduced devices dominate in these markets, with cost reduction up to the present day has in part been achieved due to the near-ubiquitous use of silicon substrates within the electronics industry and requiring very similar processing and deposition techniques. The most popular design of photovoltaic cell as of 2015 by a significant margin is the diffused-emitter crystalline or poly-crystalline silicon solar cell [19]. Such devices use screen-printed contacting which is inexpensive and simple to fabricate, and feature surface texturing and anti-reflection coatings to increase performance. More advanced devices at a somewhat higher price point feature buried contacts, which mitigate some of the disadvantages of the screen-printing method and utilise a laser scribe to form a groove of high aspect ratio, which is plated with the metallisation

material and forms the contact. This method reduces the shading loss of the contact from around 10-15% down to 2-3% [51] whilst in some cases improving the charge carrier collection ability due to a reduction in parasitic resistance. The emitter of such devices can be optimised for this type of contacting method with very a highly doped shallow emitter region to enhance the collection of short wavelength light. Price points have continued to fall to around $0.50/watt, [52] while the total *balance of system* cost, which includes all other components of the photovoltaic system, is now a significant factor.

2.3.3 Amorphous Silicon

The deposition of silicon thin films from silane gas can result in a non-crystalline solid, amorphous silicon. This type of material lacks the bond length consistency of conventional silicon, and therefore the crystalline structure with four satisfied covalent bonds cannot be maintained without forming dangling bond or floating bond defects. Materials which can easily form this amorphous, non-crystalline network generally have a bond number of 2.7 or less [37]. The presence of hydrogen within the silane gas allows these unsatisfied covalent bonds to be passivated using a hydrogen atom, and therefore forms a chemically satisfied structure. The bonded hydrogen atom is invisible to x-rays but becomes apparent with proton magnetic response, infrared spectroscopy and SIMS. Nonetheless, amorphous silicon has a significantly higher number of defects compared to the crystalline material, and therefore has very different optoelectronic properties. Table 2.1 shows a comparison of the charge carrier mobility in crystalline silicon and hydrogenated amorphous silicon.

Material	**Charge Carrier**	**Mobility (cm^2/Vs)**
c-Si	Electron	1400
c-Si	Hole	450
a-Si:H	Electron	10
a-Si:H	Hole	1

Table 2.2: Typical charge carrier mobility in silicon

The electronic configuration of amorphous and crystalline silicon also differs significantly. Crystalline silicon has clearly defined valence and conduction bands, forming a fixed band gap with a very low density of available electronic states available within it. As amorphous silicon lacks any long-range bond-length consistency it is not possible to clearly define a band gap for the material. Amorphous silicon has a large density of energetically available states within certain regions, with a decreasing exponential band-tail from these areas with fewer states. Within this gap, in addition to the energetically available states within these tails there exist defect states with significantly reduced charge carrier mobility; these states are representative of the d-centres and defects within the material, which are de-localised and behave as traps for charge carriers resulting in a very low charge carrier mobility within these regions. The exponential band-tails

are representative of the bond-length disorder throughout the film, and can vary in magnitude depending on the quality of the material and the extent of the disorder in the network. The valence band-tail is wider than that of the conduction band-tail, and is used to determine the *Urbach* tail of the spectrum. Typically, this band tail width is if the order 0.5eV.

Due to these energy levels, the band-edge energies are not clearly defined and so the material does not feature a conventional band-gap; instead a *mobility gap* exists between the two bands and energy is required to promote charge carriers beyond this region of limited carrier mobility. This configuration is shown in figure 2.9. For amorphous silicon, the magnitude of this ambiguous mobility gap can be determined using its optical absorption coefficient, which gives rise to the optical *Tauc* band-gap.

Amorphous silicon material is subject to the Staebler-Wronski Effect, a phenomenon whereby the electronic properties of the material are altered after a period of exposure to light. The effect causes an elevation in defect density within the material, which increases the recombination current and therefore causes a reduction in photovoltaic performance. The effect was discovered in 1977 by D. Staebler and C.Wronski [53, 54], proposing that the effect is due to the hydrogen bond switching model. This mechanism demonstrates that a recombining charge carrier can provide enough energy to break a weak Si-Si bond within the highly-disordered matrix, which is soon filled by a hydrogen atom. A *dangling bond* is therefore created which serves as an electron trap and reduces the electrical performance of the material [55]. Annealing of the material has been shown to reverse the effect, however this is seldom practical after the thin-film has been integrated into a photovoltaic module.

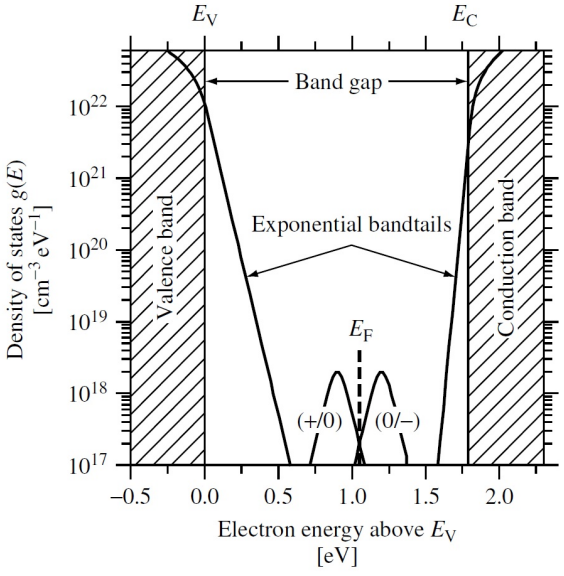

Figure 2.9: Electronic band structure of amorphous silicon [37]

2.3.4 Amorphous Silicon Solar Cells

The material properties of crystalline silicon are not the most ideal for use as photovoltaic material, as its energy band gap is indirect which provides a weak absorption coefficient in the visible range. For this reason the crystalline silicon absorber layers must be several hundred microns thick or have extensive light-trapping enhancements. A method of eradicating this significant expense and performance disadvantage is to deposit thin films of amorphous silicon material on to inexpensive substrates such as glass, aluminium or flexible polymers. The deposition of amorphous silicon results in a very different material to crystalline silicon. Due to the reduction in long-range atomic order, the material behaves as a direct band-gap absorber in the visible range, but with a much higher density of defect states within the energy band gap. This 'mobility gap' is wider at 1.6 - 1.7eV compared to the 1.12eV band-gap of crystalline silicon, resulting in reduced sensitivity to longer wavelength light [56]. The thin films can therefore be deposited in thicknesses less than $1\mu m$, using around 1% of the silicon material of a crystalline device. These cells are therefore suited to inexpensive indoor applications such as calculators and watches, as well as integration into window glass and building facades due to their cheaper fabrication costs and enhanced deposition flexibility.[57].

The initial experiments with amorphous silicon occurred in 1965 by Sterling & Swann using Plasma Enhanced CVD [58], as opposed to earlier techniques which utilised PVD thermal evaporation. PVD-evaporated films do not feature any hydrogen passivation of the unsatisfied covalent bonds therefore were not considered to be device grade material. The later PECVD investigations determined that silicon thin films deposited using CVD were potentially of device quality but no mention of doping, p-n junctions or solar applications were mentioned. More detailed investigations of amorphous silicon deposited using CVD occurred in 1969 by Chittick, Alexander and Sterling [59], detailing various deposition conditions. The first evidence of photo-activity in the intrinsic films was observed in this investigation, showing the optimum deposition temperature of 300 °C. The doping mechanism was first investigated but it was reported that this was not possible in amorphous silicon films. In 1970, the drift mobility of the PECVD generated amorphous thin films was investigated by Spear & LeComber [60] and was shown to be around $10\text{cm}^2/\text{V/s}$.

Three years later in 1973, R.J. Loveland, W.E. Spear, & A. Al-Sharbaty [61] demonstrated a high photo-response from amorphous silicon thin films. Spear & LeComber first discovered the doping mechanism in 1975, [62] showing that the electrical conductivity of amorphous silicon deposited using PECVD can be altered over many orders of magnitude, using doping levels of $5 \times 10^{-6}\text{at/cm}^3$, producing pentavalent and trivalent bonded impurities. Soon followed the implementation of a p-n junction produced by PECVD amorphous silicon in 1976, and it was stated that the rectification and photovoltaic response are qualitatively similar to a crystalline p-n junction [63]. However, due to the extremely low carrier mobility within doped regions of hydrogenated amorphous silicon, the conventional p-n structure utilised by crystalline silicon solar cells provides

very low energy conversion efficiencies. Finally, the first attempt at a solar cell device was performed by Carlson & Wronski in 1976 [64], using an innovative P-I-N structure, as opposed to the p-n junction design devised earlier. This type of design creates a large depletion region across the thick intrinsic absorber layer, allowing for photon absorption. This was performed using PECVD at substrate temperatures of 250 °C - 400 °C, and featured very thin layer of p-type silicon, followed by $1\mu m$ of intrinsic material, followed finally by several nm of n-type silicon material. It was noted that the energy conversion efficiency of this device was 2.4%

The deposition of amorphous silicon is generally performed using plasma-enhanced CVD, with small-scale investigations performed on Hot-Wire CVD [65]. It is necessary to optimise the deposition conditions to obtain devices with good performance, as silicon films with good optical and electrical performance are strongly process dependant. Deposition chamber geometry, RF power, chamber pressure, substrate temperature and gas flow rates (including hydrogen ratio) are all inter-linked conditions which influence the quality of the silicon films. Thoroughly optimised devices have an energy conversion efficiency of around 8-9%, after the initial stabilisation due to light soaking and effects of the Staebler-Wronski Effect (SWE), a phenomenon explained in section 2.3.1.

Despite the advantages, amorphous silicon photovoltaic devices have failed to capture a significant amount of the large-scale photovoltaic market. Many fabrication facilities have discontinued their terrestrial and commercial amorphous product lines in favour of the high-efficiency crystalline based devices [66]. Nonetheless, recent advances have seen very large area depositions of amorphous silicon devices, with efficiencies of 6.6%[22] and 7.84% [67] reported in sizes up to $5.7m^2$. Laboratory scale devices have undergone many optimisations, resulting in $1cm^2$ devices reaching 10.02% efficiency with an a-SiC:H layer [68], and a device featuring a micro-crystalline absorber layer attaining an efficiency of 13.4% [69]. Typical reported amorphous silicon devices without light trapping schemes report energy-conversion efficiencies of 6.5 - 7.5% [70] depending on reactor geometry, deposition conditions and substrate materials used.

2.4 Optical Design

Several optical loss mechanisms can affect the amount of the incident light which is able to be absorbed in a practical cell, including shading by the metallic contact grid, parasitic absorption by non-active layers within the device, transmission of long-wavelength light due to insufficient device thickness, and most significantly light reflection from the device interfaces. Due to the significant performance losses which can result from reflection from the top surface, detailed attention is paid to the optical topography. The use of anti-reflection coatings, light-trapping and path-length enhancement technologies can significantly improve the performance of a device, while the use of these technologies can also allow for a reduction in device thickness [71].

The principles of nano-photonics have been widely demonstrated in nature, with photonic structures being found in a wide variety of animals and plants including photonic reflectors, diffraction gratings and liquid crystals. Certain species of birds and insects such as butterflies, feature beautiful vivid colours which appear to change as they are observed at different angles. These colours are due not to pigment but rather a photonic diffraction grating tailored specifically to produce the range of colours observed [72]. Other examples of such structures include the eyes of a number of moth species, which feature a coating of zero-order diffraction gratings significantly reducing reflection and increase the moth's vision at night. These periodic structures additionally provide hydrophobic and self-cleaning properties to the eyes, further increasing their performance.

Such optical phenomena have been used for hundreds of years to create artefacts such as stained glass, enamelled ceramics and glass vessels using only gold nano-particles to create vivid variations in colour [73]. An everyday example of this occurrence can be observed on the surface of a compact disc, which features a diffraction grating of the order of light wavelength visually showing a wide variety of colours depending on the angle from which it is observed. These discs do not contain any pigments, the digital patterning on the surface of the disc is in the 700-800nm range which provides interactions within the visible range of the electromagnetic spectrum[74].

Photon energy propagating through a medium which is not vacuum is subject to the refractive index of that material, which cause the photons to slow down. This is caused by the interactions between the photon energy and the atoms within the material of propagation, within which absorption and subsequent re-emission occurs. This refraction can provide a change in direction of the wave depending on its angle of incidence, and is described by Snell's Law, detailed in equation 2.14. This suggests that the angle of incidence, with respect to the normal of the interface, will be equal to the angle of reflection. If the refractive index of the first material is smaller than that of the second, the angle of transmittance through the second material will be smaller than the angle of incidence, while if it is greater the angle will be larger [75].

Dielectric confinement occurs when a high-index material is surrounded by a low index material, and the index difference is such that the beam is refracted to an angle greater

than 90 degrees. This is the basis of the operation of optical fibres, a two-dimensional optical confinement, in which total internal reflection occurs repeatedly throughout the length of the fibre. The wavelength is restricted when the wave is confined, only certain wavelengths will propagate throughout the material.

$$n_1 \sin(\theta_i) = n_2 \sin(\theta_t) \tag{2.14}$$

Where:
n_1 = Refractive index of first material
n_2 = Refractive index of second material
θ_i = Angle of incidence
θ_r = Angle of reflection

2.4.1 Anti-Reflection

A performance loss arises from the transition of the incoming light rays at interfaces of differing material types. A change of refractive index occurs at these positions, and therefore some light is reflected back from the surface of the device in accordance with Snell's Law. The reflectance due to the interface between silicon and air at the surface of an untreated silicon substrate can be as high as 36%, [76] which is a significant loss of potential collected energy. The positioning of a *step* intermediate refractive index material, an *effective medium* in the form of a dielectric layer between two surfaces with a large refractive index disparity results in a significantly reduced surface reflection, with the ideal intermediate refractive index being $n_1 = \sqrt{n_0 n_2}$. Crystalline silicon has a refractive index of n_2=4.3 at a wavelength of 500nm, while the refractive index of air is significantly lower at n_1=1. For crystalline silicon this illustrates an ideal intermediate layer refractive index value of $n_1 = 2.1$. Dielectric materials such as silicon dioxide and silicon nitride exhibit refractive indices of n_0=1.46 and n_0= 2.07 respectively, and the use of such layers reduce the reflection from a silicon substrate from around 39% with no anti-reflection to 23% with a single intermediate layer. [77]

The use of additional layers, known as a double or multi-layer coating, can reduce this reflectance value further. Additionally, it is possible to use a property of light propagation throughout media of different refractive index to further reduce the surface reflection by means of destructive interference. If the thickness of the anti-reflection coating is very carefully selected, then the resultant electromagnetic wave reflected from the top surface and the wave reflected from the active layer interface can be tuned to be out of phase by 180°. This has the effect of reducing the reflected light amplitude to zero at this wavelength and therefore maximising absorption. The thickness of the intermediate layer must be equal to $\frac{\lambda}{4n_1}$ for the optimum results. It is therefore possible using a dielectric layer of optimised thickness to alter the phase of the light propagation through a material, which can generate constructive or destructive interference to suit the application [78]. The real (n) and imaginary (k) optical constants of a selection of

photovoltaic materials are presented graphically in figures 2.10 and 2.11 below. As can be observed, a large optical disparity exists between semiconductor absorber layer and substrate material (glass), with indium-tin oxide and silicon nitride providing values mid-way between each and therefore serving as an effective medium.

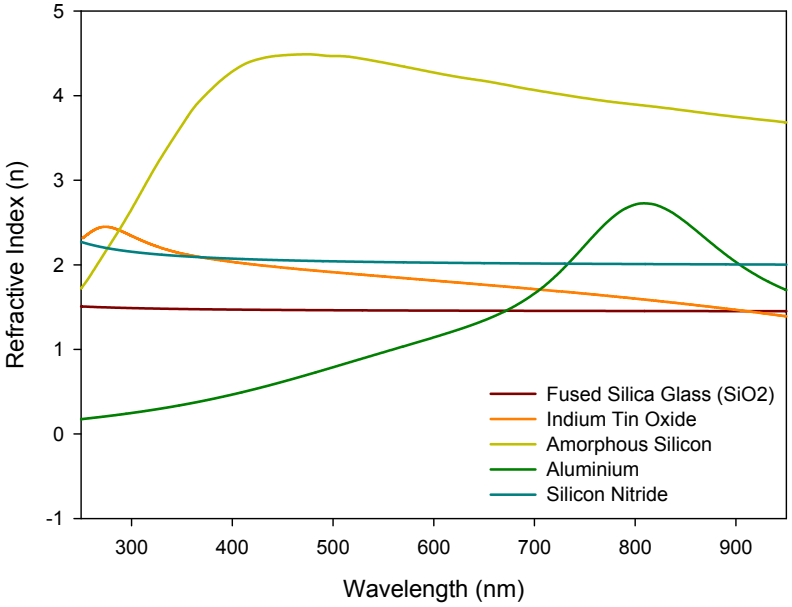

Figure 2.10: Refractive index (n) of photovoltaic materials (data from [79])

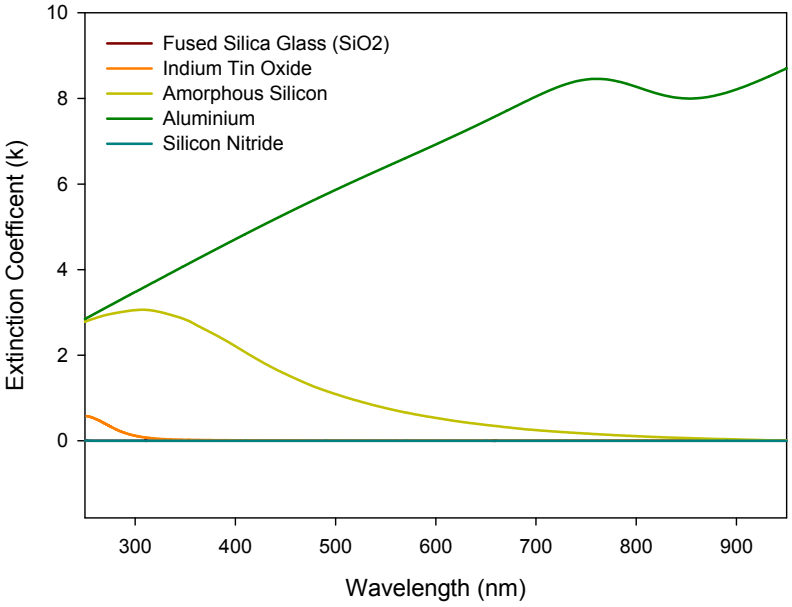

Figure 2.11: Extinction coefficient (k) of photovoltaic materials

2.4.2 Light Trapping

It is demonstrated that conventional silicon solar cells, and to a greater extent amorphous silicon cells exhibit poor light absorption characteristics within the near-infrared region (800-1100nm). As discussed in section 2.3, a trade-off exists between the thickness of the device and the region of the spectrum which the device is most sensitive to. Devices are often optimised to absorb the high-energy blue and ultraviolet photons, with an insufficient absorber layer thickness for the near infra-red photons. Additionally, a commercial incentive to reduce absorber layer thicknesses exists, in order to reduce device costs and maximise throughput.

The absorption of light in a material is defined by the Lambert-Beer law. This states as a monochromatic light ray enters an absorbing medium, the light intensity drops exponentially with the distance into the medium as the photons are absorbed [80]. It is defined as per equation 2.15:

$$I(\lambda) = I_0(\lambda)e^{-\alpha(\lambda)t} \tag{2.15}$$

Where:
I_0 = Incident intensity
α = Absorption coefficient
t = Depth in to absorber

Increasing this absorption of light can be achieved by increasing the physical or effective thickness of the medium or by increasing the absorption coefficient of the medium at the wavelength range of interest. An increase in the absorption of photons directly influences the photo-generated current and therefore the efficiency of the device. All practical thin-film photovoltaic devices feature a back reflector, to allow light which is not absorbed in the first pass to undertake another journey through the absorber layer. The use of back reflectors allow for the device thickness to be substantially reduced, with the constituent material having a significant influence on performance. The optical reflectance of a series of commonly used reflector metals [81] is detailed in figure 2.12.

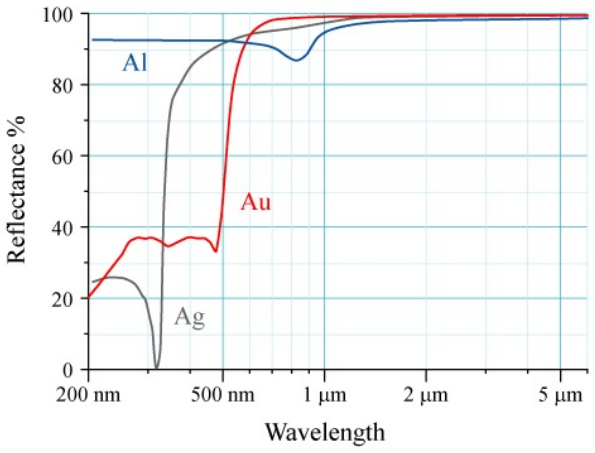

Figure 2.12: Optical reflectance of mirror materials

One such method to further increase the optical path length is to utilise a textured substrate on which the device layer is deposited. A randomly textured surface at the device layer interface serves to randomise the direction of the incident light through the absorber layer and increase the optical path length in the majority of cases. If the light is scattered at a wide angle from the normal angle of incidence, optical confinement can occur which traps the light within the absorber region ensuring efficient collection. Conformal fabrication processes which deposit absorber layers in a superstrate configuration atop of the texturing treatments will result in absorber layers which mirror the original texturing, creating further such interfaces throughout the device [82]. Texturing of the back reflector in this way can result in scattering of poorly absorbed light back in to the absorber layer, increasing the effective thickness by many times.

Increasing light trapping effects within conventional crystalline silicon photovoltaic devices is often achieved using anisotropic KOH etching, which results in the formation of micron-scale inverted pyramid texturing. The relatively simple KOH process has minimal overheads and is used to reveal the (111) facets of the silicon substrate to provide a texture of pyramidal shapes with a 54.7° degree slope. The KOH etch has a strong preference of crystallographic orientation, therefore the etch rate for (100) plane is significantly faster than on the (111) plane. The reaction is self-limiting, as once the (111) planes meet at the base of the pyramid structure, the (100) plane is no longer exposed and the etch rate drops significantly. Using the KOH solution on a silicon substrate with the (100) plane at the surface will therefore result in the formation of structures such as those shown in figure 2.13. These structures are typically 5-10μm wide and can be modelled by simple ray-tracing techniques, and if used in combination with a single-layer AR-coating such as Si_3N_4 result in a very effective anti-reflection scheme [83].

These techniques, however, cannot be used on amorphous silicon based devices as primarily the material does not feature the same silicon lattice arrangement as crystalline material, and therefore KOH would not preferentially etch in any direction. The dimensions of such structures also vastly exceed the thickness of a typical thin-film silicon photovoltaic device and therefore are unsuitable for all such thin film devices.

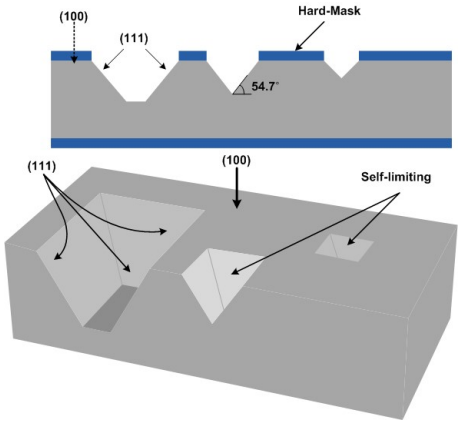

Figure 2.13: Inverted pyramid structures produced using KOH

It is calculated by Cody and Yablonovitch [82] that assuming the interfaces are ideal Lambertian scatterers, such texturing treatments have the potential to increase localised light intensity by $2n^2$, (where n = refractive index of absorber material) compared to the incident. This results in a $4n^2$ increase in effective absorption within the semiconductor bulk region and corresponding enhancement to charge carrier generation. For crystalline silicon with a refractive index of 3.5, the $4n^2$ limit corresponds to a path length enhancement of a factor of approximately 50 times [84]. While this calculation assumes an absorber layer thickness in excess of the wavelength of incident light, it is shown that enhancement can also be attained using thin film devices [85].

A series of commercially-available substrates with pre-applied transparent conductive oxides (TCOs) are available and extensively used throughout this investigation. These substrates feature a variety of textured features which serve to scatter incoming light as described in this section. A selection of the most popular commercially available TCOs is detailed in table 2.3 below, together with their specified resistivity, optical transmittance within the 400-800nm range and the RMS roughness measured using AFM [73].

Type	**Thickness (nm)**	**Resistivity (Ω sq)**	**Transmission (%)**	**Haze (%)**	**Roughness (nm)**
Pilkington TEC-8	650	8	≤ 80	12	40.9
Pilkington TEC-15	350	15	≤ 82	≤ 0.7	10.9
Pilkington NSG	650	8	≤ 80	12	39.7
Asahi U-Type		10	≤ 85	-	38.1
Asahi AN10		10	≤ 83	-	30

Table 2.3: Commercially available TCO materials [86, 87]

The result of using these textured TCO materials is an increase in the photo-current and efficiency of the resultant devices compared to the use of a planar TCO layer, as demonstrated by R.S.A. Sesuraj and D. Payne [88, 87] The commercially available TCO materials are often fabricated using doped tin oxides including indium-doped tin oxide (90% In_2O_3, 10% SnO_2) or fluorine-doped tin oxide (SnO_2:F) to produce a *haze*. An alternative to this material is aluminium-doped zinc oxide (Al:ZnO), which has advantages such as a natural roughness observed when the material is deposited using PECVD [89].

The deposition of the silicon device layer on top of a textured substrate material can pose challenges to the deposition mechanism and result in films of reduced electronic quality. Discontinuous films, pin-holes and varied device thickness can all result from the PECVD deposition on to rough substrate materials, which serve to increase the reverse saturation current of the device and hence impair the V_{oc} [90]. The use of texturing will also increase the effective surface area of the device, increasing the surface recombination rate. Devices which do not use TCO coated glass as the substrate material, such as crystalline silicon and heterojunction devices, are not able to benefit from the haze and light-scattering characteristics of the commercial TCO materials, and additional

wafer texturing steps during fabrication are required such as KOH. Alternative methods of achieving the light-scattering qualities of these techniques are therefore desirable, which include the use of optical methods such as predominantly deposition of metal nano-structures within the window layers to achieve the desired scattering without the disadvantages of increased substrate roughness due to texturing. Figures 2.14, 2.15 and 2.16 detail the results of scanning electron microscope (SEM) images and measured atomic-force microscopy (AFM) micro-graphs of TEC-8, TEC-15 and Asahi U-Type TCO materials on glass substrates, with peak roughness shown.

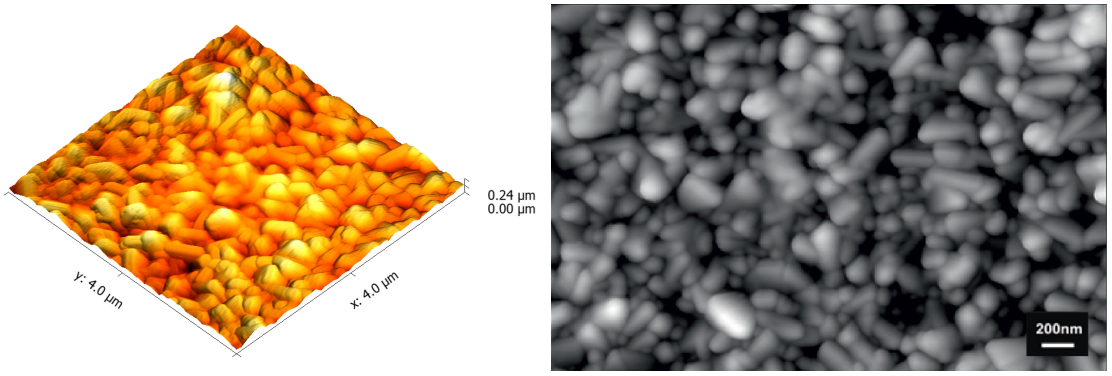

Figure 2.14: AFM (a) and SEM (b) Measurement of TEC-8 TCO

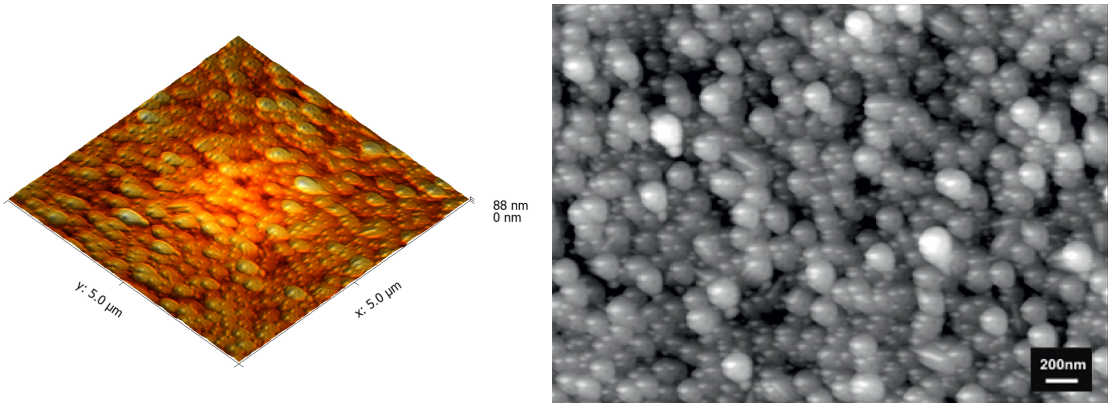

Figure 2.15: AFM (a) and SEM (b) Measurement of TEC-15 TCO

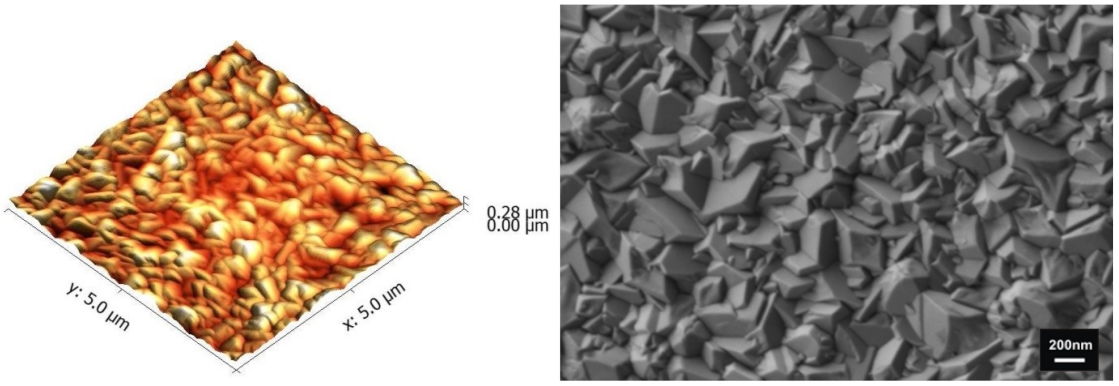

Figure 2.16: AFM (a) and SEM (b) Measurement of Asahi-U TCO

2.4.3 Plasmonic Resonance

Incoming electromagnetic waves such as light can give rise to a *plasmon* within a metallic medium. This is an electromagnetic wave existing either at the interface between two materials with differing dielectric constant signs or within the bulk of the material. Incident photons have the ability to couple with surface plasmons and cause a propagation of charge over the surface parallel to the interface known as a surface plasmon polariton. Examples of this topography include dielectric and metals in direct contact [91].

The operation of surface plasmon polaritons are that of oscillations within a free electron gas, such as those found in conductive media such as metal. Conducting materials, as opposed to semiconductors and insulators, possess a very high density of free electrons at room temperature, which constitute a free electron gas or *cloud* within the material. Within a metal, a neutral plasma exists such that there are an equal number of mobile negative charges as fixed (lattice) positive charges. The overall charge on the material is therefore neutral, however due to the free movement of such particles, regions of negative and positive charge can exist over very small areas. Electromagnetic radiation interacts with the electron cloud, within the wavelength ranges from x-ray to infra-red. Interactions with the nucleus of the atom requires significantly higher levels of energy, within the gamma-ray region of the spectrum. [92]

If a weakly-bound charge carrier is separated from its host atom within the metal lattice, due to excitation from external stimuli such as light, a coulomb force is created between the charge carrier and the fixed positive ionic core. Due to the movement of the particle back towards the static positive charge, kinetic energy is accumulated which is maximised as it passes the static charge. This leads to an oscillation as the particle slows, changes direction and once again passes the charged region. The decay of the localised surface plasmon energy can occur radiatively or non-radiatively, with different consequences to the operation of the photovoltaic device. Radiative decay of the excitation causes the re-radiation of a photon energy resulting in scattering of the electromagnetic wave, whilst non-radiative decay can result in the creation of electron-hole pairs within either the conduction band or a transition between the d- and sp-bands of the semiconductor, for intra- and inter-band transitions respectively, which do not contribute to light scattering [91].

It is possible to confine the plasmon wave within a very small particle structure which creates a localised surface plasmon (LSP). At this scale the distinction between surface and bulk material is lost and the plasmon charges can propagate freely throughout the material, displacing the conduction electrons within the metal ionic lattice. The wave will propagate through the particle and reflect from the physical boundaries, creating a resonant cavity for the wave. The resonance frequency can therefore be controlled by variations of the particle dimensions, however the ability to accurately fabricate the nano-meter scale features required to demonstrate this effect were not available until the

1980s at which point there was a significant increase in activity in this research area.

The presence of a metal nano-structure of the appropriate dimensions within the window layer of a solar cell therefore causes a pronounced light scattering effect, tunable to a particular range of wavelengths. This approach however has the potential to reduce the absorption of the high-energy blue light below the resonance wavelength, due to Fano interference effects [92]. An alternative topography is to position the nano-structure at the rear surface of the cell. In this geometry the incident blue light is directly absorbed and does not interact with the nano-structures, while the red light that is poorly absorbed in a single pass through the cell is strongly scattered.

The effects of the composition, size, shape and surrounding medium all influence the behaviour of the optical nano-structures, and therefore must be optimised for the photovoltaic application. The surrounding medium initially influences the operation of such particles, with the plasmonic resonance frequency (w) decreasing as the dielectric constant, and hence refractive index of the medium is increased. Studies of this effect include McFarland et al, which demonstrate a shift in resonance frequency of a Ag nano-particles immersed in a range of dielectric solvents [93]. The composition of the nano-particle additionally influences the resonance frequency, with materials which fulfil the conditions for supporting a surface plasmon wave at optical wavelengths including silver (Ag) gold (Au) copper (Cu) and aluminium (Al) amongst others offering various characteristics [94]. It can be observed in this work that aluminium provides the most enhancement for applications requiring deep-ultraviolet enhancement, while silver provides more enhancement within the visible and near-infrared regions and exhibits a lower attenuation of the electromagnetic field.

Additional material properties such as the susceptibility to form oxides further influences the material choice, resulting in Ag and Au becoming the most suitable for photovoltaic applications. [95, 96] The shape of the nano-particle further provides variations of the influence of the particles, due to the effects of the change in polarization. These include spheres, cylinders, discs, cubes and triangles amongst other shapes, and numerical simulation is used in order to determine the enhancement. The strongest effects of variations in resonant frequency are observed with diameter changes of the nano-structures, with two distinct modes of operation. For particle sizes of radius less than 10nm, quantum-mechanical effects dominate, whilst the behaviour of larger particles depend on Mie-theory [97]. It is additionally noted that a shift to particles with smaller dimensions causes the resonant behaviour to occur at shorter wavelengths, which is desirable for thin-film devices, however this additionally causes a higher percentage of photons to be absorbed non-radiatively and therefore not contribute to scattering [91].

The periodicity of such particles is also a significant contributor to their performance as a light-scattering mechanism. The area under which the nano-particle arrays are active can be up to ten times their physical size, and so a fairly sparse distribution of particles can yield a very effective light scattering effect [98]. Particles with a periodicity of the order of the wavelength of light can additionally behave as a diffraction grating [99]. If

the spacing is less than the critical wavelength then scattering does not occur aside from in the direction of transmission, while if it is roughly equal to the wavelength, scattering only occurs parallel to the grating. While particle arrays within a homogeneous medium will scatter light broadly in all directions, when placed near an interface with a material of a higher electrical permittivity, the light will be preferentially scattered toward it [98].

Fabrication of such nano-structures can be achieved in a variety of ways. The predominant method of manufacture is the annealing of a thin layer of Ag material on the surface of a substrate, which results in the formation of self-organised metal island films [88]. These nano-particles have a random distribution of shapes and dimensions and so interact effectively with a broad range of wavelengths, however this arrangement often results in particles of a hemispherical shape. Therefore the resonant oscillations throughout the particle are out of phase causing a reduction in forward scattering performance. Such particles in direct contact with the high refractive index semiconductor surface tends to cause increased reflectance and so therefore a thin dielectric or TCO buffer layer is often incorporated [91]. It is possible to use photo- or electron-beam lithography to define an array of periodic nano-structures, which results in particles with perfectly repeatable and controllable dimensions and therefore a much sharper peak in resonant response. This method is however much more expensive and time consuming and can only be performed on certain material substrates.

The concept of collective oscillations of free electrons within a homogeneous medium was first proposed in 1955 by D. Pines [100], but it was not until 1969 that is was suggested by M. Kerker that controlled light scattering could be achieved using the phenomena [101]. A practical device which utilises these techniques to enhance the absorption of silicon based devices was introduced in 1996 by H. Stuart and D. Hall [102], who stipulated that a 160nm SOI-waveguide device could be enhanced in performance by the application of metal-island films of 10nm consisting of silver, gold or copper. An order of magnitude increase in light absorption was achieved in the long wavelength range, using a lithium-flouride based dielectric layer and annealing for 120 minutes in nitrogen at $300°C$. Recently, the concept of surface plasmon resonances in metallic nano-particles is routinely exploited in various applications such as single molecule detection [103], nano-lens structures [104], optical microscopy [105] and photonic devices [106].

Modern lithographic and simulation techniques in 2003 allowed for K. Kelly and E. Coronado et al [107] to further investigate the influence of the design of the particle arrays, including the shape and size of the particles and their dielectric surroundings. Practical devices were presented in 2005 by D. Schaadt and B. Feng [108], detailing the enhancement of photo-current in silicon p-n junction diodes using the application of Au colloidal solution with a view towards application in photo-detectors, imaging arrays and photovoltaics. D. Deracs and S. Lim et al presented [109] in 2006 metallic nano-particle arrays fabricated by hot-wire CVD, with particle application via Au colloidal solution applied up to five times, with indium-tin oxide deposited by RF sputtering forming the 20nm separation between particles and the device later. An 8.3% improvement

in device efficiency was observed, with a suggestion that greater improvement would be possible with alternative particle formation methods with a greater particle density. S. Pillai and K. Catchpole et al [110] presented a broad study of silver nano-particle based enhancement of both wafer-based and thin-film silicon solar cells, reporting an enhancement of several times for the long wavelength region. Nano-particle arrays in this study were fabricated using thermal evaporation of thin layers of 10 - 22nm silver followed by annealing at $200^{\circ}C$ for 50 minutes. It is reported that metal particles fabricated using silver layers thinner than 14nm provide maximum overall enhancement in the visible as well as the near infra-red wavelength regions. It is also reported that this technique increases the performance of SOI-based light emitting diodes, with the authors releasing a further article the same year on the enhancement of LEDs [111].

K. Catchpole and A. Poleman continued to focus on the optical enhancement of solar cells using particle plasmons, with a design principles article released in 2008 [112] stipulating that silver particles provide greater path length enhancement than gold, and cylindrical and hemispherical particles increase the path length to a greater extent than straightforward spherical arrays. A review paper was also released the same year [113], reviewing progress both theoretical and experimental made in the preceding years with a view towards the determination of an optimum particle distribution. It is noted that inexpensive methods of fabrication such as soft nano-imprint lithography are suitable for such structures and negate the need for expensive e-beam lithography. In 2009, F. Beck, Catchpole and Poleman released an article [114] demonstrating the tuning of localised surface plasmons via arrays of Ag nanoparticles formed by metal-island film annealing. Particles were deposited on both glass and $200\mu m$ crystalline silicon substrates, formed by the thermal evaporation of 14nm Ag thin films which were subsequently annealed at $260^{\circ}C$ for 30 minutes. Optical absorption spectra derived from transmittance and reflectance measurements were performed, which determined that the resonant frequency could be shifted to a 200nm longer wavelength by varying the dielectric environment from SiO_2, Si_3N_4 and TiO_2. It was stated that the positioning of the nano-particle arrays at the rear of the device, adjacent to the back reflector as opposed to at the front avoids the interference effects below the resonance frequency and associated absorption losses, and therefore arrays positioned at the rear of the device and tuned to longer, poorly absorbed wavelengths can improve optical performance by 2.3 times.

A. Poleman and H. Atwater contributed to an article released in 2010 by V. Ferry and M. Verschuuren [115], detailing a similar outcome of rear-mounted nano-particle arrays on 160nm amorphous-silicon solar cells, fabricated using soft nano-imprint lithography. The advantages of such a fabrication method are detailed and compared to annealed metal island films, colloidal particles and electron-beam lithography, and a device is fabricated with 290nm Ag particles with a 500nm pitch. Angle-resolved photo-current spectroscopy was used to determine that a strong enhancement to device quantum efficiency occurs between the 550 - 800nm wavelength range. A review article was released the same year by Poleman and Atwater, [98] which summarises the research in the field to date. Optical

simulations were performed by A. Centeno and J. Breeze [116] the same year, illustrating the behaviour of spherical and hemispherical particles positioned at the front surface of a silicon substrate. This study determined that the contact region between the particles and the silicon is significant on the forward scattering efficiency, and a dielectric region is essential for optimum performance. It is also determined that the periodicity of the particles has an influence on the scattering performance, and particles spaced in excess of 100nm apart have the highest performance. H. Tan, R. Santbergen and A. Smets et al [117] continued the research in to thin-film devices with self-organised particles positioned at the rear, releasing an article in 2012 detailing a technique which provides a $2mA/cm^2$ increase in the performance of an amorphous silicon photovoltaic device. It states that the temperature of anneal of a silver metal-island film is an important variable to determine surface coverage and particle diameter, which determines the extent and wavelength of the enhancement with particles formed at $400°C$ vastly outperforming those formed at $200°C$.

Simulation technologies in recent years have made possible the investigation of a wide variety of exotic shapes, which was exploited by S. Zhou and Q. Li in 2013 [118] determining using simulation of the Gielis' super-formula that an optimal lens-like structure results in the greatest enhancement. It was demonstrated by Wiley et al [119] using DDA simulations that the use of non-spherical shapes, particularly those with sharp corners causes a red-shifting of the resonance frequency and scattering spectra, due to the accumulation of charges in the corners reducing the restoring Coulomb force. A. Basch and F.J. Beck in 2012 demonstrated [120] a doubling of photo-current using the *snow globe coating* technique in addition to the presence of Ag nano-particles to form highly diffuse back reflectors; while an article exploring the positioning of metal-island film based nano-particles within the front, rear and both TCO regions released in 2015 by J. Winans and C. Hungerford [121] comprehensively reviewed the performance advantages of each, finding that a nano-particle array in both the front TCO region and rear back reflector region results in the optimum performance. It was noted that Ag nano-particles must be embedded within a dielectric medium or coated with a thin film of MgF_2 to prevent oxidation and an causing an offset of the particle dimensions.

In summary, this section has detailed the silicon solar cell structures with appreciable market share, and their development history and device performance records. Their methods of operation, and potential for optimisation has been explored including optical light scattering technologies. The following study aims to explore these optimisations in the field of the enhancement of the hydrogenated amorphous P-I-N devices described in section 2.3, by fully exploring the deposition parameter space including those which are currently not well-documented such as the use of argon dilute gas at various concentrations within the deposition chamber. The optical enhancement of such devices is then evaluated, employing self-organised metal island films to increase optical absorption, and comparisons are drawn to periodic array by method of simulation to determine if these methods are beneficial to amorphous silicon P-I-N devices.

Chapter 3

Experimental Techniques

In order to produce photovoltaic devices and light-scattering structures discussed within this study, several fabrication and measurement techniques must be performed. This section describes these techniques and provides further detail on their operation, the physical phenomena behind their function and how these techniques can be optimised to provide the most efficient devices and structures.

3.1 Cleaning

It is essential to ensure that the glass substrate material is perfectly clean before deposition is performed. Contamination of the substrate can cause many performance-reducing effects, including poor adhesion of the deposited film, reduced photovoltaic performance due to trapped charges and shunting due to pin-holes shorting the active region of the device. Therefore a series of thorough sample cleaning techniques must be undertaken. Specifically, a contaminant such as a dust particle can cause a defect in the uniformity of the deposited film causing surface roughness, due to the PECVD deposition technique having non-conformal step coverage. Additionally, if the particle is removed during subsequent chamber pumping steps or substrate handling, the TCO of the substrate will become exposed. Metallisation over this region will directly contact the TCO and cause a short circuit *shunt* condition. If substrates have been handled in order to dice the material into the size required, then the first step in cleaning is to use a simple degreaser. This has been shown to remove a significant amount of contamination and dust particles from the shipping package.

The standard cleaning technique before deposition is to initially rinse the sample with de-ionized water to remove any surface particles, followed by thorough cleaning of the sample with acetone solvent in order to remove organic materials from the sample. After the majority of the acetone has evaporated away, the sample is thoroughly cleaned using isopropanol alcohol (IPA). A final spray with nitrogen assists the drying of the sample and removes any additional particles. It is also suggested that a nitrogen spray is performed if the samples are left in the open for any length of time.

3.2 Deposition

Thin-film deposition of amorphous silicon can be achieved using a variety of methods, which can be divided into two main categories, physical vapour deposition (PVD) based on physical processes such as sputtering and evaporation; and chemical vapour deposition (CVD) in which the precursors react and/or decompose on the substrate resulting in the desired material. Investigations involving physical vapour deposition of thin film silicon are possible, however this investigation is focused on the chemical vapour deposition of silicon. Within this section the principles of plasma-enhanced CVD and hot-wire CVD will be introduced.

3.2.1 Plasma-Enhanced CVD

The CVD thin-film process used in this investigation to fabricate the amorphous P-I-N devices is plasma-enhanced chemical vapour deposition. PECVD is a very well established technique for depositing silicon thin films for photovoltaic cells and the microelectronics industry, producing device-grade material with excellent uniformity. The technique uses an ionized plasma glow discharge within a vacuum chamber to disassociate the source gases into their elemental components, which are deposited on to the heated substrate material. The plasma itself is an ionized medium of gas which is macroscopically neutral, in which the ionization is achieved by providing additional energy to the medium, in the case of PECVD this is achieved by inducing an electric field throughout the medium. RF electrodes are positioned above and below the substrate, which when active cause chemical vapour deposition to occur whilst the substrate is kept at much lower temperatures than would otherwise be required. This allows the use of inexpensive substrate materials such as glass or plastic, reducing the potential cost of thin film devices and also permits the deposition of amorphous thin films directly on to un-oxidised crystalline materials without recrystallization occurring during growth. Shortcomings of this technique are the complexity and expense of the deposition equipment, potential instability of the RF plasma under certain conditions, and predominantly ion bombardment damage to the growing films leading to films of poor electronic quality in unoptimised situations.

The system used in this investigation is an Oxford Instruments PlasmaLab System 100. The system is a computer controlled and fully automated capacitive single-chamber PECVD reactor, and is capable of a wide range of operating parameters including substrate, gas and chamber wall temperature, chamber pressure, gas flow rates and RF power in addition to the deposition time. The system is capable of producing amorphous and micro-crystalline silicon thin films, and is also capable of including germanium. Doping of the growing layers is achieved using diborane and phosphine gases, diluted in hydrogen and argon. The system uses capacitively-coupled RF electrodes positioned above and below the substrate to generate gas plasma of 13.56MHz. Power is variable up to 50W, which provide the energy to break down the precursor gases whilst

minimizing ion bombardment damage which can be caused to the growing thin films under higher power levels typical of inductively-coupled plasma systems (ICP). LF dual frequency excitation at 100 - 300kHz is also provided by the system, although it is not used in this investigation. Impedance matching is courtesy of a digital close-coupled automatic impedance matching unit, controllable via software.

The system contains an electrically-heated substrate stage with PID regulator, which can heat up to 400 °C in the current configuration. Chamber pressure is regulated within the reactor using a programmable automatic pressure control (APC) valve and a turbo / base pump combination with integrated nitrogen pump purge. This combination ensures that the pressure within the chamber is maintained at the desired value for a wide variety of process gas flow rates, and allows the varied control of gas turbulence within the reactor whilst maintaining steady pressure. The system features a fast-entry load-lock system connected to the deposition chamber via gate valves, which allows loading and unloading whilst the main chamber remains under vacuum. Both chambers are pumped by Edwards rotary pumps with the deposition chamber additionally equipped with an Adixen turbo pump. This allows the sample to be transferred from atmospheric pressure down to 10^{-6} mT in less than one minute.

Operation of the system is achieved via the use of a desktop PC running OIPT PC2000 software, which provides complete control over all of the deposition conditions and vacuum operations. Gas is supplied to the system via a separate supply module, which contains programmable mass flow controllers (MFCs) for each process gas, supplied to the deposition chamber via a full-diameter uniform shower-head arrangement. Operation is performed using a system of recipes, each of which can contain multiple gas flow, plasma or vacuum steps in any order. Recipes are programmed in advance, and can be stored in the software to be run when required.

The operation principle of PECVD is the excitation and relaxation of highly energetic electrons and ions, supplied by RF electric field. The electrons within the precursor gas pumped into the chamber gain significant energy from the applied electric field, which heats the electrons to an energy of around 1eV. Ions and gas molecules are thermalized to the temperature of the reactor chamber, maintained at room temperature or below. For the deposition of silicon films, it is possible to use a various of gases including: SiH_4, Si_2H_6, SiF_4, $SiCl_3H$, $SiCl_2H_2$ and similar. Silane (SiH_4) is the most studied and widely used by a significant margin, mainly due to the presence of atomic hydrogen. The electric field accelerates the electrons within the chamber, which causes excitation and disassociation of the silane molecules to various degrees. The type of disassociation, ionization or attachment depends on the RF power applied to the chamber from which the electrons gain energy, and the mean-free path which depends on the pressure of the chamber. For example, at 70eV electron energy, 58% silane radicals and 42% ionized silane molecules are produced [122].

Within the plasma, the majority of the radicals produced are SiH_2 and SiH_3 molecules, with a small number (10%) of SiH and Si species. These are the primary reactions which

are dominant when the mean-free path is greater than the inter-electrode distance, but reactions do occur between the products of the primary reactions within the chamber. SiH_3 gas precursors are often considered to be the most suitable for device grade material deposition [122]. Additionally, a wide variety of species are present which react with the substrate to different degrees depending on the conditions of the process. High-energy electrons ionized from the radicals are usually confined within the plasma bulk and rarely interact with the substrate unless their potential is high enough, while positive ions will be accelerated towards the substrate at the plasma sheath boundary, at an energy proportional to the plasma potential. Negative ions are additionally confined within the plasma in the same way as the electrons and so rarely interact, but can form powders of diameter $\geq 10nm$ which can impinge on the substrate and affect the film quality during growth. Powder formation within the deposition chamber of apparatus using a silane plasma have been extensively studied, [123] as the resultant thin-film contamination caused by the formation of powder presents a significant concern limiting device reliability and manufacturing productivity. The formation of powder within the reaction chamber is a three step process, caused by the interaction of SiH_4 and Si_2H_5 which causes cluster growth of particles approximately 2nm in size. In the following step these particles coagulate into particles of approximately 100nm size, and finally the reaction saturates with particles of 120nm released from the plasma and on to the substrate or chamber wall. Increases in process gas temperature, the design of the reactor including the use of grooved electrodes, and the use of a modulated plasma and reduced RF power are all shown to reduce the formation of such contaminants. In this investigation, the variation of RF power is used to reduce dust formation within the chamber. Photons generated by the plasma also interact with the growing film, however their effect has not been fully investigated [122].

A transition region exists between the ionized plasma gas and the reactor walls, which serves as a potential barrier to keep the electrons confined within the plasma itself. The RF power is capacitively coupled to the electrodes to minimise reflected power, and this creates a *sheath* potential barrier region which prevents the free electrons, negatively charged ions and powders from leaving. The electrons can respond immediately to the applied potential while the ions respond much more slowly due to their larger mass. The range of frequencies to which an electron will respond can be calculated to be up to 900MHz [124], whilst the larger mass of the ionized particle limits its response to under 1MHz. These ions therefore only respond to the average potential across the medium, and will be accelerated to the chamber walls leading to ion bombardment effects during deposition. If the reactor geometry features an RF electrode which is smaller than the grounded areas of the chamber, as is commonly the case with research laboratory reactors, then the chamber is defined as asymmetric and a DC bias will be generated on the RF electrode. This is not the case with the PlasmaLab System 100 used in this investigation. The bias is defined by the ratio of RF powered regions as opposed to grounded regions and is given by the area law. At low pressures common

to the deposition of amorphous silicon, the energy of the ions within the plasma is simply the difference between the plasma potential and the grounded substrate. At higher pressures the ions do not have a mean free path throughout the sheath region, and therefore the potential is reduced. As the size of the substrate and therefore the electrodes are increased, the systems tend to become more symmetrical and therefore there is no DC bias present on the RF electrode. This has the effect of increasing the ion potential and intensifies the effects of ion bombardment. A compromise needs to be made in order to achieve high deposition rates and acceptable device quality films without the formation of powders within the chamber [125].

3.2.2 Hot-Wire CVD

The hot-wire CVD technique is an innovative method of performing chemical vapour deposition at low substrate temperatures, in a similar fashion to PECVD. The source gases are catalytically disassociated into their elemental components using several heated filaments, at between 1,600 - 2,000 °C. The filament material is generally tungsten (W) or tantalum (Ta), depending on the temperature of the process and gas chemistry used. Advantages of this technique over the PECVD systems used currently in industrial processes are the lack of any RF glow discharge acting on the substrate material, which can impede film growth rate and produce material of lower electronic quality [126]. It is additionally possible to scale up a hot-wire CVD reactor to much larger volume than is practical with PECVD whilst maintaining good uniformity, by adding additional filament area and associated vacuum chamber size. This advantage can lead to lower production costs for the thin film materials due to a much larger area per deposition run. A subset of the fabrication work within this investigation are performed using hot-wire CVD employing an EcherKon Nitor 301 vacuum deposition system.

3.2.3 Electron-Beam Evaporation

The metallisation of the contact regions on the silicon layers, evaporation of metal-island films and deposition of indium-tin oxide is performed using electron-beam evaporation. Two systems are used in this investigation, a Leybold Optics BAK600 and a Leybold Optics LAB700. These systems consist of large vacuum chambers pumped to a vacuum level of 10^{-5} to 10^{-6} mBar. An electron beam source is directed to a crucible containing source material granules which are heated to melting point by the beam. This causes the material to vaporize within the chamber and condense on the substrate which is suspended above. The substrate rotates within the chamber to ensure a uniform coating, the thickness of which is determined using a crystal sensor mounted adjacent to the substrate. The deposition rate is controlled by varying the cathode filament current, which is overseen by the Inficon IC/5 programmable logic controller unit.

The deposition of 500nm of aluminium takes approximately 33 minutes at a deposition rate of 2.5 Å/s, while the deposition of silver is performed more slowly at 1.0Å/s. 5 x

5 cm substrates are attached to the rear of a 4″ (100mm) circular disc and are placed into one of the 4″ apertures inside the evaporator chamber. The substrates are attached using Kapton tape and must be securely sited. The chamber can house six substrates in total, while five of the P-I-N device shadow masks are available. For conductivity measurements of intrinsic material, a grated aperture shadow mask is used to create the contacts for this measurement. A plasma ion source is fitted to the chamber of the LAB700 system which allows the deposition of indium-tin oxide, together with argon and oxygen MFCs. The substrate is heated to 200°C in this configuration and the resultant deposition rate is set to 1Å/s for uniform deposition.

3.2.4 Rapid Thermal Annealing

Thermal annealing of samples is central to the investigation in chapter 6 of this study, in order to form metal-island film structures of the order of the wavelength of incident light. The nucleation process and complete process steps are detailed in section 6.3.

Rapid thermal annealing is the manufacturing process in which a semiconductor sample can be heated to an accurately controlled temperature for a pre-determined time period. Highly precise heating and cooling ramp steps can be defined, in order to prevent thermal stresses within the thin film or potential substrate breakage.

The system used in this investigation is a Jipelec JetFirst 200C rapid thermal annealer. This system is equipped with an array of 16 tubular halogen infrared lamps behind a quartz window, mounted above the substrate platen. The lamps and the reaction chamber are cooled using a process cooling water circuit and interlocks prevent opening the chamber at temperatures above 200°C. Temperature regulation is by means of a PID controller and an array of thermocouples for heating below 900°C or pyrometer for temperatures up to 1200°C. PID parameters must be calibrated for each sensor and substrate material to ensure accurate regulation and minimise overshoot.

The recipe used for the rapid thermal anneal of amorphous silicon / Ag films on glass is as follows. This recipe shows the anneal routine for 60 minutes at 250°C, and the temperature set-points within this recipe are selected to maintain a temperature ramp rate of less than 2°C / sec.

- Pump chamber to high vacuum [0:30]
- Enable N_2 purge valve [0:30]
- Ramp temperature to set-point 250°C [2:00]
- Hold temperature at set-point [60:00]
- Ramp temperature to set-point 0°C [2:00]
- Disable N_2 purge valve [0:30]
- Temperature cool-down step [5:00]

3.2.5 Electron - Beam Lithography

Electron-beam lithography is used within the future work section of this study, allowing maximum flexibility to create and modify designs directly from CAD files. These designs are exposed using a photo-resist chemical in a similar manner to photo-lithography, where exposed regions are removed for etch or deposition with the use of positive resist or cross-linked and hardened where exposed with negative resist. Using this method, a proposed design can be outlined and exposed on a substrate material without the need for an expensive hard-mask to be created, and if modifications to the design are required these can be performed on the CAD design to reflect the optimisations.
Using the electron-beam method, resolution down to 10nm can be achieved which far exceeds that of optical lithography which greatly enhances the ability to fabricate sub-wavelength structures. Fine / coarse split exposures additionally allow for a mixture of very fine resolution exposure coupled with rapid turnaround of more course regions of the layout. The specification of the JEOL JBX-9300 FS Electron-beam lithography system used in this study is detailed in table 3.1.

Variable	**Unit**	**Value**
Electron Beam Diameter	(nm)	4
Resolution	(nm)	1
Accelerating Voltage	(kV)	100
Beam Current	(pA)	50 - 100,000
Scan Speed	(MHz)	50
Writing Area	(Inch)	9
Line Width	(nm)	≤ 20
Field Stitching Accuracy	(nm)	≤ 20
Overlay Accuracy	(nm)	≤ 25

Table 3.1: JEOL e-beam lithography system specification

Disadvantages of this technique include significantly increased exposure time per substrate, which while dependent on feature detail can span several hours. The running cost of such exposures is additionally much higher than photo-lithography systems, and therefore for repeated exposures or volume production this method is not suitable.
Similar resolution and flexibility can be achieved using the Nano-Imprint Lithography technique [127], which uses an inexpensive transfer imprint resist *stamp* to transfer a pattern to a substrate. This *stamp* itself is fabricated using electron-beam lithography and subsequently allows for the duplication of its pattern quickly and inexpensively onto many substrates. A minimum feature size of 10nm has been achieved using this technique, mirroring the resolution of the electron-beam technique whilst the patterning time for each wafer is vastly reduced.

3.3 Characterisation

3.3.1 Ellipsometry

The standard method of measuring thin film device thickness is the use of spectroscopic ellipsometry. This technique illuminates a small area of a deposited sample with linearly polarized light, which is reflected from the sample surface and changes in the p- and s- components are observed. In this investigation, an automated angle J A Woolam M-2000D Ellipsometer with 150mm X-Y mapping stage is used, which provides highly accurate measurements from 193 - 1690nm with the NIR Extension. This wide wavelength range enables sampling at lithography line, 193nm, 248nm, and 365nm; while simultaneous collection at longer wavelengths ensures accurate thickness of transparent films such as conductive oxides characteristic for absorbing at shorter wavelengths.

A model is constructed on the measurement system which describes the composition of the sample, and this is then compared to the experimental data where variables can be altered to find the closest match. Regression algorithms are used to search for the lowest possible global values of mean-squared error (MSE). The result is a measurement system capable of nanometre-scale thickness variations, and is therefore essential in defining deposition rates and optimum device thicknesses of the photovoltaic samples.

Figure 3.1 details the main window of the measurement software, CompleteEase, with a fitted model for amorphous silicon on glass. As can be observed, the measured Psi and Delta values have an excellent mathematical fit, using a model which specifies parametrized a-Si of 337.4nm atop a Cauchy modelled glass substrate of 1mm. A measured roughness of 1.2nm is observed and a band gap of 1.66eV.

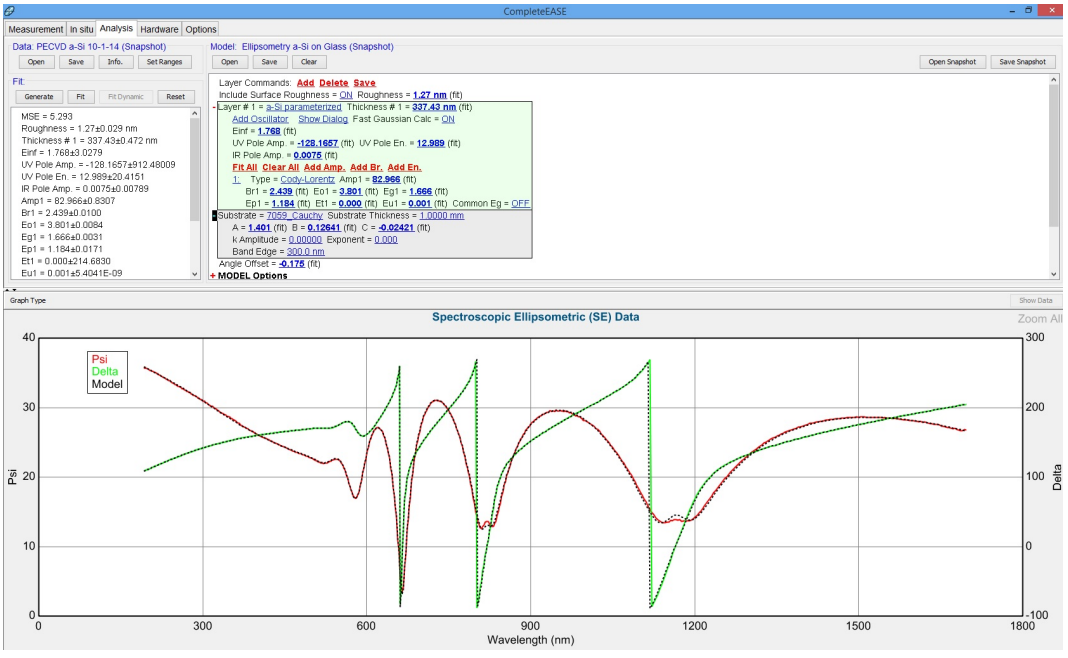

Figure 3.1: CompleteEase main window

3.3.2 Raman Spectroscopy

It is important to verify the crystallinity of deposited silicon thin films, to ensure that materials devised as amorphous do in fact have no crystalline fraction. This is achieved by Raman spectroscopy, which produces a spectra which clearly distinguishes between the two forms. The Raman spectroscopy technique operates using the principle of inelastic scattering of laser emission directed towards a sample. Laser radiation causes the momentary excitation of the electron density within the material, which is detected using CCD or photo-multiplier detection stages together with notch filters or holographic gratings (respectively) to reject Raleigh scattered radiation from the measurement. The measured offset or *Raman shift* from the excitation wavelength corresponds to the vibrational state of the molecules within the material under test.

In this investigation, a Rienshaw InVia Raman Spectrometer is used which provides three laser lines: 532nm, 633nm and 785nm wavelengths at power levels 55mW, 17mW and 200mW respectively. Care must be taken to ensure that the laser penetration depth is suitable for the sample, as the laser penetration reduces with shorter wavelength laser excitation. The 532nm laser penetrates approximately 100nm through a silicon sample, while a longer wavelength 785nm laser will penetrate much further, up to 800nm. Therefore in this investigation which explores silicon thin films of thickness below 400nm and a glass substrate material, a laser emission wavelength 532nm is preferred.

Covalent bonds within crystalline silicon are symmetrical with identical bond lengths and angles. This results in a sharp Raman peak around 521cm^{-1}, whilst pure amorphous material is significantly less orderly with various bond angles and lengths with many dangling and potentially unsatisfied bonds. This results in a much more broad spectrum centred around 480cm^{-1} as shown in figure 3.2.

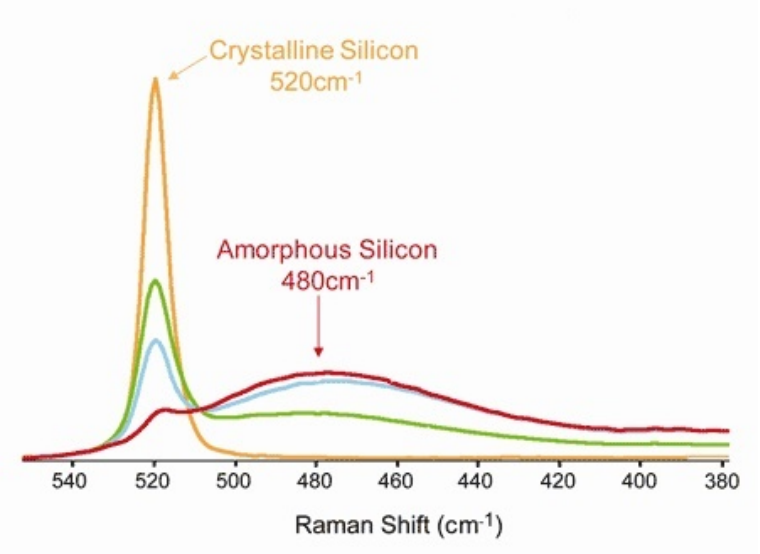

Figure 3.2: Example Raman spectra of amorphous and crystalline silicon

3.3.3 I-V Measurement

The I-V characteristics of the photovoltaic device are fundamental in determining its electrical performance, and are explained in detail in section 2.2.1. Constants such as the energy conversion efficiency, fill factor, short-circuit current, open circuit voltage, maximum power point, and equivalent series- and shunt resistances can all be derived from the device I-V response. The I-V curve of a typical small amorphous silicon photovoltaic device is depicted in figure 3.3.

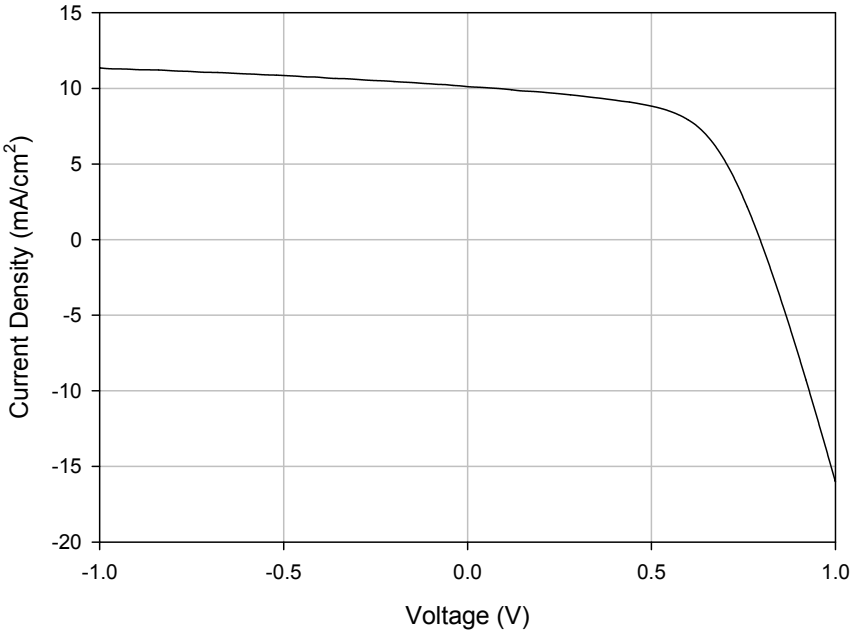

Figure 3.3: I-V curve of a photovoltaic device

The measurement of the I-V characteristic is performed using an Abet technologies SUN 3000 Solar Simulator, which allows the measurement of electrical performance of photovoltaic devices and material thin films under AM1.5 illumination. The system features a xenon-arc lamp, calibrated to the AM1.5 solar spectrum which is focused on the sample. The specialised equipment designed to house the samples is designed to suspend the sample at the optimum distance from the lens to ensure accurate light delivery whilst allowing rapid measurement of the 9-position test pattern. The measurement is performed using a LabView software, and a Keithley 2400 SourceMeter under RS-232 control to enable automated I-V curve and efficiency calculations. V_{oc}, I_{sc}, fill factor, maximum power, efficiency and various other attributes are presented, alongside the I-V and power characteristic which are exported for analysis. The sample is not temperature controlled within the apparatus in this investigation and therefore the effects due to substrate heating cannot be neutralized, for this reason the lamp remains incident on the sample for the shortest duration during the measurement to avoid heating effects.

3.3.4 Conductivity

The electronic properties of the silicon thin-films are essential in determining the quality and passivation effectiveness of the deposition. This is achieved using an ABET Technologies Sun 3000 solar simulator, coupled with a Keithley 2400 SourceMeter under RS-232 control via a custom-designed LabView measurement program. The input to this system can be configured to measure from freely-positioned contact probes on an elevated stage, on which the sample contact points can be manually positioned to measure specific regions. Aluminium contact regions are defined as per figure 3.4. For charge conductivity measurements, the sample is illuminated under the calibrated xenon-arc lamp whilst a voltage of 10 V is applied between the contacts. The photo-current flow through the device is then measured, which is used to determine the photo-conductivity using equation 3.1 below. Three measurements are taken, with the measurement probes contacting the first, second and third pair of measurement strips in succession. The median value of conductance is recorded for each set of measurements. The investigation is then repeated with the sample positioned within a dark cabinet with cable pass-through, to obtain the dark current and dark-conductivity. The ratio between the dark and photo-conductivity is indicative of the photo-activity of the device and hence the electrical quality of the deposited silicon film.

$$\sigma = \frac{(I)}{(V)}\frac{(L)}{(Wt)} \ (S\,cm^{-1}) \tag{3.1}$$

Where:
I = Recorded current flow (A)
V = Applied voltage (V)
L = Length of sample (cm)
W = Width of sample (cm)
t = Thickness of sample (cm)

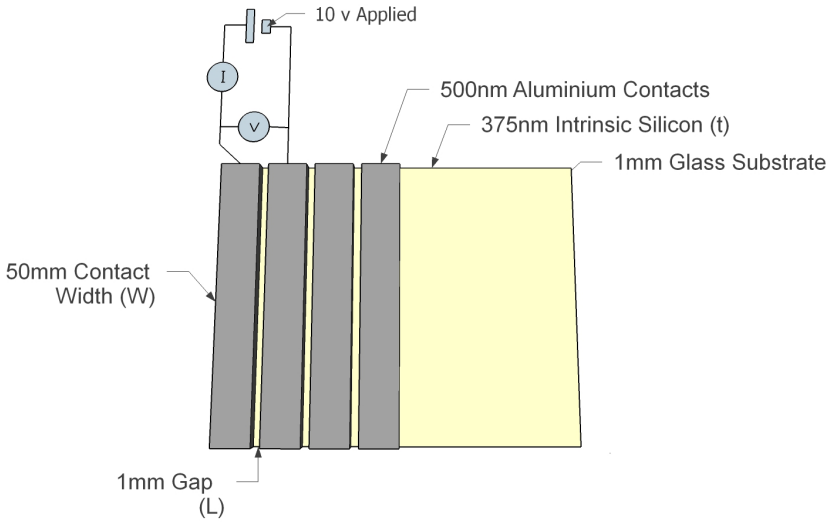

Figure 3.4: Silicon sample with conductivity measurement contacts

Figure 3.5 details the measurement probes on the first measurement position of the sample under test. The ABET Technologies SUN 3000 solar simulator measurement system is presented in figure 3.6, showing the Keithley 2400 SourceMeter and host PC.

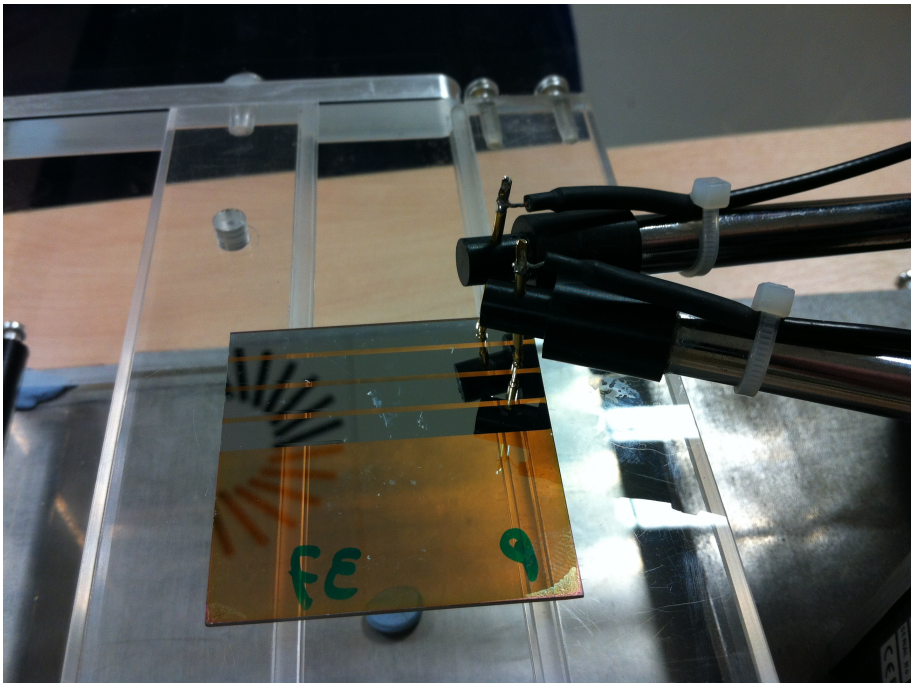

Figure 3.5: Conductivity measurement probe position

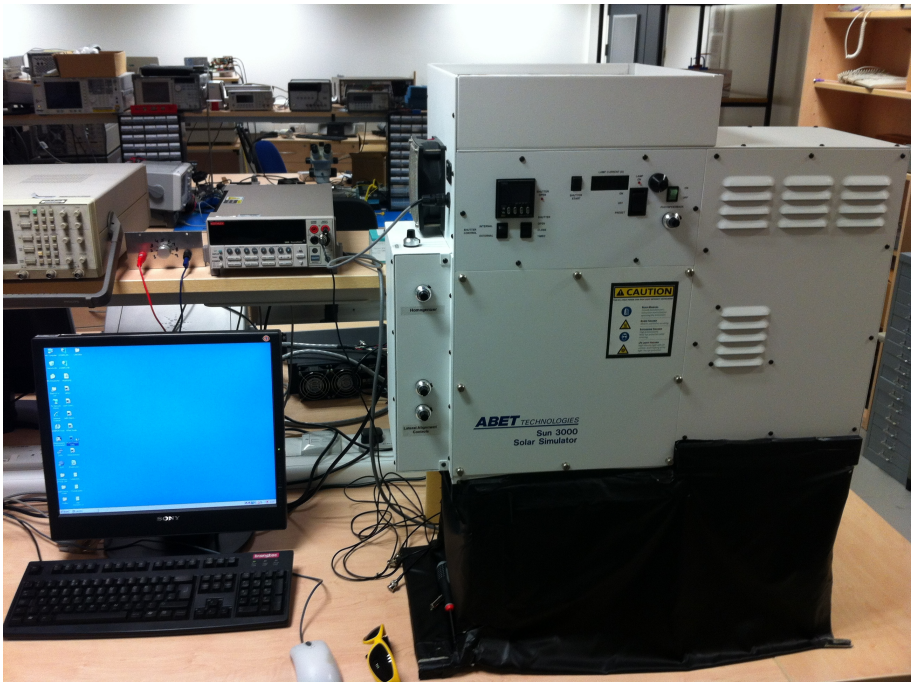

Figure 3.6: Conductivity measurement apparatus

3.3.5 Charge Carrier Lifetime

The measured charge carrier lifetime of a semiconductor material is representative of the charge carrier diffusion length. These values significantly contribute to the overall performance of a photovoltaic device, and therefore enhancement to this value through methods of defect passivation and reduction of impurities is a potential route to increased photovoltaic performance. Charge carriers within a semiconductor material are optically excited using a calibrated flash-lamp, and a measure of the average time they remain in this excited state is the carrier lifetime.

The measurement is performed using the Sinton WCT-120 carrier lifetime measurement system, which provides a contactless quasi-steady-state photo-conductance measurement, ideal for evaluating material quality and surface passivation techniques during fabrication. This is achieved using the Eddy-current method, [39] in which a conducting coil is supplied with an alternating current which produces a magnetic field around the sensor area. If a sample of semiconductor material is placed within the sensor region, an electric field opposed to those within the coil are induced within the semiconductor whilst it is illuminated using the xenon flash-lamp. Variations in charge conductivity within the semiconductor material corresponding to the density of defects and carrier lifetime influence the phase and amplitude of the generated eddy currents, which are detected by changes to the impedance of the coil. The sensor region in the WCT-120 is maintained at a controlled temperature for repeatable measurements.

The results are presented within a Microsoft Excel spreadsheet, providing graphical analysis of the photo-conductance, inverse lifetime vs carrier density, implied V_{oc} and minority carrier lifetime. Figure 3.7 (a) shows the main components of the system and figure 3.7 (b) presents the measured carrier lifetime graph. Stabilised values of lifetime are read from a selection of active cells within the results sheet (not shown).

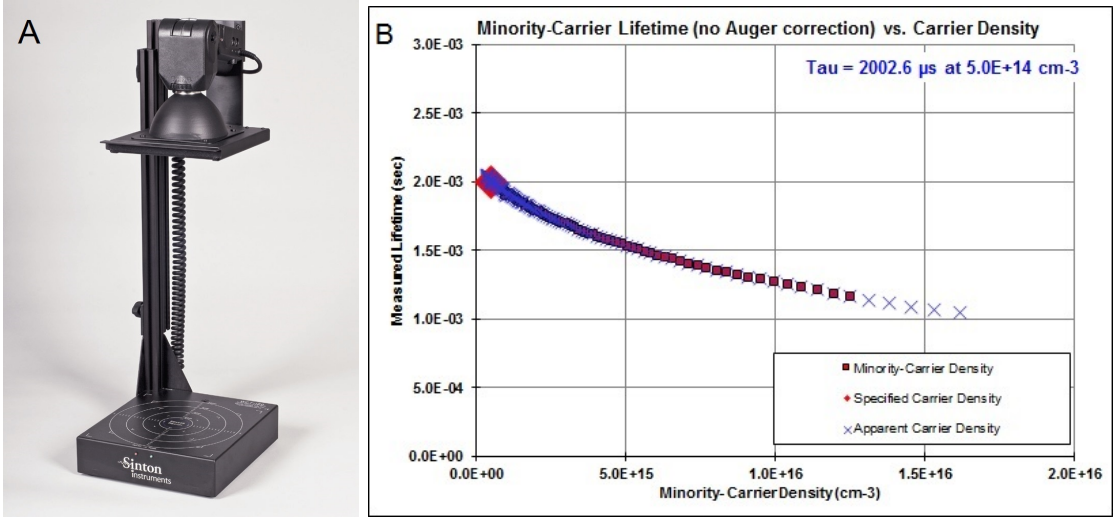

Figure 3.7: Carrier lifetime measurement apparatus

3.3.6 Quantum Efficiency

The quantum efficiency of a photovoltaic device is the ratio of charge carriers generated and collected by the device to the number of photons incident on it. It is expressed as a spectral response as a function of wavelength, and can provide comprehensive analysis of the optical response of a solar cell. The sample is irradiated using a monochromatic light source based on a Bentham TMc300 single mono-chromator and a xenon/quartz halogen light source, which is directed onto the sample under test giving coverage over the spectral range 300 - 1100nm. Measurement is performed using a 497 current pre-amplifier supplying a computer-controlled 496 DSP lock-in amplifier which requires no manual adjustment. The system is fitted with a temperature controlled vacuum chuck, which maintains mechanical stability and ensures a good electrical connection to devices with a rear mounted contact whilst ensuring the temperature of the device under test remains constant by means of a cooling water circuit and remote chiller unit. A light biasing source allows DC broadband illumination of a multi-junction device, the photo-current from which is separated from the output signal by a transformer unit.

If all photons incident on the photovoltaic device are absorbed and collected, then the quantum efficiency value is rated as 100% and the QE measurement will be unity across the wavelength range. All practical photovoltaic devices will exhibit a curve somewhat lower than this due to mostly unavoidable recombination effects and interface reflection. Values significantly below this value highlight design and / or fabrication shortcomings in the device, as are detailed in figure 3.8. Poor performance is indicated by the shifting of the curve towards lower QE values indicated on the y-axis in the regions highlighted by the arrow labels in figure 3.8, whilst an improved QE curve will shift towards the higher y-axis values in all regions, in the opposite direction to the arrows.

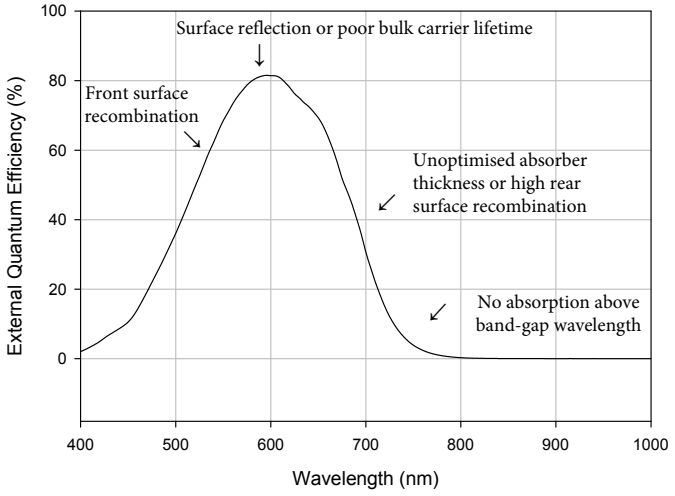

Figure 3.8: Quantum efficiency of a photovoltaic device

The recombination of optically generated charge carriers at the front surface of the device illustrate that the passivation of the exposed device surface is ineffective, which results

in recombination of the easily-absorbed blue region of the spectrum. Reduced charge carrier lifetime within the bulk of the device affects the performance of the overall QE curve and is particularly noticeable within the green / yellow region, whilst insufficient absorber layer thicknesses affect the absorption in the long-wavelength red region. Few photons are absorbed from the region shorter than 350nm wavelength as the power contained within the AM1.5 solar spectrum in this region diminishes significantly. Such carriers would be collected very close to the device surface and therefore be subject to high levels of surface recombination velocity, while absorption is reduced to zero at wavelengths below the band gap of the device material.

The external quantum efficiency measured using this method also details the effect of optical losses such as surface reflection and optical transmission. This can be advantageous for observing the effects of optical designs such as light trapping structures, however for device diagnosis the internal quantum efficiency can be observed. This is a corrected quantum efficiency curve with losses due to transmittance and reflectance neglected and therefore highlights only collectable photons within the device. In order to obtain the internal quantum efficiency, the transmittance and reflectance of the device must also be measured as described in the following section.

3.3.7 Optical Absorption, Transmittance and Reflectance

In order to characterise the optical performance of a sample, including analysis of the absorption, measurements of optical transmittance and reflectance must be performed. This is undertaken using an integrating sphere as detailed in figure 3.9.

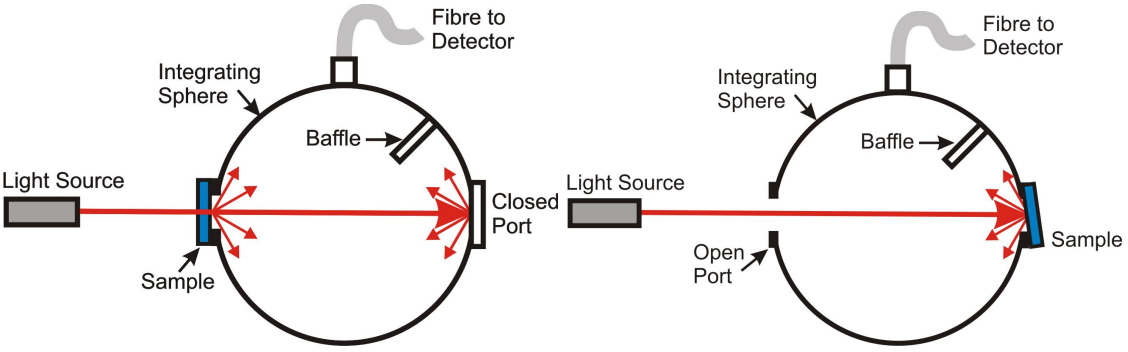

Figure 3.9: Integrating sphere operation

The integrating sphere features a highly-reflective diffuse interior coating which ensures that all light is uniformly scattered across the interior surface, regardless of the point of origin. A detector is fitted to the surface of the sphere which measures the optical power within the sphere, and is measured using the Bentham PVE300 detection electronics. The sphere can be configured to measure the optical reflectance by placing the sample at the rear port, or the optical transmittance by placing the sample in front of the entry port and closing the rear port. The optical absorption of the sample can then be calculated if the input power per wavelength is known.

3.4 Simulation

As is detailed in section 2.4, the numerical simulation of light scattering arrangements is essential in determining their optimum formation. A vast parameter space is available and simulation allows a broad number of experimental results to be collected quickly. For the type of optical structures desired in this work, several techniques can be considered.

3.4.1 Ray Tracing

This technique is a method of mapping the propagation of electromagnetic waves including light through various systems including absorber and reflector materials. The use of this technique for optical applications dates back to the 1900s, and can be extended for the simulation of light scattering from textured substrates [128]. It is however only suitable for features of large geometry and therefore is unsuitable for the modelling of nano-scale features.

3.4.2 Mie theory

The Lorenz-Mie solution to Maxwell's equations is an analytical technique to determine the scattering of a plane wave encompassed by a homogeneous medium on interaction with a spherical particle. The solutions were devised by Gustov Mie in 1908 [129], and is the closest approximation of the scattering caused by such particles in classical physics. The calculations take the sphere radius and refractive index of its constituent material and determine the scattering and extinction due to the presence of the particle. Limitations of the technique include the stipulation that the surrounding medium in such simulations must have an extinction coefficient of zero, and the technique is only valid for spherical shaped particles in excess of 10nm [130].

3.4.3 Finite-Difference Time Domain

The Finite Difference Time Domain (FDTD) technique overcomes the limitations of the previously mentioned techniques, and evaluates the electromagnetic wave propagation in the time domain. This technique allows for the numerical analysis of a system of differential equations, to allow modelling of computational electrodynamics such as the interactions between plane wave light and materials such as metal, dielectric, semiconductor or free space. The propagation of wavelength-limited light waves throughout materials with specified refractive indices can be easily modelled using this technique, providing results in the frequency domain following a Fourier transform.

The FDTD method is a mesh-based analysis technique, which computes the solution to Maxwells equations in a specified region of a model, known as a Cartesian Yee cell [131]. This is achieved by first separating the partial-differential forms of the solution using central-difference approximations, then solving the resultant finite-difference equations

by means of the electric-field vector followed by the magnetic field vector in the time domain until a steady-state behaviour is maintained. The specified Yee cell lattice is staggered throughout the simulation grid such that each E-Field cell overlaps each H-field cell about their mid-points. This arrangement is detailed in figure 3.10.

An iterative change in the time derivative (the *E-Field*) is dependant of the change of the rotation of the three-dimensional vector (the *H-Field*) or curl. This is therefore solved using the time-stepping method, which presents the updated solution to the E-Field as a result of its current stored value and the curl of the H-Field in space. The same arrangement is used to concurrently evaluate the H-Field in a time-staggered *leap-frog* scheme. The following cell region is then evaluated, and simulation resolution can be specified by means of the resolution of the constituent cells.

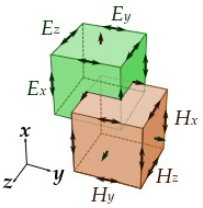

Figure 3.10: Cartesian Yee cell [132]

In this work, the Lumerical FDTD Solutions software package is used [133], as this package allows a wide variety of materials and shape configurations to be explored, and reports data such as optical reflectance, transmittance, wave propagation and power absorption. The main window of the FDTD solutions software package is displayed in figure 3.11, which shows the objects tree on the left-hand pane with a multi-layer model defined, the various perspective views of the defined model in the centre, and the the details of optimisation sweeps configured on the right-hand pane. Various regions of dielectric, metal and semiconductor are shown in the objects tree alongside a plane wave source and a range of monitors. Further details on *Lumerical FDTD Solutions* and the specification of structures and measurements are detailed in Chapter 5.

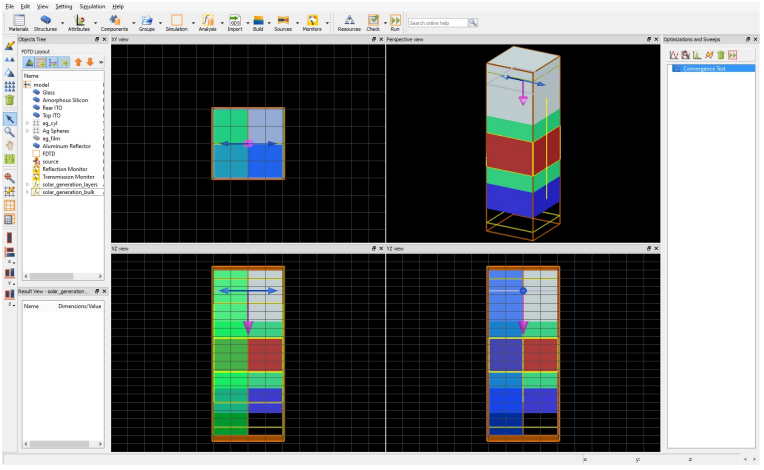

Figure 3.11: Lumerical FDTD Solutions main window

Chapter 4

Amorphous Silicon Photovoltaic Devices

4.1 Introduction

The purpose of this investigation is to determine the deposition conditions which result in optimum optical and electronic quality, to ensure the highest electronic performance and optical absorption characteristics. These characteristics will contribute to an increase in photovoltaic performance. Proper understanding of the effects of the many possible deposition conditions are essential when attempts are made to improve the optical and electrical performance of a solar device made using the PECVD technique.

A repeatable process with low variation between deposition runs under identical deposition parameters is desirable, as is a uniform deposition rate across the work-piece and the reactor platen. High performance photovoltaic devices are defined as those which exhibit these properties in addition to a purely amorphous film structure verified by spectroscopic ellipsometry and Raman spectroscopy, highest achievable photo-activity of several orders of magnitude and P-I-N photovoltaic device performance comparable with those detailed in recent literature for this type of device specified in section 2.3.4. Absolute deposition rate is not considered as a performance metric in this investigation, however it is noted when such deposition rates change significantly within the results.

This section describes how the variation in the process conditions whilst using PECVD for deposition of amorphous silicon thin films can affect the resultant performance of the solar device. From this investigation, the starting point conditions for development of a deposition process can be readily known, which will help to reduce the development time. The optimum deposition conditions for maximum optical and electronic device performance, process reliability and ease of deposition are identified within this section.

4.2 Experimental Detail

In this investigation, deposition is performed using an Oxford Instruments PlasmaLab System 100 deposition tool, as described in section 3.2.1. The deposition conditions for PECVD are variable, and include gas flow rates, chamber pressure, substrate temperature, RF power, and deposition time. The geometry of the deposition reactor chamber and RF electrodes also affect the performance of the reaction, and therefore the data ascertained for this experiment will only be repeatable using an identically specified system. The dilution of the process gases and the choice of dilute gas can also significantly influence the electrical performance. The dilution of process gas in varying levels of hydrogen, which contributes to the formation of the amorphous silicon network, and in argon which does not contribute but influences the deposition performance and the resultant device quality is investigated. Each individual layer of the P-I-N structure must be optimised in thickness, which forms the basis of the process development routine.

The first step of the fabrication process is to determine the optimum deposition conditions for each layer. Beginning with complete silicon P-I-N devices may lead to a quicker series of results, however the data obtained from these results will tell very little about the internal behaviour of the cell and make it difficult to diagnose poor performance or seek higher efficiencies. For these purposes, it is essential to fabricate individual thin film single layers using varying deposition conditions, and thoroughly examine their optical and electrical performance before committing these conditions to a complete device. The first step is to examine the dark and photo conductivities (σ), optical band gap (E_g), optical transmittance and reflectance at various wavelengths and thin film thickness. From these experiments it is possible to determine specific deposition problems such as inefficient doping of layers or contamination of intrinsic material.

Once optimum layer quality has been obtained, the deposition of amorphous P-I-N structures on glass substrates using the optimised single-layer conditions can be undertaken, which will confirm the optical and electrical performance of the amorphous silicon layers. The device can then be examined by means of an I-V curve and quantum efficiency measurements, which can be used to determine the energy conversion efficiency (η), fill factor, V_{oc}, I_{sc}, and maximum power output. In addition, the effects of controlling the rate of reaction using a dilution of inert argon gas will be investigated, to examine the effects on the electrical properties of the resultant silicon thin films.

The initial set of conditions provided by the system manufacturer for the deposition of basic amorphous silicon thin films is used as a commencement point for the optimisation process. Each parameter will be independently varied throughout a range of conditions detailed in each sub-section, whilst the remaining variables in the investigation will be maintained as per the base-line conditions to ensure the effects of independent parameters are highlighted. These initial deposition conditions for intrinsic and doped regions, together with the the intrinsic deposition rate are presented in table 4.1.

Variable	**Unit**	**Value**
RF Power	(W)	10
Chamber Pressure	(mTorr)	1000
Substrate Temperature	(°C)	250
Gas Flow Rate (Silane)	(sccm)	100
Gas Flow Rate (Hydrogen)	(sccm)	0
Gas Flow Rate (Argon)	(sccm)	475
Gas Flow Rate (Diborane in doped layers)	(sccm)	5 - 15
Gas Flow Rate (Phosphine in doped layers)	(sccm)	5 - 15
Deposition Rate	(nm/sec)	0.42

Table 4.1: Initial deposition conditions

4.3 Deposition

4.3.1 Intrinsic Layers

The intrinsic regions of the P-I-N device structure are fundamental in defining the performance of the solar device. This region performs all of the photon absorption and conversion into charge carriers, the passivation of the amorphous matrix is therefore very important in this region and must be free from all contamination which could provide Shockley-Reid-Hall recombination centres. While the atomic hydrogen species in the SiH_4 source gas is often sufficient, dilution in additional hydrogen is investigated.

A series of intrinsic layers have been fabricated in order to determine the effects of the various conditions. Results are presented in the form of dark and photo conductivities (σ) presented on the same axis, which illustrate the intrinsic layer performance. Conductivity measurements of purely intrinsic material with no dopants or contamination will ideally exhibit a very low measured value under dark conditions, with a significant increase in conductivity observed when the material is illuminated. A larger difference ratio between dark and photo conductivities indicates efficient photon absorption.

Contamination of the amorphous silicon material with impurities can also detrimentally affect the performance of this layer, resulting in significantly impaired I_{sc} values, regardless of other conditions. It is therefore essential that the deposition chamber is clean of all metal and other contamination, and dopant gases sufficiently cleared from the chamber using flows of inert gas after the doped layers. The initial deposition conditions based on practice depositions are used as a baseline, and conditions not under test have been kept constant for all depositions. Based on the results this investigation, it is possible to determine under which conditions the optimum electrical properties from silicon material will be obtained.

In this investigation, the deposition will be performed on 50 x 50mm uncoated glass slides of thickness 1mm placed on a 150mm unpolished carrier wafer within the PECVD deposition reactor. All depositions are performed following a 'standard clean' recipe and chamber reconditioning step to ensure no foreign contamination within the films.

4.3.1.1 Variation of RF Power on Intrinsic Layers

The RF power can significantly affect the deposition time and electrical quality of silicon thin films. A higher RF power provides more kinetic energy to the species within the chamber increasing the deposition rate, however higher RF power levels can cause the deposition of thin layers to become difficult to accurately control, and cause increased dust formation within the chamber reducing device yield. Lower RF power reduces ion bombardment damage caused to the growing films and can lead to higher quality material, however this can also reduce the number of weakly-bound hydrogen bonds within the silicon which would otherwise be broken by the plasma. Use of the lowest RF power can therefore result in a silicon film which is much more susceptible to the Staebler-Wronski effect. For these reasons, the range of power levels investigated is from 10W to 30W in steps of 5W. In this investigation, deposition conditions aside from RF power are as per the initial deposition conditions specified in table 4.1. Conductivity parameters under dark and illuminated conditions are shown as a function of RF power in figure 4.1, tabular results are listed in table 4.2.

Power (W)	**Photo Conductivity** $S\,cm^{-1}$	**Dark Conductivity** $S\,cm^{-1}$	**Ratio**	**Notes**
10	2.3×10^{-5}	3.8×10^{-8}	608	OK
15	1.8×10^{-5}	5.6×10^{-8}	327	OK
20	1.2×10^{-5}	9.8×10^{-9}	1243	Pinholes
25	7.0×10^{-6}	4.8×10^{-9}	1449	Pinholes + Dust
30	7.5×10^{-6}	5.6×10^{-9}	1317	Pinholes + Dust

Table 4.2: RF power variations 10 - 30W and resultant conductivities

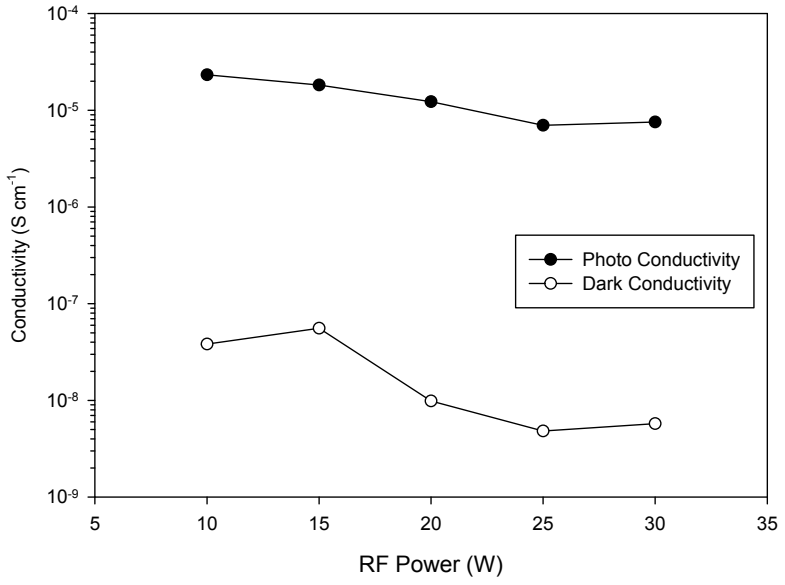

Figure 4.1: Conductivity vs. RF power

4.3.1.2 Variation of Chamber Pressure on Intrinsic Layers

Chamber pressure is influenced by both the gas flow rates and the APC valve position, and determines the number of airborne species with which the plasma can interact. High chamber pressures result in a faster deposition rate and a lower quality deposition under certain circumstances, as the ad-atoms have less time to find an energetically favourable site resulting in a higher level of bond-length disorder. Lower chamber pressures can cause intermittent problems stabilising the RF plasma due to a reduction in airborne species, particularly when combined with low RF power, therefore 300mT is the minimum pressure. In this investigation, deposition conditions aside from chamber pressure are as per the initial deposition conditions specified in table 4.1. Conductivity parameters under dark and illuminated conditions and measured optical absorption coefficient parameters are shown as a function of chamber pressure, varied from 300mT to 1000mT shown in figures 4.2 and 4.3 respectively, while tabular results are listed in table 4.3.

Pressure (mTorr)	**Photo Conductivity** $S\,cm^{-1}$	**Dark Conductivity** $S\,cm^{-1}$	**Ratio**	**Notes**
300	4.3×10^{-5}	6.2×10^{-8}	699	Plasma Failure
350	1.6×10^{-5}	2.7×10^{-8}	592	OK
400	1.6×10^{-5}	3.1×10^{-8}	501	OK
500	1.7×10^{-5}	9.5×10^{-8}	176	OK
750	4.1×10^{-6}	5.8×10^{-8}	71	OK
1000	2.4×10^{-6}	3.1×10^{-8}	77	OK

Table 4.3: Chamber pressure 300 - 1000mT and resultant conductivities

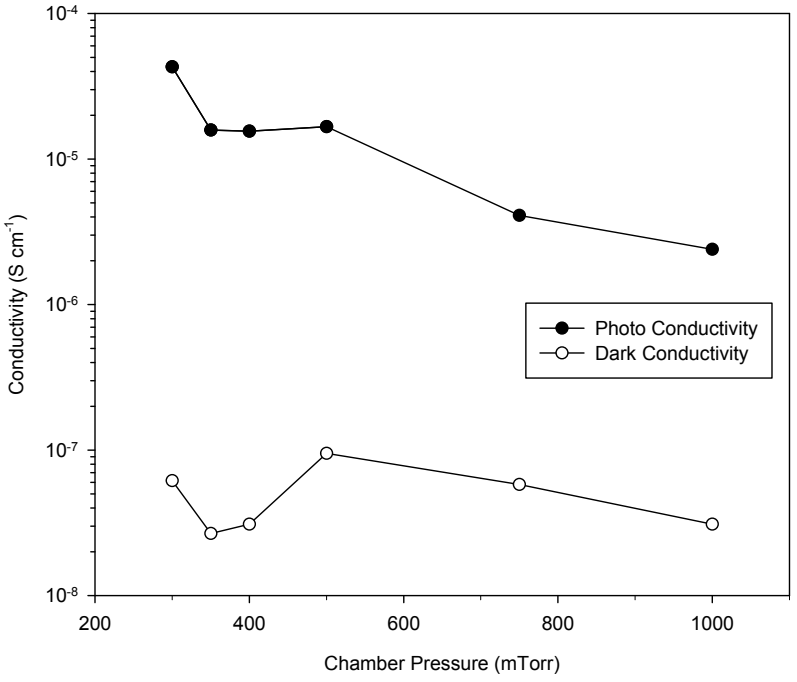

Figure 4.2: Conductivity vs. chamber pressure

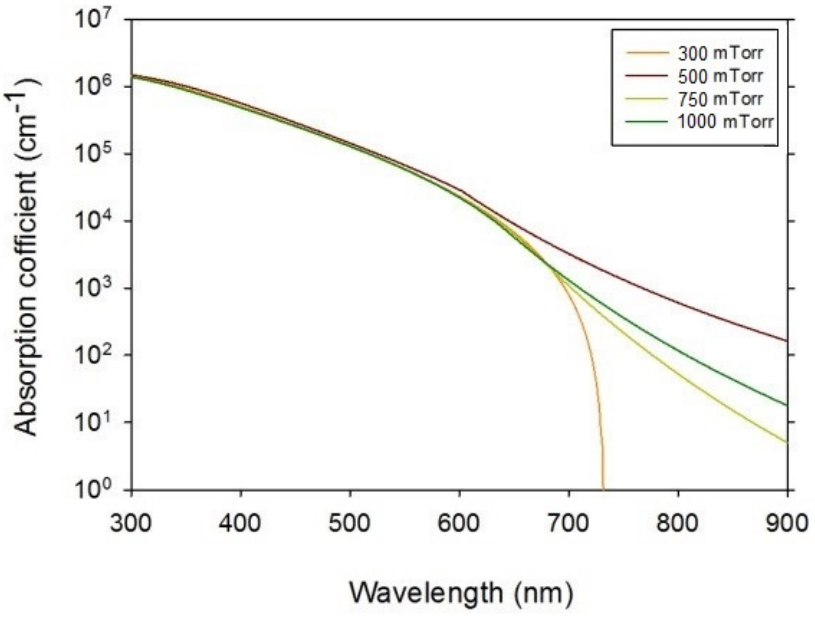

Figure 4.3: Optical absorption vs. chamber pressure

4.3.1.3 Variation of Substrate Temperature on Intrinsic Layers

Substrate temperature affects the speed of film formation of the surface of the substrate, and can also alter the crystallinity of the resultant film. This is due to the application of more thermal energy to the process gases as they reach the substrate providing more time for the ad-atoms to desorb across the surface and find a suitable site. Significantly higher temperatures in excess of 400°C can cause annealing of the amorphous material and micro-crystalline formation which is undesirable for this investigation. In this investigation, deposition conditions aside from substrate temperature are as per the initial deposition conditions specified in table 4.1. Conductivity parameters under dark and illuminated conditions and measured optical absorption coefficient parameters are shown as a function of substrate temperature, varied from 150°C to 350°C in steps of 50°C shown in figures 4.4 and 4.5 respectively, while tabular results are listed in table 4.4.

Temperature (°C)	**Photo Conductivity** $S\,cm^{-1}$	**Dark Conductivity** $S\,cm^{-1}$	**Ratio**	**Notes**
150	2.0×10^{-7}	3.8×10^{-8}	5.3	Low Rate
200	1.3×10^{-5}	1.3×10^{-8}	1000	OK
250	7.6×10^{-5}	6.6×10^{-9}	11515	OK
300	2.4×10^{-4}	6.1×10^{-7}	393	OK
350	2.4×10^{-4}	4.0×10^{-6}	60	OK

Table 4.4: Substrate temperature variations and resultant conductivities

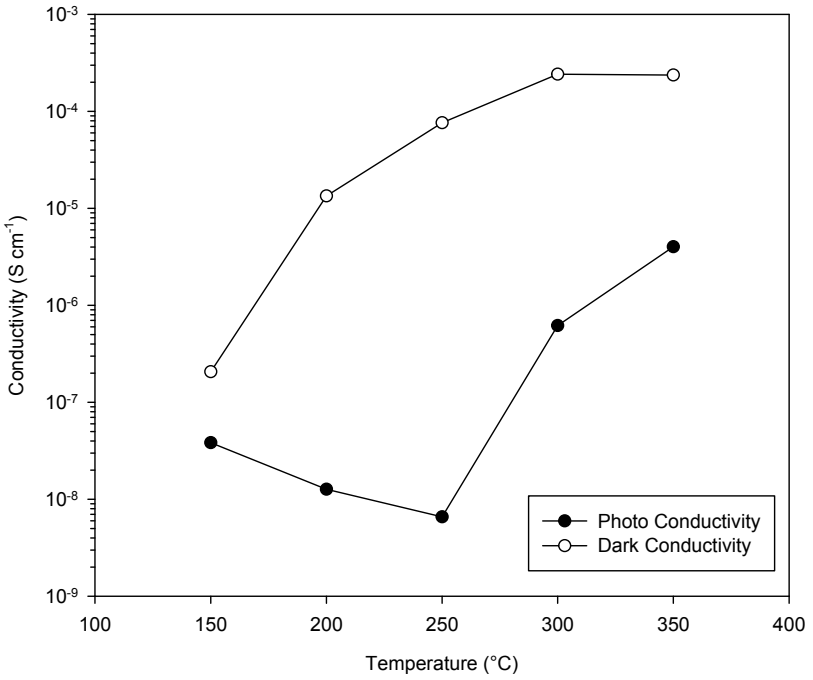

Figure 4.4: Conductivity vs. substrate temperature

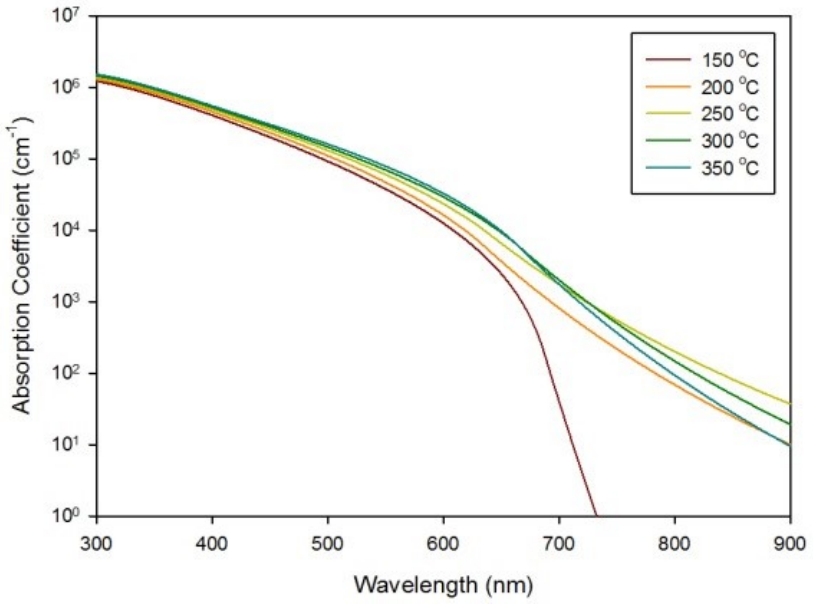

Figure 4.5: Conductivity vs. substrate temperature

4.3.1.4 Variation of Hydrogen Dilution on Intrinsic Layers

The hydrogen content of the process gas will affect the crystallinity and deposition rate of the silicon films. Multi-crystalline material is undesirable as its properties differ significantly from that of amorphous, which an excess of hydrogen gas during deposition will produce. In this investigation, deposition conditions aside from hydrogen flow rates are as per the initial deposition conditions specified in table 4.1. Conductivity parameters under dark and illuminated conditions are shown as a function of hydrogen inclusion (1:1 - 1:10) shown in figure 4.6, while tabular results are listed in table 4.5. All other deposition conditions are maintained as per the base-line conditions shown in table 4.1. The onset of crystallinity is verified using spectroscopic ellipsometry reporting the optical band-gap and Raman spectroscopy reporting the Raman shift of measured films shown in section 4.3.1.5.

Hydrogen Dilution	**Photo Conductivity** $S\,cm^{-1}$	**Dark Conductivity** $S\,cm^{-1}$	**Ratio**	**Notes**
1:1	6.9×10^{-4}	5.7×10^{-6}	122	OK
1:2	1.1×10^{-3}	1.6×10^{-5}	70	OK
1:4	2.1×10^{-3}	2.9×10^{-5}	74	OK
1:10	2.5×10^{-3}	6.9×10^{-6}	360	$\mu c - Si$

Table 4.5: Hydrogen dilution variations 1:1 to 1:10 and resultant conductivities

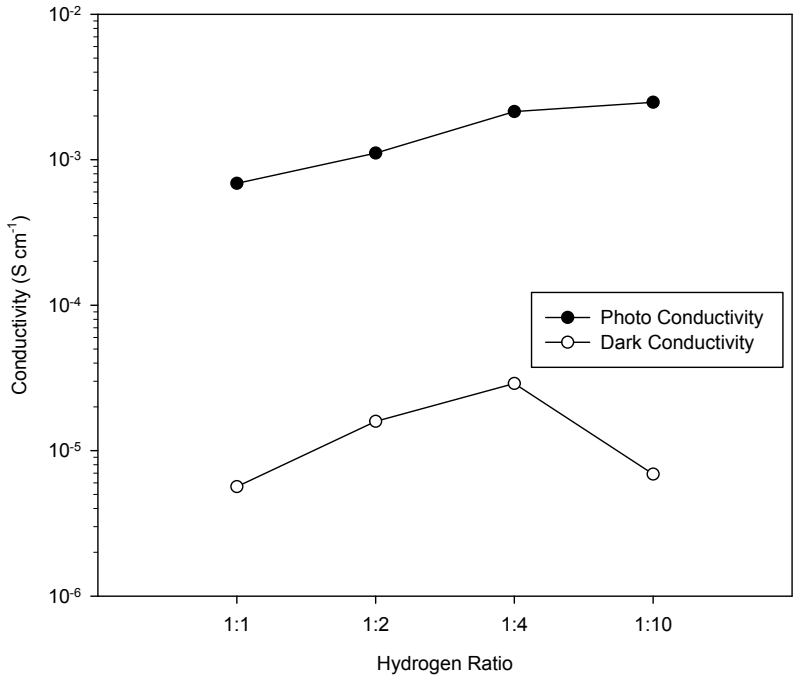

Figure 4.6: Conductivity vs. hydrogen dilution

4.3.1.5 Thickness Uniformity Measurements of Intrinsic Layers

The variation in thickness across the sample is of fundamental importance to the performance of the resultant photovoltaic devices. Device layer thicknesses must be precisely controlled in order to obtain the maximum electrical performance. The ideal silicon thin film will be of a consistent thickness across the entire device, with unavoidable variations due to the plasma deposition only occurring at the edge regions.

Material thicknesses are determined using spectroscopic ellipsometry measured across many points of the sample and analysed with reference to the desired thickness. Figure 4.7 below details the ellipsometry result of a 360nm intrinsic layer. This layer was deposited at the optimum deposition conditions shown in table 4.6 on a 5 x 5cm uncoated glass slide of 1mm thickness. The measured average uniformity on this sample was 3.14nm +/- 1nm, though it is clear from observing the surface plot that the majority of this uniformity variation originates from the edge regions of the sample. The mathematical model used was that of two layers; the first consisting of a 7059 Cauchy glass substrate of 1mm thickness followed by parameterised a-Si material with a Cody-Lorentz oscillator with fitted parameters. Substrate backside correction is enabled in this model, as is angle offset correction.

A general trend is observed in multi-point ellipsometric measurements that deposition uniformity does not vary to a significant degree throughout the parameter variations within this investigation, while those with the slower deposition rates (such as low RF power and low chamber pressure) result in the most repeatable deposition uniformity.

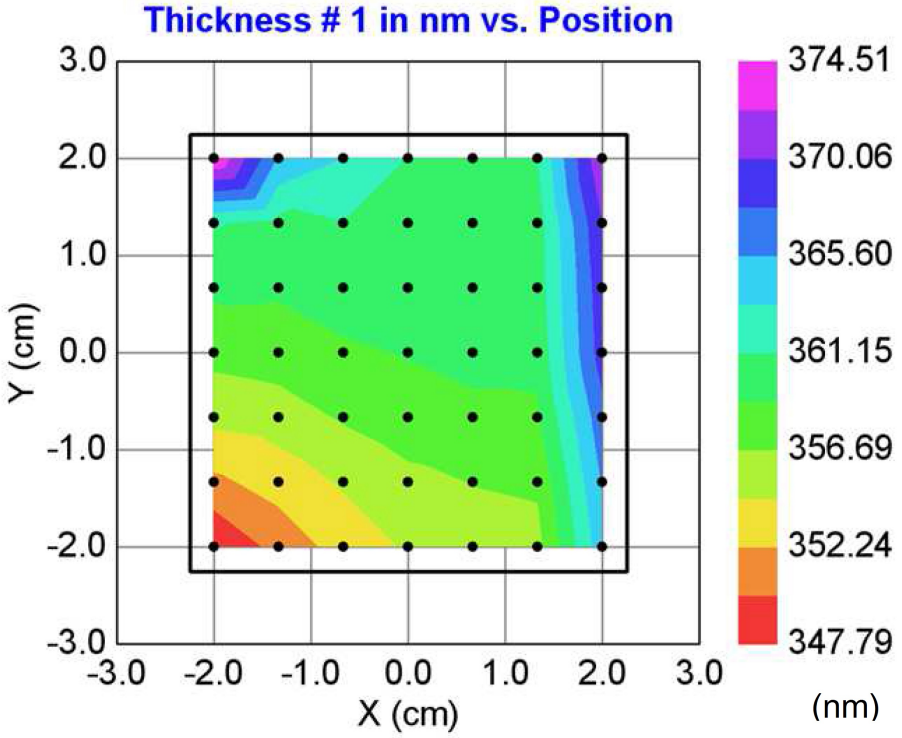

Figure 4.7: Thickness profile determined by spectroscopic ellipsometry

4.3.1.6 Raman Spectroscopy Measurements of Intrinsic Layers

In order to determine the crystallinity of the fabricated thin films, Raman spectroscopy is performed to ascertain the crystalline fraction as described in section 3.3.2. It is observed that for investigation 4.3.1.4, the crystalline fraction increases with increased dilution of silane in hydrogen, with a corresponding reduction in deposition rate.

The Raman spectra of films deposited under high hydrogen dilutions of 1:1 and 1:10 shown in figure 4.8, under excitation wavelength of 532nm. Films prepared with a hydrogen dilution ratio of 1:10, depicted in red demonstrate a sharp peak at $520cm^{-1}$ indicating regions of crystalline phase amongst the broad peak of the mixed micro-crystalline and amorphous material. films prepared at 1:1 hydrogen dilution ratio are depicted in black and show a smaller broad peak at $480cm^{-1}$ which indicates the purely amorphous material which results.

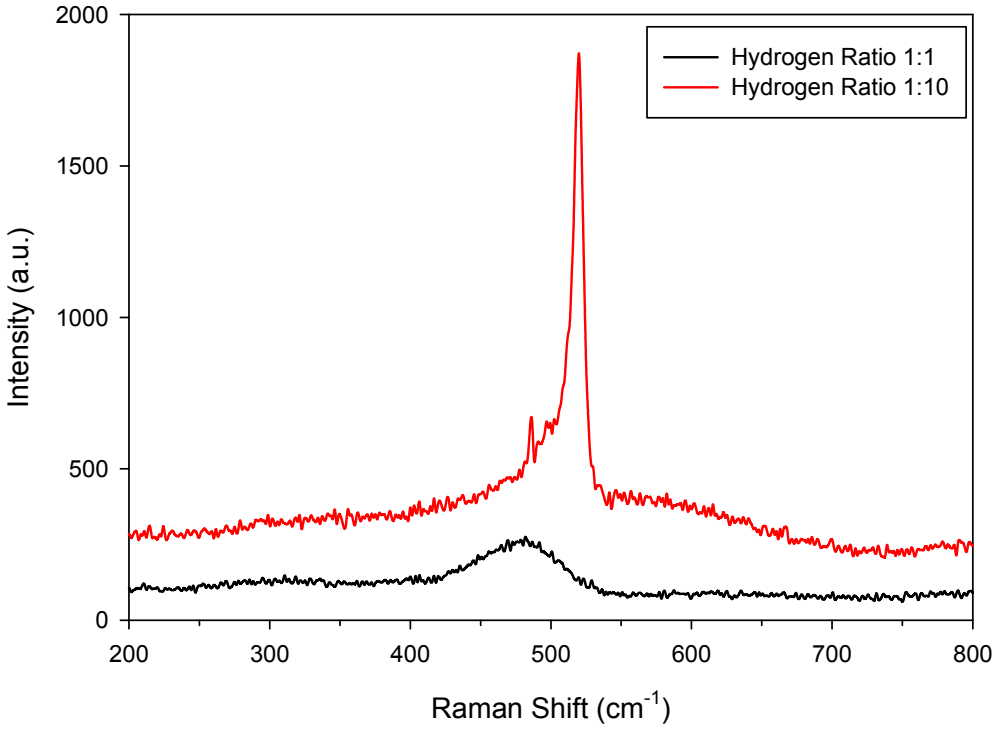

Figure 4.8: Raman measurement of 1:1 and 1:10 hydrogen ratio

4.3.1.7 Analysis

From investigation 4.3.1.1 it can be observed that as the RF power is increased, the dark and to a lesser extent the photo-conductivity of the layers decrease and the photo / dark conductivity ratio increases, indicating enhanced photo-activity and favourable electronic performance. While this is desirable, the additional dust formation within the chamber forming pinholes within the film causes low device yield. To ensure controllable deposition, 10W is used for the optimum material.

Investigation 4.3.1.2 illustrates the effect of chamber pressure variations. In this investigation, the optimum electronic quality is observed at the lower chamber pressures, while chamber pressures of 300mT result in an unreliable plasma deposition. 350mT is therefore deemed the reliable optimum value. Optical results highlight a reduction in absorption coefficient for longer wavelength energy with films deposited at the lowest chamber pressure, with those below 500mT exhibiting a peak in absorption. Short wavelength optical absorption is unaffected by chamber pressure variations.

Investigation 4.3.1.3 shows the variation of substrate temperature, which can be seen to exhibit a large peak in photo-activity at 250°C. Optical results highlight a reduction in absorption coefficient for longer wavelength energy with films deposited below 200°C, with films deposited at 250°C exhibiting a peak in absorption in the long wavelength region. Short wavelength optical absorption varies to a much lesser extent with films deposited at 250°C and 300°C showing the greatest optical absorption.

Investigation 4.3.1.4 presents various dilutions of silane and hydrogen, which show that the optimum conditions are found with an equal 1:1 ratio of the two constituents. Increasing the dilution past this level significantly reduces the deposition rate, and microcrystalline material is formed as ratios of 1:10 are approached which is demonstrated by a narrowing of the optical band gap from 1.7eV towards 1.5eV and lower (not shown in this section). This is verified using Raman spectroscopy measurements in investigation 4.3.1.6. A 1:1 ratio is therefore used for the optimum amorphous material.

A summary of the optimum results obtained from the intrinsic layer investigations, which are used in the fabrication of P-I-N photovoltaic devices in this section are presented in table 4.6.

Variable	**Unit**	**Value**
RF Power	(W)	10
Chamber Pressure	(mTorr)	350
Substrate Temperature	(°C)	250
Gas Flow Rate (Silane)	(sccm)	50
Gas Flow Rate (Hydrogen)	(sccm)	50

Table 4.6: Intrinsic region optimum conditions

4.3.2 Doped Layers

In order to create a functioning photovoltaic device, a junction must be formed using thin layers of doped amorphous silicon deposited either side of the absorber region, as described in section 2.3.3. The next step in the optimisation process is to determine the optimum concentration of dopant gas in the p-type and n-type regions. If the dilution of the dopant gases is too high then the electric field generated by the layer will not be sufficient and the V_{oc} will be reduced. If the doping concentration is too high then the recombination losses in the region will dominate. Low concentrations are expected to illustrate intrinsic behaviour similar to the films shown in section 4.3.1, and dark conductivity is quickly expected to approach photo conductivity as the dopant concentration is increased.

Due to the atomic substitution mechanism of doped hydrogenated amorphous silicon, described in section 2.3.2, the doping efficiency is greater in the n-type regions than within the p-type. A higher concentration of p-type dopant gas will therefore be required compared to the n-type to achieve the equivalent dopant levels throughout the silicon thin film. Optimum deposition conditions carried forward from the previous experiment and not under test have been kept constant and are summarised in table 4.6. Target thin-film layer thicknesses are between 60nm and 80nm on glass substrates, in order to allow for measurable conductivity through the layer. The resultant dark and photo-conductivity measurements and the dark/photo activity ratios for each investigation are then presented. The phosphine and diborane supply to the system is 10% diluted in high-purity argon gas in order to ensure safety and effective control over the doping of the devices. Table 4.7 details the dopant ratio gas percentage values and corresponding gas flow rates within the deposition system.

Dopant Ratio (%)	**Dopant Flow** (sccm)	**Silane Flow** (sccm)	**Hydrogen Flow** (sccm)
0.2	1	50	50
0.4	2	50	50
0.6	3	50	50
0.8	4	50	50
1.0	5	50	50
1.2	6	50	50
1.4	7	50	50
1.6	8	50	50
1.8	9	50	50
2.0	10	50	50
2.2	11	50	50
2.4	12	50	50

Table 4.7: Dopant gas percentage corresponding flow rate

4.3.2.1 P-type Dopant Concentration

Optimisation of the p-type region is vital in achieving high performance from a photovoltaic device, as it is often the first *window* layer which the incoming light encounters. This region has a very low charge carrier lifetime and therefore photons absorbed are almost always lost via recombination. For this reason, the layer must be kept extremely thin whilst still providing an adequate electric field over the device. In this investigation, diborane gas (B_2H_6) is mixed with a flow of silane gas in concentrations of 0.2% to 2.4% shown in figure 4.9 while tabular results are shown in table 4.8.

Concentration (%)	**Photo Conductivity** $S\ cm^{-1}$	**Dark Conductivity** $S\ cm^{-1}$	**Ratio**
0.2	3.6×10^{-5}	8.8×10^{-6}	4
0.8	2.7×10^{-5}	3.7×10^{-6}	7
1.2	4.1×10^{-5}	1.5×10^{-5}	3
1.6	4.0×10^{-5}	1.9×10^{-5}	2
2.0	7.7×10^{-5}	4.9×10^{-5}	2
2.2	5.1×10^{-5}	3.4×10^{-5}	2
2.4	4.7×10^{-5}	3.1×10^{-5}	1

Table 4.8: Diborane concentration variation

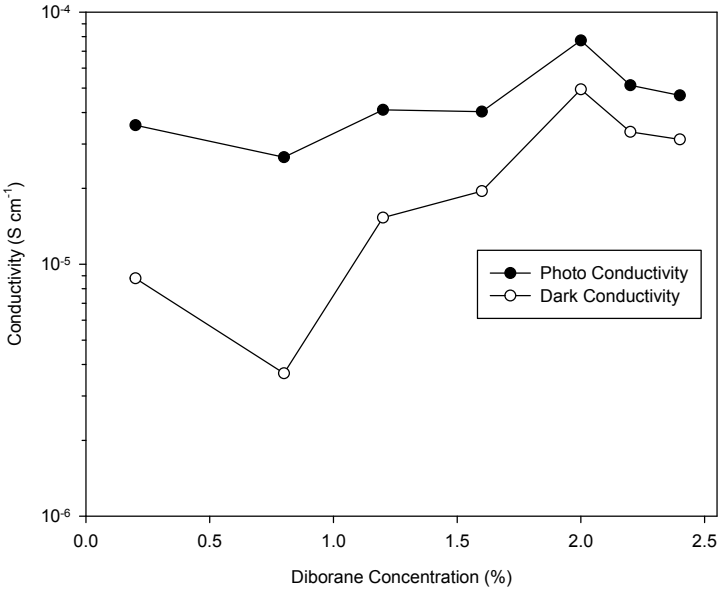

Figure 4.9: Conductivity vs. diborane concentration

4.3.2.2 N-type Dopant Concentration

Optimisation of the n-type region is also significant in determining the performance of a device, as this layer is positioned immediately before the back reflector and therefore light propagates through this region both before and after reflection and/or potential optical scattering. In this investigation, the gas phosphine (PH_3) is mixed with a flow of silane gas in concentrations of 0.2% to 2% shown in figure 4.10 while tabular results are shown in table 4.9.

Concentration (%)	**Photo Conductivity** $S\,cm^{-1}$	**Dark Conductivity** $S\,cm^{-1}$	**Ratio**
0.2	8.8×10^{-4}	9.1×10^{-8}	4
0.4	1.0×10^{-2}	4.5×10^{-3}	7
0.6	1.0×10^{-2}	1.0×10^{-2}	3
0.8	3.9×10^{-3}	3.9×10^{-3}	2
1.0	3.6×10^{-3}	3.6×10^{-3}	2
1.2	2.6×10^{-3}	2.6×10^{-3}	2
1.4	2.1×10^{-3}	2.1×10^{-3}	1
1.6	1.9×10^{-3}	1.9×10^{-3}	1
1.8	1.1×10^{-3}	1.1×10^{-3}	1
2.0	1.3×10^{-3}	1.3×10^{-3}	1

Table 4.9: Phosphine concentration variation

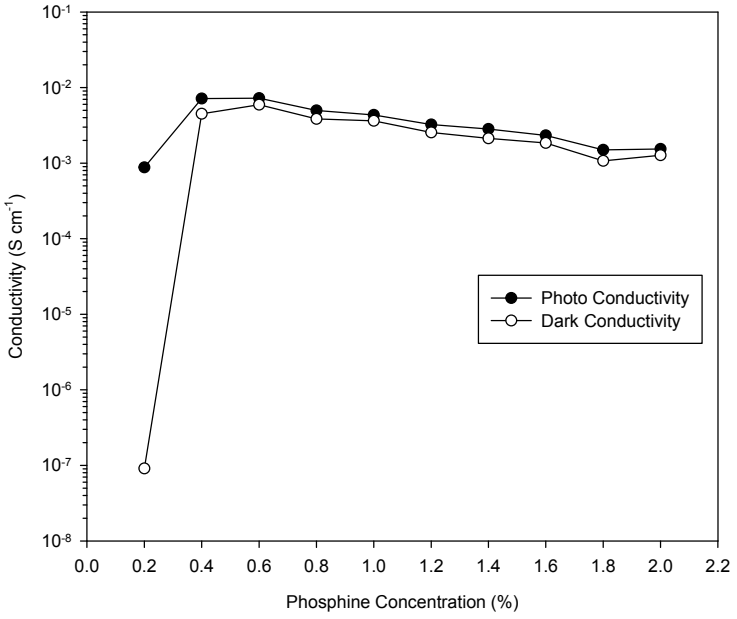

Figure 4.10: Conductivity vs. phosphine concentration

4.3.2.3 Active Dopant Levels

A series of doped regions deposited are examined using secondary ion mass spectroscopy (SIMS) to determine the level of doping within the layer, shown in figures 4.11 and 4.12. P-type dopant concentrations of film thicknesses of approximately 60nm are shown for concentrations of 1.2%, 1.6% and 2.0% dilution; while n-type concentrations are shown for 0.8%, 1.2% and 2.0% dilution for layers of approximately 80nm thickness. Secondary ion mass spectroscopy measurements presented in this section were performed at Loughborough Surface Analysis Ltd.

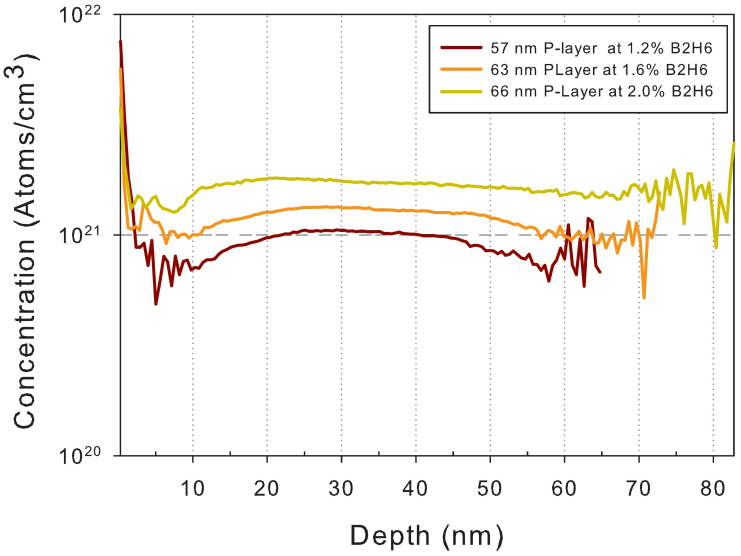

Figure 4.11: Doping levels of p-type region

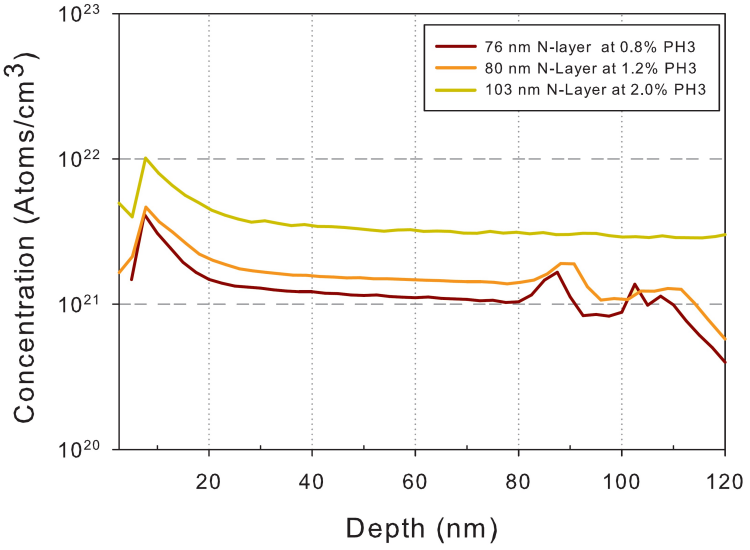

Figure 4.12: Doping levels of n-type region

4.3.2.4 Analysis

Based on the results detailed in investigation 4.3.2, it is possible to determine under which conditions the optimum electrical properties for the doped layers will be obtained. The optimum conditions are defined as the concentration at which the dark and photo-conductivity ratio falls to a level of 2x or less, and further concentration of dopant gas causes a reduction in conductivities illustrating that charge carrier mobility is impeded.

From the p-type investigation detailed in figure 4.9, it can be observed that the silicon thin film begins doped-like behaviour at concentrations exceeding 1%, with the lowest ratio before conductivity is reduced occurring at 2% dilution of p-type dopant. This corresponds to a diborane flow rate of 10 sccm. From the n-type investigation, figure 4.10 illustrates doped like behaviour at concentrations of 0.8 - 1.2%, corresponding to a phosphine flow rate of 4 - 6 sccm. Conductivity is gradually impeded with further increases to the phosphine concentration. Due to its position at the rear of the device, it is possible to fabricate an n-type region with greater thickness compared to the p-type, and a reduced doping concentration.

To verify the doping effectiveness, and quantify the doping level for a given gas flow rate, secondary ion mass spectroscopy (SIMS) measurements are performed on doped regions of thicknesses between 57 - 103nm. As can be observed from figure 4.11, the doping levels achieved in the p-type region for dopant dilutions of 0.8%, 1.2% and 2.0% are strongly centred around the 10^{21} cm^{-3} region, with a peak in doping observed within the first 5 nm. Concentrations of 2%, corresponding to a dopant gas flow of 10 sccm provide the most continuous doping throughout the film thickness, therefore to the very narrow thickness requirement of this layer, this flow rate is selected.

It can be observed from figure 4.12 that the 1.2% dilution of diborane provides a comparable and most consistent doping throughout the layer, with doping levels centred around 10^{21} cm^{-3} which corresponds to a phosphine gas flow rate of 6 sccm. A concentration of 2% provides higher doping up to 10^{22} cm^{-3}. To ensure reliable doping but without creating excess recombination, the concentration of 1.2% is chosen which corresponds to a phosphine gas flow rate of 6 sccm.

4.3.3 P-I-N Structure Devices

Based on the optimum results from the single layer investigations detailed in table 4.6, a series of P-I-N structures are fabricated in order to determine the effects of variations in layer thickness. The conditions have been maintained at the optimum found in the previous section for all variables excluding the deposition time of the layer under investigation. Other layers are maintained at fixed thicknesses as detailed in the investigation. The resultant cell efficiency, FF, V_{oc} and I_{sc} for each investigation are presented.

TCO glass substrates are chosen to perform the deposition of amorphous silicon P-I-N structures. The TCO coating is electrically conductive and allows the front contact of the device to be free of any metallisation to provide the optimum surface for thin-film silicon deposition. Pilkington NSG TEC-8 (Transparent Electrically Conductive) and TEC-15 glasses are specially selected to have the lowest series resistances within the Pilkington range, whilst in the case of TEC-8 producing a certain amount of haze ideally suited to the deposition of amorphous silicon and TEC-15 providing the ideal planar substrate for the investigation of optical enhancements, as described in section 2.5.2. The resistivity of the TEC-8 glass is approximately 6-9 $\Omega.cm$, while TEC-15 is approximately 14 - 16 $\Omega.cm$ making for an excellent contact materials. Rear contacting of the device is performed using deposition of 500nm aluminium on to the highly-doped n-type silicon, using e-beam assisted evaporation through a 9-region stencil mask.

Each fabricated substrate of dimension 50 x 50mm features a 5mm edge region on which no deposition is performed, achieved by masking this region during deposition. The purpose of this is to allow electrical contacting to the front TCO region once the cell is fabricated. Three contact pins are fixed within the measurement apparatus, as described in section 3.3.3. Each substrate features nine individual photovoltaic cells of dimension 10 x 10 mm, all of which are tested for I-V response in succession. The highest performance device is selected as the characteristics reported for the entire substrate under test, and other measurements are neglected as this represents the capabilities of the deposition routine most effectively. Duplicate measurements are avoided as prolonged light exposure effects during measurement can cause a reduction in values.

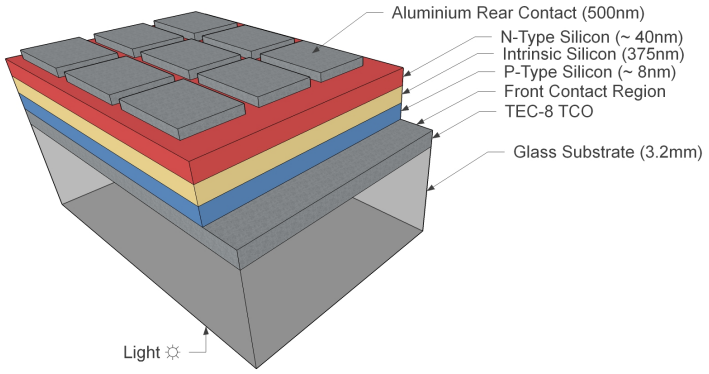

Figure 4.13: Amorphous silicon P-I-N structure on TEC-8 TCO

4.3.3.1 Variation of P-type Layer Thickness

The p-type layer thickness is fundamental in determining the performance of the photovoltaic device. For this reason this is very sensitive to thickness variations and must be kept shallow whilst retaining adequate electrical ability to provide charge carrier separation. Parameters are shown as a function of p-layer thickness, plotted against cell efficiency, fill factor, V_{oc} and I_{sc}, shown in figures 4.14 and 4.15 respectively. Layer thickness is varied from 8nm to 15nm in steps of 2nm for the first three thicknesses and 3nm in the final deposition thickness, whilst intrinsic and n-type layer thicknesses remain at 375nm and 40nm respectively.

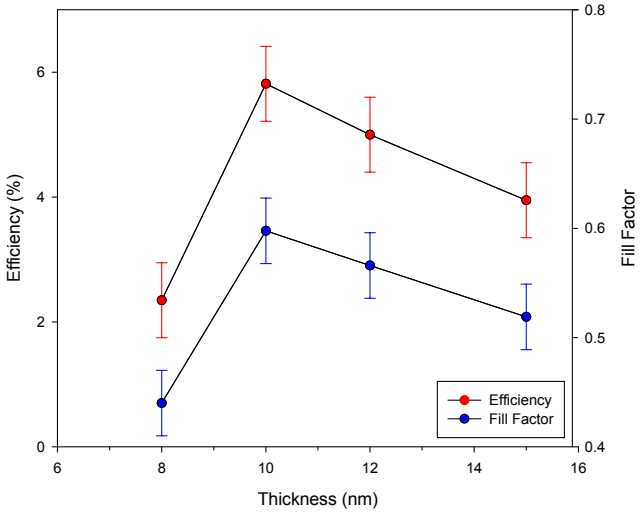

Figure 4.14: P-type layer thickness vs. efficiency and fill factor

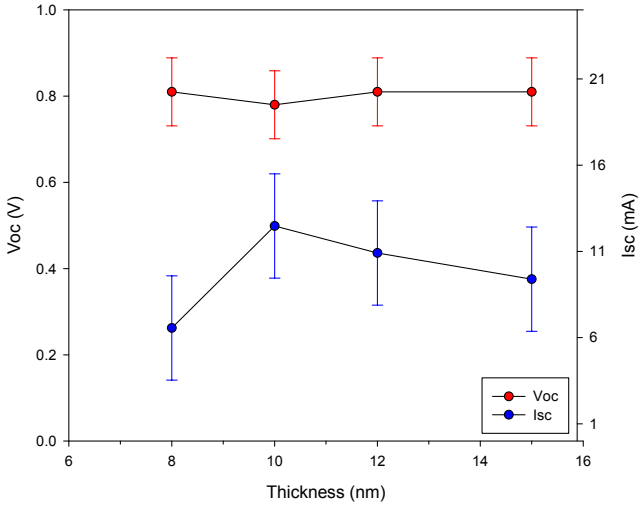

Figure 4.15: P-type layer thickness vs. V_{oc} and I_{sc}

4.3.3.2 Variation of Intrinsic Layer Thickness

The intrinsic layer is the layer in which the vast majority of photons are absorbed within the P-I-N device architecture, so the layer must exhibit exceptional properties such as dark / photo conductivity ratio. A peak in performance will exist for this layer; if it is too thin then absorption will be reduced and I_{sc} will suffer, whilst if it is too wide then the electric field will be reduced causing impaired V_{oc} and the potential for trapped charges within the central region where the electric field is diminished.

Parameters are shown as a function of intrinsic layer thickness, plotted against cell efficiency, fill factor, V_{oc} and I_{sc}, shown in figures 4.16 and 4.17 respectively. Layer thickness is varied from 360nm to 390nm in steps of 10nm, whilst p-type and n-type layer thicknesses remain at 10nm and 40nm respectively.

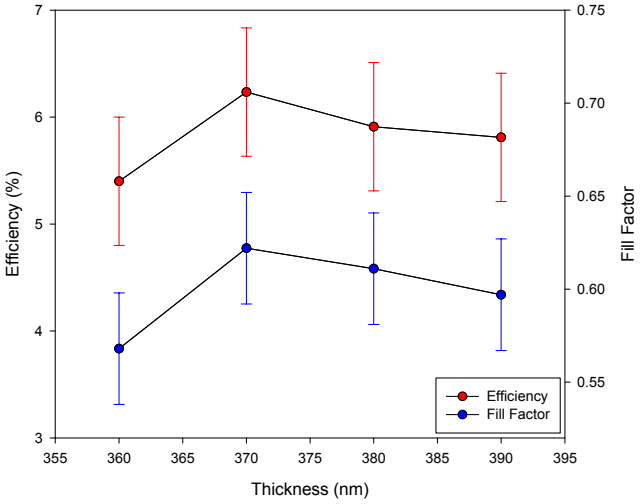

Figure 4.16: Intrinsic layer thickness vs. efficiency and fill factor

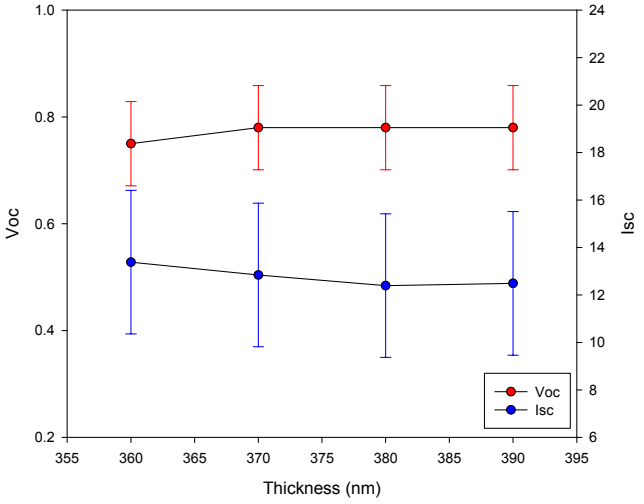

Figure 4.17: Intrinsic layer thickness vs. V_{oc} and I_{sc}

4.3.3.3 Variation of N-type Layer Thickness

In a similar way to the p-region, this layer serves to create the electric field and does not contribute to carrier generation to any significant degree. It is however the layer which the unabsorbed light photons need to penetrate and be reflected from the rear contact reflector, to be absorbed within the intrinsic layer on their second pass.

In order to reduce recombination losses, the doping levels in this region are lower than in the p-type to help reduce the number of defects. The layer must therefore be thicker in order to create an adequate electric field. Parameters are shown as a function of n-type layer thickness, plotted against cell efficiency, fill factor, V_{oc} and I_{sc}, shown in figures 4.18 and 4.19 respectively. Layer thickness is varied from 30nm to 60nm in steps of 5nm, whilst p-type and intrinsic layer thicknesses remain at 12nm and 375nm respectively.

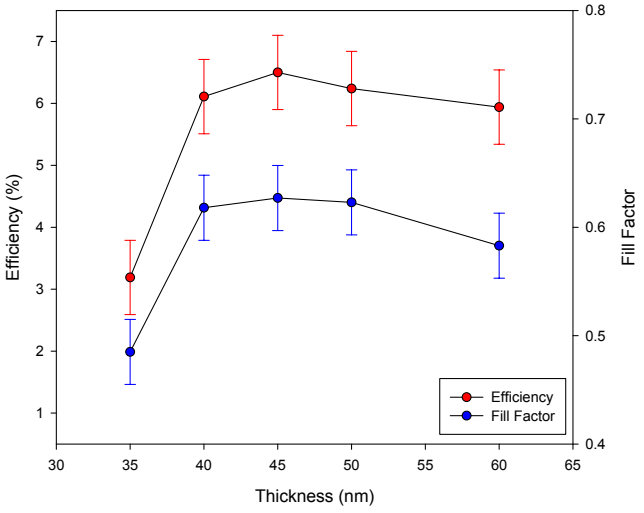

Figure 4.18: N-type layer thickness vs. efficiency and fill factor

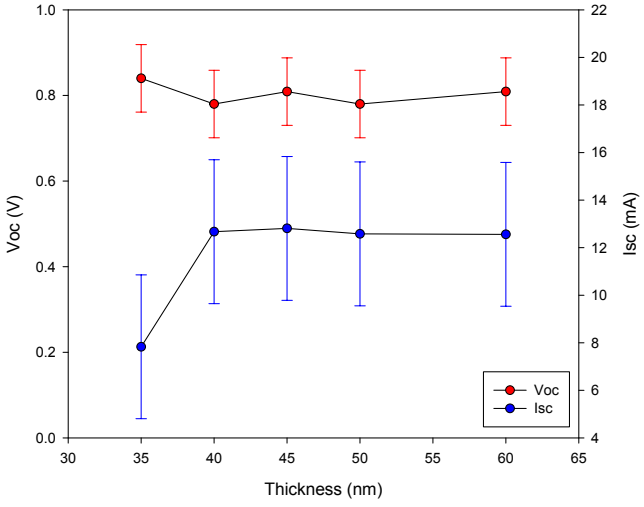

Figure 4.19: N-type layer thickness vs. V_{oc} and I_{sc}

4.3.3.4 The use of Argon as Dilute Gas

In order to realize high quality amoprphous silicon thin films, it is essential to maintain accurate control over the deposition rate. In particular for the p-type doped regions investigated in section 4.3.3.1, the tolerance for the highest efficiency can be extremely narrow. There is also the possibility of the plasma discharge taking between 1 - 2 seconds to start at the beginning of the deposition at low pressures and power levels; this can lead to an ambiguous deposition time and errors in repeatability. It has been determined in section 4.3.1.4 that dilution of the process gas in hydrogen causes a reduction in deposition rate but at the expense of the formation of micro-crystalline material, so an alternative method of reducing the deposition rate is the dilution in inert argon gas.
A selection of amorphous P-I-N devices are fabricated, using the optimised deposition parameters from the investigations within this section. Parameters are shown as a function of argon flow rate, plotted against energy conversion efficiency and fill factor of the measured P-I-N device, shown in figure 4.20. Argon flow rate is varied from 0 sccm to 500 sccm.

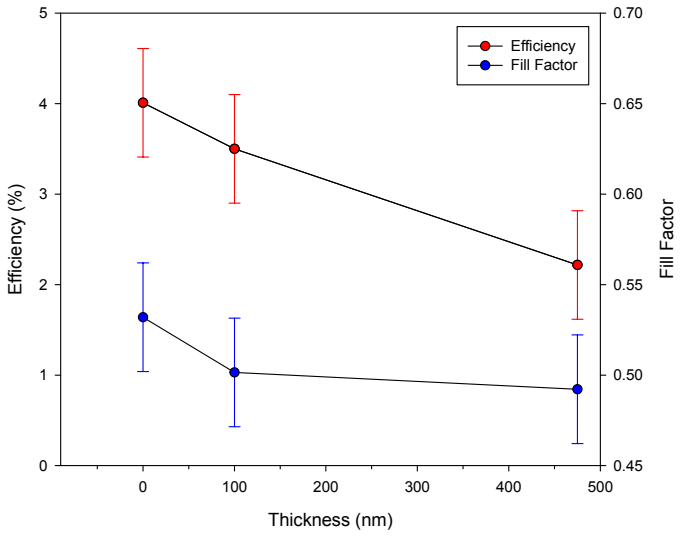

Figure 4.20: Argon dilution vs. efficiency and fill factor

4.3.3.5 Error and Repeatability between Device Regions

Within this investigation, thin film single layer and P-I-N device performance results are reported. For each measurement of photo- and dark-conductivity, three measurements are taken from the thin film as discussed in section 3.3.4; while for the P-I-N devices nine measurements are taken from across the device surface as shown in figure 4.13. Deposition uniformity variations, substrate contamination, plasma edge effects and contact series resistances all contribute to the measurement variation observed on each device.

For each measurement of conductivity, the median value is selected to represent the electrical performance of the thin film in order to neglect outliers and measurement / contacting errors. For each measurement of the P-I-N devices, the maximum performance region is selected. A typical set of cell efficiency results from the nine measurement regions, for two successive P-I-N device depositions is detailed in table 4.10.

Region	**First Cell (%)**	**Second Cell (%)**	**Variation**	**Percentage**
9	5.23	5.65	0.4	7%
8	5.20	5.52	0.3	6%
7	4.93	5.60	0.7	12%
6	4.83	5.50	0.7	12%
5	4.93	5.52	0.6	11%
4	4.75	5.49	0.7	13%
3	4.66	4.70	0.1	1%
2	4.62	5.19	0.6	11%
1	3.99	5.04	1.1	21%
Average	4.79	5.35	0.6	10%

Table 4.10: Efficiency device performance variation

A general trend can be observed that devices 7, 8 and 9 have the highest energy conversion efficiencies, followed by 4, 5, and 6, whilst 1, 2 and 3 are generally the most poorly performing. It is thought that two mechanisms are responsible for this variation, related to both the method of fabrication and the measurement technique. As cells 7, 8 and 9 are positioned adjacent to the front contact strip, a shorter distance of TCO material exists between contact and device. Regions 1, 2 and 3 therefore exhibit resistive losses due to the greater width of TCO material which particularly affects the V_{oc} of the measured device. Furthermore, and partly due to the TCO width, it is noted that the order of measurements results in a period of prolonged light exposure for the final devices which are measured. Light exposure under one-sun conditions serve to reduce the photovoltaic performance, particularly the I_{sc} due to effects described in section 2.3.3

For this reason, device variation across cell regions are not compensated for, but rather device variation between two successive depositions under identical conditions. It can be observed in table 4.10 that cell efficiencies vary by an average of 0.6%, a 10% variation in values.

Error bars are therefore presented on the efficiency, fill factor, V_{oc} and I_{sc} graphs in this section of the appropriate calculated values to compensate for this variation in device performance. Error bars are not presented on conductivity measurement graphs due to the use of a logarithmic scale on these result graphs.

Further analysis of error and variation has been performed on the fill factor, open-circuit voltage and short-circuit current values providing values for variation in each.

Variable	**Region**	**First Cell**	**Second Cell**	**Variation**	**Percentage**
Fill Factor	9	0.60	0.58	0.02	3%
Fill Factor	8	0.60	0.58	0.02	3%
Fill Factor	7	0.58	0.58	0.00	0%
Fill Factor	6	0.58	0.55	0.03	5%
Fill Factor	5	0.59	0.57	0.02	4%
Fill Factor	4	0.58	0.57	0.01	2%
Fill Factor	3	0.56	0.47	0.09	19%
Fill Factor	2	0.53	0.51	0.02	4%
Fill Factor	1	0.50	0.52	0.02	4%
Average		0.57	0.55	**0.03**	2.82%
V_{oc} (V)	9	0.82	0.74	0.1	11%
V_{oc} (V)	8	0.82	0.72	0.1	14%
V_{oc} (V)	7	0.82	0.72	0.1	14 %
V_{oc} (V)	6	0.79	0.74	0.1	7 %
V_{oc} (V)	5	0.8	0.72	0.1	11 %
V_{oc} (V)	4	0.8	0.72	0.1	11 %
V_{oc} (V)	3	0.8	0.74	0.1	8 %
V_{oc} (V)	2	0.8	0.72	0.1	11 %
V_{oc} (V)	1	0.8	0.72	0.1	11 %
Average (V)		0.81	0.73	**0.08**	10.88 %
I_{sc} (mA)	9	10.57	13.05	2.5	19 %
I_{sc} (mA)	8	10.53	13.09	2.6	20 %
I_{sc} (mA)	7	10.28	13.2	2.9	22 %
I_{sc} (mA)	6	10.28	13.3	3.0	23 %
I_{sc} (mA)	5	10.42	13.46	3.0	23 %
I_{sc} (mA)	4	10.11	13.35	3.2	24 %
I_{sc} (mA)	3	10.28	13.51	3.2	24 %
I_{sc} (mA)	2	10.74	14.01	3.3	23 %
I_{sc} (mA)	1	9.84	13.3	3.5	26 %
Average (mA)		10.34	13.36	**3.02**	22.61%

Table 4.11: Fill Factor, V_{oc} and I_{sc} device performance variation

4.3.3.6 Analysis

It can be observed that small variations in the p-type layer thickness result in the most profound variations in cell performance. 10nm thickness appears to be the optimum point which maximises cell performance, although a slight drop in I_{sc} is also observed. The intrinsic region thicknesses vary over a much wider range, with 370nm being the optimum. At this stage it can be observed from the I_{sc} and V_{oc} charts that as the layer thickness is increased, the I_{sc} appears to decrease slightly due to greater charge carrier recombination within the thicker region while the V_{oc} remains constant once a thickness of 370nm is reached. The n-type layer shows a much less profound difference, with the 35nm thickness showing a lower performance than regions thicker than 40nm.

Results of investigation 4.3.3.4 show that the use of argon gas as a dilution additive to the process gases has a detrimental effect to the device performance, which shows a significant decrease in cell performance and fill factor as the argon dilution is increased. It is thought that the effect of the addition of argon, while chemically inert, causes increased ion bombardment damage to the growing films, increasing the amorphous disorder and displacing hydrogen passivation atoms from the matrix. This therefore significantly reduces the electrical performance of the layer.

Based on the results from is section, a set of optimised deposition thicknesses for a complete P-I-N device can be stated. A summary of the results from the variations in the P-I-N layer thickness investigation is presented in table 4.12. The silicon deposition conditions such as substrate temperature and chamber pressure are presented previously in table 4.6.

Variable	**Unit**	**Value**
Optimum Thickness	P-type (nm)	10
	Intrinsic (nm)	375
	N-type (nm)	45
	Total (nm)	430
P-Layer Deposition Time	(min:sec)	00:16
I-Layer Deposition Time	(min:sec)	23:42
N-Layer Deposition Time	(min:sec)	02.52
Deposition Rate (P-Layer)	(nm/sec)	0.60
Deposition Rate (I/N-Layer)	(nm/sec)	0.26

Table 4.12: P-I-N device optimum thicknesses

4.3.3.7 Highest Performing Cell Characteristics

A photovoltaic device is fabricated based on the optimum conditions found in this investigation, in order to evaluate the highest performance achievable. The deposition conditions presented in table 4.6 and the region thicknesses detailed in table 4.12 are used to fabricate the device which is prepared as per the design of investigation 4.3.3. The 9-region topography as shown in figure 4.13 is used for measurement and metallisation, resulting in photovoltaic devices with dimensions of 10 x 10mm.

The measured performance characteristics and derived values such as as series resistance, shunt resistance and maximum power point are detailed in table 4.13. The I-V curve and quantum efficiency data for the device is presented in figures 4.21 and 4.22. As can be observed, the devices feature a good V_{oc} and a strong I_{sc}, with a good fill factor leading to an excellent maximum overall efficiency of 6.5%. The maximum power point is at 6.5mW, which corresponds to a current of 10.84 mA and a voltage of 0.6 V. The quantum efficiency shows high absorption in all regions expected of an amorphous silicon device, being particularly responsive to the blue and ultraviolet regions and a strong, even peak between 450nm and 600nm. Additionally the R_{sh} value is adequately low which indicates an effective contacting method with minimal resistive losses.

These devices fabricated on glass substrates and consisting entirely of amorphous silicon material compare favourably with optimised devices reported in section 2.4.2, such as those reported by Fonrodna et al [22] with 6.6% and Rech et al [70] with 6.5% efficiencies, as discussed in detail in section 2.3.4. It is important to highlight that these devices do not feature any anti-reflection treatments on the planar glass surface aside from simple TCO texture, as is commonplace on production devices. An increase in device performance can therefore be expected if optical enhancement designs are integrated into the substrate surface and / or back reflector design, as discussed in section 2.4.

Variable	**Unit**	**Value**
V_{oc}	(V)	0.81
I_{sc}	(mA)	12.81
V_{mp}	(V)	0.60
I_{mp}	(mA)	10.84
Maximum Power	(mW)	6.50
Fill Factor		0.63
Efficiency	(%)	6.50
R_s	Ω	19.3
R_{sh}	Ω	305

Table 4.13: Measured characteristics of P-I-N device

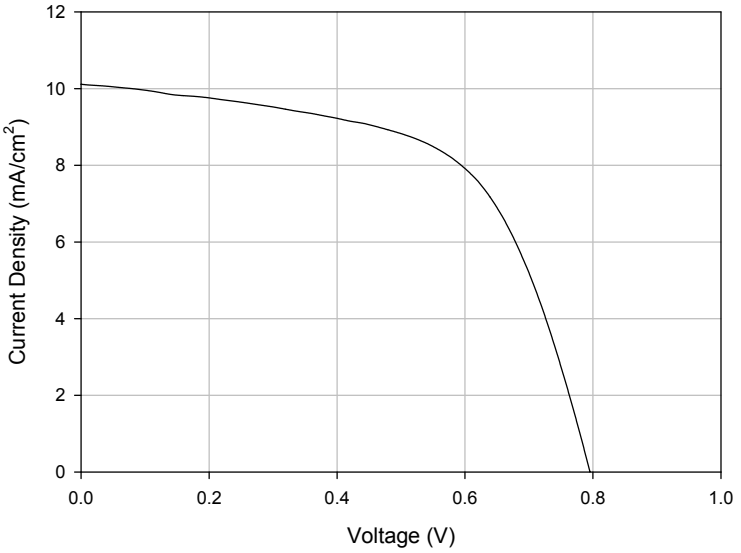

Figure 4.21: I-V curve of highest performance device

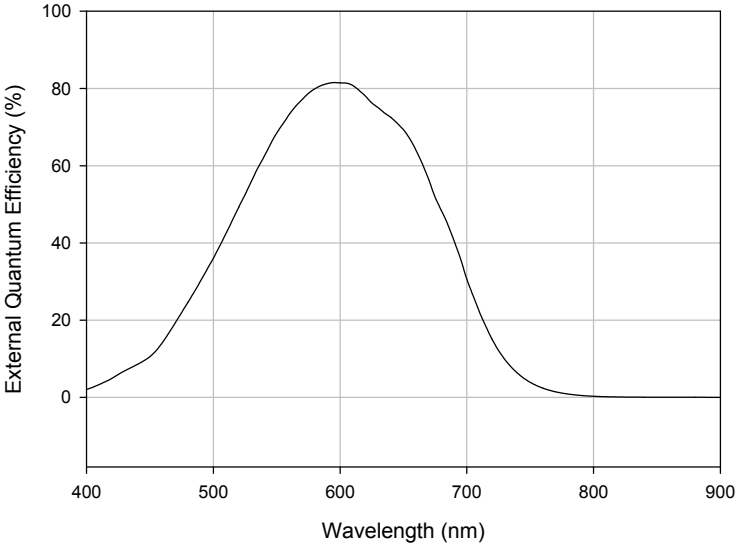

Figure 4.22: Quantum efficiency of highest performance device

4.3.3.8 Optical Effects of Substrate Material

In order to observe the effects of the TCO coated substrates detailed in section 2.4.2 on the P-I-N device performance, a series of devices are fabricated to identical specification and I-V measurements performed. Pilkington TEC-8 and TEC-15 substrates are investigated, with deposition conditions are as detailed section 4.3.3.6. It is significant to highlight that device thickness optimisation was performed on TEC-8 TCO substrates, and therefore optimum device thicknesses particularly for the p-type region may not be optimised for TEC-15 substrates. The process optimisation of deposition conditions, however, was performed on uncoated glass slides and therefore a disadvantage should not be observed with using TEC-15 material. Measurement results and the I-V characteristic are presented in table 4.14 and figure 4.23 respectively.

Variable		**TEC-8**	**TEC-15**
Efficiency	(%)	6.01	5.53
Fill Factor		0.65	0.56
Max Power	(mW)	5.9	4.5
V_{oc}	(V)	0.74	0.78
I_{sc}	(mA/cm^2)	12.53	10.31
V_m	(V)	0.55	0.55
I_m	(mA)	10.73	8.09

Table 4.14: P-I-N device with TEC-8 and TEC-15 substrates

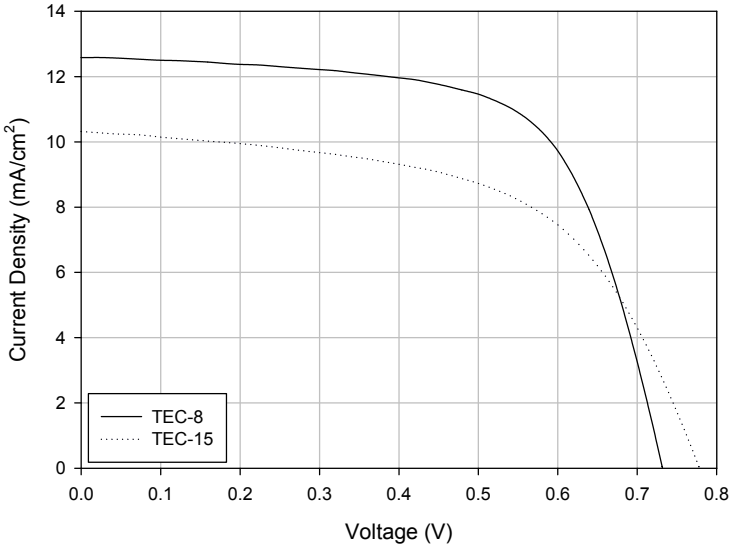

Figure 4.23: Comparison of TEC-8 and TEC-15 TCO materials

It can be observed that the results from the TEC-8 TCO substrates show an approximately 0.5% increase in energy conversion efficiency, compared to the devices deposited on TEC-15 substrates. It is thought that the optical *haze* introduced by the TEC-8 materials increase light absorption and contribute to the enhanced performance of these devices, which can be characterised by the 21% increase in short circuit current density. Open-circuit voltage is reduced by 5% on TEC-8 substrates, which is likely due to the increased surface roughness of the material causing an uneven deposition of the very thin p-type region at the surface of the device.

This open-circuit voltage result somewhat counteracts the effects of the increased sheet resistance of the TEC-15 material which would typically serve to reduce the voltage value. This suggests that the effects of the surface roughness on the p-type region exceed the influence of the sheet resistance. A device layer thickness process optimisation on TEC-15 may provide a slightly improved P-I-N device performance. It is possible that a thinner p-type region would be more effective using TEC-15 TCO as the surface roughness is significantly reduced.

4.4 Conclusion

In this chapter, a full optimisation process was performed in order to fabricate amorphous silicon photovoltaic devices. The optimum deposition conditions using plasma-enhanced CVD are identified, to achieve fabrication of silicon thin films with maximum photo-activity and a minimal value of performance variation between subsequent depositions. Thin-film crystallinity and uniformity are assessed using Raman spectroscopy and ellipsometry respectively. The doping efficiency is explored, resulting in silicon thin films with consistent doping throughout a wide variety of thickness values, verified using SIMS measurements. A full P-I-N device is fabricated, with optimised layer thicknesses designed to attain maximum energy conversion efficiency and fill factor, with a device performance of 6.5% achieved. The use of Argon as a dilute gas is additionally explored, with a number of dilution rations investigated. Finally the effects of deposition of different substrate materials is investigated, with the optical enhancement of the device performance noted on substrate materials with a haze introduced. Further optimisation may be possible using design-of-experiments methods to calculate the relationships between inter-dependant deposition conditions, using the Minitab statistical analysis software package. This technique was not used in this investigation due to the requirement to investigate broad parameter spaces to assist with machine verification.

In order to enhance the optical performance of the photovoltaic devices without the potential negative effects introduced by roughness on the substrate surface, a series of optical nano-particle arrays will be investigated using numerical simulation, on silicon thin-film absorber layers in chapter 5. A selection of self-organised metal-island film based particle arrays are fabricated in chapter 6 to observe the effects of such treatments on amorphous silicon thin film based devices.

Chapter 5

Simulation of Nano-particle Arrays

In order to determine the optimum dimensions for the nano particle array topography, optical simulation is performed using the Lumerical FDTD Solutions package [133] as described in section 3.4.3. A series of Ag nano-particle arrays are simulated within a structure featuring an amorphous silicon absorber layer, and their dimensions are varied across a wide range of variables as identified from literature described in section 2.4.3.

Within this investigation, initially the base-line model specification is described in detail, including the model geometry and arrangement of sources and monitors in 3D space. A convergence test is performed to ascertain the appropriate trade-off between mesh accuracy and computational resources. Thickness variations of the ITO region are then performed, and reflectance measurements taken.

Data is presented in *Total Integrated Reflectance*, which is the result from all wavelength points integrated across this range and provides an accurate figure of merit for comparison of results and rejection of outliers. Reflectance simulations are then undertaken, on particle arrays featuring Ag spheres or circular discs positioned within the front or rear TCO material. Ag is selected as the most suitable nano-particle material based on literature described in section 2.4.3. The radius of the particle, the position within the ITO region (and proximity to semiconductor or reflector) the height of the disc shapes and the constituent material of the back reflector in each case is varied over several steps to visualise the configuration exhibiting the lowest value of optical reflection from the region. A simulation of optical power absorption within the amorphous silicon region is then performed based on the optimum parameters from the reflectance measurements, in order to investigate the amount of light contributing to charge carrier generation as opposed to parasitic absorption within the region.

5.1 Model Specification

The initial simulation model is constructed with no active particle arrays in order to verify the simulation technique and provide a base-line measurement to compare device performance. Materials are selected from the built-in material database within FDTD Solutions, or added from sampled data sources, which accurately describe the dispersive properties of the constituent materials within a model such as refractive index and absorption characteristics. The model is constructed to follow the structure of devices fabricated in chapter 6 and consists of the following optical topography:

- Glass Substrate, SiO_2 Palik model - PML, 625nm within the FDTD boundaries.
- Front Indium Tin Oxide, FDTD model - 200nm thickness.
- Amorphous Silicon, sampled data model from [79] - 400nm thickness.
- Rear Indium Tin Oxide, FDTD model - 200nm thickness.
- Metallic Back Reflector, Al / Ag Palik model - 300nm thickness

Layer thicknesses are selected to minimise computational resources required such as encompassing only 625nm of glass material, whilst using a thickness range which allows for ease of measurement and analysis within the results such as the use of 400nm a-Si. The simulation boundaries are specified as 400nm in the x- and y-directions, configured as symmetric and anti-symmetric boundary conditions respectively, in order to create an infinitely repeating unit cell structure. This configuration takes advantage of the plane of symmetry through the middle of the simulation region, reducing simulation resource requirements by approximately four times. This is indicated by a blue or green overlay covering half of the simulation mesh region. The z-direction is configured as a *Perfectly Matched Layer* (PML) which continues the medium in contact with the boundary infinitely. The substrate material is configured in such a way at the upper boundary, whilst a space is intentionally left at the lower boundary. The plane-wave light source is located within the glass substrate layer directed towards the device encompassing all of the x- and y-region. For all simulations in this study, the plane source is configured to simulate wavelengths in the range 300-1100nm, with 160 frequency points.

The reflectance monitor is a 2-dimensional Z-normal frequency-domain powers monitor positioned 150nm above the light source, while an identically configured transmittance monitor resides 150nm behind the reflector. In this investigation, the transmittance monitor is used to verify that no light escapes the reflector region and the region thickness is appropriate. A two-dimensional frequency domain power monitor is positioned centrally throughout all absorber layers to measure plane wave propagation, and a three-dimensional frequency domain power monitor is positioned around the amorphous silicon absorber layer to measure electrical generation rate and total absorbed power.

The figure 5.1 details the glass substrate material in grey, with the plane wave excitation source within depicted by the purple arrow. This is followed by the ITO region in green. The amorphous silicon absorber layer is shown in red, followed by the second green ITO and finally the blue back reflector. The three-dimensional FDTD simulation mesh region is shown as the inside of the orange rectangle, while the transmittance and reflectance monitors are illustrated by the yellow bars behind reflector region and above the plane source respectively. The arrangement can be viewed from a three-dimensional perspective as in figure 5.2.

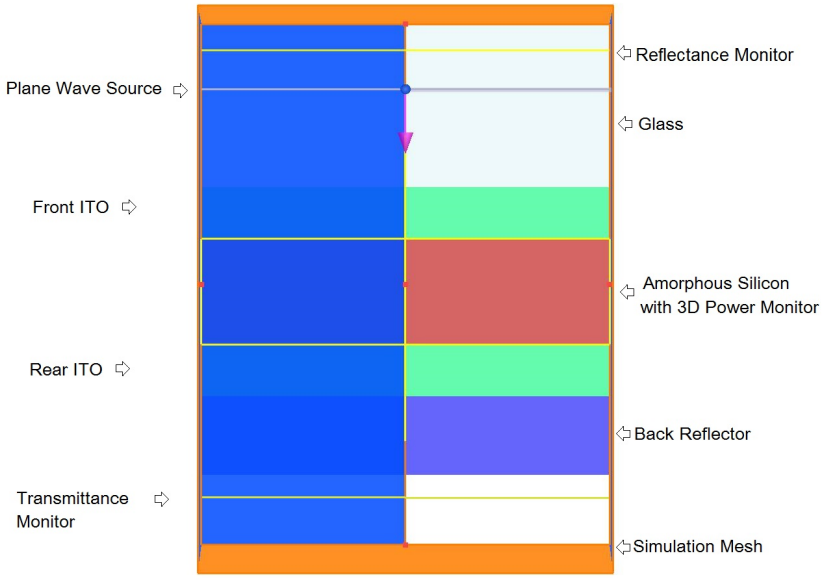

Figure 5.1: Silicon sample under illumination

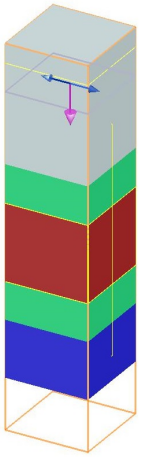

Figure 5.2: Silicon sample in perspective view

5.2 Convergence Testing

Numerical simulations of this type exhibit a trade-off between numerical error and simulation time and memory consumption. Error cannot be practically eliminated but can be reduced to an acceptable level in which its contribution to the final result can be neglected. FDTD Solutions mesh settings feature a *Mesh Accuracy* setting which within the auto non-uniform meshing algorithm sets the measurement points per wave period. This can be positioned between 1 and 8, which correspond to a λ/dx values between 6 - 34 points per period. A convergence test can be used to determine the appropriate simulation configuration which satisfies the trade-off, with several runs of the same type of simulation conditions at various accuracy settings. The structure detailed in figure 5.1 is simulated for each setting, and reflectance results at an arbitrary wavelength of 708nm are detailed in figures 5.3 and 5.4.

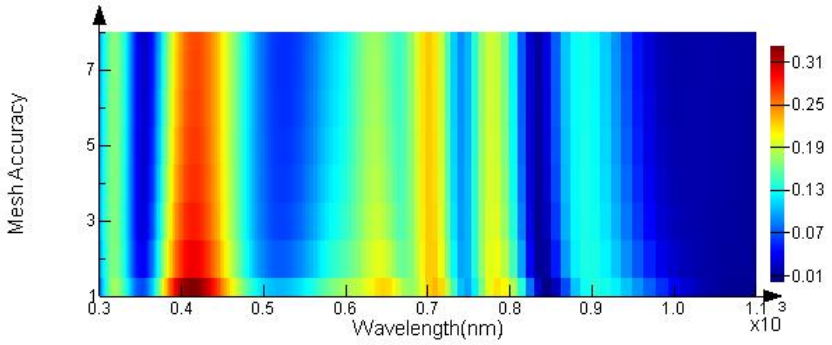

Figure 5.3: Mesh accuracy vs optical reflectance (% - Colour Bar)

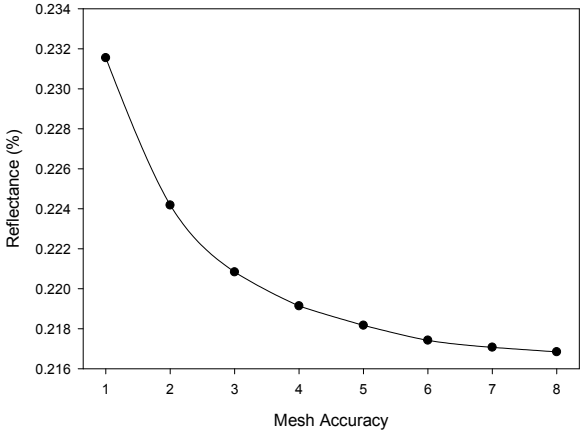

Figure 5.4: Mesh accuracy at 708nm

As can be observed, the optical characteristics can be seen to change dramatically with varying mesh accuracy settings. It can be deemed that values of mesh accuracy in excess of 5 reduce the simulation error to less than 2% of the previous values. This convergence pattern is confirmed by the values obtained by [134], showing that this range of mesh accuracy is sufficient for this investigation.

5.3 Simulation of ITO Thickness

The thickness of the ITO region within the device can significantly alter the optical reflectance and absorption characteristics. As discussed in section 2.4, the ITO region is a source of parasitic absorption which increases with layer width, however it can also be tuned in thickness to cause constructive interference and therefore enhance the optical performance in certain wavelength regions.

5.3.1 Variation of Front ITO Thickness

Within this simulation the thickness of the region of ITO positioned between the glass substrate material and the silicon absorber layer is varied from 50 to 200nm, in steps of 10nm, in order to observe the optical properties. A region of ITO at the rear remains unchanged at 200nm thickness. Results are presented in figures 5.5 and 5.6.

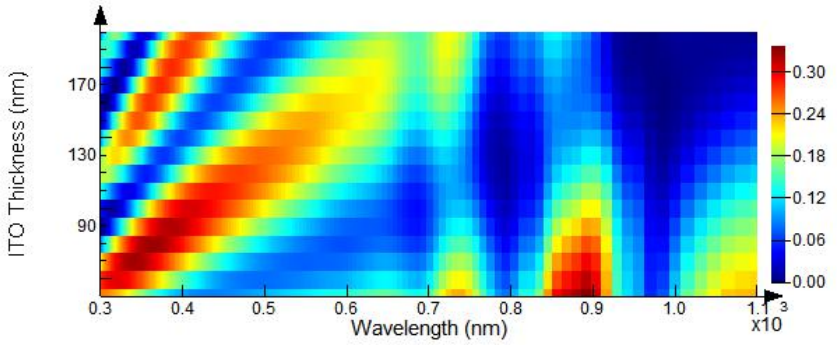

Figure 5.5: ITO thickness vs optical reflectance (% - Colour Bar)

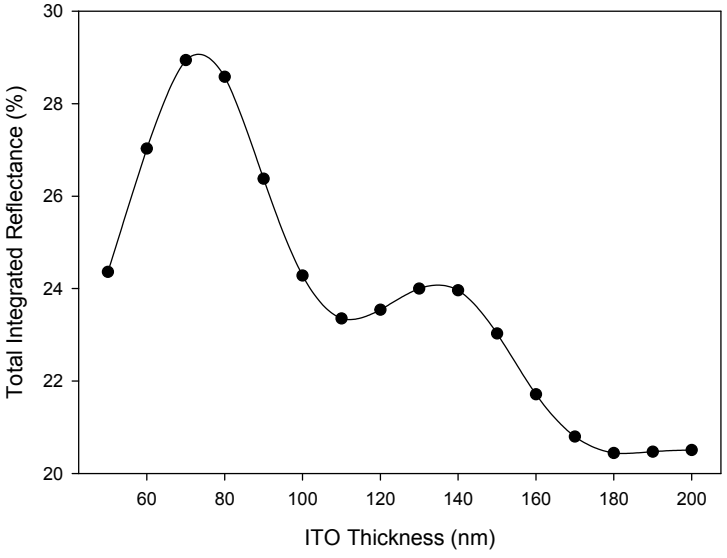

Figure 5.6: Front ITO thickness vs integrated reflectance

5.3.2 Variation of Front without Rear ITO Layer

Within this simulation the thickness of the region of ITO positioned between the glass substrate material and the silicon absorber layer is varied from 50 to 200nm, in steps of 10nm, in order to observe the optical properties. The region of ITO at the rear of the absorber layer is removed in order to simulate the optical effects of this topography. Results are presented in figures 5.7 and 5.8.

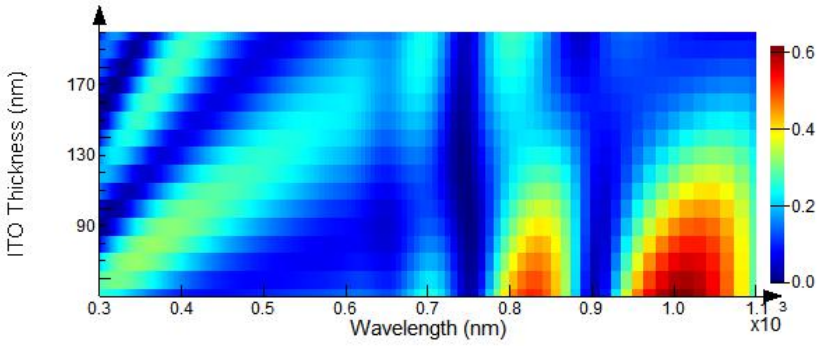

Figure 5.7: ITO thickness vs optical reflectance (% - Colour Bar)

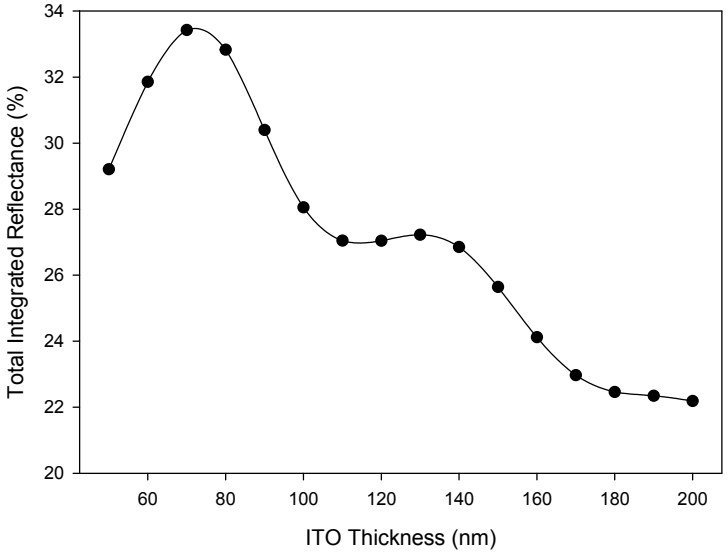

Figure 5.8: Front ITO thickness vs integrated reflectance

5.3.3 Variation of Rear without Front ITO Layer

Within this simulation the thickness of the region of ITO positioned between the silicon absorber layer and the back reflector material is varied from 50 to 200nm, in steps of 10nm, in order to observe the optical properties. The region of ITO at the front of the absorber layer is removed in order to simulate the optical effects of this topography and to observe correlation with the practical investigations in section 6.3.4. Results are presented in figures 5.9 and 5.10.

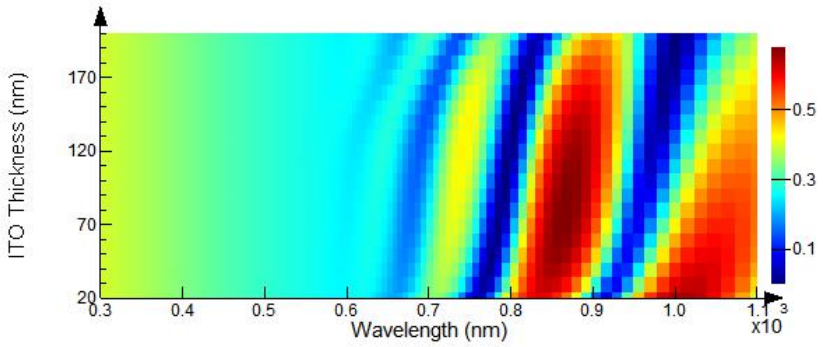

Figure 5.9: ITO thickness vs optical reflectance (% - Colour Bar)

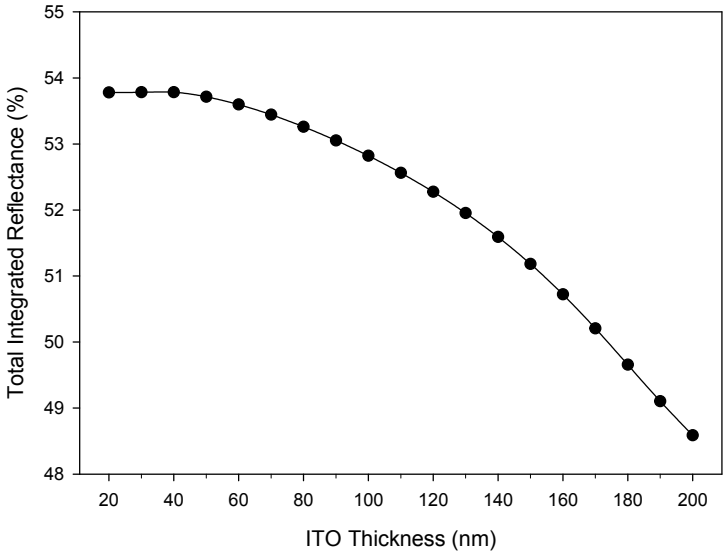

Figure 5.10: Rear ITO thickness vs integrated reflectance

5.3.4 Analysis

The results from this investigation are presented in table 5.1. As can be observed from investigation 5.3.1, which features both front and rear ITO regions and varies the front thickness, the lowest optical reflectance of 20.4% occurs at front ITO thicknesses between 180 - 200nm. The reduction in reflectance is expected to scale with increasing layer thickness as more parasitic absorption occurs and serves to reduce the volume of light transmitted within the layer. A localised minimum of 23.3% occurs at 110nm thickness, which is of primary importance as this suggests that layer thicknesses in multiples of these values contribute to the lowest optical reflectance. It can additionally be seen from the red-coloured regions shown on the surface plot in figure 5.5 that thinner ITO regions produce higher levels of reflectance at shorter wavelengths which shift to longer wavelengths with increasing layer thickness. A significant peak in reflectance also occurs at 850 - 900nm for layer thicknesses below 100nm which is reduced to nominal levels above these dimensions.

Investigation 5.3.2 shows a similar investigation to 5.3.1 with the rear ITO region removed from the structure. Whilst an abrupt change of refractive index occurs at the rear interface between semiconductor and metal, the purpose of this region is optical reflection and so any additional reflectance due to change of optical media will serve to increase performance. The reflectance characteristic is similar to the previous investigations, however the overall reflectance is approximately 2% higher due to the removal of the rear ITO causing a reduction of parasitic absorption within this layer. Finally investigation 5.3.3 illustrates the optical topography of the pseudo-devices fabricated in section 6.3.4, with no front ITO region and a variation of the rear ITO thickness. The resultant reflectance characteristic is almost linear with material thickness with no localised minimum as seen in previous examples.

It can be recognised from these investigations that a 'tuning' of the front ITO thickness is possible, resulting in a localised minimum reflectance value at approximately 110nm which is likely not due to parasitic absorption. Variations of the rear ITO region do not result in this type of pattern and therefore this region should be kept as thin as possible for maximum optical performance and the reduction of parasitic losses. Practically this region must be fabricated to a sufficient thickness to encompass the nano-particle arrays and where none are situated, sufficiently thick to keep resistive losses to a minimum.

ITO Position	**ITO Thickness**	**Optimum**	**Reflectance**
Front	50 - 200nm	**180nm**	20.4%
Front (No Rear)	50 - 200nm	**200nm**	22.2%
Rear (No Front)	50 - 200nm	**200nm**	48.6%

Table 5.1: Summary of ITO thickness variation

5.4 Reflectance Simulation of Ag Nano-particle Arrays

The purpose of optical simulation within this study is to determine the optimal configuration of nano-particle size, shape, position and surrounding medium for light scattering within the amorphous silicon photovoltaic device. This can be achieved by measuring the percentage of optical reflectance from the surface, which is affected by the amount of light absorbed by the photovoltaic device.

The investigation is broadly split into several categories, detailed in figure 5.11. The device structure features an array of metallic particles in the form of spheres or flat discs. These particle arrays are positioned either at the front of the silicon absorber layer or at the rear adjacent to the metallic reflector. The reflector material is varied in each investigation, with both aluminium and silver simulated. Each set of investigations are performed for all topologies, varying particle radius, height, and the distance from the absorber layer and reflector or surface. A close-up view of the parameters to be varied is detailed in figure 5.12.

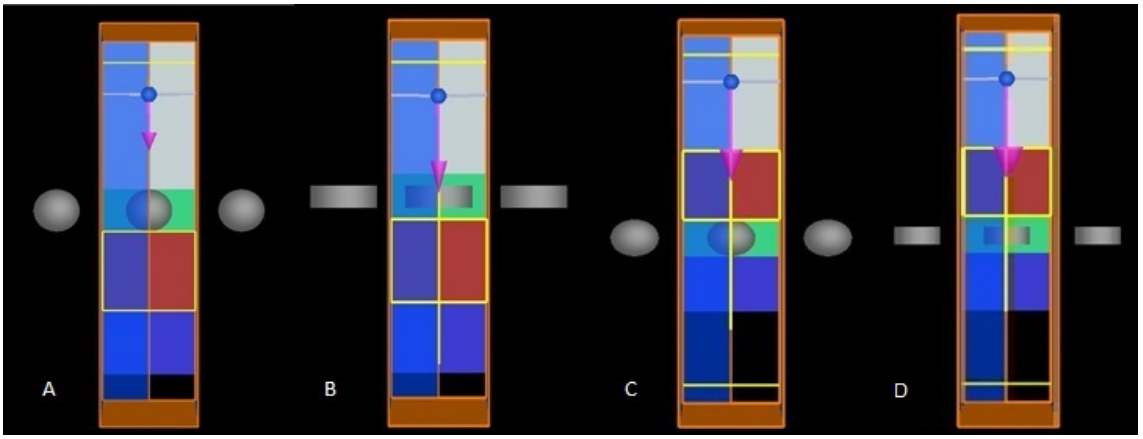

Figure 5.11: Spheres (a) and discs (b) on front and on rear (c) and (d)

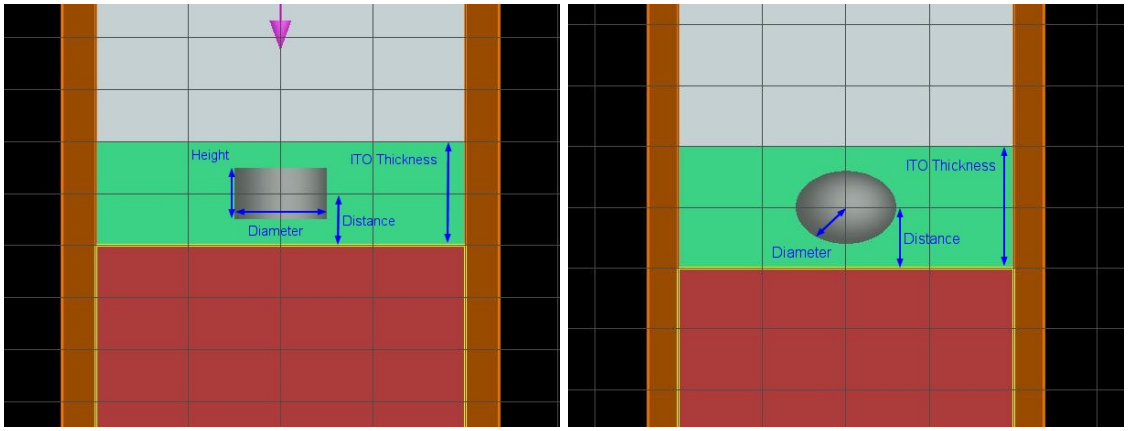

Figure 5.12: Particle variables

5.4.1 Front-Mounted Particles

To determine if an improvement is achieved over an elementary structure without such nano-particle structures, base-line measurements for each reflector type are performed for each device topography, and this is overlaid on the results graph as the dashed lines. In order to provide a *figure of merit* result for comparison of each device topography, this section contains measurements of optical reflectance integrated across the wavelength range. Each ITO region is simulated only when a particle array is within it and therefore no rear ITO is included in the simulation model of particle arrays within the front ITO.

Within this investigation, a parameter sweep is performed for the fabrication variable under test. The dimensions which will be varied are depicted in bold type in table 5.2, and the corresponding parameters optimised in the design layout view are shown in figure 5.12. The particles are embedded within an ITO region positioned between the glass and silicon. This ITO region thickness is varied to accommodate the particle arrays and ranges from 100 to 300nm.

Particle	**ITO Thickness**	**Radius**	**Distance**	**Height**	**Reflector**
Discs	100nm	**20 - 140nm**	50nm	50nm	Al
Discs	100nm	100nm	**25 - 75nm**	50nm	Al
Discs	200nm	**20 - 140nm**	100nm	100nm	Al
Discs	200nm	100nm	**50 - 150nm**	100nm	Al
Discs	200nm	100nm	100nm	**50 - 200nm**	Al
Spheres	100nm	**5 - 50nm**	50nm	-	Al
Spheres	200nm	**20 - 100nm**	100nm	-	Al
Spheres	200nm	50nm	**50 - 150nm**	-	Al
Spheres	300nm	**20 - 140nm**	150nm	-	Al
Spheres	300nm	100nm	**100 - 200nm**	-	Al
Discs	100nm	**20 - 140nm**	50nm	50nm	Ag
Discs	100nm	100nm	**25 - 75nm**	50nm	Ag
Discs	200nm	**20 - 140nm**	100nm	100nm	Ag
Discs	200nm	100nm	**50 - 150nm**	100nm	Ag
Discs	200nm	100nm	100nm	**50 - 200nm**	Ag
Spheres	100nm	**5 - 50nm**	50nm	-	Ag
Spheres	200nm	**20 -100nm**	100nm	-	Ag
Spheres	200nm	50nm	**50 - 150nm**	-	Ag
Spheres	300nm	**20 - 140nm**	150nm	-	Ag
Spheres	300nm	100nm	**100 - 200nm**	-	Ag

Table 5.2: Nano-particle array parameters

5.4.1.1 Disc Radius Optimisation in 100nm ITO

The results of the simulations for the disc radius variation in 100nm ITO, between 20 - 140nm is depicted in the surface plots in figures 5.13 (a) and (b). Figure 5.14 depicts the integrated results over the wavelength range 300 - 1100nm for each disc radius. Disc height is fixed at 50nm and position is central in this investigation.

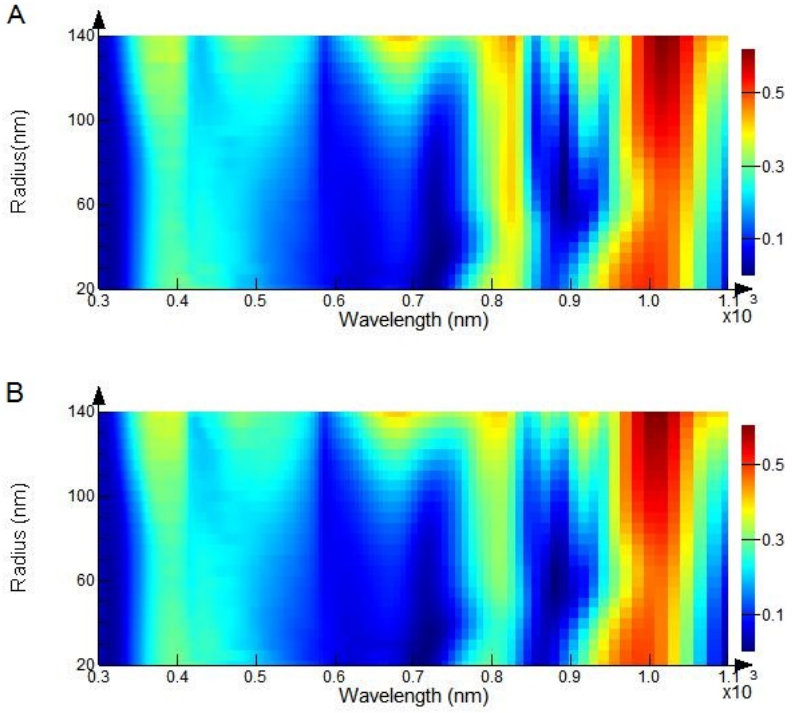

Figure 5.13: Radius vs reflectance (% - colour bar) - Ag(a) and Al(b) reflector

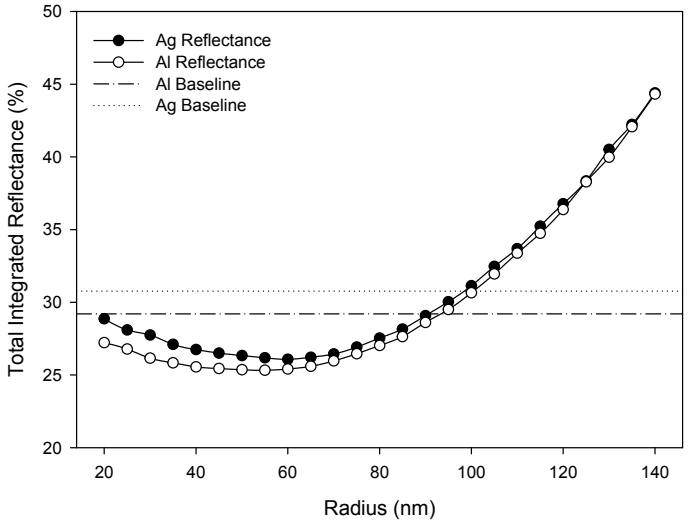

Figure 5.14: 100nm ITO disc radius integrated reflectance

5.4.1.2 Disc Distance Optimisation in 100nm ITO

The results of the simulations for the disc distance variation from the Si surface in 100nm ITO, with centre point between 25 - 75nm is depicted the surface plots in figures 5.15 (a) and (b). Figure 5.16 depicts the integrated results over the wavelength range 300 - 1100nm for each disc position. Disc height is fixed at 50nm and radius 100nm in this investigation. The indicated axis range is shown as 225 - 275nm as the origin position is calculated from 200nm below the Si surface.

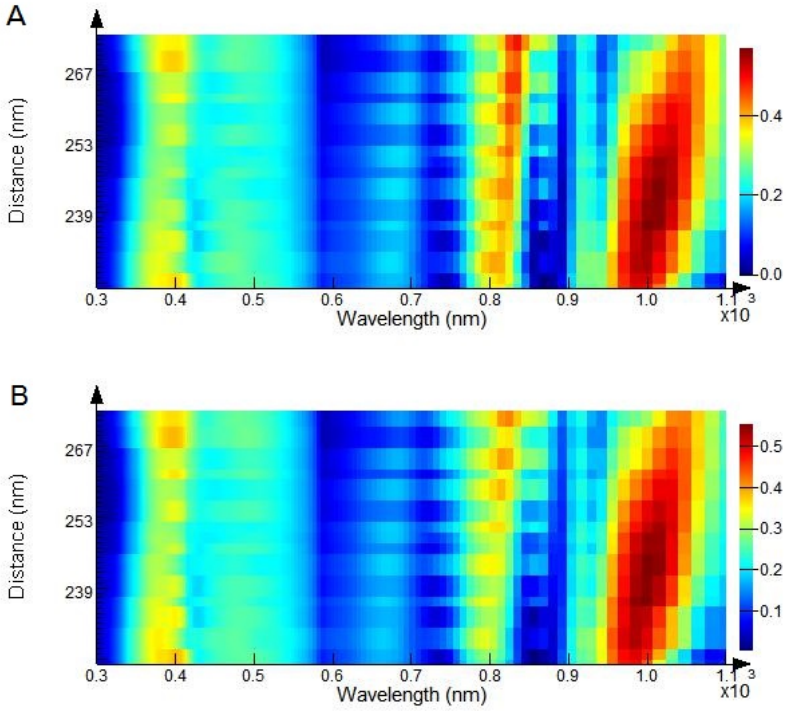

Figure 5.15: Distance vs reflectance (% - colour bar) - Ag(a) and Al(b) reflector

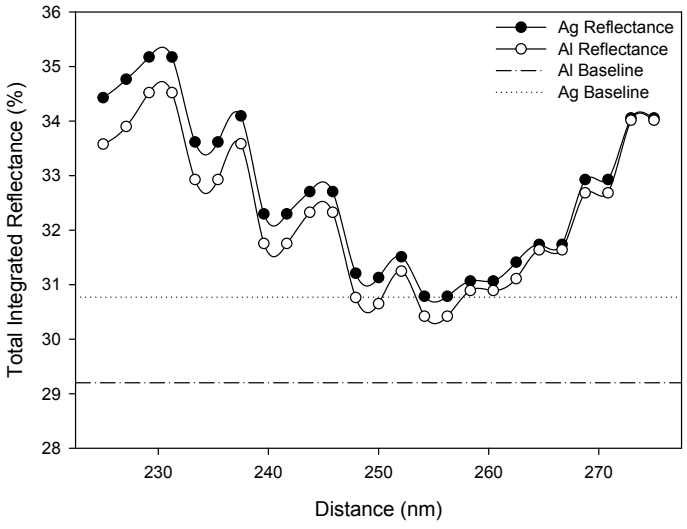

Figure 5.16: 100nm ITO disc distance integrated reflectance

5.4.1.3 Disc Radius Optimisation in 200nm ITO

The results of the simulations for the disc radius variation in 200nm ITO, between 20 - 140nm is depicted in the surface plots in figures 5.17 (a) and (b). Figure 5.18 depicts the integrated results over the wavelength range 300 - 1100nm for each disc radius. Disc height is fixed at 100nm and position is central in this investigation.

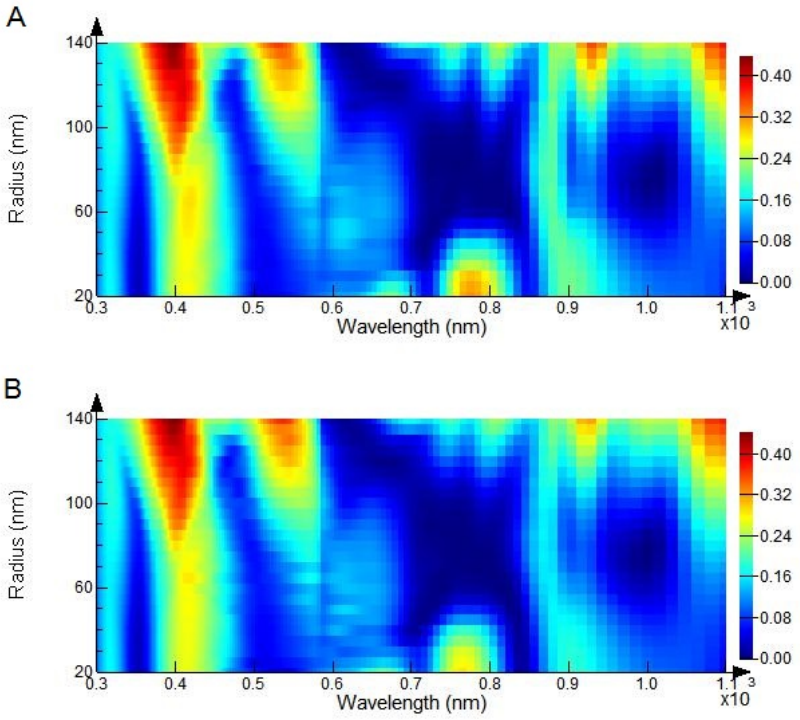

Figure 5.17: Radius vs reflectance (% - colour bar) - Ag(a) and Al(b) reflector

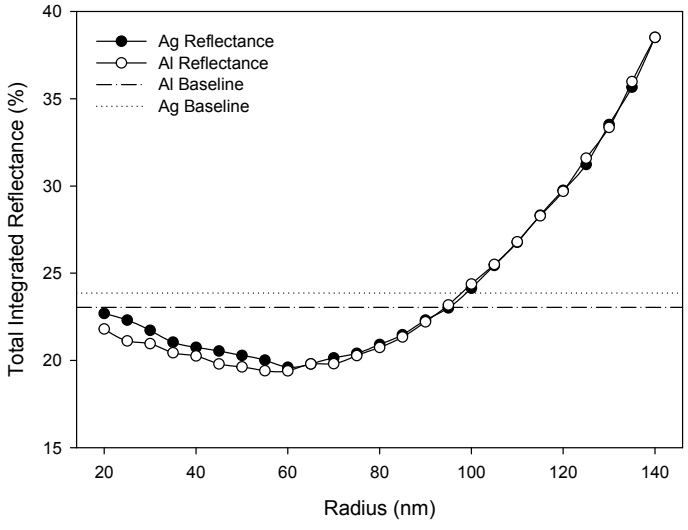

Figure 5.18: 200nm ITO disc radius integrated reflectance

5.4.1.4 Disc Distance Optimisation in 200nm ITO

The results of the simulations for the disc distance variation from the Si surface in 200nm ITO, with centre point between 50 - 150nm is depicted in the surface plots in figures 5.19 (a) and (b). Figure 5.20 depicts the integrated results over the wavelength range 300 - 1100nm for each disc position. Disc height is fixed at 100nm and radius 100nm in this investigation. The indicated axis range is shown as 250 - 350nm as the origin position is calculated from 200nm below the Si surface.

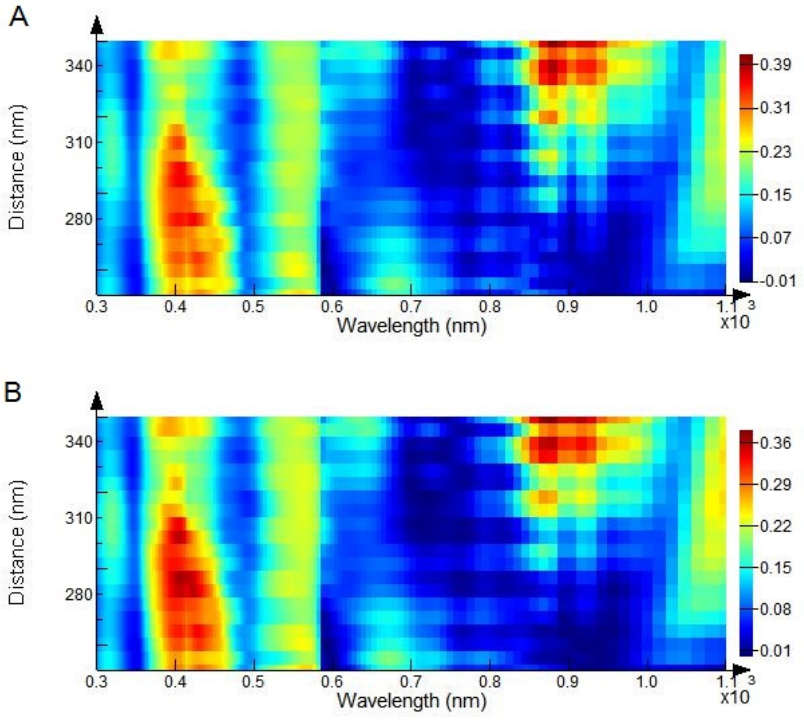

Figure 5.19: Distance vs reflectance (% - colour bar) - Ag(a) and Al(b) reflector

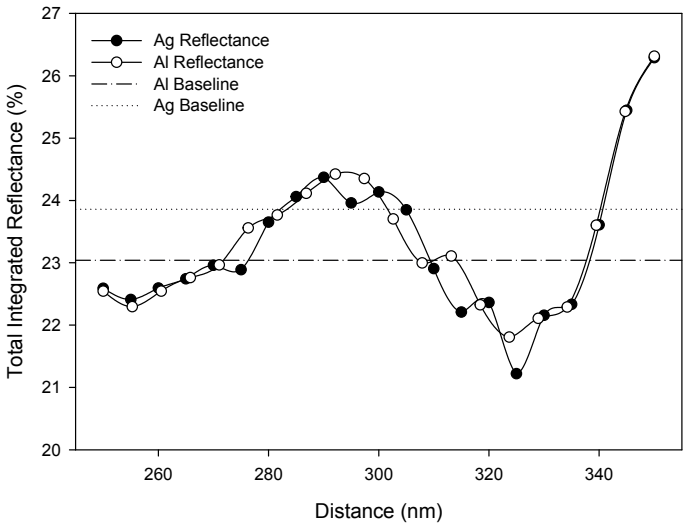

Figure 5.20: 200nm ITO disc distance integrated reflectance

5.4.1.5 Disc Height Optimisation in 200nm ITO

The results of the simulations for the disc height variation in 200nm ITO, between 50 - 200nm is depicted in the surface plots in figures 5.21 (a) and (b). Figure 5.22 depicts the integrated results over the wavelength range 300 - 1100nm for each disc height. Disc radius is fixed at 100nm and position is central in this investigation.

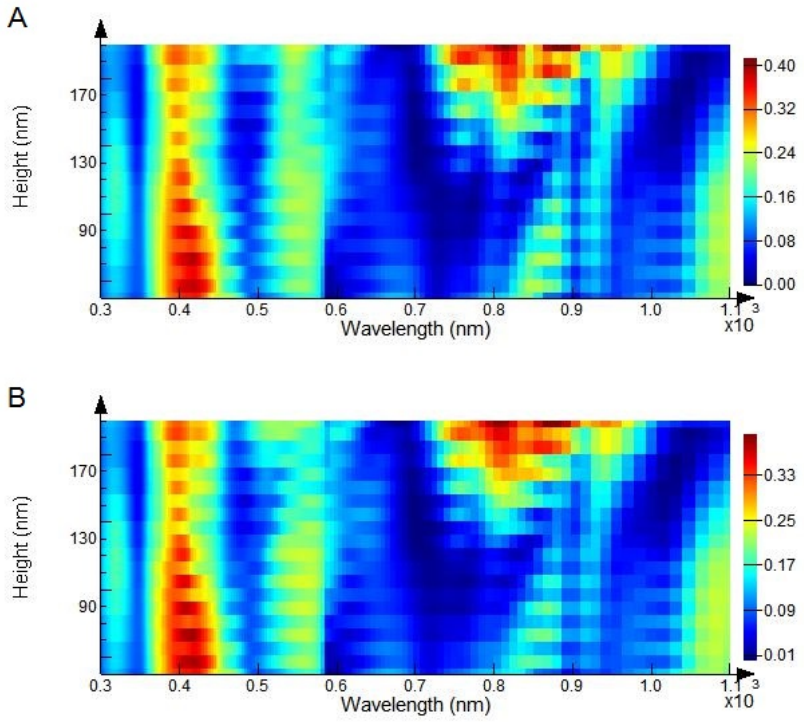

Figure 5.21: Height vs reflectance (% - colour bar) - Ag(a) and Al(b) reflector

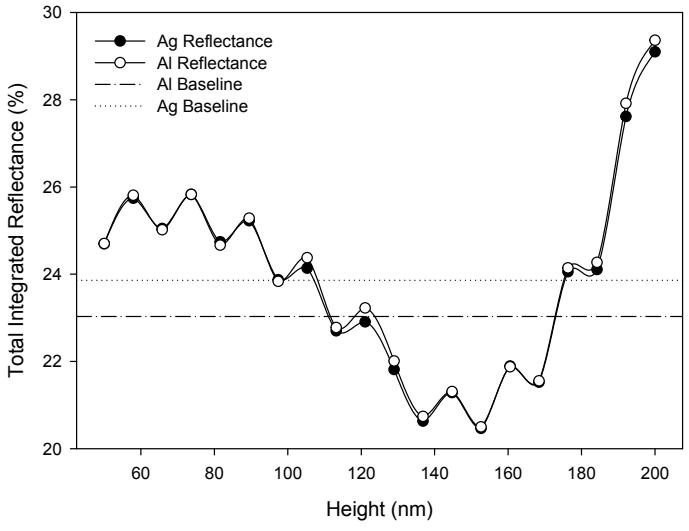

Figure 5.22: 200nm ITO disc height integrated reflectance

5.4.1.6 Sphere Radius Optimisation in 100nm ITO

The results of the simulations for the sphere radius variation in 100nm ITO, between 5 - 50nm is depicted in the surface plots in figures 5.23 (a) and (b). Figure 5.24 depicts the integrated results over the wavelength range 300 - 1100nm for each sphere radius. Sphere position is central in this investigation.

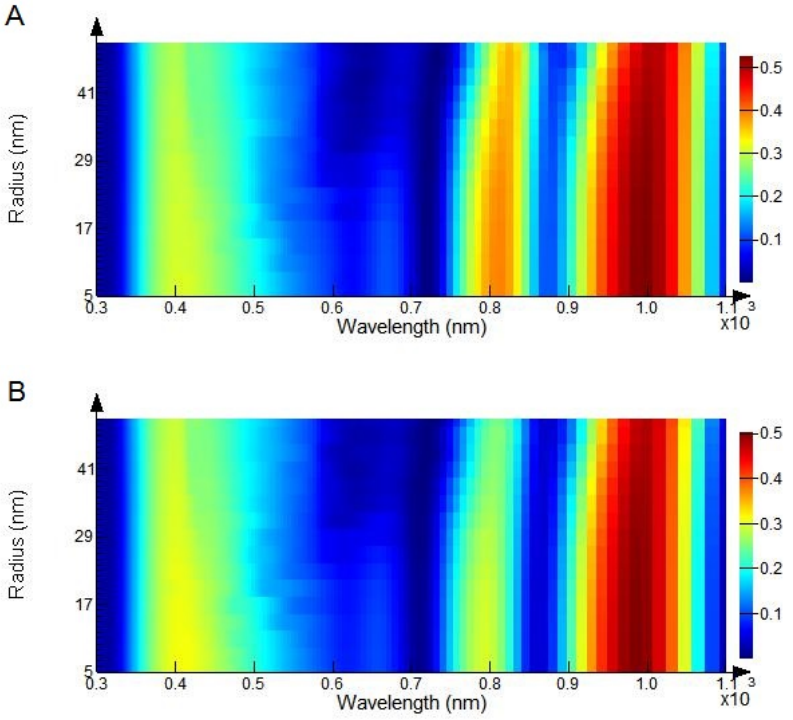

Figure 5.23: Radius vs reflectance (% - colour bar) - Ag(a) and Al(b) reflector

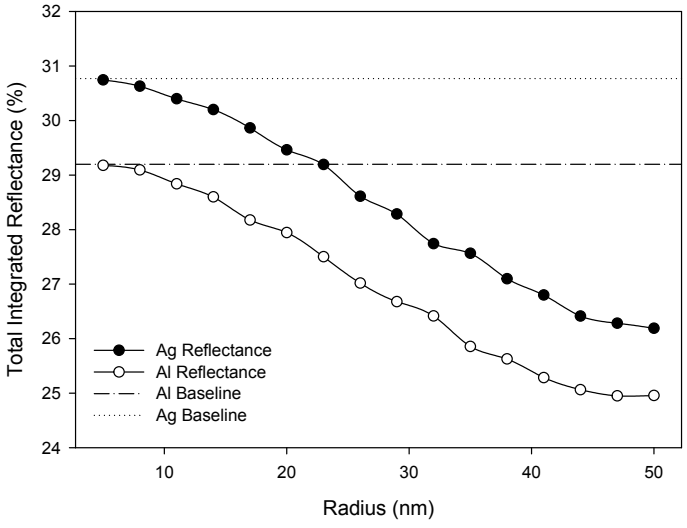

Figure 5.24: 100nm ITO sphere radius integrated reflectance

5.4.1.7 Sphere Radius Optimisation in 200nm ITO

The results of the simulations for the sphere radius variation in 200nm ITO, between 20 - 100nm is depicted in the surface plots in figures 5.25 (a) and (b). Figure 5.26 depicts the integrated results over the wavelength range 300 - 1100nm for each sphere radius. Sphere position is central in this investigation.

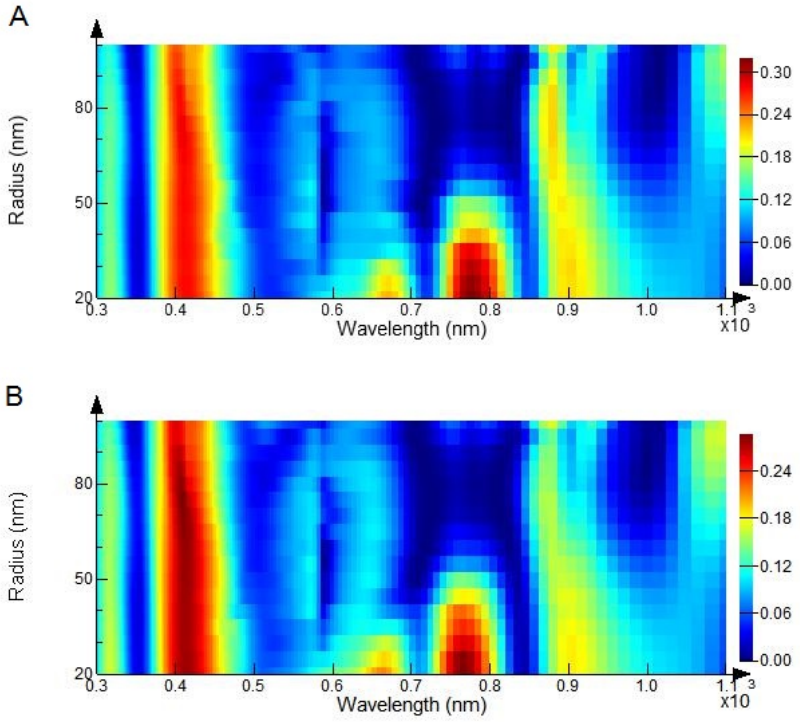

Figure 5.25: Radius vs reflectance (% - colour bar) - Ag(a) and Al(b) reflector

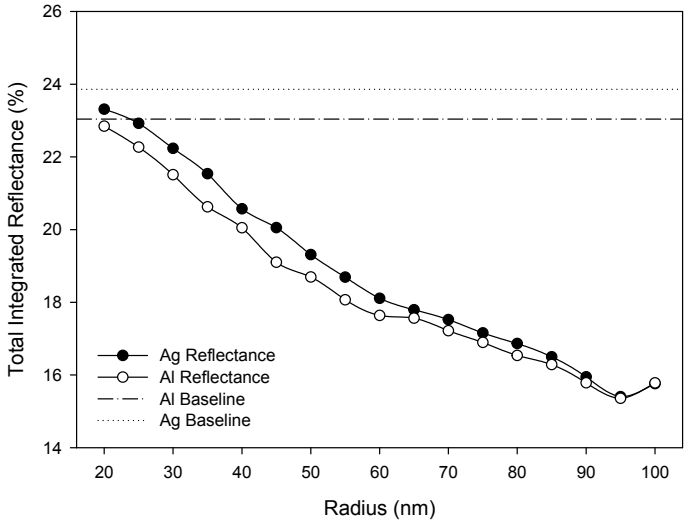

Figure 5.26: 200nm ITO sphere radius integrated reflectance

5.4.1.8 Sphere Distance Optimisation in 200nm ITO

The results of the simulations for the sphere distance variation from the silicon surface in 200nm ITO, with centre point between 50 - 150nm is depicted in the surface plots in figures 5.27 (a) and (b). Figure 5.28 depicts the integrated results over the wavelength range 300 - 1100nm for each sphere position. Sphere radius is fixed at 500nm in this investigation. The indicated axis range is shown as 150 - 250nm as the origin position is calculated from the centre of the sphere and 100nm below the Si surface.

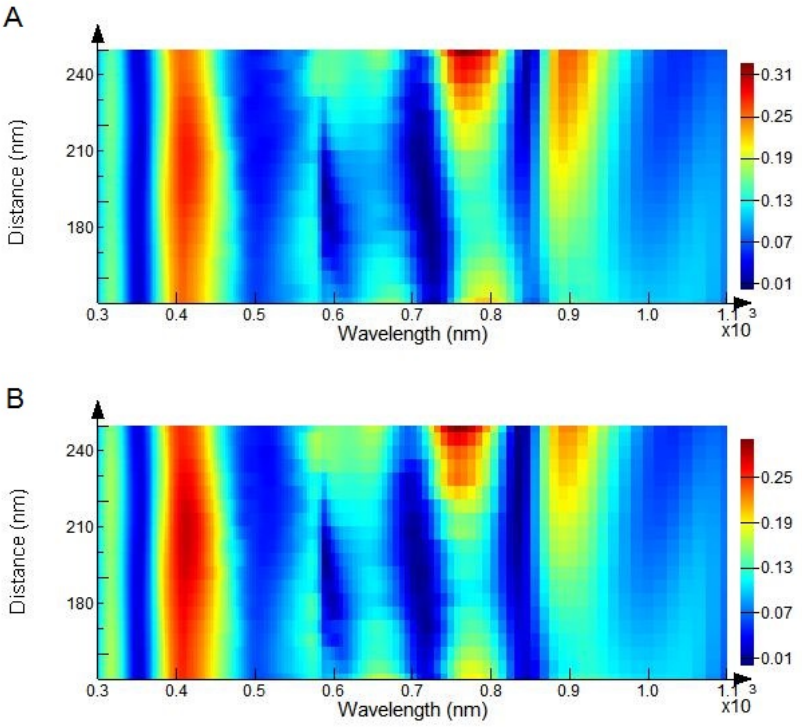

Figure 5.27: Distance vs reflectance (% - colour bar) - Ag(a) and Al(b) reflector

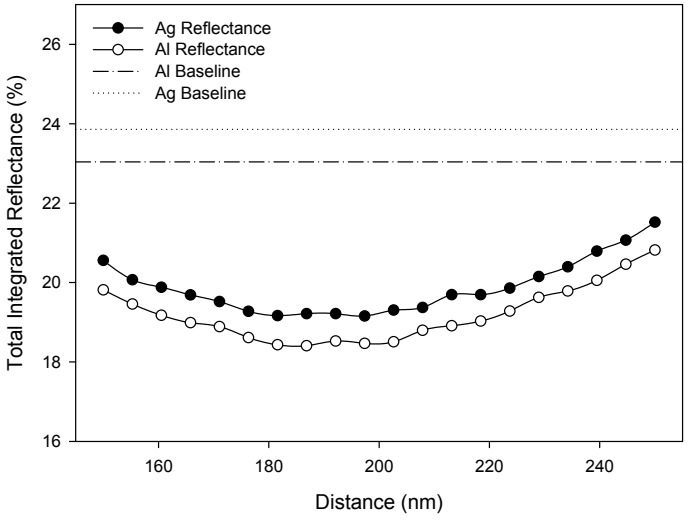

Figure 5.28: 200nm ITO sphere distance integrated reflectance

5.4.1.9 Sphere Radius Optimisation in 300nm ITO

The results of the simulations for the disc radius variation in 300nm ITO, between 20 - 140nm is depicted in the surface plots in figures 5.29 (a) and (b). Figure 5.30 depicts the integrated results over the wavelength range 300 - 1100nm for each sphere radius. Sphere position is central in this investigation.

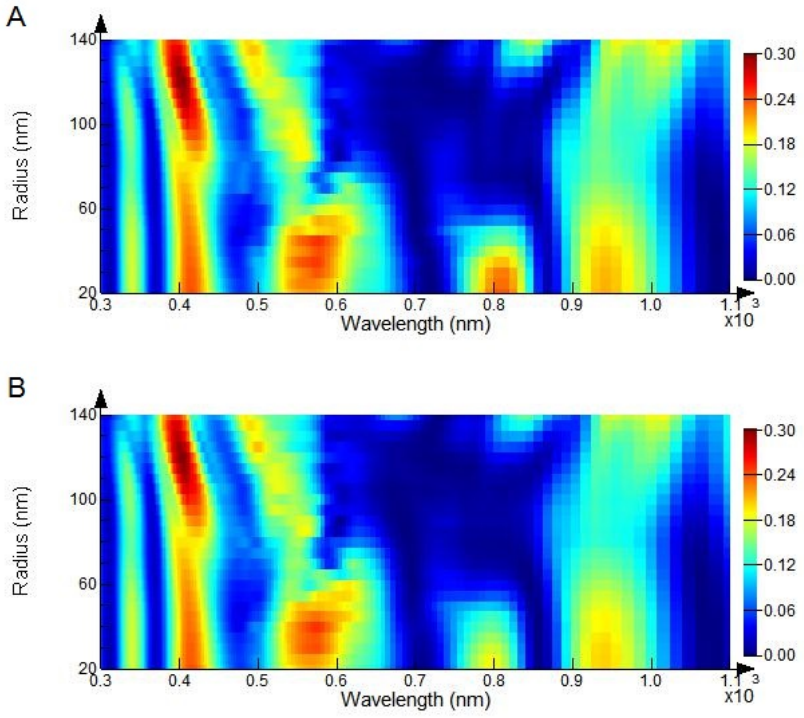

Figure 5.29: Radius vs reflectance (% - colour bar) - Ag(a) and Al(b) reflector

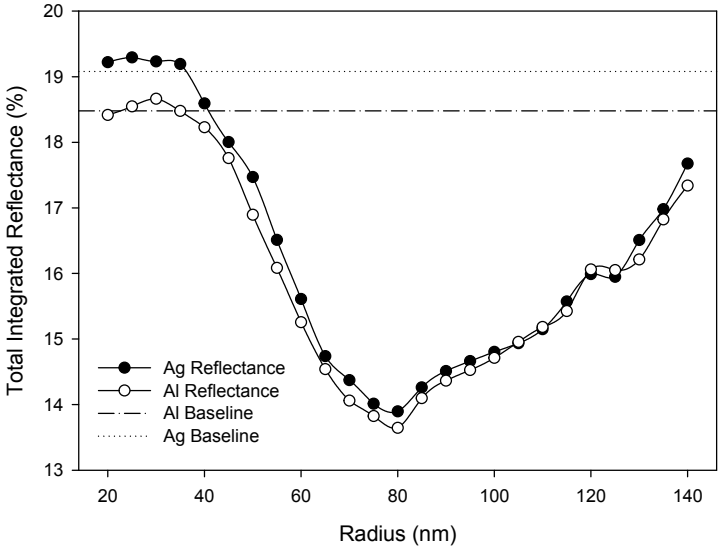

Figure 5.30: 300nm ITO sphere radius integrated reflectance

5.4.1.10 Sphere Distance Optimisation in 300nm ITO

The results of the simulations for the sphere distance variation from the silicon surface in 300nm ITO, with centre point between 100 - 200nm is depicted in the surface plots in figures 5.31 (a) and (b). Figure 5.32 depicts the integrated results over the wavelength range 300 - 1100nm for each sphere position. Sphere radius is fixed at 100nm in this investigation. The indicated axis range is shown as 100 - 200nm as the origin position is calculated from the centre of the sphere.

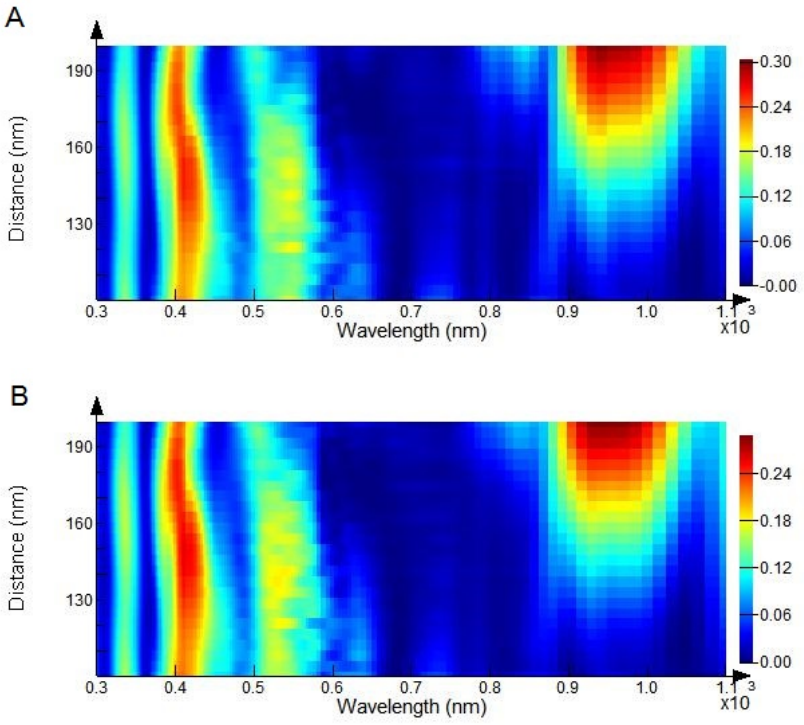

Figure 5.31: Distance vs reflectance (% - colour bar) - Ag(a) and Al(b) reflector

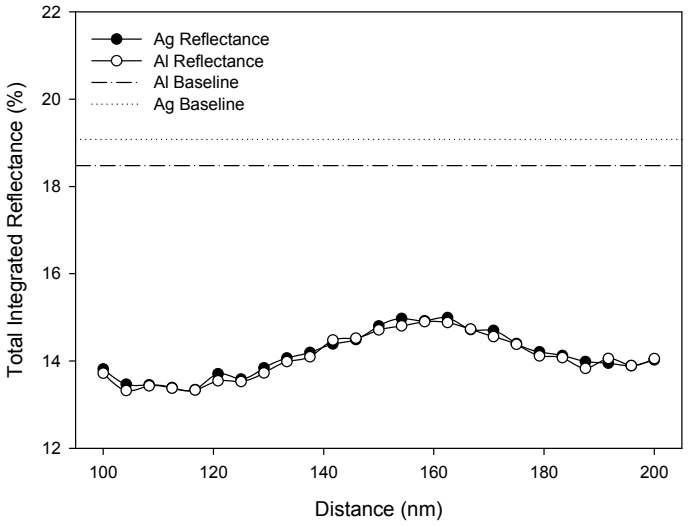

Figure 5.32: 300nm ITO sphere distance integrated reflectance

5.4.1.11 Summary of Results

The simulated values of reflection are summarised in table 5.3.

Particle	ITO Thickness	Variable	Value	Reflectance	Reflector
Discs	100nm	Radius	**55nm**	25.32%	Al
Discs	100nm	Distance	**54nm**	30.42%	Al
Discs	200nm	Radius	**60nm**	19.40%	Al
Discs	200nm	Distance	**125nm**	21.22%	Ag
Discs	200nm	Height	**153nm**	20.50%	Al
Spheres	100nm	Radius	**47nm**	24.95%	Al
Spheres	200nm	Radius	**95nm**	15.36%	Al
Spheres	200nm	Distance	**87nm**	18.41%	Al
Spheres	300nm	Radius	**80nm**	13.65%	Al
Spheres	300nm	Distance	**104nm**	13.32%	Al

Table 5.3: Summary of front particle results

From investigation 5.4.1.9, it can be seen that the lowest value of integrated reflectance for particle arrays at the front of the absorber layer was achieved using spherical particles of radius 80nm within 300nm ITO and an aluminium reflector. The value of integrated reflectance appears to exhibit a sharp trough at this radius, with values either side increasing reflectance accordingly while for all values provide an integrated reflectance lower than the baseline. Peaks in integrated reflectance appear between 520 - 600nm and to a lesser extent 800 - 830nm which are reduced for particle sizes larger than 120nm. Reflectance is reduced marginally for all values with an aluminium reflector compared to those with a silver reflector. Investigation 5.4.1.10 shows that the positioning of the particle close to but not in contact with the absorber surface results in a marginally reduced integrated reflectance value.

Investigation 5.4.1.7 shows a range of particle sizes within 200nm ITO. The lowest integrated reflectance is achieved with a particle radius of 95nm, with a linear reduction in reflectance with increasing particle size. It can be observed that maximum particle size, in which the particle is in contact with the absorber layer, increases the integrated reflectance value in opposition to the trend. Peaks in reflectance appear between 750 - 800nm and to a lesser extent 650 - 700nm which are reduced for particle sizes larger than 120nm. As before, integrated reflectance is reduced marginally for all values with an aluminium reflector compared to those with a silver reflector. Investigation 5.4.1.8 shows that as before the positioning of the particle close to but not in contact with the absorber surface results in a marginally reduced reflectance value.

Spherical particles in 100nm ITO do not reduce integrated reflectance to the same extent, however a similar trend is observed where reflectance is reduced for increasing values of sphere radius. It is not possible to exceed a sphere radius of 100nm in this investigation as the particle will exceed the dimensions of the ITO region.

Investigation 5.4.1.1 shows the simulation of disc-shaped particles in 100nm ITO, which only reduce integrated reflectance for values of radius below 90nm and to a lesser extent than spheres in the same material. The maximum reduction is experienced at a radius of 90nm, with an aluminium reflector providing marginally the greatest reduction. Investigation 5.4.1.2 shows that the positioning of the particle mid-way between the surface and absorber layer provides the maximum reduction, but with unusual 'step' like patterns for every odd value.

The 200nm ITO thickness in investigation 5.4.1.3 shows a similar trend with the maximum reduction occurring at 90nm radius and an increase in integrated reflectance for particles with radius exceeding 200nm. The positioning investigation 5.4.1.4 does not follow the previous trend, with only particles positioned within 40nm of the semiconductor or 30nm of the surface providing a reduction. Finally investigation 5.4.1.5 shows that the optimum disc height is between 140 - 160nm but with the same unusual 'step' patterns as shown previously.

General trends show that spherical particles provide lower values of integrated reflectance as expected from the theory in section 2.4.3 due to a lack of sharp features. Particle sizes of between 80 - 95nm radius appear to reduce reflectance to the greatest extent, with the particle positioned near to the semiconductor and within 200nm ITO material. Particles in direct contact with the semiconductor serve to reduce the anti-reflection effect, as does the use of a silver reflector material as opposed to aluminium. The 'step' like results measured in the disc-shape investigations may be due to interference from the disc surface behaving as a planar reflector to incident light at certain wavelengths. From table 5.3 it can be seen that values of integrated reflectance are reduced for increased ITO thicknesses, it is likely that optical losses due to parasitic absorption in the ITO layer contribute to the reducing values and are not contributing to charge carrier generation within the Si absorber layer.

5.4.2 Rear-Mounted Particles

Similar to the previous investigation in section 5.4.1, optical simulations have been performed of nano-particle arrays at the rear surface of amorphous silicon absorber layers, adjacent to a rear reflector. Due to the differences in optical device topography, it is not possible to directly compare device performance between devices with front and rear mounted particle arrays, but the optimised characteristics for each can independently be sought.

Within this investigation, a parameter sweep is performed for the fabrication variable under test. The dimensions which will be varied are depicted in table 5.4 in bold type as in the previous investigation. The particles are embedded within an ITO region positioned between the silicon absorber layer and back reflector. This ITO region thickness is varied to accommodate the particle arrays and ranges from 100 to 300nm.

Particle	**ITO Thickness**	**Radius**	**Distance**	**Height**	**Reflector**
Discs	100nm	**20 - 140nm**	50nm	50nm	Al
Discs	200nm	**20 - 140nm**	100nm	100nm	Al
Discs	200nm	100nm	**50 - 150nm**	100nm	Al
Discs	200nm	100nm	100nm	**10 - 150nm**	Al
Spheres	100nm	**5 - 50nm**	50nm	-	Al
Spheres	200nm	**20 - 100nm**	100nm	-	Al
Spheres	200nm	50nm	**50 - 150nm**	-	Al
Spheres	300nm	**20 - 140nm**	150nm	-	Al
Spheres	300nm	100nm	**100 - 200nm**	-	Al
Discs	100nm	**20 - 140nm**	50nm	50nm	Ag
Discs	200nm	**20 - 140nm**	100nm	100nm	Ag
Discs	200nm	100nm	**50 - 150nm**	100nm	Ag
Discs	200nm	100nm	100nm	**10 - 150nm**	Ag
Spheres	100nm	**5 - 50nm**	50nm	-	Ag
Spheres	200nm	**20 - 100nm**	100nm	-	Ag
Spheres	200nm	50nm	**50 - 150nm**	-	Ag
Spheres	300nm	**20 - 140nm**	150nm	-	Ag
Spheres	300nm	100nm	**100 - 200nm**	-	Ag

Table 5.4: Nano-particle array parameters

5.4.2.1 Disc Radius Optimisation in 100nm ITO

The results of the simulations for the disc radius variation in 100nm ITO, between 20 - 140nm is depicted in the surface plots in figures 5.33 (a) and (b). Figure 5.34 depicts the integrated results over the wavelength range 300 - 1100nm for each disc radius. Disc height is fixed at 50nm and position is central in this investigation.

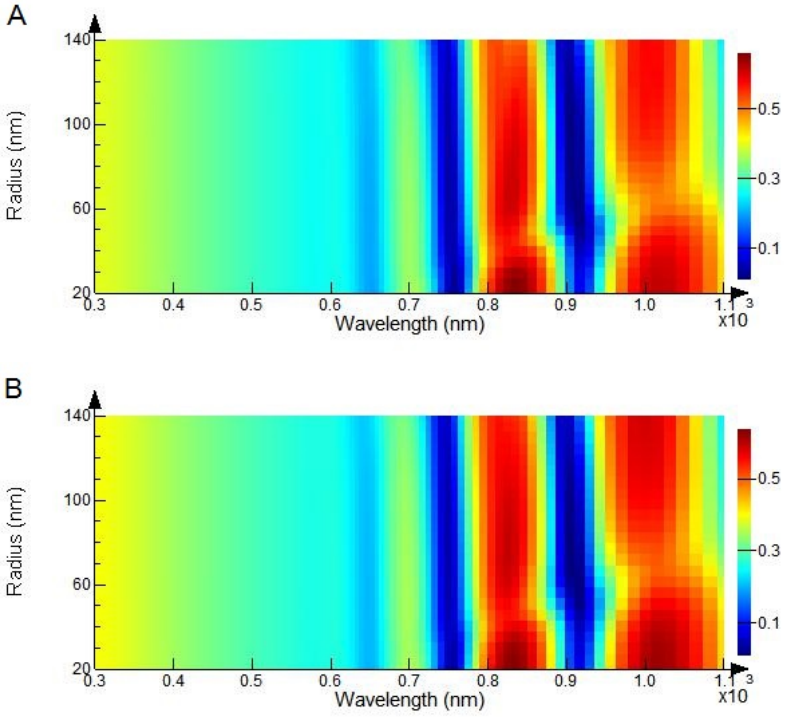

Figure 5.33: Radius vs reflectance (% - colour bar) - Ag(a) and Al(b) reflector

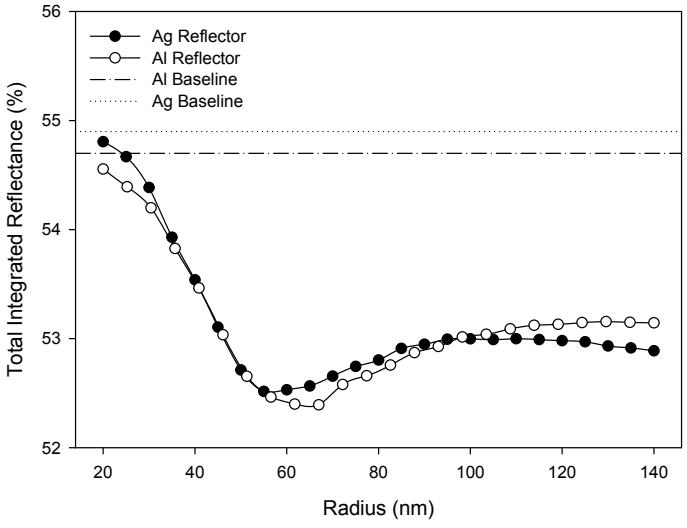

Figure 5.34: 100nm ITO disc radius integrated reflectance

5.4.2.2 Disc Radius Optimisation in 200nm ITO

The results of the simulations for the disc radius variation in 200nm ITO, between 20 - 140nm is depicted in the surface plots in figures 5.35 (a) and (b). Figure 5.36 depicts the integrated results over the wavelength range 300 - 1100nm for each disc radius. Disc height is fixed at 100nm and position is central in this investigation.

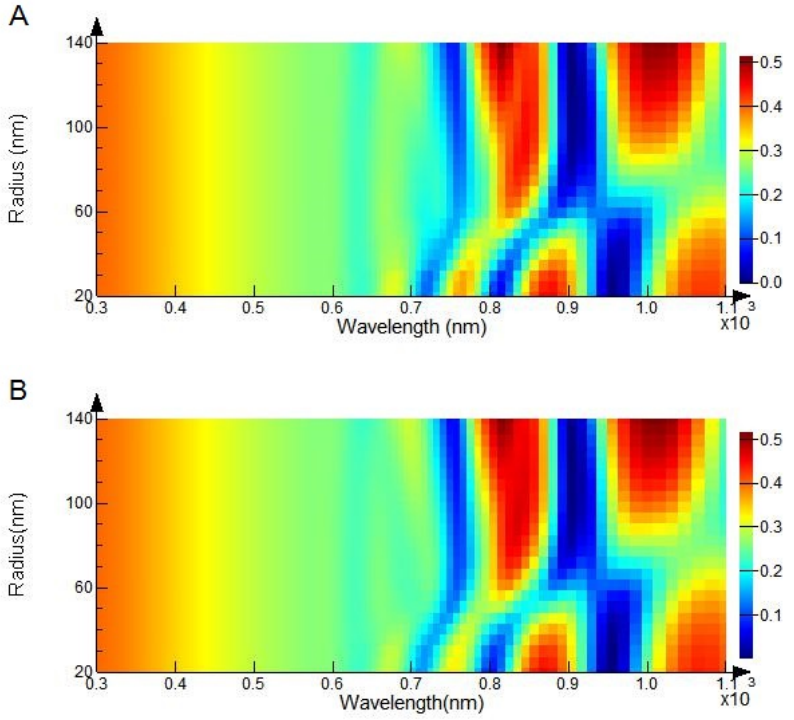

Figure 5.35: Radius vs reflectance (% - colour bar) - Ag(a) and Al(b) reflector

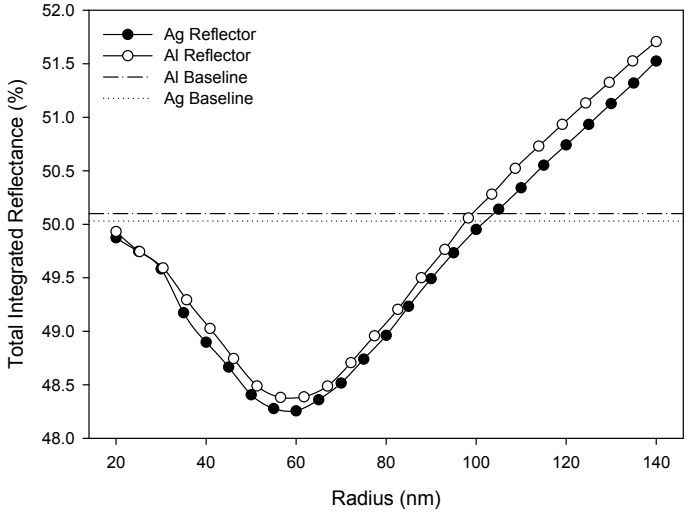

Figure 5.36: 200nm ITO disc radius integrated reflectance

5.4.2.3 Disc Distance Optimisation in 200nm ITO

The results of the simulations for the disc distance variation from the Si surface in 200nm ITO, with centre point between 50 - 150nm is depicted in the surface plots in figures 5.37 (a) and (b). Figure 5.38 depicts the integrated results over the wavelength range 300 - 1100nm for each disc distance. Disc height is fixed at 100nm and disc radius 100nm. The indicated axis range in the figures is from -150nm to -50nm as the origin is calculated from the silicon region edge. -150nm corresponds to the particle adjacent to the reflector while -50nm to particles next to the silicon region.

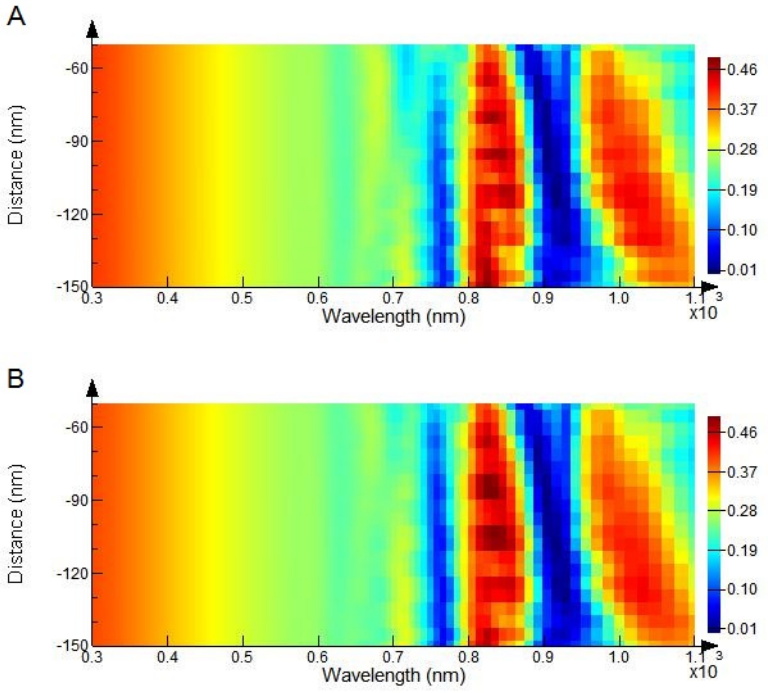

Figure 5.37: Distance vs reflectance (% - colour bar) - Ag(a) and Al(b) reflector

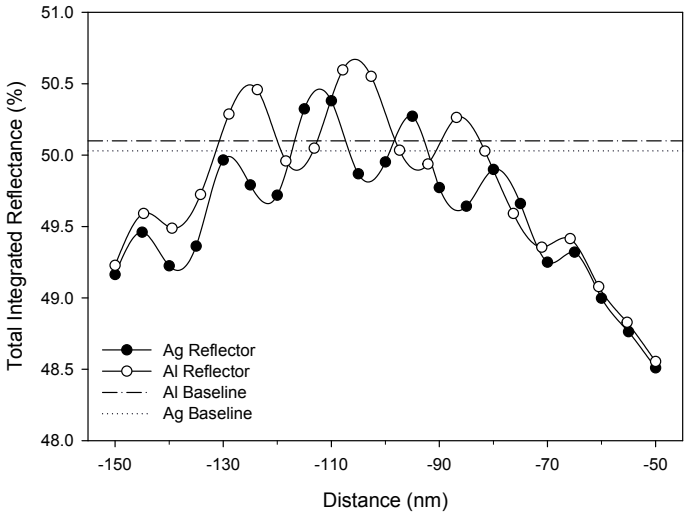

Figure 5.38: 200nm ITO disc distance integrated reflectance

5.4.2.4 Disc Height Optimisation in 200nm ITO

The results of the simulations for the disc height variation in 200nm ITO, between 10 - 150nm is depicted in the surface plots in figures 5.39 (a) and (b). Figure 5.40 depicts the integrated results over the wavelength range 300 - 1100nm for each disc height. Disc radius is fixed at 100nm and position is central in this investigation.

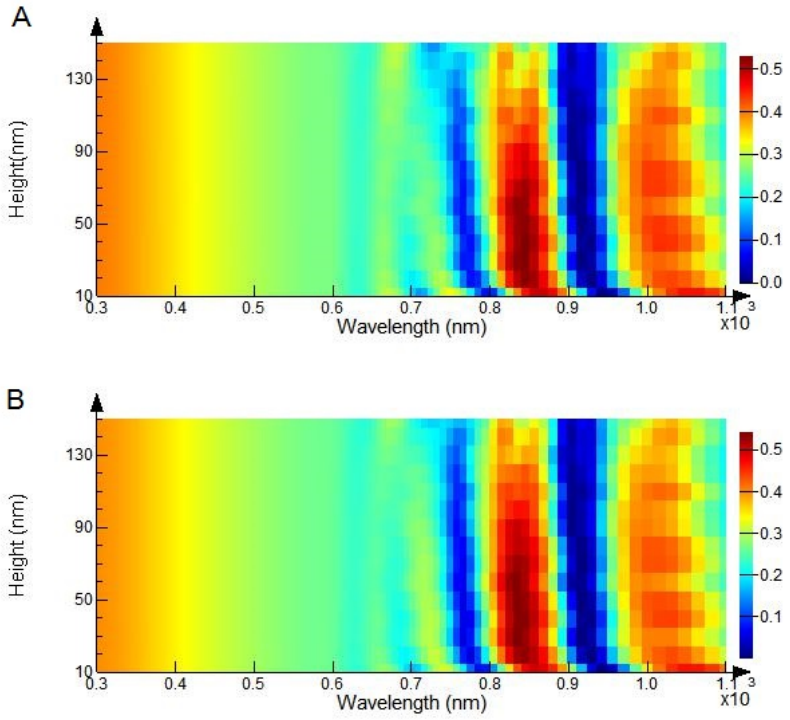

Figure 5.39: Height vs reflectance (% - colour bar) - Ag(a) and Al(b) reflector

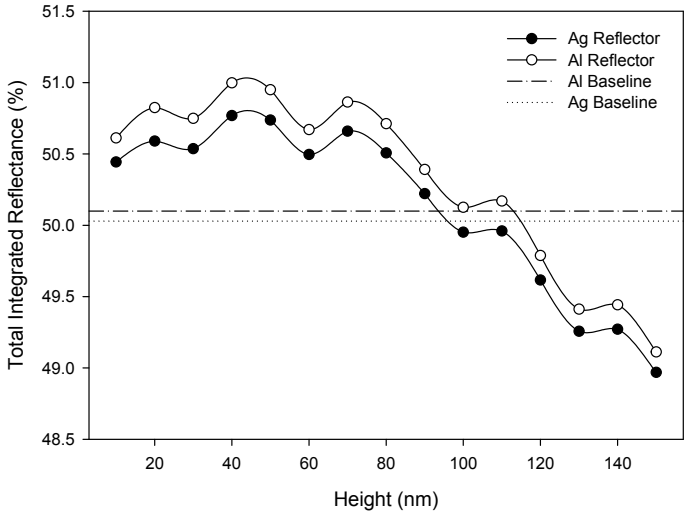

Figure 5.40: 200nm ITO disc height integrated reflectance

5.4.2.5 Sphere Radius Optimisation in 100nm ITO

The results of the simulations for the sphere radius variation in 100nm ITO, between 5 - 50nm is depicted in the surface plots in figures 5.41 (a) and (b). Figure 5.42 depicts the integrated results over the wavelength range 300 - 1100nm for each sphere radius. Sphere position is central in this investigation.

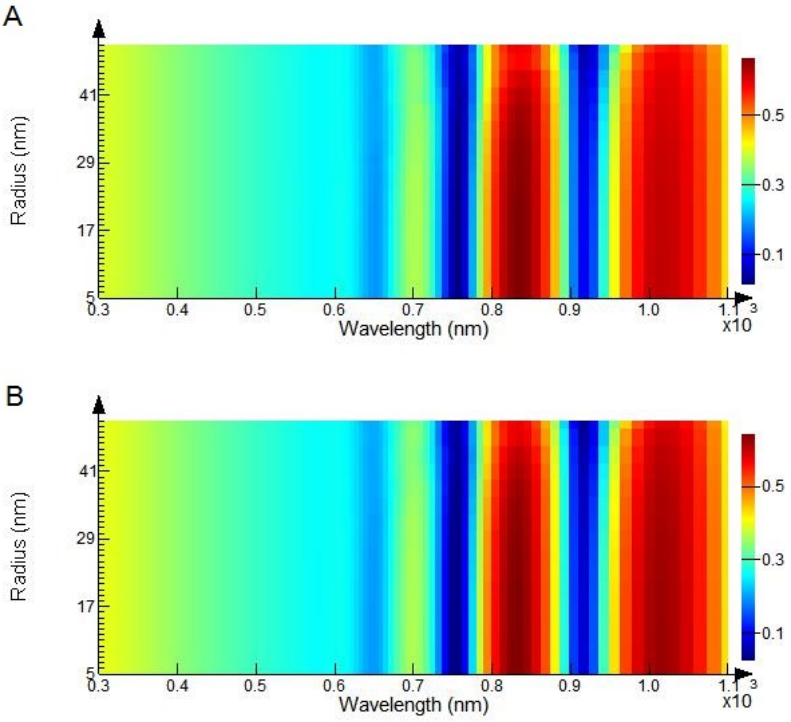

Figure 5.41: Radius vs reflectance (% - colour bar) - Ag(a) and Al(b) reflector

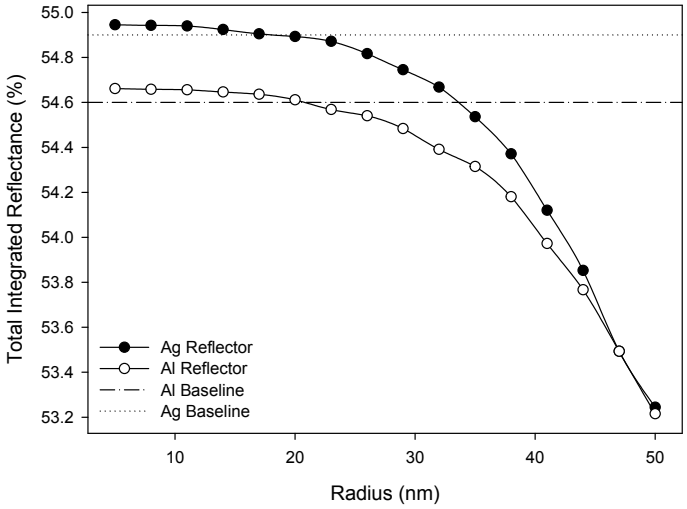

Figure 5.42: 100nm ITO sphere radius integrated reflectance

5.4.2.6 Sphere Radius Optimisation in 200nm ITO

The results of the simulations for the sphere radius variation in 200nm ITO, between 20 - 100nm is depicted in the surface plots in figures 5.43 (a) and (b). Figure 5.44 depicts the integrated results the wavelength range 300 - 1100nm for each sphere radius. Sphere position is central in this investigation.

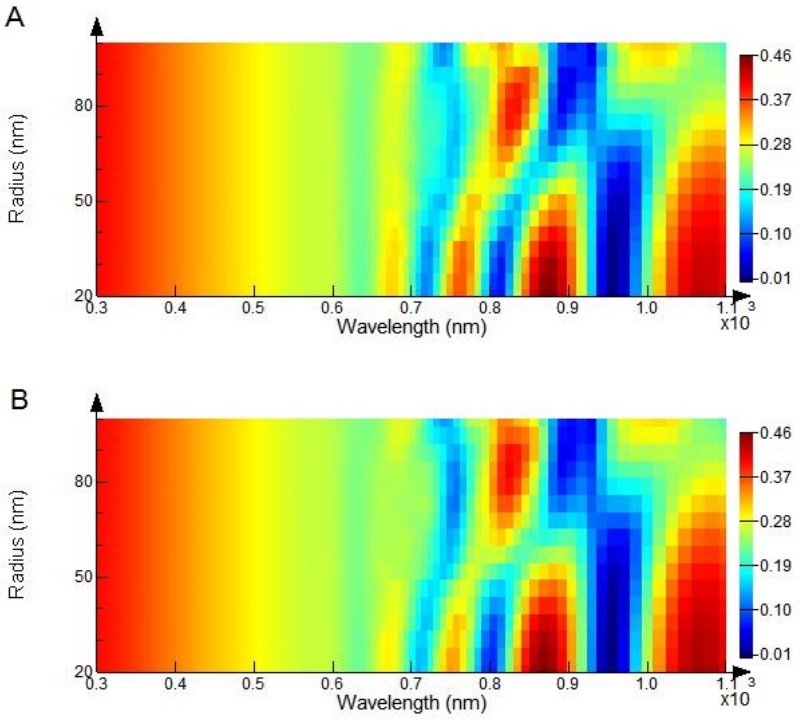

Figure 5.43: Radius vs reflectance (% - colour bar) - Ag(a) and Al(b) reflector

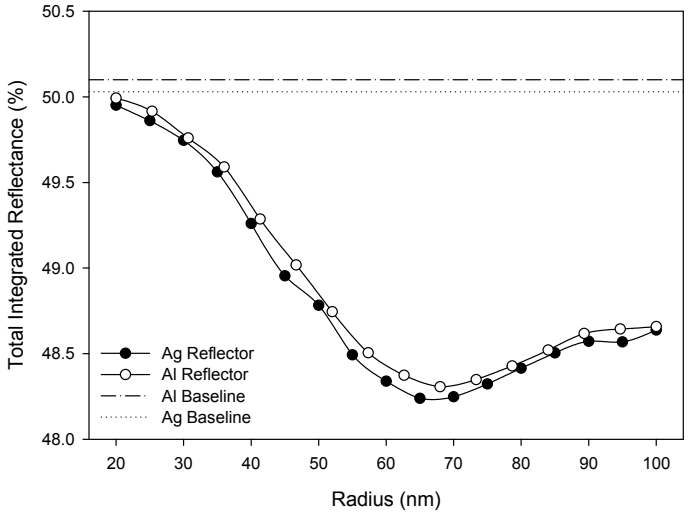

Figure 5.44: 200nm ITO sphere radius integrated reflectance

5.4.2.7 Sphere Distance Optimisation in 200nm ITO

The results of the simulations for the sphere distance variation from the silicon surface in 200nm ITO, with centre point between 50 - 150nm is depicted in the surface plots in figures 5.45 (a) and (b). Figure 5.46 depicts the integrated results over the wavelength range 300 - 1100nm for each sphere distance. Sphere radius is fixed at 50nm in this investigation. The indicated axis range in the figures is from -150nm to -50nm as the origin is calculated from the silicon region edge. -150nm corresponds to the particle adjacent to the reflector while -50nm to particles next to the silicon region.

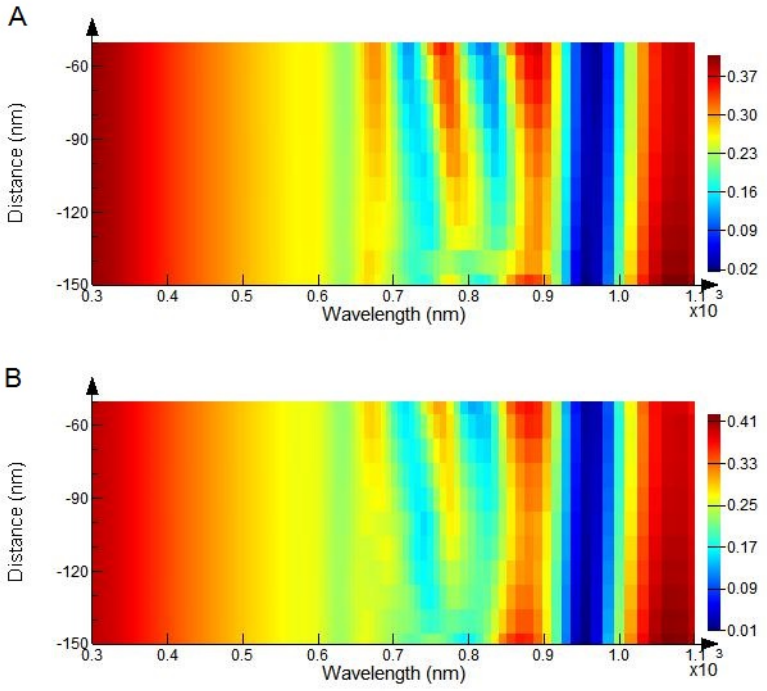

Figure 5.45: Distance vs reflectance (% - colour bar) - Ag(a) and Al(b) reflector

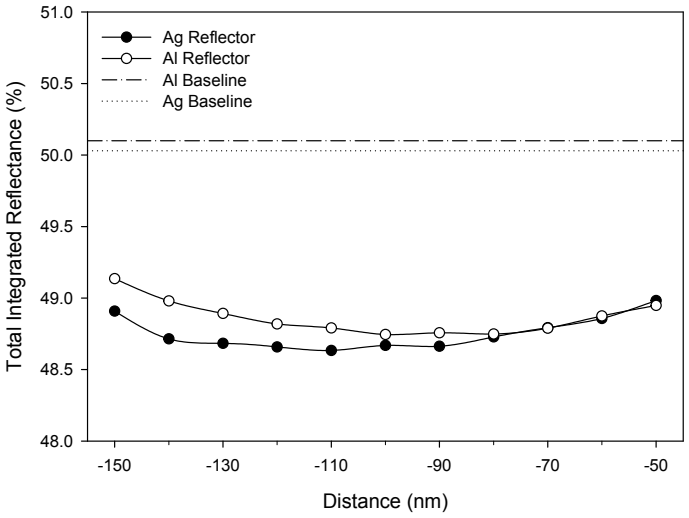

Figure 5.46: 200nm ITO sphere distance integrated reflectance

5.4.2.8 Sphere Radius Optimisation in 300nm ITO

The results of the simulations for the disc radius variation in 300nm ITO, between 20 - 140nm is depicted in the surface plots in figures 5.47 (a) and (b). Figure 5.48 depicts the integrated results over the wavelength range 300 - 1100nm for each sphere radius. Sphere position is central in this investigation.

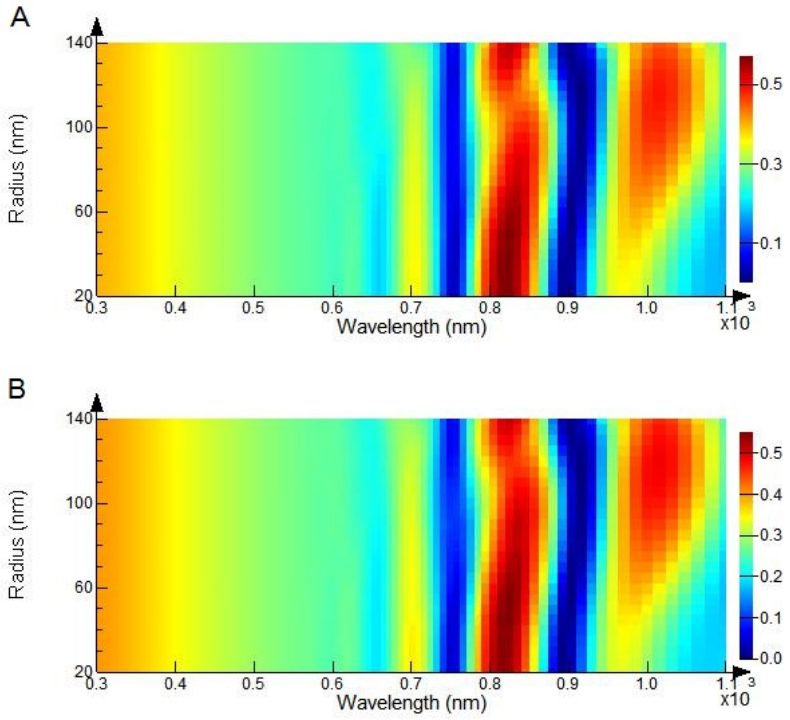

Figure 5.47: Radius vs reflectance (% - colour bar) - Ag(a) and Al(b) reflector

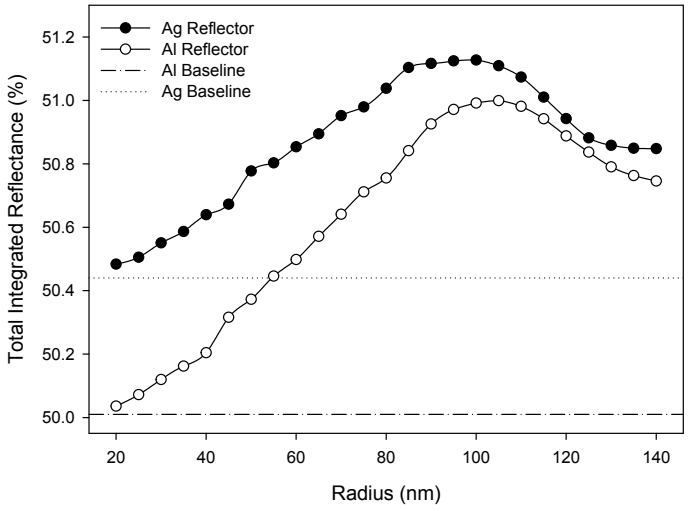

Figure 5.48: 300nm ITO sphere radius integrated reflectance

5.4.2.9 Sphere Distance Optimisation in 300nm ITO

The results of the simulations for the sphere distance variation from the silicon surface in 300nm ITO, with centre point between 100 - 200nm is depicted in the surface plots in figures 5.49 (a) and (b). Figure 5.50 depicts the integrated results over the wavelength range 300 - 1100nm for each sphere distance. Sphere radius is fixed at 100nm in this investigation. The indicated axis range in the figures is from -200nm to -100nm as the origin is calculated from the silicon region edge. -200nm corresponds to the particle adjacent to the reflector while -100nm to particles next to the silicon region.

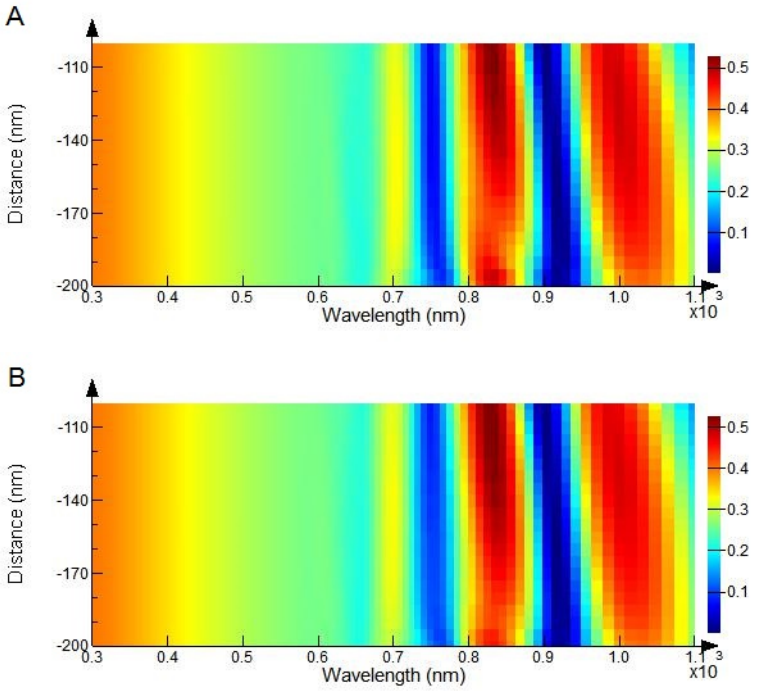

Figure 5.49: Distance vs reflectance (% - colour bar) - Ag(a) and Al(b) reflector

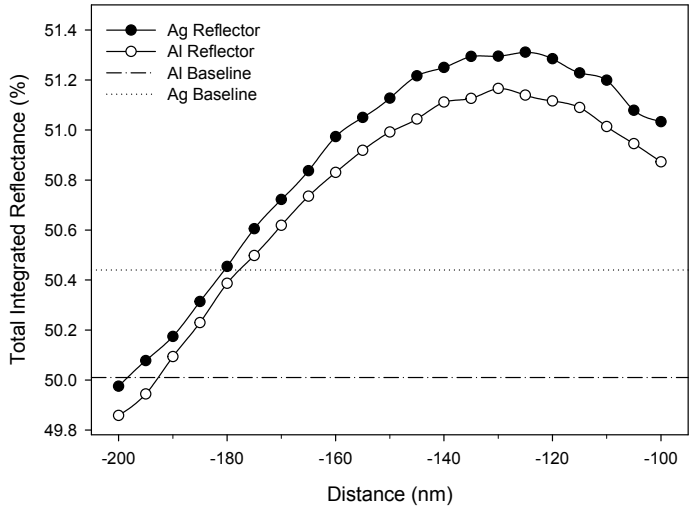

Figure 5.50: 300nm ITO sphere distance integrated reflectance

5.4.2.10 Summary of Results

The simulated values of reflection are summarised in table 5.5.

Particle	ITO Thickness	Variable	Value	Reflectance	Reflector
Discs	100nm	Radius	**67nm**	52.39%	Al
Discs	200nm	Radius	**160nm**	48.26%	Ag
Discs	200nm	Distance	**50nm**	48.51%	Ag
Discs	200nm	Height	**150nm**	48.97%	Ag
Spheres	100nm	Radius	**50nm**	53.22%	Al
Spheres	200nm	Radius	**65nm**	48.24%	Ag
Spheres	200nm	Distance	**110nm**	48.63%	Ag
Spheres	300nm	Radius	**20nm**	50.48%	Al
Spheres	300nm	Distance	**200nm**	48.97%	Al

Table 5.5: Summary of rear particle results

Investigation 5.4.2.6 shows that the lowest value of integrated reflectance for particle arrays at the rear of the absorber layer was achieved using spherical particles of radius 65nm within 200nm ITO and a silver reflector. The value of integrated reflectance appears to drop sharply with increasing radius, increasing slightly for larger particle sizes above 140nm. All values provide an integrated reflectance lower than the baseline. Investigation 5.4.1.7 shows that the positioning of the particle mid-way between the absorber layer and back reflector results in a slightly reduced reflectance value, although reflectance remains reduced with a silver reflector if the particle is positioned closer to the absorber layer in this simulation.

Investigation 5.4.2.8 shows the particle radius variation within 300nm ITO, which unusually shows an increase in integrated reflectance for all sizes. The lowest reflectance is achieved with the particles of smallest dimensions, 40nm in this case, however this remains higher than the base-line measurement. It is shown in investigation 5.4.2.9 that this increase in integrated reflectance can be mitigated by positioning the particle arrays adjacent to the absorber layer. As in the previous investigations, spherical particles in 100nm ITO do not reduce integrated reflectance to the same extent, however a similar trend is observed where reflectance is reduced for increasing values of sphere radius.

Investigation 5.4.2.1 shows disc-shaped particles in 100nm ITO, which reduce integrated reflectance sharply with increasing values of disc radius up to 90nm, but to a lesser extent than spheres in the same material. An aluminium reflector provides marginally the greatest reduction up to 100nm radius, at which point a silver reflector becomes favourable. The 200nm ITO thickness in investigation 5.4.1.2 shows a similar trend with the maximum reduction occurring at 60nm radius and an increase in integrated reflectance for particles with radius exceeding 100nm. The positioning investigation

5.4.1.3 follows the trend in the previous simulations, with only particles positioned within 40nm of the semiconductor or 30nm of the surface providing a reduction, with the same 'step' like interference patterns. Finally investigation 5.4.1.5 shows that the preferable disc height is in excess of 100nm with the optimum at 150nm.

As demonstrated previously in section 5.4.1, general trends show that spherical particles provide lower values of integrated reflectance as expected from the theory in section 2.4.3 due to a lack of sharp features. Particle sizes of between 120 - 130nm appear to reduce the reflectance to the greatest extent, with the particle positioned mid-way between the the semiconductor and reflector, and within 200nm ITO material.

It is notable that the values of integrated reflectance obtained from this investigation are significantly higher than those observed in the previous 5.4.1 investigation. This is expected as the device topography is dissimilar which influences the optical performance. Specifically, the front interface of the device in this investigation is between glass and amorphous silicon, while in investigation 5.4.1 the interfaces are glass and ITO followed by ITO and amorphous silicon. This transition has a more gradual change of refractive index as described in section 2.4.1 and therefore calculated integrated reflectance is significantly lower. Whilst variations in particle characteristics influence the optical reflectance from the surface of a device structure, these measurements are not matched to the absorption characteristics of the amorphous silicon layer and therefore may not be those which provide the optimal charge carrier generation. Section 5.5 describes more detailed three-dimensional simulation involving power absorption monitoring within the amorphous silicon region.

5.5 Power Absorption Simulation

In order to determine if the topography which results in the lowest value of reflectance corresponds to increased charge carrier generation, the optical power absorption within the silicon thin film can be calculated. Values of lowest reflectance in the previous investigations 5.4.2 and 5.4.3 may not be the optimal conditions for charge carrier generation within the absorber layer, as effects such as surface reflectance, parasitic absorption and non-radiative decay of plasmon energy can also cause a reduction in optical reflectance and are impossible to determine from a reflectance monitor alone. Power absorption monitoring is a three-dimensional simulation throughout the absorber layer, and therefore the computational resources required to perform the simulations are significantly higher. Due to this constraint, the condition which varies the optical reflectance percentage by the greatest extent, the particle radius, will be varied in this simulation. Calculated power absorption from the three-dimensional frequency-domain power monitor are automatically normalised to the AM1.5 spectrum.

5.5.1 Model Specification

An amorphous silicon light absorption layer is considered and therefore the device topography is altered accordingly to represent a thin-film silicon photovoltaic device with greater accuracy than within the reflectance investigations. Spherical particles are in distributed in either the front or rear ITO regions as shown below, with values of radius varied from 50 to 100nm in steps of 20nm positioned centrally. Both ITO regions remain in this simulation. Radius is chosen as the variable as it has shown to influence the reflectance to the greatest extent, while spherical particles are considered to be optimal shape for plasmonic operation. The device topography is as follows:

- Glass Substrate, SiO_2 Palik model - PML, 625nm within the FDTD boundaries.
- Front Indium Tin Oxide, FDTD model - 200nm thickness.
- Amorphous Silicon, sampled data model from [79] - 400nm thickness.
- Rear Indium Tin Oxide, FDTD model - 200nm thickness.
- Aluminium Back Reflector, Al Palik model - 300nm thickness

The simulation is run firstly with spherical nano-particle arrays positioned within the front ITO region, with their diameter varied over the range 100 - 200nm in steps of 20nm positioned centrally within the ITO. The second simulation is run with the nano-particle arrays positioned within the rear ITO region, adjacent to the aluminium back reflector. A base-line measurement with no particles is included for reference and overlaid in each results graph.

5.5.2 Results

The calculated power absorption within the amorphous silicon region per wavelength is presented in figures 5.51 and 5.52 for particles positioned within the front and rear ITO respectively. Figure 5.53 shows the integrated power absorption over all wavelengths for each simulation.

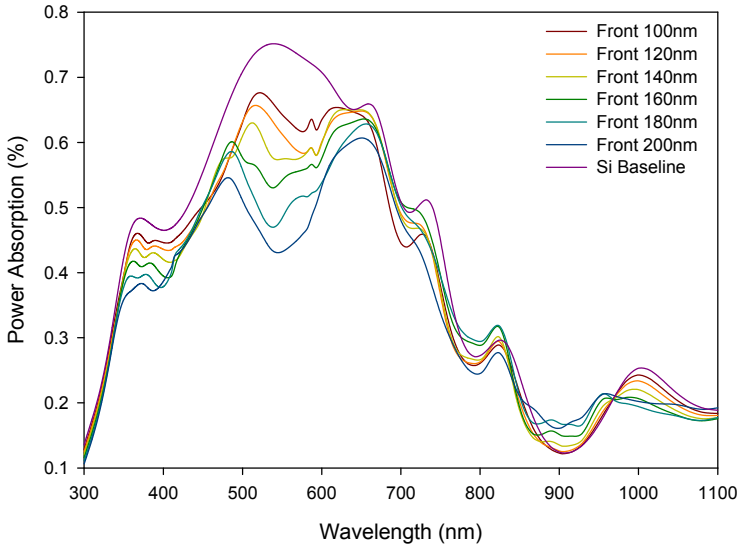

Figure 5.51: Power absorption vs wavelength for device stack with various radius spherical Ag nano-particle arrays in the front ITO

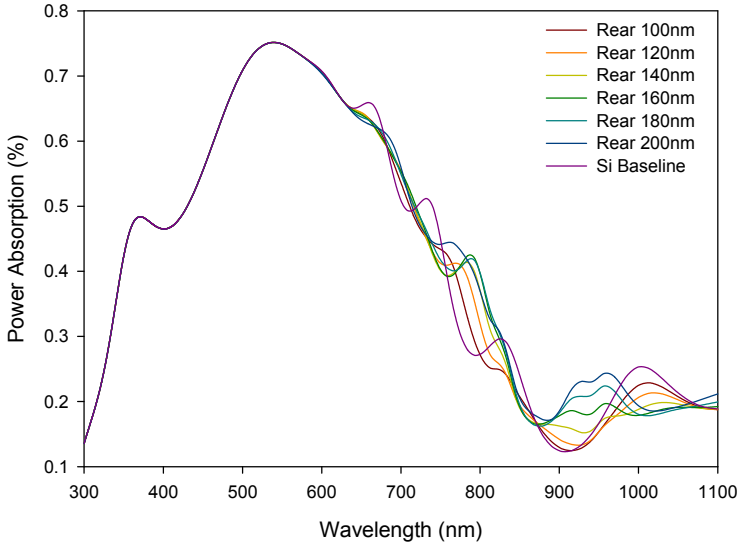

Figure 5.52: Power absorption vs wavelength for device stack with various radius spherical Ag nano-particle arrays in the rear (b) ITO

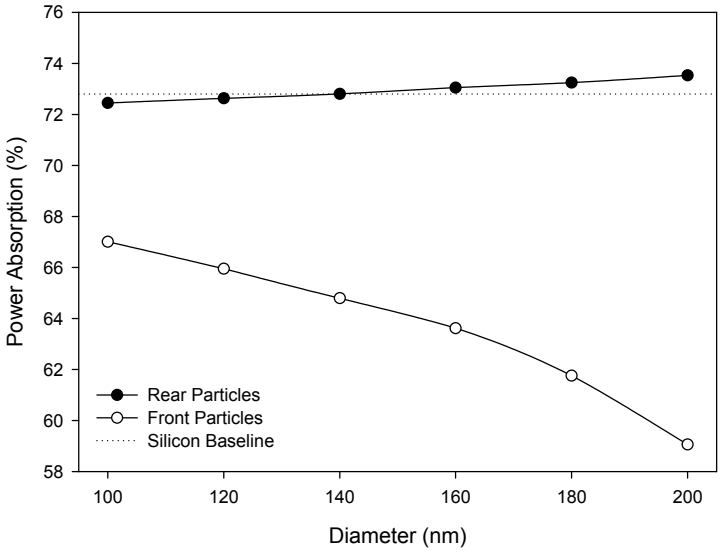

Figure 5.53: Integrated power absorption

5.5.3 Analysis

The simulated values of particle diameter at both front and rear of the absorber layer, together with the calculated power absorption are summarised in table 5.6. The percentage improvement in optical power absorption compared to the base-line measurement is also presented.

Position	**Diameter**	**Power Absorption (%)**	**Improvement (%)**
Front	100nm	67.01	-7.95
Front	120nm	65.94	-9.40
Front	140nm	64.79	-11.00
Front	160nm	63.62	-12.61
Front	180nm	61.76	-15.17
Front	200nm	59.06	-18.87
Rear	100nm	72.45	-0.48
Rear	120nm	72.63	-0.22
Rear	140nm	72.80	0.01
Rear	160nm	73.05	0.35
Rear	180nm	73.24	0.62
Rear	200nm	73.59	**1.01**
Si	None	72.79	-

Table 5.6: Summary of power absorption results

From investigation 5.5, it can be seen that all particles mounted at the front of the absorber layer negatively affect power absorption by a significant degree, with the lowest loss of just under 8%. Values of particle radius of increasing size serve to reduce the

absorption further so it is reasonable to deduce that front mounted particles are detrimental to device performance with this device configuration. This is in contrast to the reflectance monitor simulations performed in section 5.4.1 which suggest that the optical reflectance is reduced in certain configurations and therefore significant loss mechanisms are causing a reduction of light passing in to the absorber region. It is thought that particles mounted at the front serve to shade the absorption from the semiconductor region in some cases, particularly in the wavelength regions centred around 500nm.

Particles mounted within the rear ITO of the device are demonstrated to enhance optical power absorption in a number of cases. Particle diameters in excess of 160nm increase optical absorption by 1% or more, with particle sizes below this size causing a very slight reduction. It can therefore be ascertained that the positioning of nano-particle arrays within the ITO adjacent to the back reflector of the device can enhance optical performance. It can additionally be seen from figures 5.51 and 5.52 that no optical loss occurs in the short wavelength region from 450 - 600nm with the particles in the rear ITO, whilst significant losses are evident with the particles mounted at the front. Power absorption in the longer wavelength region that is weakly absorbed by the silicon shows a small peak from around 700nm compared to devices with no nano-particle arrays.

5.6 Conclusion

It has been demonstrated by means of simulation that the optical absorption and reflection of a silicon thin film with an array of metallic nano-particles can be varied over a wide range, by means of adjusting the size, shape, position and constituent material of the nano-particle. Positioning of arrays within the front or rear TCO materials are simulated, together with optimisation of the TCO thickness for either and both of these configurations. It has been found that the optical power absorption in the active layer of an amorphous silicon P-I-N device can be slightly increased by the incorporation of these particle arrays within the rear TCO material adjacent to a metallic back reflector, which serve to scatter transmitted light and therefore increase the effective optical path length through the active layer. Careful optimisation of the design is required to achieve the enhancement in performance to avoid parasitic absorption and reduction in performance. It is noted that enhancement due to light scattering at the rear of the device is strongly dependent on the absorber layer thickeness, and therefore it is expected that the potential enhancement due to methods simulated in this chapter are likely to improve with a reduction in absorber layer thickness. Whilst an improvement of 1% achieved from a 200nm particle positioned at the rear ITO can be considered modest, this simulation has only considered the effect of one spherical particle within the semiconductor region with a symmetrical unit cell. Varied packing density of an array of such particles across the surface of a photovoltaic device are likely to increase this performance gain, and also do not neglect inter-particle transition of scattered light.

Chapter 6

Self-Organised Nano-particle Arrays

6.1 Introduction

Based on the light-trapping schemes described in section 2.4.3 and simulations in chapter 5, a series of samples and devices featuring self-organised nano-particle arrays are fabricated, and their optical and electrical performances are analysed. The placement of an array of metal nano-particles of the correct dimensions results in interactions with incoming light photons, and the effects of these phenomena are investigated. Self-organised metal-island films are formed by the heating of very thin layers of a selection of metals, the surface tension of which causes the film morphology to agglomerate in to a random array of metal particles. An increase in the optical scattering of the wavelength range shorter than 730nm which amorphous silicon thin films are sensitive to is desirable to increase the performance of these devices, and the particle size, shape and morphology is tailored for this range of operation.

6.2 Experimental Detail

The initial investigation is focused on the deposition and processing of thin film silver layers, incorporating a wide range of Ag nano-particle arrays. In order to determine the temperature at which the nano-particles begin to form metal-island films and cause interactions with incident light, the initial silver depositions will be performed on plain 1mm thick glass substrates of size 25 x 75mm using electron-beam evaporation within a Leybold Optics BAK600 deposition system as described in section 3.2.3. The samples are subsequently annealed at a temperature from 175°C to 400°C for a fixed period of 60 minutes, using the Jipelec rapid thermal annealer described in section 3.2.4. Optical measurements of transmittance and reflectance are then carried out, across a wavelength range of 400 - 1100nm.

A subsequent investigation is performed on a surface of intrinsic amorphous silicon, as an absorber layer deposited on a 1mm thick glass substrate to the optimum conditions described in section 4.3.1. The purpose of this investigation is to determine at which temperature range and for which duration of annealing results in the optimum structure of metal island films, so the shape and characteristics of the resultant particles are explored using SEM imaging. A 15nm layer of silver is deposited on the device layer, which is subsequently annealed at temperatures from 200°C to 300°C for between 30 and 90 minutes. The resultant silver layers are observed using optical and SEM imaging to confirm the size, shape and periodicity of the particles; while initial optical measurements of transmittance and reflectance are made using an integrating sphere to calculate the optical absorption of the thin films, and allow focus on to the optimum range of deposition conditions in the following investigation.

Once the optimum region of conditions is found, a further set of devices is fabricated featuring 10nm and 15nm silver films on a device optical stack which corresponds to a completed photovoltaic device. This will include an additional thin film of transparent conducting oxide to separate the particles from the silicon device layer, and replicate the complete device structure. Temperatures are varied between 250°C to 400°C annealed for a fixed duration. Two categories of device are to be studied, a substrate configuration set with the particles facing the front and a superstrate configuration with the particles at the rear of the device, adjacent to an opaque silver reflector separated by further transparent conducting oxide. These investigations aim to experimentally determine the optimum anneal conditions to provide absorption enhancement in the silicon region.

A sub-set of the superstrate particle configurations are then selected with the highest optical absorption in the required wavelength range, and a further set of samples is fabricated with variations in the separation distance between the particle arrays and the back reflector, in order to observe the effects of the interaction between these two layers. The superstrate configuration is selected to mitigate the phenomenon of disrupted effective particle sizes when deposited near to a metallic reflector material.

Finally, the optimum set of deposition conditions are applied to a set of metal-island films within a plasmonic back-reflector assembly of an amorphous silicon photovoltaic device, and the electrical performance is compared to a range of devices with no such treatments in order to determine if a performance improvement can result.

6.3 Self-Organised Nano-Particle Arrays

6.3.1 Glass Substrates - Preliminary Investigation

6.3.1.1 Sample Specification

In order to determine the temperature at which the metal-island films begin nucleation, the initial depositions are performed on glass substrates and optical microscopy performed. Optical measurements of transmittance and reflectance are taken, in order to ascertain under which conditions an optical improvement is achieved. 15nm silver films evaporated using e-beam assisted deposition are annealed for 60 minutes in nitrogen under temperatures of 175 - 400°C in steps of 25°C. These conditions have been selected to reproduce the scattering effects detailed in literature reviewed in section 2.4.3.

A diagram of the device topography is shown in figure 6.1:

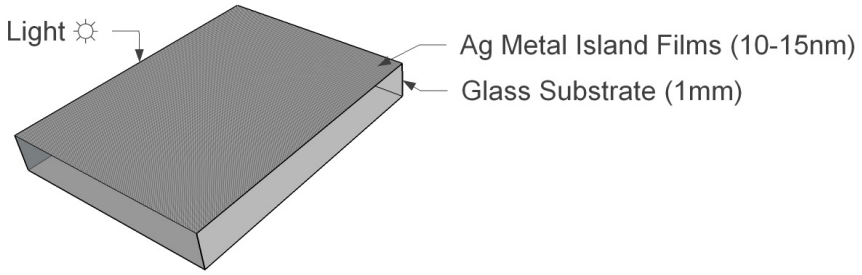

Figure 6.1: Topography of initial silver layers investigation

An optical microscope image of the resultant metal-island films at 150x magnification taken in a high-contrast mode is shown in figure 6.2, in which the discontinuous film formed after high temperature processing can be observed:

Figure 6.2: 150x optical microscope image of metal-island films on glass

6.3.1.2 Optical Measurements

The full results of the optical transmittance vs wavelength for each sample can be seen in figure 6.3, while the optical reflectance vs wavelength for each sample can be seen in figure 6.4. A control measurement of uncoated glass is not shown in this investigation as optical absorption statistics are not calculated for the samples studied in this section.

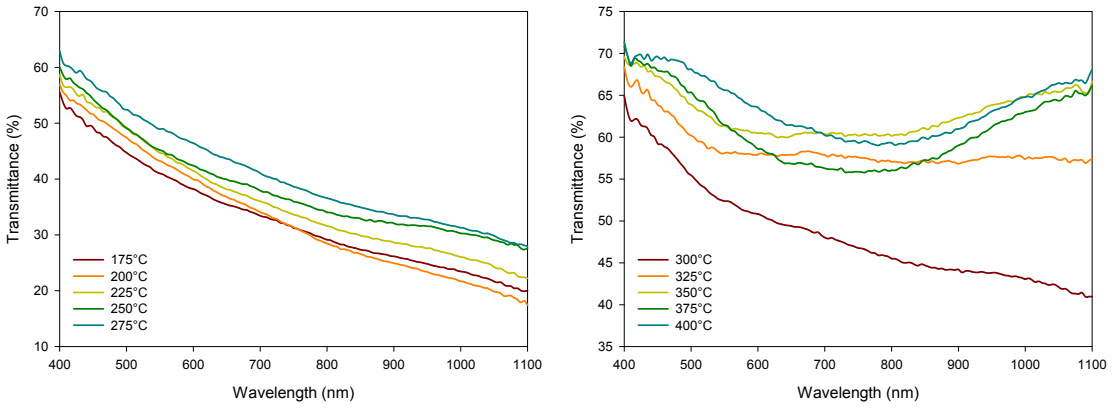

Figure 6.3: Optical transmittance 175°C - 275°C (a) and 300°C - 400°C (b)

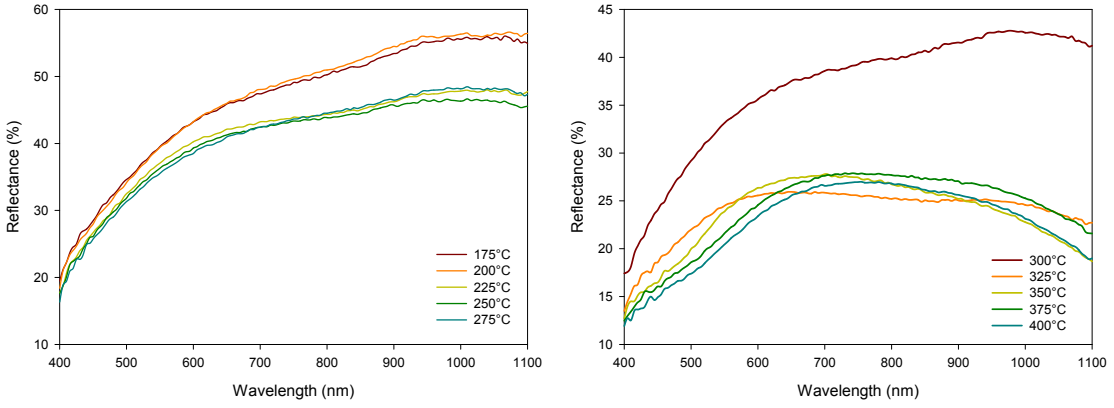

Figure 6.4: Optical reflectance 175°C - 275°C (a) and 300°C - 400°C (b)

6.3.1.3 Results

As can be observed from the results from section 6.3.1, the placement of silver nano-particles on a transparent substrate changes the characteristic optical transmittance and reflectance across the measured wavelength range. From annealing temperatures between 175°C and 275°C, the optical transmittance is shown to increase and the reflectance decrease as the metal island films are formed. At 300°C the transmittance and reflectance cross as shown in figure 6.5, with a large increase in transmittance and corresponding reduction in reflectance. Further increases in anneal temperature do not significantly affect the optical properties in this configuration.

The full data set of deposition conditions and measured average optical transmittance and reflectance values, across the wavelength range 400 - 1100nm are detailed in table 6.1:

Layer Thickness (nm)	**Temperature** ($^{\circ}C$)	**Anneal Duration (min)**	**Transmittance** (%)	**Reflectance** (%)
15	175	60	33.1	46.3
15	200	60	33.3	46.6
15	225	60	36.1	41.2
15	250	60	38.4	40.4
15	275	60	40.9	40.1
15	300	60	48.4	36.8
15	325	60	58.6	23.9
15	350	60	62.8	23.6
15	350	60	60.9	24.1
15	400	60	63.6	22.7

Table 6.1: Deposition Set Parameters

The average reflectance and transmittance values, across the full wavelength range for each temperature range can be observed in figure 6.5:

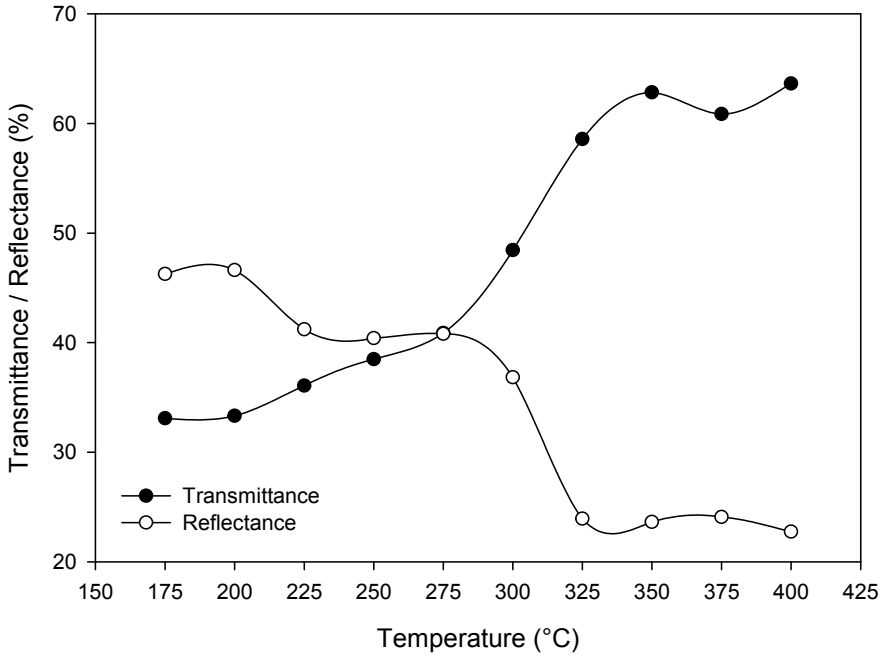

Figure 6.5: Reflectance and transmittance of annealed silver layers on glass

6.3.2 Amorphous Silicon on Glass - Optimal Anneal Conditions

6.3.2.1 Sample Specification

Based on the results from section 6.3.1, a further set of samples are prepared on an amorphous silicon coated glass substrate, in order to determine the optimum temperature and duration of annealing. The use of the amorphous silicon absorber layer is in order to obtain an estimate of the optical absorption measured in this section, and allows for imaging of the device layers using scanning electron microscope with a reliable contrast.

The detailed process flow for device fabrication is as follows:

1. Acetone and IPA cleaning of glass substrate.
2. Deposition of 375nm of intrinsic amorphous silicon using PECVD.
3. Deposition of 15nm silver using e-beam assisted evaporation.
4. Thermal annealing at temperatures and durations detailed in table 6.2.

The initial depositions are performed over a wide range of conditions are in order to infer the optimum particle formation conditions, and perform initial measurements of optical characteristics. A diagram of the device topography is shown in figure 6.6:

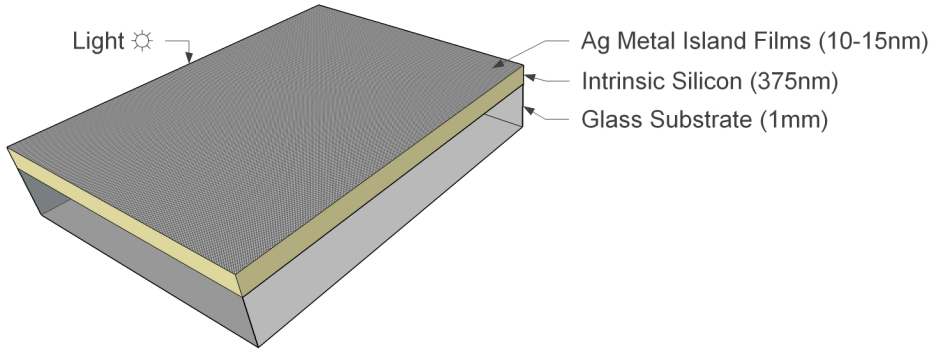

Figure 6.6: Topography of metal-island films on amorphous silicon

6.3.2.2 Evolution of Particle Formation

The resultant metal-island films have been imaged using optical microscope throughout stages of their formation, in order to observe the phases of nucleation of the particles. Figures 6.7, 6.8, 6.9, 6.10 and 6.11 detail the annealed metal films at 300°C after 0, 30, 40, 50 and 60 minutes respectively, at 150x magnification.

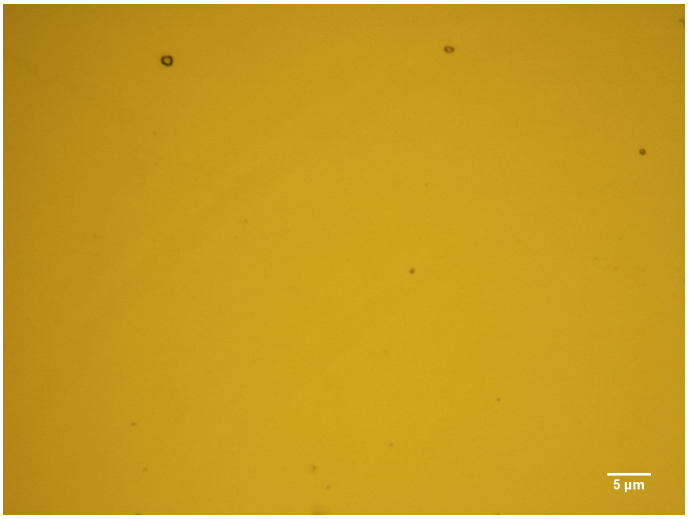

Figure 6.7: Optical image of silver film on a-Si before annealing

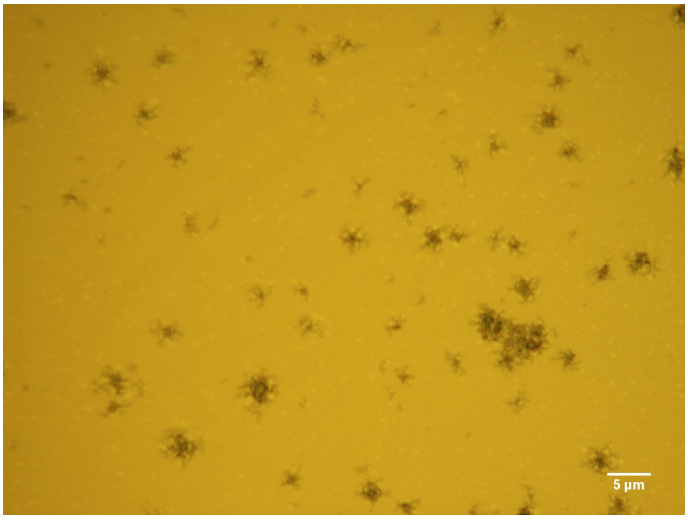

Figure 6.8: Optical image of silver film on a-Si after annealing for 30 minutes

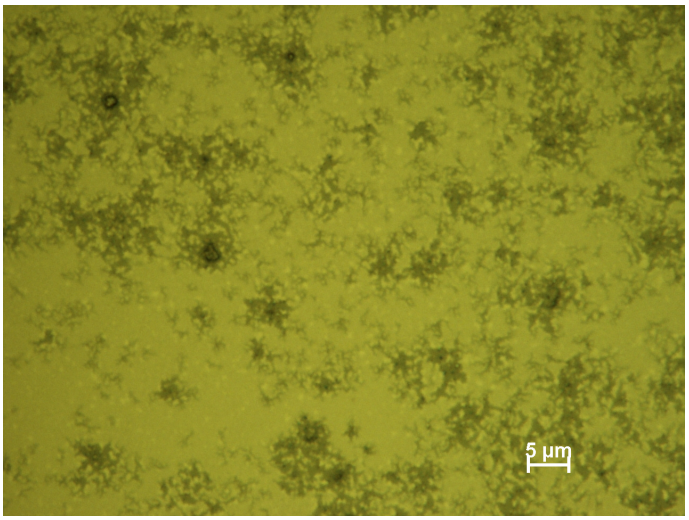

Figure 6.9: Optical image of silver film on a-Si after annealing for 40 minutes

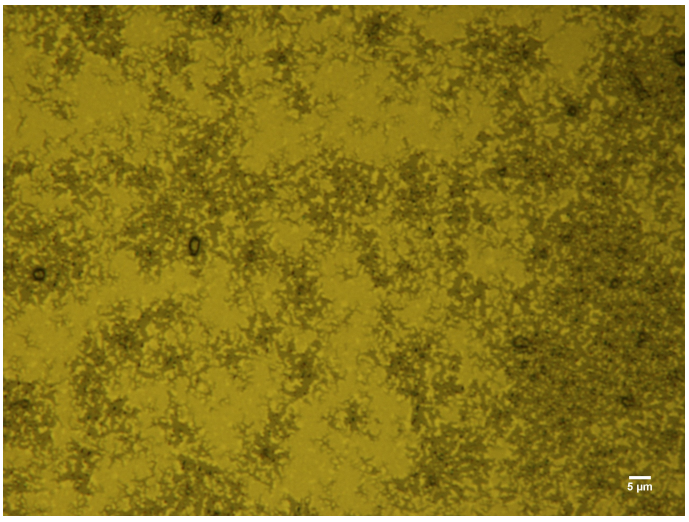

Figure 6.10: Optical image of silver film on a-Si after annealing for 50 minutes

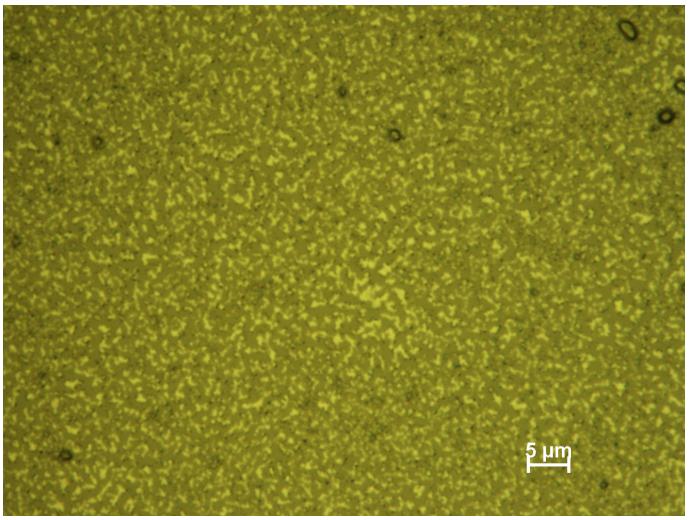

Figure 6.11: Optical image of silver film on a-Si after annealing for 60 minutes

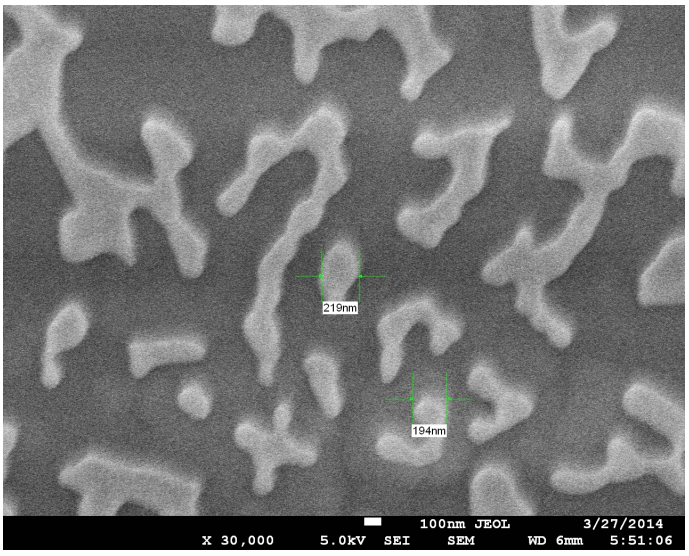

Figure 6.12: SEM image of silver nano-particles annealed for 60 minutes

A gradual change in film morphology can be seen in figures 6.7 - 6.11, showing that even coverage of the observation area is achieved after 60 minutes of annealing time. Figure 6.12 shows a scanning electron microscope image of the annealed nano-particles after 60 minutes, at 30,000x magnification. The particles produced by the anneal process can be seen to exhibit high levels of disorder and vary in dimensions to a large degree. A small number of circular-like particles can be observed with a diameter range of 100 - 250nm.

6.3.2.3 Optical Measurements

The optical absorption of the samples has been measured using the integrating sphere, performed over the wavelengths of 400 - 1000nm. Absorption spectra for the 30, 50, 70 and 90 minutes annealed samples are shown as a function of wavelength with the silicon only baseline in figures 6.13 and 6.14:

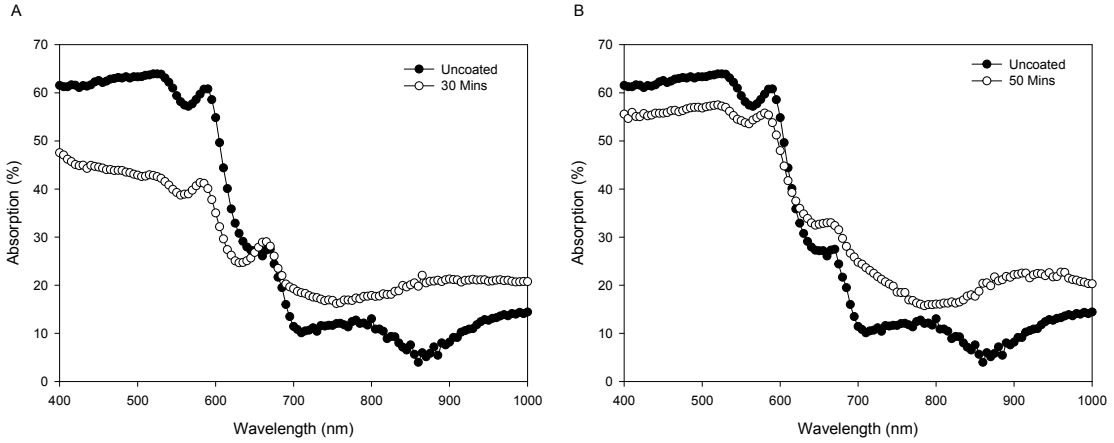

Figure 6.13: Optical absorption after 30 (a) and 50(b) minutes anneal

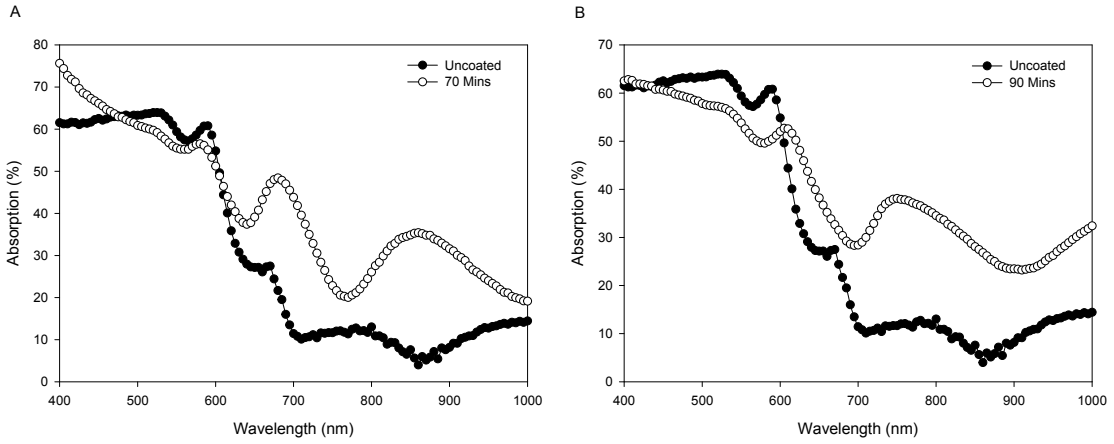

Figure 6.14: Optical absorption after 70 (a) and 90 (b) minutes anneal

6.3.2.4 Results

The resultant absorption values for each temperature and anneal duration are presented, alongside the silicon baseline, in figure 6.19. Figures 6.15, 6.16, 6.17 and 6.18 show individual transmittance and reflectance at temperatures of 300°C, 275°C, 250°C and 225°C respectively. Very little variation was observed between anneal durations at 200°C and therefore this data is shown only in the results summary in figure 6.19 .

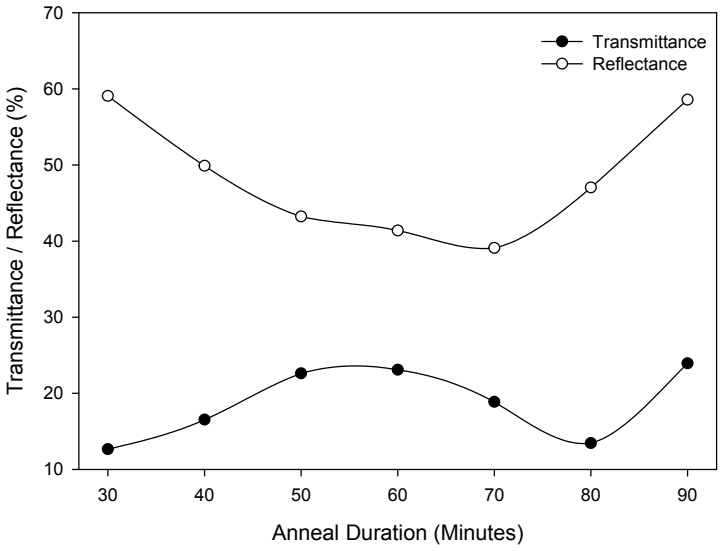

Figure 6.15: Anneal duration at 300°C

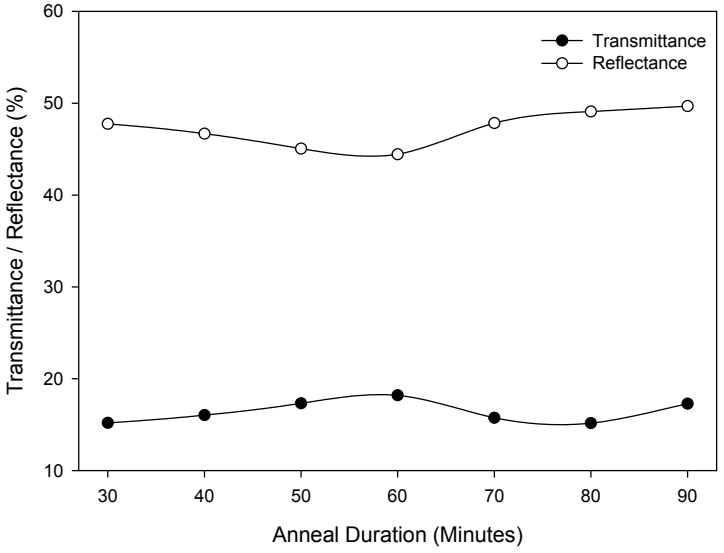

Figure 6.16: Anneal duration at 275°C

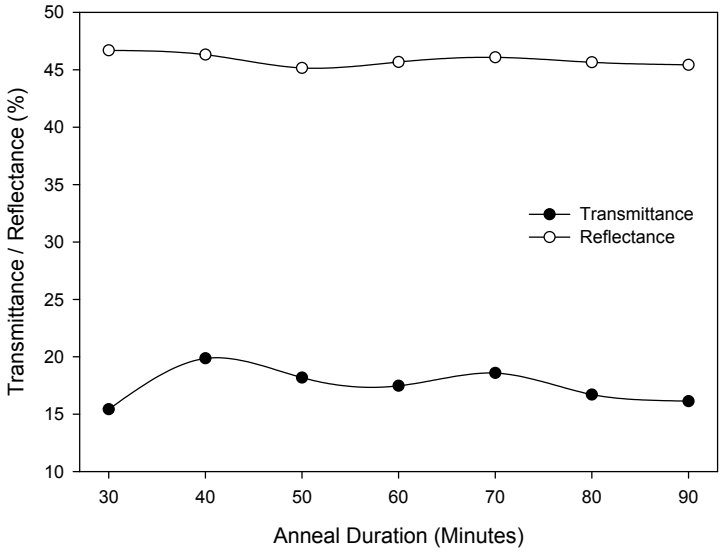

Figure 6.17: Anneal duration at 250°C

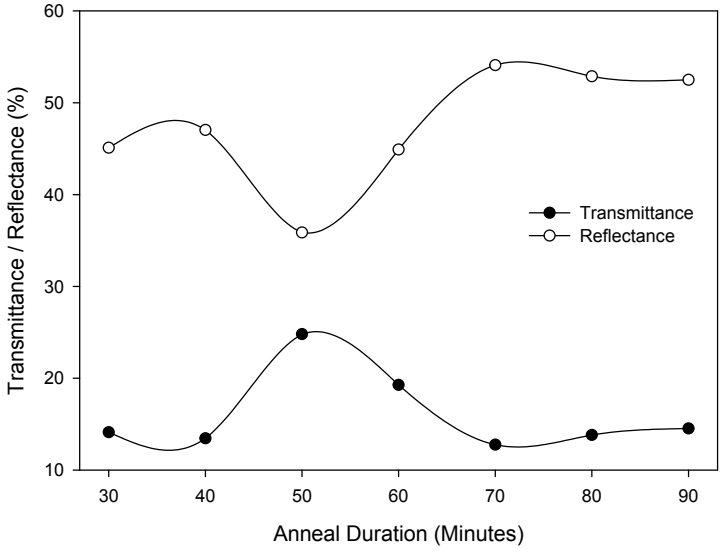

Figure 6.18: Anneal duration at 225°C

It can be observed from figure 6.15 that the most profound effects on transmittance and reflectance occur at temperatures of 300°C, with a sharp reduction in reflectance and increase in transmittance occurring after 50 minutes of anneal. The transmittance and reflectance are both further reduced by increased anneal time up to a duration of 70 minutes, after which an increase in reflectance is observed. Figure 6.16 shows that a far less pronounced change occurs after annealing at 275°C, with 60 minutes of annealing shown to provide the greatest change at this temperature. Further annealing serves to reduce transmittance and increase reflectance. The investigation at 250°C appears to show similar results to that of the investigation at 275°C, with 50 - 60 minutes anneal

showing the optimum enhancement. The investigation at $225°C$ shows an anomalous peak in transmittance and corresponding drop in reflectance centred around 50 minutes anneal, however this peak remains lower than the optimum result at $300°C$

To summarise, it is shown that temperatures below $300°C$, 50 - 60 minutes anneal duration provides the optimum enhancement conditions, while durations in excess of 60 minutes produce no significant enhancement to the optical absorption and cause a slight reduction. At $300°C$ the lowest reflectance and corresponding highest transmittance is achieved after 70 minutes. Silver layers annealed at temperatures of $200°C$ do not appear to be influenced by the duration of anneal, showing the lowest values of optical absorption with no significant increase compared to plain silicon observed.

The full data set of average optical absorption values, measured across wavelengths 400 - 1100nm for each temperature and duration of anneal are detailed in table 6.2:

Anneal Duration (minutes)	**Temp** $200°C$	$225°C$	$250°C$	$275°C$	$300°C$
30	32.45	36.99	37.88	37.06	28.27
40	32.56	37.08	33.82	37.28	33.58
50	30.92	39.32	36.66	37.62	34.16
60	32.15	35.82	36.85	37.37	35.54
70	30.63	33.15	35.32	36.42	42.04
80	32.74	33.31	37.65	35.75	39.51
90	31.16	32.98	38.44	33.03	40.78
Uncoated	30.30				

Table 6.2: Anneal temperature and duration average absorption (%)

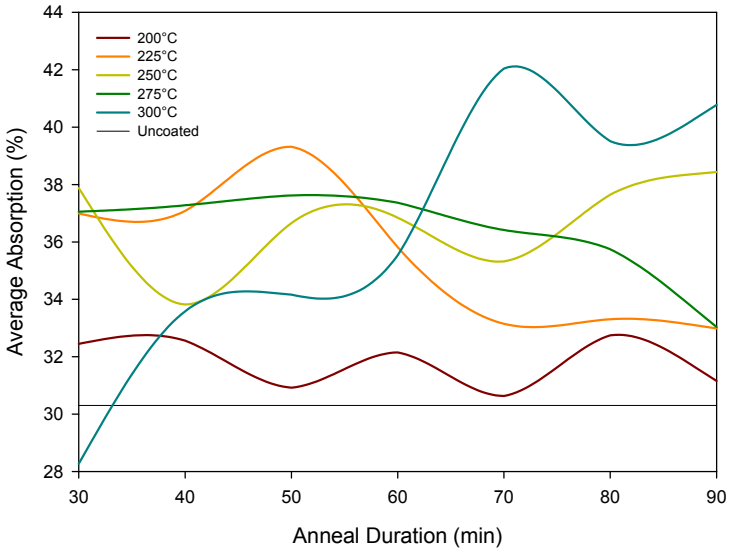

Figure 6.19: Anneal temperature and duration average absorption comparison

6.3.3 Comparison of Ag Film Thickness

6.3.3.1 Introduction

Based on the initial investigation, Ag metal island films are deposited in thicknesses of 10nm and 15nm, in order to determine the influence of film thckness on the optical absorption. Films are deposited on to a device structure featuring a 100nm region of transparent conducting oxide and amorphous silicon absorber layer. This more closely resembles that of a photovoltaic device and is fabricated in order to measure the optical absorption. The anneal duration is fixed at 60 minutes whilst the anneal temperature is varied over a the range $250°C$ to $400°C$ based on the results from section 6.3.2. A diagram of the device topography is shown in figure 6.20.

The detailed process flow for device fabrication is as follows:

1. Acetone and IPA cleaning of glass substrate.
2. Deposition of 375nm of intrinsic amorphous silicon using PECVD.
3. Deposition of 100nm of ITO using e-beam assisted evaporation.
4. Deposition of 10 or 15nm of silver using e-beam assisted evaporation.
5. Thermal annealing of the device over a range of temperatures for 60 minutes.

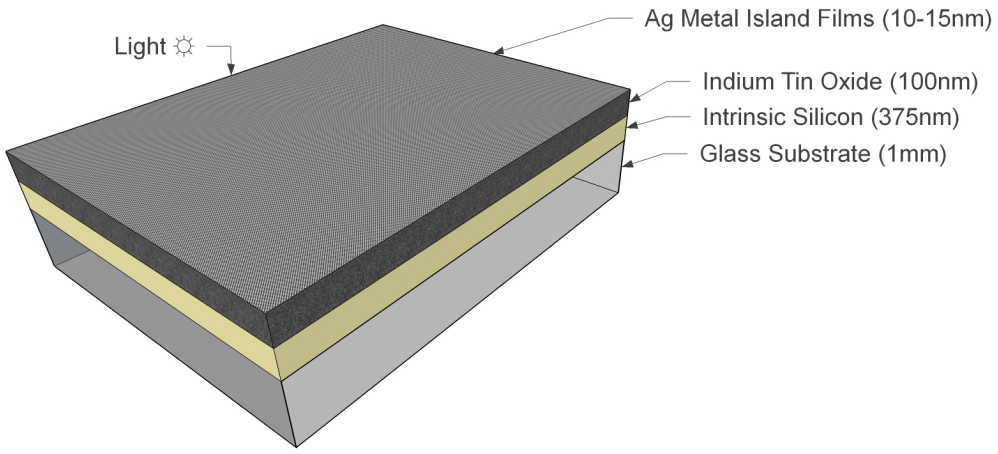

Figure 6.20: Topography of Ag thickness investigation

6.3.3.2 Optical Measurements

The optical absorption of the samples has been measured using the integrating sphere, over the wavelength range of 400 - 1000nm. The optical absorption provides an indication of the amount of incident light which is not transmitted through or reflected from the device, and therefore higher values of optical absorption correspond to either increased potential charge-carrier generation or increased parasitic absorption outside of the silicon thin film, such as by the particles themselves. A subset of these measurements are detailed in figures 6.21 and 6.22, showing absorption spectra for the 15nm and 10nm films annealed at $350°C$ and $400°C$ respectively.

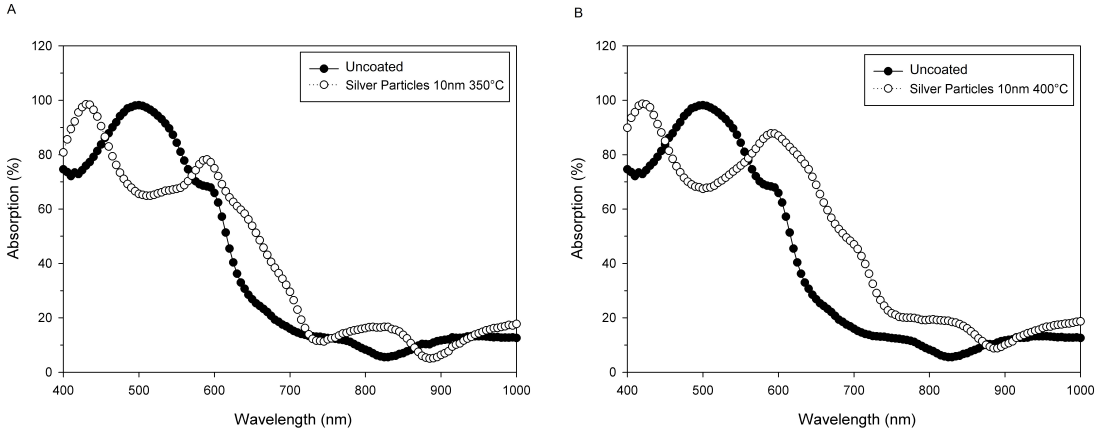

Figure 6.21: Optical absorption of 10nm films at $350°C$ (a) and $400°C$ (b)

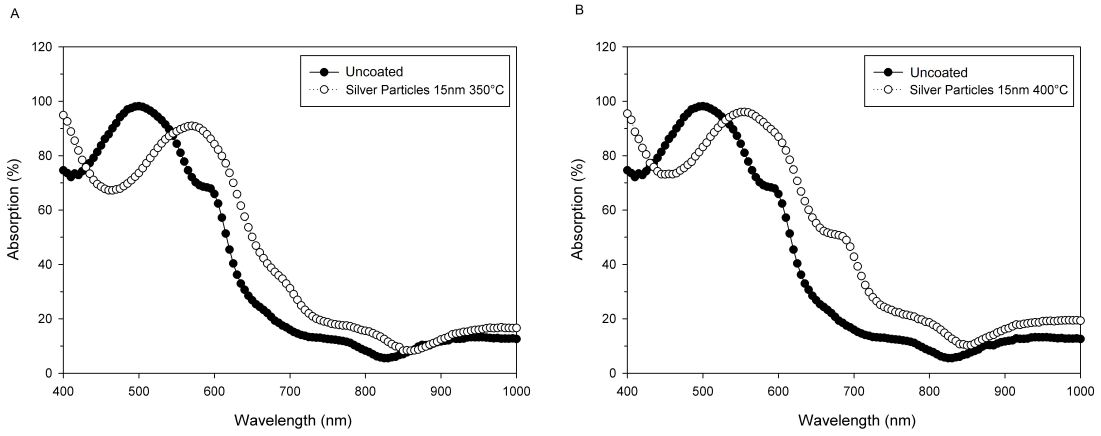

Figure 6.22: Optical absorption of 15nm films at $350°C$ (a) and $400°C$ (b)

Figures 6.23 and 6.24 show the variation in optical transmittance and reflectance, as the temperature is increased from $250°C$ to $400°C$.

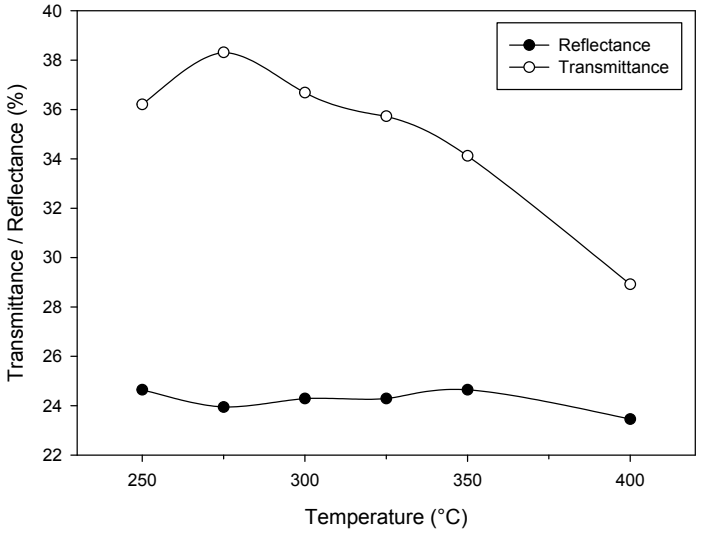

Figure 6.23: Reflectance and transmittance of annealed 10nm films

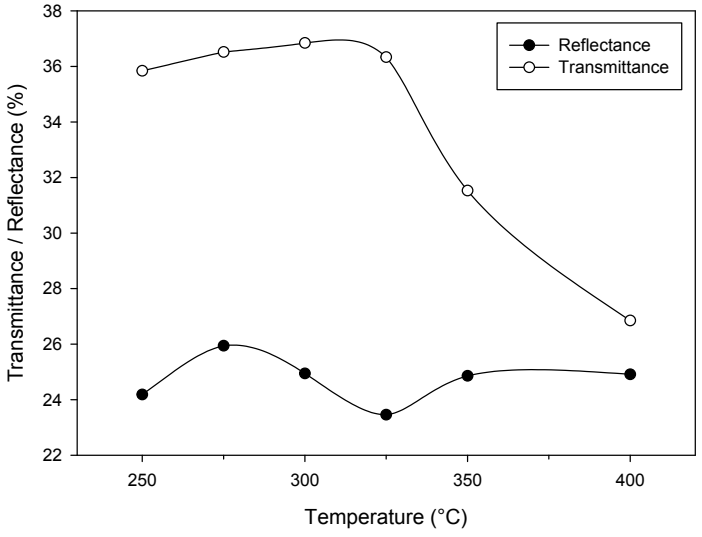

Figure 6.24: Reflectance and transmittance of annealed 15nm films

It can be observed that a similar characteristic trend exists for both 10nm and 15nm films, with the transmittance value falling significantly at anneal temperatures of $300°C$ and above. 15nm films exhibit higher values of reflectance with a reduction occurring at $325°C$, whilst 10nm films show a fairly constant value of reflectance throughout. At the highest anneal temperature of $400°C$, transmittance is reduced to the greatest extent in both films, with 15nm films showing the lowest value and therefore the highest optical absorption within the film.

The complete set of sample results are illustrated in figure 6.25, detailing the average absorption values across the wavelength range 400 - 1100nm for each. It can be observed that the samples with 10nm and 15nm Ag thin films annealed at $400°C$ demonstrate the maximum absorption across the wavelength range, with the 15nm sample providing fewer peaks and enhancement over a more broad wavelength range. The optical losses which occur at short wavelengths below 600nm are also reduced in this data set compared to those at lower temperatures. The normalised optical absorption compared to uncoated silicon and TCO material is illustrated in figure 6.26, showing the absorption enhancement compared to uncoated samples vs wavelength.

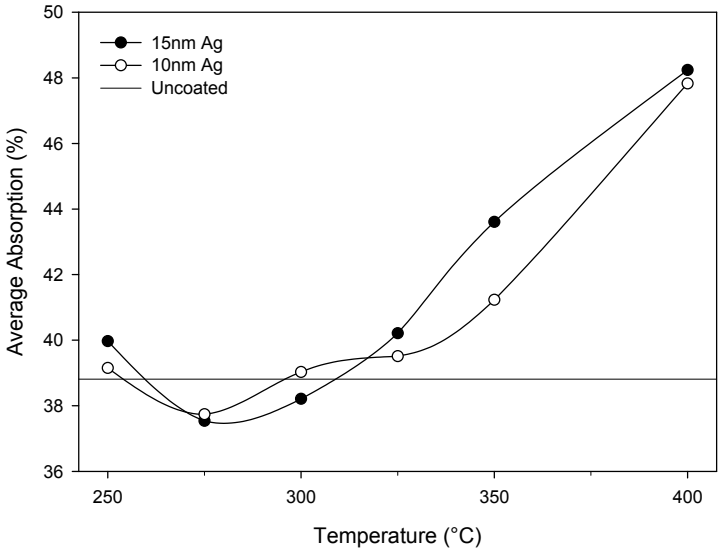

Figure 6.25: Optical absorption samples comparison

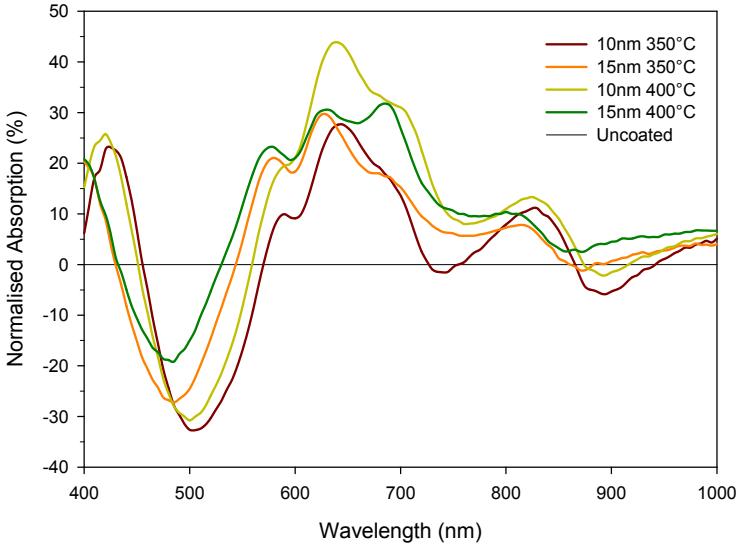

Figure 6.26: Optical absorption improvement

6.3.3.3 Analysis

It can be observed that at wavelengths between 550 - 900nm, optical absorption is enhanced to a noticeable degree for both 10nm and 15nm coated films, while between 450 - 550nm a significant decrease in absorption, and hence increase in transmittance or reflectance, is noted. It is not possible to differentiate between parasitic absorption losses due to the presence of the particle arrays in this investigation.

The complete set of sample results are illustrated in figure 6.25, detailing the average absorption values for each. It can be observed that samples annealed above $300°C$ exhibit the highest values of average absorption, with those annealed at $400°C$ showing the peak measured absorption. A maximum average optical absorption value of 48% was attained from the 15nm Ag film, while the 15nm annealed silver films all appear to marginally show the highest absorption compared to those based on 10nm films at temperatures above $325°C$, with the most significant variation occurring at $400°C$.

The full anneal temperature investigation deposition conditions, together with results for average optical absorption are detailed in table 6.3:

Layer Thickness (nm)	**Anneal Temperature** ($°C$)	**Anneal Duration (min)**	**Average Absorption (%)**
15	400	60	48.24
15	350	60	43.61
15	325	60	40.21
15	300	60	38.21
15	275	60	37.54
15	250	60	39.97
10	400	60	47.63
10	350	60	41.23
10	325	60	39.51
10	300	60	39.03
10	275	60	37.74
10	250	60	39.15
Uncoated	0	0	38.81

Table 6.3: Anneal temperature deposition set parameters

6.3.4 Nano-particle Arrays with Ag Reflector

6.3.4.1 Introduction

Based on the previous investigation, a set of samples will be prepared featuring a silver rear reflector, in the superstate configuration as would be the case in a full photovoltaic device. The experimental variables are performed identically to those in the previous investigation to allow for comparison of results. The 375nm silicon absorber layer is deposited on the glass substrate, followed by an 100nm layer of indium tin oxide and thin Ag film in both 10nm and 15nm thicknesses as in investigation 6.3.3. This structure is then annealed at temperatures ranging from $250°C$ to $400°C$ for a fixed duration of 60 minutes, followed by the deposition of 100nm layer of indium tin oxide to encapsulate the particles. A 100nm Ag film is then deposited as the back reflector material, this thickness is limited by the deposition process and is therefore thinner than the reflector layers fabricated in the investigation in chapter 4. The purpose of this investigation is to observe the amount of light which is being reflected from the device and the extent which is being absorbed as opposed to an uncoated sample. A diagram of the device topography is shown in figure 6.27.

The detailed process flow for device fabrication is as follows:

1. Acetone and IPA cleaning of glass substrate.
2. Deposition of 375nm of intrinsic amorphous silicon using PECVD.
3. Deposition of 100nm of indium tin oxide using e-beam assisted evaporation.
4. Deposition of 10 or 15nm of silver using e-beam assisted evaporation.
5. Thermal annealing of the structure from $250°C$ to $400°C$.
6. Deposition of 100nm ITO using e-beam assisted evaporation.
7. Deposition of 100nm of silver for back reflector using e-beam assisted evaporation.

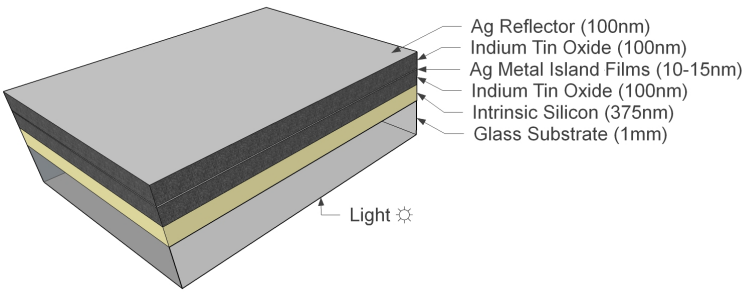

Figure 6.27: Topography of Ag reflector silver layers investigation

6.3.4.2 Optical Measurements

The optical reflectance of the samples has been measured using the integrating sphere, performed over the wavelength range of 400 - 1000nm. The optical reflectance provides an indication of the amount of light which is not absorbed within the first (incident) and second (reflected) pass through the device, and therefore lower values of optical reflectance correspond to a higher optical absorption and a higher potential charge-carrier generation or parasitic absorption. A subset of these measurements are detailed in figures 6.28 and 6.29; showing absorption spectra for the 10nm and 15nm films annealed at 350°C and 400°C respectively.

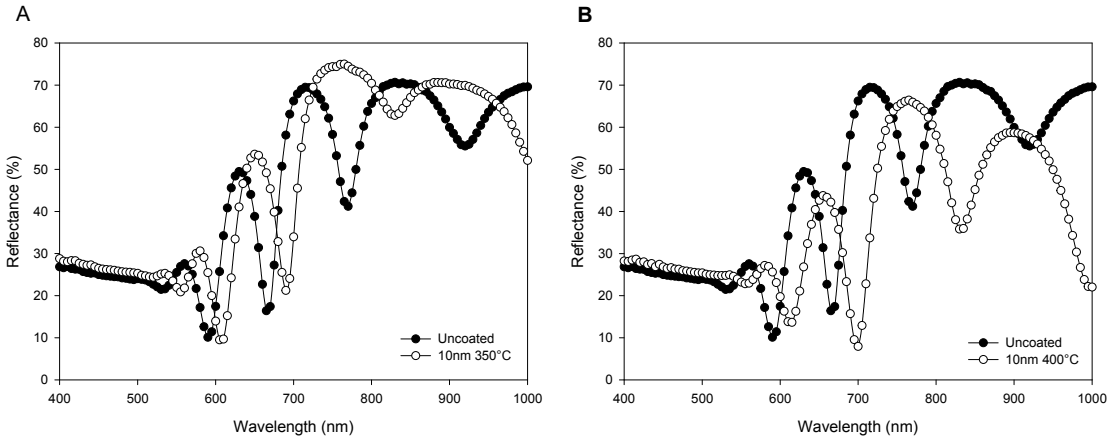

Figure 6.28: Optical reflectance of 10nm films at 350°C (a) and 400°C (b)

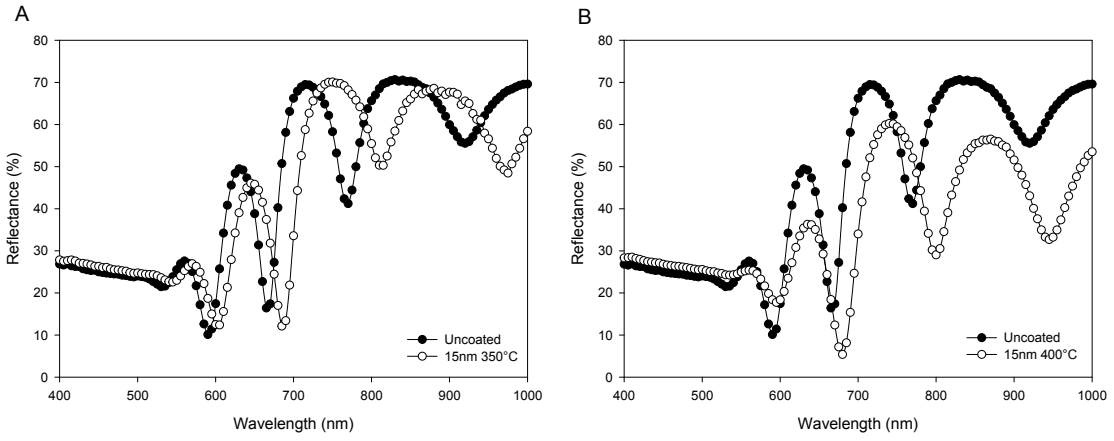

Figure 6.29: Optical reflectance of 15nm films at 350°C (a) and 400°C (b)

6.3.4.3 Analysis

The complete set of sample results are illustrated in figure 6.30, detailing the average reflectance values across the wavelength range 400 - 1100nm for each. The extent to which the samples reduce optical reflectance is illustrated in figure 6.31, showing the reflectance reduction compared to plain silicon samples vs wavelength. It can be observed that, similar to the previous investigation the 10nm and 15nm samples annealed at $400°C$ demonstrate the minimum reflectance across the wavelength range, with the 15nm sample providing the lowest reflectance overall.

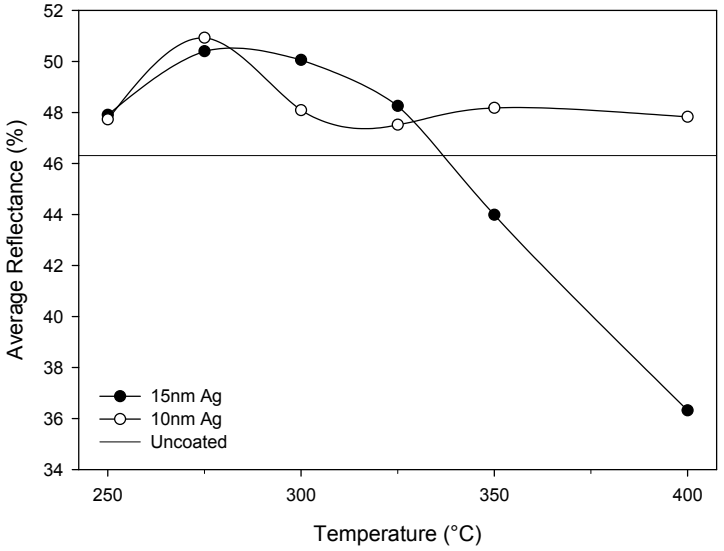

Figure 6.30: Ag film thickness optical reflectance samples comparison

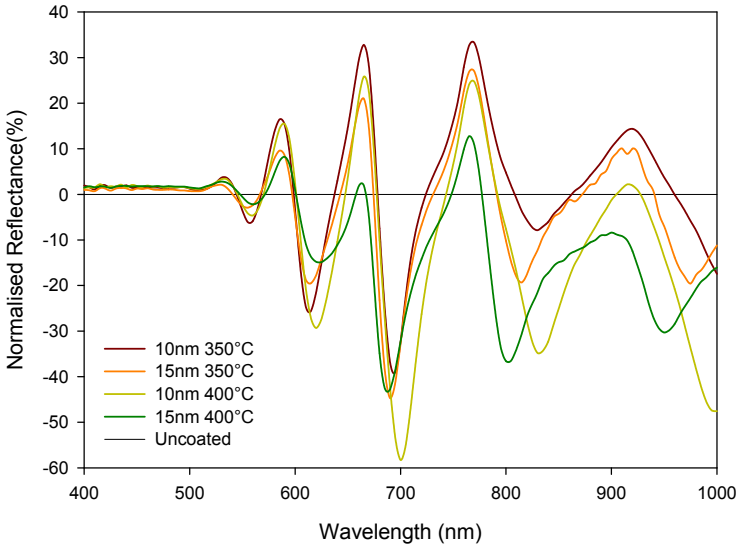

Figure 6.31: Ag film thickness normalised reflectance

It can be observed that at wavelengths starting from 550nm, optical reflectance is somewhat reduced, particularly in the range above 750nm. A number of peaks and troughs are illustrated, which are shifted slightly towards a longer wavelength. A slight red-shifting of the reflectance peaks can be observed, which oscillate over a wide range of reflectance values as the wavelength is increased. This can be attributed to an influence on the driving field by interference effects due to the optical stack and mirror topography.

The complete set of sample results are illustrated in figure 6.30, detailing the average reflectance values for each. It can clearly be observed that samples based on 15nm films annealed above $350°C$ exhibit the lowest values of optical reflectance, with those annealed at $400°C$ showing the peak reduction. 10nm annealed films do not appear to reduce the reflectance below that of the silicon base-line regardless of temperature.

The full back-reflector temperature investigation deposition conditions, together with results for average optical reflectance are detailed in table 6.4:

Layer Thickness (nm)	**Anneal Temperature ($°C$)**	**Anneal Duration (min)**	**Average Reflectance (%)**
15	400	60	36.32
15	350	60	43.99
15	325	60	48.26
15	300	60	50.06
15	275	60	50.40
15	250	60	47.91
10	400	60	37.99
10	350	60	48.18
10	325	60	47.52
10	300	60	48.09
10	275	60	50.93
10	250	60	47.73
Uncoated	0	0	46.31

Table 6.4: Ag reflector deposition set parameters

Comparing these results to those from investigation 6.3.3, it can be observed that the anneal temperatures which result in the lowest values of optical transmittance and reflectance and therefore highest calculated absorption are also those which exhibit the lowest values of reflectance in this investigation. Anneal temperatures of $400°C$ can be seen to maximise absorption and reduce optical reflectance for 15nm Ag films, however those with 10nm Ag films do not appear to reduce the optical reflectance from the device in this investigation to the same extent.

6.3.5 Variation of ITO Thickness

6.3.5.1 Introduction

In order to fully investigate the influence of the proximity of the nano-particle arrays to the Ag back reflector, a set of samples is prepared featuring a variation of TCO thickness between the nano-particle arrays and the rear reflector of the device. As in the previous investigation 6.3.4, the intrinsic amorphous silicon absorber layer is deposited on the glass substrate, followed by 100nm layer of indium tin oxide and a 10nm Ag thin film. In this investigation, 15nm film thickness is not explored. A fixed anneal temperature of $350°C$ for a duration of 60 minutes is used in this investigation, as appreciable optical absorption characteristics are shown at this temperature and duration in previous investigations. A further variable thickness layer of indium tin oxide is then deposited, over the range 20 - 100nm in steps of 20nm, followed by a 100nm Ag reflector. A diagram of the device topography is shown in figure 6.32

The detailed process flow for device fabrication is as follows:

1. Acetone and IPA cleaning of glass substrate.
2. Deposition of 375nm of intrinsic amorphous silicon using PECVD.
3. Deposition of 100nm of indium tin oxide using e-beam assisted evaporation.
4. Deposition of 10nm of Ag using e-beam assisted evaporation.
5. Thermal annealing of the structure at $350°C$.
6. Deposition of 20 - 100nm variable thickness ITO using e-beam assisted evaporation.
7. Deposition of 100nm of Ag for back reflector using e-beam assisted evaporation.

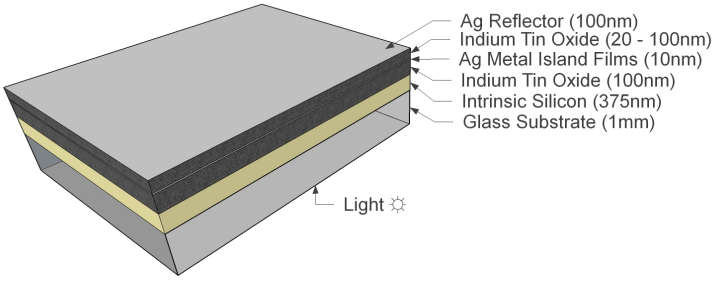

Figure 6.32: Topography of variable ITO investigation

6.3.5.2 Optical Measurements

The optical reflectance of the samples has been measured using the integrating sphere, performed over the wavelength range of 400 - 1000nm. The optical reflectance provides an indication of the amount of light which is not absorbed within the first (incident) and second (reflected) pass through the device, and therefore lower values of optical reflectance correspond to a higher optical absorption and a higher potential charge-carrier generation or parasitic absorption. A subset of these measurements are detailed in figures 6.33 and 6.34; showing absorption spectra for the ITO thicknesses of 20, 40, 60 and 80nm respectively.

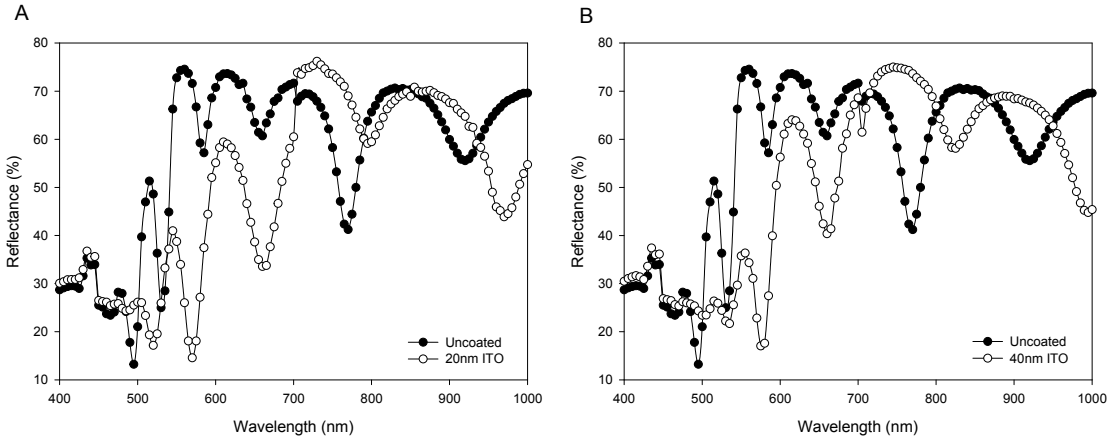

Figure 6.33: Optical reflectance of 20nm (a) and 40nm (b) ITO Thickness

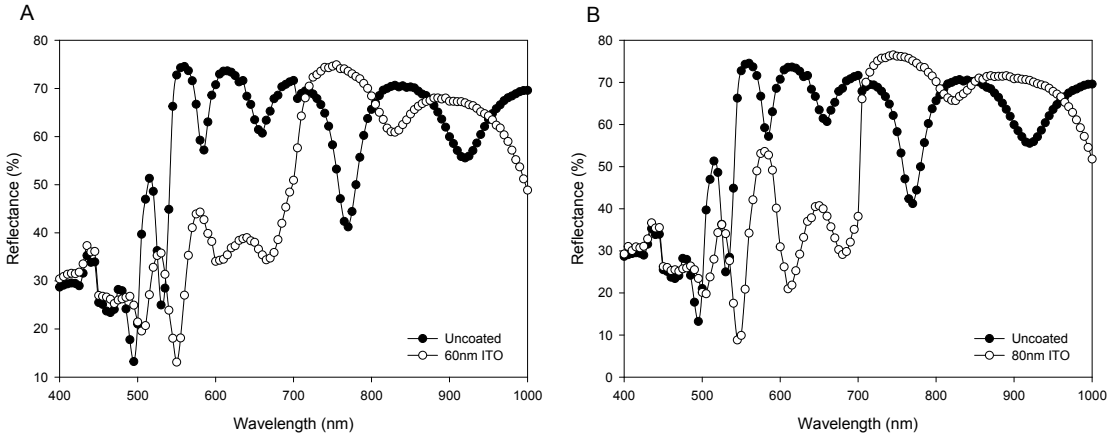

Figure 6.34: Optical reflectance of 60nm (a) and 80nm (b) ITO Thickness

6.3.5.3 Analysis

The complete set of sample results are illustrated in figure 6.35, detailing the average reflectance values for each. It can clearly be observed that all samples provide a reduction in the optical reflectance from the device compared to the uncoated sample, however it must be remembered that the increased thickness of the TCO material additionally provides parasitic absorption and therefore an apparent reduction in reflectance.

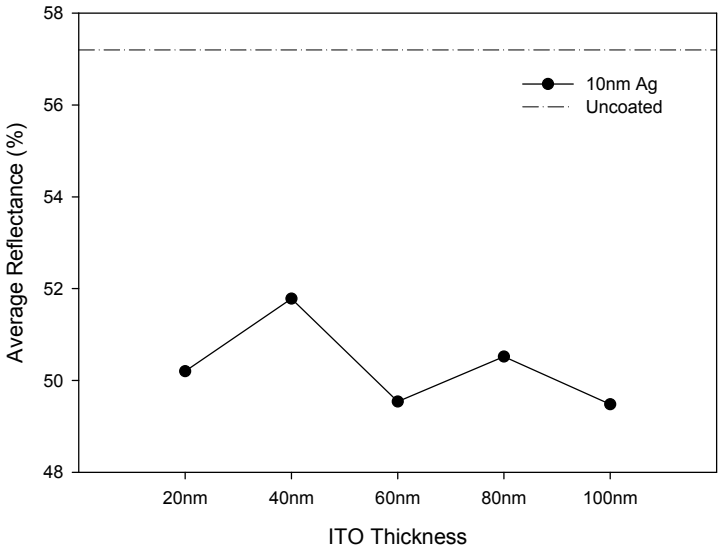

Figure 6.35: Variable TCO thickness average reflectance

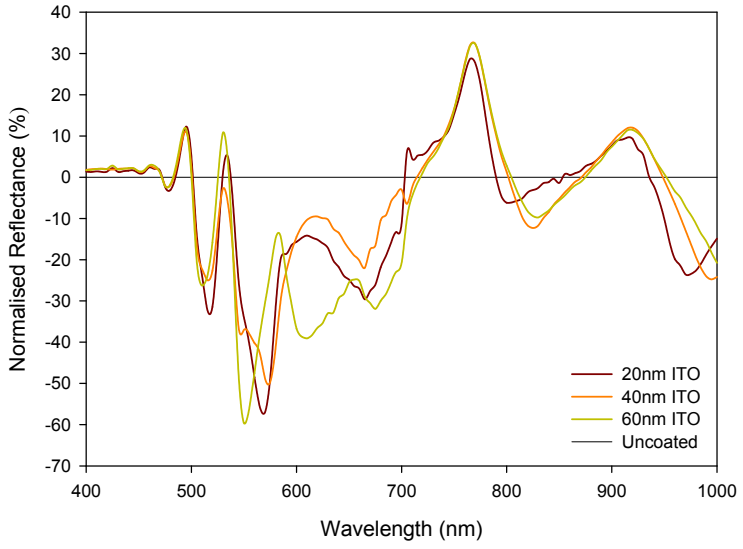

Figure 6.36: Variable TCO thickness normalised reflectance

The extent to which the samples influence the optical reflectance is illustrated in figure 6.36, showing a reduction in reflectance at shorter wavelengths at the expense of an increase centred around 800nm, compared to uncoated samples vs wavelength. It can be observed from figure 6.35 that the thinnest TCO layer of 20nm provides a reduced average reflectance value, compared to those seen at 40nm. The average reflectance is then reduced again at 60nm and 100nm thickness, which indicates that a TCO layer in thickness multiples of 20nm between the Ag reflector and nano-particle array appear to provide the optimum reflectance reduction whilst minimising parasitic absorption. The full variable-ITO back-reflector temperature investigation deposition conditions, together with results for average optical reflectance are detailed in table 6.5:

Sample ID	**ITO Thickness (nm)**	**Average Reflectance (%)**
A	20	57.2
B	40	50.2
C	60	51.8
D	80	50.5
E	100	49.5
Uncoated	0	57.21

Table 6.5: ITO thickness variation parameters

6.4 Photovoltaic Devices with Nano-particle Arrays

Based on the best performing self-organised nano-particle arrays measured in the previous section, a full photovoltaic device is fabricated in order to determine the performance enhancement which can be sought by using such particle arrays within the devices. The photovoltaic devices will be based upon the amorphous silicon P-I-N cells fabricated within section 4.3.3, with the exception of the substrate which will be Pilkington TEC-15. This is in order to eliminate the performance increase introduced by the haze of TEC-8 substrates, so that the sole effects of the nano-particle array and its interaction with light can be observed. Due to this, a resultant decrease in base-line energy conversion efficiency will be observed as is the case in section 4.3.3.8. The light trapping schemes explored in section 6.3 are applied to the P-I-N devices in this section.

In order to fabricate a functional photovoltaic silicon P-I-N device, the maximum temperature is required to be restricted. The amorphous silicon cannot endure temperatures in excess of $300°C$ without a loss of the bonded hydrogen and creation of dangling bonds within the film. Additionally, at temperatures in excess of $400°C$, the amorphous silicon begins to re-crystallise and form a nano-crystalline layer which is not desirable in this device. For this reason the investigations within this chapter have not exceeded $400°C$, whilst in previous experiments, degraded electrical performance is of no concern. In this investigation, the anneal temperatures are kept at $250°C$, a compromise between scattering enhancement and temperature effects on device performance and is the temperature at which the silicon deposition is performed.

6.4.1 Amorphous Silicon P-I-N Devices with optimised Nano-Particles

A device is fabricated with nano-particle arrays within the back reflector ITO region, in accordance with the highest performance simulated and practical measured devices in section 4.3.3. A further device is fabricated as a baseline measurement with identical deposition steps, without the nano-particle array deposition. The use of a back reflector of 500nm thickness is due to its secondary use as the rear contact of the device, and it therefore must be mechanically durable. A diagram of the device structure is shown in figure 6.37. The detailed process flow for device fabrication is as follows:

1. Acetone and IPA cleaning of TEC-15 substrate.
2. Deposition of amorphous silicon P-I-N structure using PECVD.
3. Evaporation of 100nm indium tin oxide through 9-port mask stencil.
4. Evaporation of 15nm silver through 9-port mask stencil.
5. Anneal of device at $250°C$ for 60 minutes.
6. Evaporation of 100nm indium tin oxide through 9-port mask stencil.
7. Evaporation of 500nm of aluminium for back reflector formation.

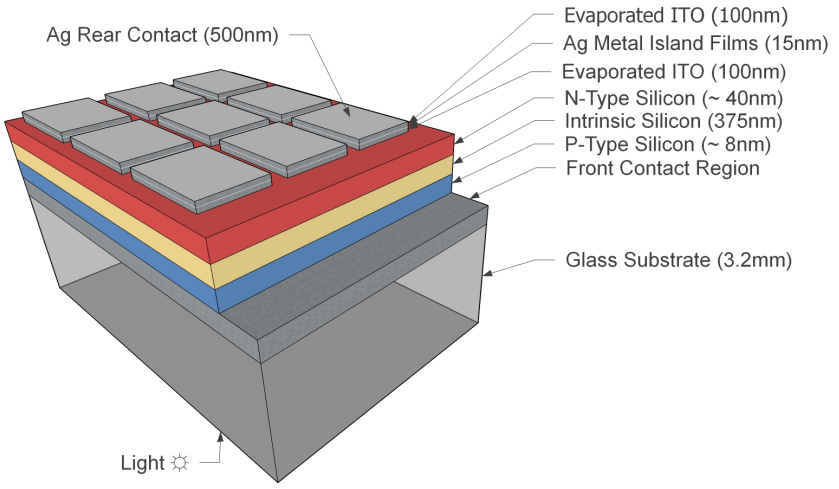

Figure 6.37: Topography of P-I-N device with nano-particles

Measured performance values for devices with and without nano-particle treatments are presented in table 6.6. It can be observed that the maximum performance P-I-N device region featuring the nano-particle array within the back reflector region exhibit a slightly higher value of short-circuit current and maximum-power point current, at the expense of slightly reduced open-circuit voltage and maximum-power point. This may be due to the slight increase in charge-carrier generation due to enhancement of long-wavelength scattering, while the addition of the silver region in the ITO layer and associated discontinuity within the film are feasible causes of the slight reduction in open-circuit and maximum power point voltage. A number of device regions in this investigation were recorded as *shunted* and therefore a full statistical analysis of device performance cannot be performed. Overall efficiency values show an enhancement within the range 1% and so it is not possible to distinguish any performance improvement from this value alone. Cell efficiency repeatability varies by a greater extent than this value, as discussed in section 4.3.1.7, and so improvements of this magnitude cannot be directly attributed to the nano-particle array enhancements.

Variable		**Uncoated**	**Ag Array**
Efficiency	(%)	4.75	4.66
Fill Factor		0.58	0.56
V_{oc}	(V)	0.80	0.80
J_{sc}	(mA/cm^2)	10.11	10.28
V_m	(V)	0.60	0.58
I_m	(mA)	7.91	8.04

Table 6.6: P-I-N device with nano-particle array parameters

The I-V and Q-E curves of the devices with and without nano-particle enhanced back reflectors are presented in figures 6.38 and 6.39:

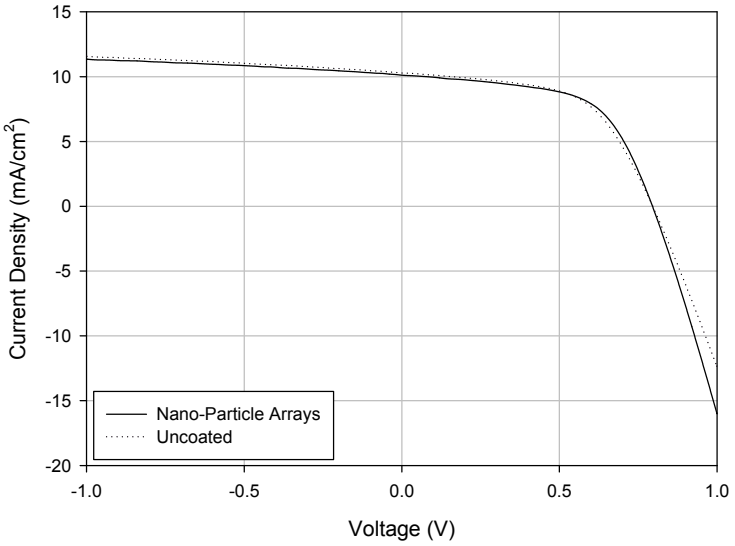

Figure 6.38: I-V curve of P-I-N devices

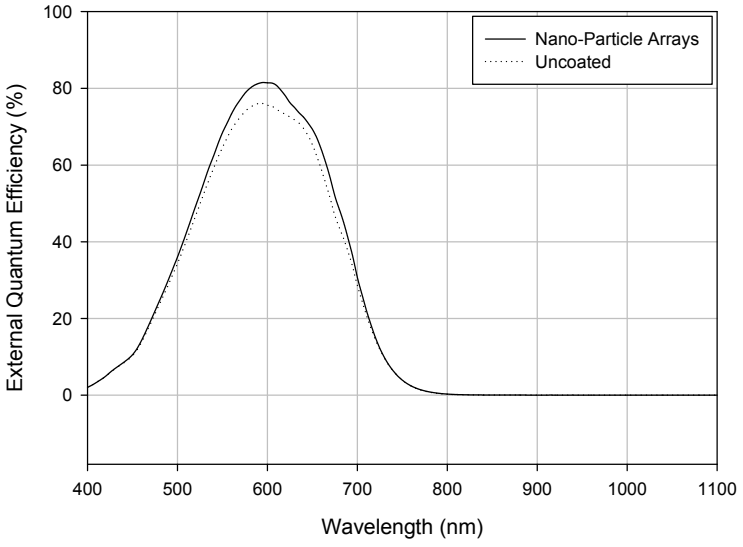

Figure 6.39: Quantum efficiency curve of P-I-N device

It can be observed from the external quantum efficiency response that the device featuring nano-particle arrays exhibits a slight increase in quantum efficiency within the range 500 - 700nm. It can therefore be deduced that the performance improvement is not localised to a particular wavelength region as is characteristic of uniform nano-particle arrays, and a broadband enhancement is produced. This type of response is characteristic of the random nature of the metal-island film based particle arrays, as is discussed in the literature in section 2.4.3.

6.5 Conclusion

In investigation 6.3.1 it was ascertained that the incorporation of an array of silver nano-particles on a transparent glass substrate interacts with incident light, and this interaction response changes depending on the temperature at which the thin-film layers are annealed. Investigations on substrates with a 375nm amorphous silicon layer in section 6.3.2 allow the absorption within the optical stack to be calculated, and have shown that $400°C$ provides the optimum anneal temperature for the formation of nano-particles with the maximum absorption characteristics. the evolution of the metal-island film formation is observed and it is determined that 60 minutes is the optimal duration of anneal for most configurations. SEM micro-graphs are taken showing a highly disordered film characteristic of broadband interactions with incident light. Investigations with thinner films of Ag at 10nm are explored in section 6.3.3, which have shown that after annealing at various temperatures these films produce a very similar result, with a slightly reduced value of optical absorption.

Samples featuring nano-particle arrays at the rear of the absorber layer in a superstrate configuration, near to an Ag reflector detailed in section 6.3.4, show similar characteristic trends with 15nm layers annealed for 60 minutes at $400°C$ providing a sharp increase in optical absorption performance. This superstrate configuration additionally mitigates the problem of parasitic absorption within the window layers on first pass of incident light, and therefore can potentially provide increased performance at the expense of slightly increased fabrication complexity. Investigations in to the optimum separation between the nano-particle array and the Ag back reflector detailed in section 6.3.5, which determine that a thin ITO layer of less than 20nm or ITO thicknesses in multiples of 20nm provide a good enhancement, whilst a general trend is observed that increased ITO thickness results in a reduction in reflectance, likely due to increased parasitic absorption within the material.

Section 6.4 details the incorporation of metal nano-particle arrays within the rear TCO material of an amorphous silicon P-I-N device, which is shown to potentially lead to an increased photon absorption and hence enhancement to the light-generated current. It is noted, however, that the resultant increase is slight, and variance between fabricated devices in section 6.3.3 far exceeds that of the enhancement measured with nano-particles present. It is therefore not possible to state the increased absorption is exclusively due to the presence of such particles. Further optimisations to the device fabrication methods to decrease such variance is required in addition to a statistical comparison of measurements from a more extensive results set. It is also noted from the results in section 6.4.1 that a greater increase in performance is illustrated from the QE measurement compared to the I-V results, this is thought to be a consequence of the light-soaking effects inherent with measurements under AM1.5 conditions.

Chapter 7

Discussion and Conclusion

The need for improvements to inexpensive, flexible thin-film solar cells such as those featuring amorphous silicon has been introduced within this thesis. The economic, packaging and supply-chain issues concerned with crystalline silicon as a photovoltaic material have been discussed, and the various potential routes to efficiency enhancement are reviewed. Maximum energy conversion efficiency at the lowest cost is desirable and the use of light-scattering technologies as a potential enhancement has been highlighted. It is concluded that the majority of research into light scattering nano-particle arrays is focussed on the enhancement of crystalline silicon device structures, and that their application to thin-film amorphous silicon devices is relatively unexplored. Furthermore, the optimum conditions for deposition of device quality amorphous silicon material, particularly the effects of the ambiguous use of argon as a dilute gas are not explicitly known. Efficient enhancement to amorphous silicon photovoltaic devices, using nano-particle arrays tuned in resonant frequency to the absorption characteristics of the material are suggested as a cost-effective solution. The purpose of this research project is to explore the enhancement to amorphous silicon photovoltaic devices through the method of process deposition condition optimisation, and optical light scattering techniques.

Within this investigation, the tools and techniques required for the fabrication and characterisation of thin-film photovoltaic materials are reviewed in detail, including the available deposition techniques, formation of contacting methods and transparent conducting oxides, formation of self-organised particle arrays using rapid thermal annealing, and the potential to use optical and / or electron beam lithography. The characterisation methods are described in detail, including optical means such as spectroscopic ellipsometry and Raman spectroscopy. The electrical measurements including current-voltage analysis and charge conductivity are described, including a devised routine of measuring the energy-conversion efficiency and photo-activity of the thin films and the corresponding contacting requirements. Quantum efficiency and transmittance, reflectance and absorption measurements are introduced, all of which are extensively used throughout later chapters of this study. The simulation methods are described at the end of this section, detailing the Finite Difference Time Domain method used.

A study of the process parameter space is performed in chapter 4 to fabricate firstly intrinsic amorphous silicon thin films, followed by doped silicon regions and finally a complete P-I-N photovoltaic device. Intrinsic amorphous silicon thin films are deposited on glass substrates with variations to the deposition parameters including RF power, chamber pressure, gas flow rates and dilution ratio of process gases. The films are measured for electrical performance, uniformity, crystallinity and optical absorption characteristics resulting in an optimised device with very high photo-activity. Doped regions of silicon thin film material are independently analysed and scrutinised with the same measurements, in addition to secondary ion mass spectroscopy which helps to determine the optimal doping levels in addition to electrical characterisation. the optimisation of P-I-N photovoltaic devices is then undertaken, deposited on Pilkington TEC-8 textured substrate materials and the device layer thickness parameter space is explored. A device with an energy conversion efficiency of 6.5% is achieved, which compares favourably with those referenced in literature as discussed. It is noted that further optimisation may achieve even higher efficiency values using statistical analysis techniques and numerical device simulation. The photovoltaic device structure reported in this section is later used as a test structure to observe the effects of the placement of self-organised Ag nano-particle array layers within the back reflector region.

Extensive simulation of the effects of nano-particle array structures have been demonstrated in chapter 5 using the Lumerical FDTD Solutions, with optical topography varied in parameters controllable during the deposition process. These parameters, initially taken from literature described within the relevant section, encompass positioning of the particles at the front and rear; particle shape variations from discs to spheres; thickness variations of the ITO region; back reflector material variations from aluminium to silver; and full optimisation of particle shape, height and position within the structure. Simulations of optical transmittance and reflectance are performed, followed by simulation of optical power absorption within the amorphous silicon region with device geometries in accordance with practical devices. Each simulation is compared to a planar structure featuring no such particle enhancements. This has determined the optimum structure topography for light scattering enhancement, and and simulations of the dielectric environment have been performed to ensure optimum reductions in surface reflection. It is concluded that the metallic nano-particle approach can be used to enhance the optical path length of the incident light, when positioned within the back reflector of an amorphous silicon photovoltaic device, with a modest gain reported.

The metal-island film technique is explored in detail in chapter 6, with the evaporation and subsequent annealing of thin metallic films to form self-organised nano-particle arrays. Initially performed on glass substrate and amorphous silicon films, followed by a complete optical stack with particle arrays positioned both on the surface of and encapsulated within a region of transparent conducting oxide. An optimum value of anneal temperature and duration is discovered which results in the maximum optical absorption within the layer. Optical measurements are performed detailing the transmittance

and reflectance of such devices, highlighting the fabrication conditions which result in the optimal enhancement to the absorption characteristic. A strong decrease in optical reflectance and corresponding reduction in transmittance is observed in many cases, and the calculated average absorption suggests that the optical stack absorbs a greater amount of incident light with nano-particle arrays present. It is, however, not possible to determine of this absorption contributes to charge carrier collection or is attributed to parasitic absorption within the metallic layer or the effects of the interfaces.

A full P-I-N structure is fabricated with the optimum metal-island film structures applied, and electrical measurements are undertaken. A slight performance improvement is observed, however it cannot be stated that the nano-particle arrays are solely responsible for this characteristic. From these measurements it can be stated that the use of textured substrates improve performance to a greater extent despite an observed reduction in open-circuit voltage due to the surface roughness of such substrates. It is proposed that many such samples are performed together with baseline measurements in order to obtain a statistical average, to ascertain if a repeatable improvement is observed. Metal-island film based devices produce a broad range of particle sizes and dimensions and therefore it is not feasible to draw a parallel between these self-organised devices and periodic arrays of spherical nano-particles simulated in chapter 5. Furthermore, it is not possible to directly compare fabrication conditions such as anneal temperature and duration with simulated results such as particle size and diameter. Additionally, simulated results are presented in units of integrated reflectance as opposed to the measured reflectance from fabricated devices. However, it is possible to observe a characteristic trend that simulations in chapter 5 suggest that an approximate 1% improvement in is possible due to the incorporation of optimised nano-particle arrays, and section 6.4, neglecting potential error, illustrates a performance improvement of approximately 1% compared to uncoated devices with no optical light-scattering treatment.

To conclude this study, it can be stated that the optimisation of the amorphous silicon process was successful, yielding a device structure which shows good electrical performance. The optimised thin films are successfully deployed as a test structure for the light-scattering treatments described in this study. Simulation has shown that improvements to device performance are possible using this method, while further optimisation of the device structures are possible using alternative methods to realise the complex light scattering solution. Further optimisation of such structures are challenging but can be accomplished using more sophisticated optical modelling with higher computational resources, which may yield further improvements. Although potential performance gains reported in this work are modest, these gains can lead to photovoltaic structures with greater power output for a given area, thinner, less wasteful device structures and increased acceptance of amorphous silicon as a thin-film material in the current challenging photovoltaic market.

7.1 Future Work

Based on the investigations undertaken within this thesis, a number of opportunities arise to further investigate the effects of nano-particle arrays in various ways. The following suggestions are proposed:

- Fabrication of a range of silicon P-I-N devices with and without nano-particle array structures, to form a statistical average and determine if a performance improvement is possible in this device.
- The electrical measurement of the enhancement of light absorption due to the presence of metal-island film treatments, by the measurement of the increase in dark / photo conductivity ratio.
- The definition of periodic nano-particle arrays using electron-beam lithography, in order to precisely tune the enhancement wavelength of the particle arrays and fabricate devices simulated in chapter 5.

7.1.1 Electrical Measurements

The reflection measurements in section 6.3 allow us to determine how much incident light is absorbed by the thin film device, and how much is reflected. It does not, however, tell us if any reduction in reflection is in fact contributing to optical charge carrier generation or attributed to parasitic absorption within one of the layers. A more detailed method of measuring this is to observe the change in photo/dark conductivity ratio for a selection of samples featuring the nano-particle array, as opposed to those that do not.

In order to measure the silicon thin films electrically, it is necessary to modify the fabrication process. Due to the essential aluminium contacting to the silicon surface required take the measurement, several modifications must be considered. The deposition of the silver array and associated ITO materials must be done in a thin strip of 2mm width, in order for the Al contacts to be deposited directly on the adjacent silicon material without providing a surface conductive path. A buffer layer of silicon dioxide is also deposited initially on the silicon to mitigate the conduction path created by the ITO material. The device is organised in a substrate configuration and the incident light is directed through the ITO / Ag stack and then into the silicon layer.

The detailed process flow for device fabrication is as follows:

1. Acetone and IPA cleaning of glass substrate.
2. Deposition of 375nm of intrinsic amorphous silicon using PECVD.
3. Masking of all areas except a 2mm central strip using cleaned glass substrates.
4. Deposition of 100nm of silicon dioxide using PECVD on to masked region.
5. Deposition of 100nm of indium-doped tin oxide using e-beam assisted evaporation.
6. Deposition of 5, 10 or 15nm of silver using e-beam assisted evaporation.
7. Thermal annealing of the device over a range of temperatures and durations to form the self-organised metal islands.
8. Deposition of variable thickness ITO using e-beam assisted evaporation.
9. Removal of mask and evaporation of Al contacts using e-beam assisted evaporation.

A diagram of the device topography is shown in figure 7.1:

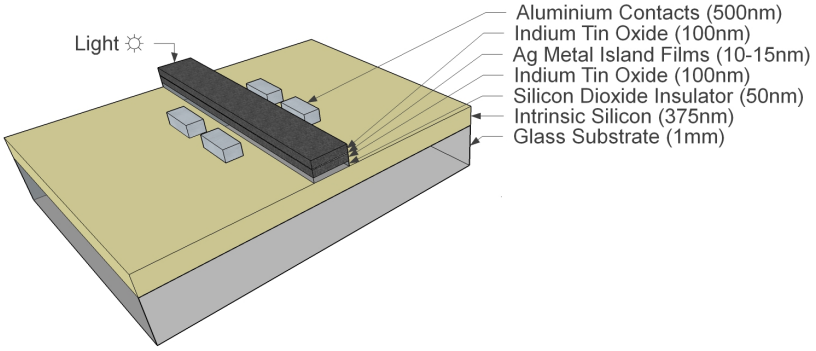

Figure 7.1: Topography of electrical measurement fabrication method

7.1.2 E-Beam Defined Periodic Nano-particle Arrays

In order to increase the performance, repeatability and to remove the constraints of temperature, the fabrication of a set of periodic spherical particles defined using electron-beam lithography is to be undertaken. Particle arrays defined by e-beam lithography can be optimised to a much greater extent, with variations in size, shape, pitch and periodicity controllable on the nanometre scale. Therefore, arrays such as this can potentially provide a light scattering effect significantly greater than that of the self-organised design and therefore an enhancement in optical absorption.

7.1.2.1 Experimental Detail

Preliminary work on this has been carried out, focused on the designing and testing of nano-particle arrays using the CAD software package Tanner L-Edit. This software allows the graphical design and layout of the desired devices in any shape or configuration within the limitation of the beam size and shot pitch. The initial layout design is depicted in figure 7.8, and consist of 200nm spherical patterns separated by a 400nm pitch centre-to-centre. In order to define the periodic array using the e-beam system, it is necessary to first perform a *dose test* to determine the optimum e-beam settings for the desired patterns. The patterns are then observed under a scanning electron microscope to determine which regions have been ideally exposed and the e-beam settings recorded. The initial patterns are therefore several regions of 500 x 500 μm patterns, each with a variation of the e-beam settings.

The silicon substrate material, of dimensions 4 x 3cm is prepared by the e-beam assisted evaporation of 200nm Ag as the back reflector followed by 70nm of indium-doped tin oxide material. This is followed by the spin-coating of MMA and PMMA photo-resist to enable the pattern definition by e-beam. The patterns are subsequently defined on the silicon substrate using the JEOL e-beam system, and developed using MIBK:IPA solution. The evaporation of the Ag layer for the definition of the spheres is then performed, followed by the lift-off processing in an acetone solution. The full process flow is detailed in section 7.2.3.2.

Pattern Design

A single circular shape is defined within the software, which itself is a grouped collection of objects including a large square and six polygons to approximate a circular shape. The resultant shape subsequently appears as a solid circle due to the resolution of the e-beam technique. In order to attempt to reduce the duration of the e-beam session, an octagonal pattern shape is attempted which requires significantly less beam time. This will be included in the dose test investigations in section 7.2.3.2.

Within the software the single circular or octagonal shape is defined as a cell, which forms an instance of an array within the top-level cell of the required size. This allows numerous instances of an identical cell to be arrayed, and any changes to the size, shape or spacing to the cell are reflected immediately within the array. Detailed in figure 7.8 is the defined circular patterns within the L-Edit software, in which can be seen the approximated circle shapes of 200nm diameter, spaced 200nm apart. These parameters are selected initially based on previous work by D. Payne [87], with the view towards further optimisation to suit the hereto-jucntion application.

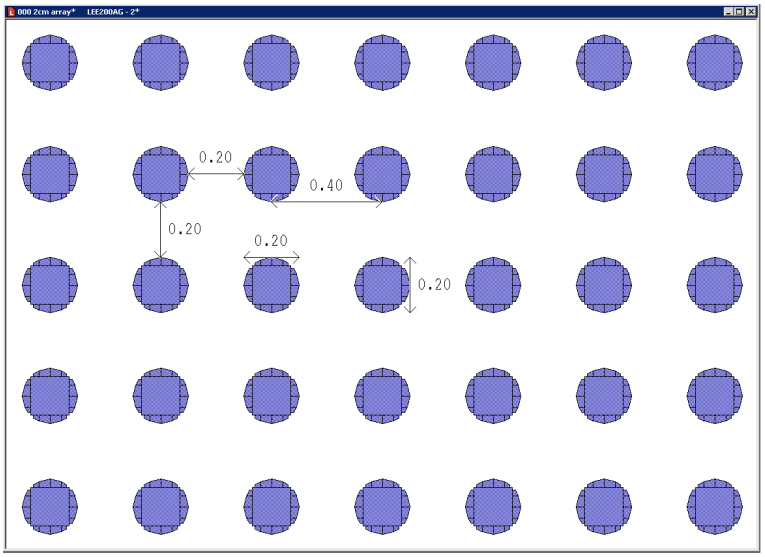

Figure 7.2: Nano-particle designs defined in L-Edit software package (measurements are in are in μm)

7.1.2.2 Nano-Particle Arrays on Si Substrates

In order to ascertain the required particle size and e-beam power to define a true 200nm particle size on the substrate, a variety of *doses* and object sizes must be attempted and examined.

The detailed process flow for device fabrication is as follows:

1. RCA cleaning of silicon wafer substrate
2. HF etch of native oxide
3. Evaporation of 200nm Ag for back reflector formation
4. Evaporation of 70nm indium-doped tin oxide
5. Spin-coating of MMA e-beam photo-resist
6. Bake photo-resist at $150°C$ for 70s
7. Spin-coating of PMMA e-beam photo-resist
8. Bake photo-resist at $180°C$ for 70s
9. Expose substrate in e-beam lithography system to define pattern
10. Develop sample in MIBK:IPA solution for 70s
11. Clean sample in IPA for 30s
12. Evaporation of 50nm Ag for back nano-particle formation
13. Immerse sample in acetone for Ag lift-off for 4 hours
14. Remove excess Ag film and clean sample using IPA
15. Dry sample using N_2 blow.

Dose Test

The initial dose test will consist of three regions of 24 samples, $500\mu m$ x $500\mu m$ in size. The particle diameter, shape and power level are varied for each, and the results observed under SEM are split in to three categories as per table 7.5:

Region	**Power Level** ($\mu C/cm^2$)	**200nm Circles**	**308nm Circles**	**200nm Octagons**
1	800	Not Visible	Not Visible	Not Visible
2	850	Not Visible	Not Visible	Not Visible
3	900	Not Visible	Not Visible	Not Visible
4	950	Not Visible	Not Visible	Not Visible
5	1000	Not Visible	Not Visible	Not Visible
6	1050	Not Visible	Not Visible	Not Visible
7	1100	Not Visible	Not Visible	Not Visible
8	1150	Not Visible	Not Visible	Not Visible
9	1200	Not Visible	Not Visible	Not Visible
10	1250	Not Visible	Not Visible	Not Visible
11	1300	Not Circular	Not Circular	Not Circular
12	1350	Not Circular	Not Circular	Not Circular
13	1400	Not Circular	Not Circular	Not Circular
14	1450	Not Circular	Not Circular	Not Circular
15	1500	Not Circular	Not Circular	Not Circular
16	1550	Not Circular	Not Circular	Not Circular
17	1600	Ideal	Ideal	Ideal
18	1650	Ideal	Ideal	Ideal
19	1700	Ideal	Ideal	Ideal
20	1750	Overexposed	Overexposed	Overexposed
21	1800	Overexposed	Overexposed	Overexposed
22	1850	Overexposed	Overexposed	Overexposed
23	1900	Overexposed	Overexposed	Overexposed
24	1950	Overexposed	Overexposed	Overexposed

Table 7.1: Dose test conditions

A diagram of the device topography is shown in figure 7.9:

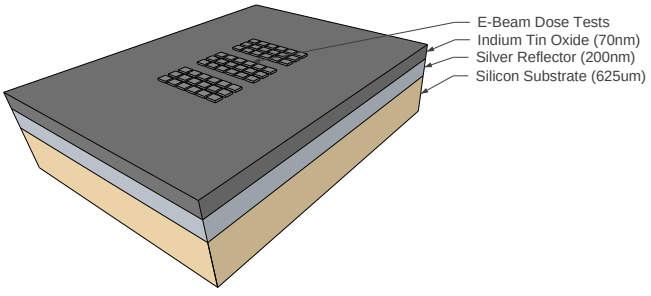

Figure 7.3: Topography of the e-beam dose test sample

Scanning-Electron Microscopy Measurements

A selection of the SEM images taken from the dose test samples are presented in figures 7.10 and 7.11:

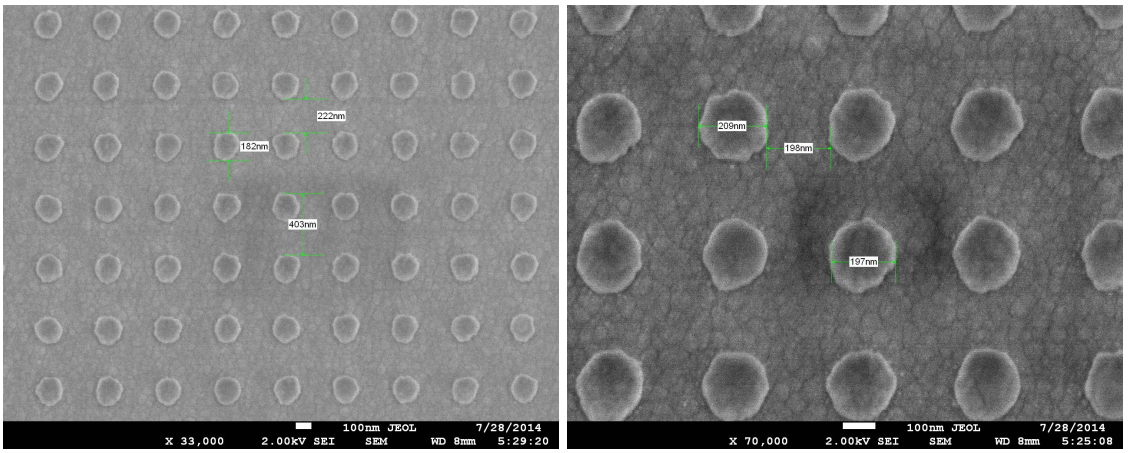

Figure 7.4: 200nm Circle patterns at 850uC and 1050uC

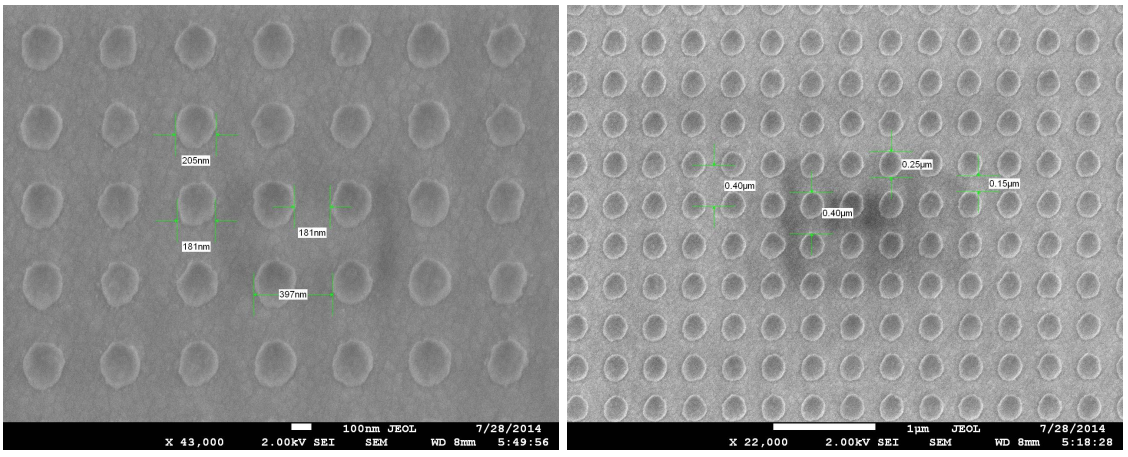

Figure 7.5: 200nm Circle patterns at 1200uC and 1450uC

As can be observed, the images of the 850μC 200nm circular patterns are under-exposed, with an approximate diameter of 180nm and spacing of 220nm. Additionally, the shapes do not appear ideally spherical, and therefore 850μC is deemed an insufficient power level. The images of the 1050μC 200nm circular patterns show a much improved shape and more accurate dimensions with reference to the defined 200nm shapes.

The images acquired from the 1200μC 200nm samples once again show a preferential circle diameter of 200nm and ideal pitch spacing of 400nm, while the images at 1450μC show enlarged defined shapes with an approximate dimension of 250nm and a spacing of 150nm. Based on the complete set of acquired images detailed in table 7.5, it can be deemed that a power level within the range of 1000 - 1200μC is preferred for optimum structure formation.

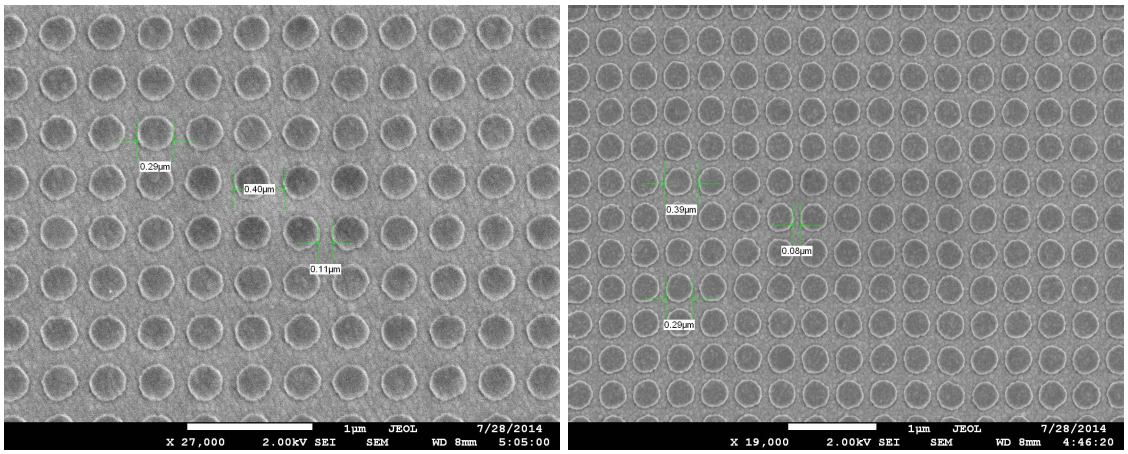

Figure 7.6: 308nm Circle patterns at 800uC and 1150uC

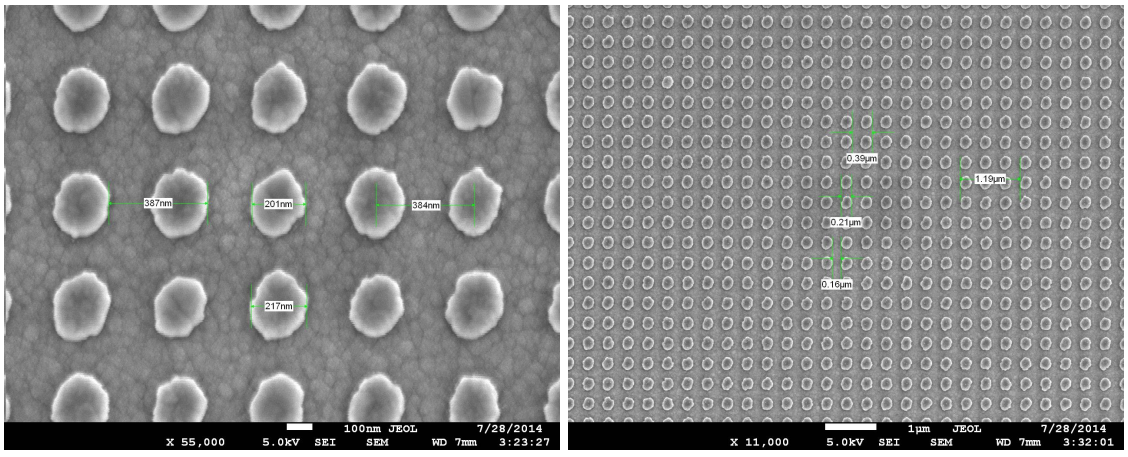

Figure 7.7: 200nm Octagonal patterns at 1500uC

The 308nm circular pattern set exhibits larger realised shapes as expected, much closer to the desired pattern sizes at lower power levels. The images of the $800\mu C$ 308nm circular patterns appear to be around 300nm in diameter with 110nm spacing, whilst at $1150\mu C$ only a slight increase is observed. The use of oversized patterns for the use of lower power levels is therefore not effective to obtain a particle diameter of 200nm.

The 200nm octagonal data set exhibits ideally sized 200nm particles at the power level of $1500\mu C$, with a pitch of approximately 400nm. The shape of the particles is an approximated circle, which is ideally suited for the light scattering application. The use of octagonal defined patterns is therefore effective at reducing the e-beam exposure time whilst retaining an acceptable particle topography. The darker regions in the images are due to charge accumulation within the TCO material during observation, a consequence of the SEM imaging process.

Figure 7.8: 3 x 24 Region dose test patterns on silicon substrate

Figure 7.9: 1x1cm Defined 200nm octagonal pattern on silicon substrate

As can be observed from the photographs in figures 7.14 and 7.15 of the deposited particle arrays, the dose test regions can be clearly observed in various levels of exposure. The particle arrays nearest the top of the image are those exposed at the higher power levels. While electron-beam lithography is prohibitively expensive for scaling to large-volume application, optimisation can be performed using this method and subsequent volume production can be achieved using techniques such as nano-imprint lithography to provide the pattern designs.

Chapter 8

Appendix I

8.1 Photovoltaic Device Development Activity

Sample ID	**Efficiency** *(%)*	**Voc** *(v)*	**FF**	**Jsc** *(mA/cm^2)*	**RF Power** *(W)*	**Temp** *($^\circ C$)*	**Pressure** *(mTorr)*	**SiH4** *(sccm)*	**H2** *(sccm)*	**B2H6 in P** *(sccm)*	**PH3 in N** *(sccm)*	*P (nm)*	**Thickness** *I (nm)*	*N (nm)*
10/01/12-B	2.45	0.81	6.75	0.44	10	205	350	50	50	10	6	11	624	35
19/01/12-B	1.60	0.77	4.64	0.44	10	300	300	50	50	10	6	11	400	35
06/02/12-B	0.94	0.71	3.23	0.40	10	300	350	50	50	10	6	6	312	12
09/02/12-B	1.66	0.79	3.94	0.53	10	275	350	50	50	10	6	10	676	48
13/02/12-C	4.27	0.73	12.28	0.47	10	200	350	50	50	10	6	8	423	50
14/02/12-C	5.05	0.69	13.01	0.55	10	200	350	50	50	10	6	9	423	50
15/02/12-B	5.57	0.69	13.90	0.57	10	200	350	50	50	10	6	10	423	50
16/02/12-B	5.62	0.69	13.32	0.61	10	200	350	50	50	10	6	8	433	50
17/02/12-C	5.48	0.69	13.64	0.57	10	200	350	50	50	10	6	8	436	40
20/02/12-C	6.52	0.78	13.23	0.63	10	250	350	50	50	10	6	8	433	40
02/03/12-C	5.90	0.75	13.70	0.56	10	250	350	50	50	10	6	8	433	40
06/03/12-C	5.40	0.68	12.92	0.61	10	250	350	50	50	10	6	9	433	40
12/03/12-D	4.50	0.77	11.40	0.50	10	250	350	50	50	10	6	8	433	40
13/03/12-C	3.90	0.77	10.90	0.46	10	250	350	50	50	10	6	8	433	40
14/03/12-A	2.50	0.81	7.08	0.43	10	250	350	50	50	10	6	8	433	40
15/03/12-B	3.16	0.81	8.15	0.47	10	250	350	50	50	10	6	8	433	40
20/03/12-C	3.38	0.79	8.00	0.54	10	250	350	50	50	10	6	8	433	40
21/03/12-C	3.26	0.77	9.35	0.44	10	250	350	50	50	10	6	8	433	40
29/03/12-C	1.20	0.79	3.82	0.39	10	250	350	50	50	10	6	8	433	40
30/03/12-B	1.01	0.77	2.92	0.44	10	250	350	50	50	10	6	8	433	40
02/06/12-A	1.40	0.72	5.19	0.37	10	250	350	50	50	10	6	8	433	40
02/06/12-B	1.23	0.76	3.69	0.43	10	250	350	50	50	10	6	6	374	19
11/06/12-B	2.03	0.81	5.34	0.46	10	250	350	50	50	10	6	8	433	40
28/06/12-A	1.60	0.77	4.87	0.42	10	250	350	50	50	10	6	6	374	19
28/06/12-B	0.55	0.73	1.77	0.42	10	250	350	50	50	10	6	6	374	19
28/06/12-C	1.96	0.83	5.40	0.43	10	250	350	50	50	10	6	6	374	19
04/07/12-A	1.22	0.70	4.54	0.38	50	250	350	200	50	10	6	4	56	40
04/07/12-B	0.21	0.78	0.73	0.36	50	250	800	200	50	10	6	4	40	40
04/07/12-C	0.27	0.74	0.90	0.40	35	250	575	150	50	10	6	4	55	40
04/07/12-D	0.25	0.79	0.80	0.39	35	250	575	150	50	10	6	4	55	40
04/07/12-E	0.38	0.75	1.30	0.38	35	250	575	200	50	10	6	4	40	40
13/07/12-A	1.00	0.79	3.49	0.35	10	250	350	50	50	10	6	6	437	39
13/07/12-B	0.80	0.79	2.51	0.39	10	250	350	50	50	10	6	6	437	39
13/07/12-C	0.78	0.79	2.44	0.40	10	250	350	50	50	10	6	7	437	39
13/07/12-D	0.63	0.75	2.01	0.41	10	250	350	50	50	10	6	8	437	39

Table 8.1: P-I-N devices development

Sample ID	**Efficiency** *(%)*	**Voc** *(v)*	**FF**	**Jsc** *(mA/cm^2)*	**RF Power** *(W)*	**Temp** *($^\circ C$)*	**Pressure** *(mTorr)*	**SiH4** *(sccm)*	**H2** *(sccm)*	**B2H6 in P** *(sccm)*	**PH3 in N** *(sccm)*		**Thickness** *I (nm)*	*N (nm)*
												P (nm)		
16/07/12-A	0.23	0.66	1.28	0.28	10	250	350	50	50	10	6	3	437	39
16/07/12-B	0.58	0.78	1.96	0.38	10	250	350	50	50	10	6	3	437	39
16/07/12-C	0.56	0.78	1.91	0.37	10	250	350	50	50	10	6	4	437	39
16/07/12-D	0.68	0.76	2.38	0.37	10	250	350	50	50	10	6	4	374	39
24/07/12-A	0.99	0.80	2.85	0.43	10	250	350	5	5	10	50	4	374	34
24/07/12-B	0.71	0.78	2.30	0.39	10	250	350	5	5	10	50	4	374	34
24/07/12-C	0.74	0.78	2.21	0.40	10	250	350	5	5	10	50	4	374	34
24/07/12-D	0.66	0.78	2.17	0.39	10	250	350	5	5	10	50	4	374	34
17/09/12-A	1.00	0.78	2.99	0.42	10	250	350	50	50	10	6	5	374	31
17/09/12-B	1.55	0.78	4.42	0.45	10	250	350	50	50	10	6	5	374	31
17/09/12-C	1.42	0.78	4.00	0.40	10	250	350	50	50	10	6	5	343	31
18/09/12-A	1.68	0.78	4.66	0.46	10	250	350	50	50	10	6	4	374	19
18/09/12-B	1.78	0.78	4.91	0.46	10	250	350	50	50	10	6	4	374	19
18/09/12-C	1.65	0.78	4.54	0.46	10	250	350	50	50	10	6	4	437	31
20/09/12-A	1.39	0.78	3.80	0.46	10	250	350	50	50	10	6	7	400	20
20/09/12-B	1.27	0.76	3.57	0.46	10	250	350	50	50	10	6	7	400	20
29/09/12-A	1.50	0.78	4.14	0.46	10	250	350	50	50	10	6	6	374	19
29/09/12-B	2.21	0.75	5.79	0.50	10	250	350	50	50	10	6	7	374	19
29/09/12-C	2.02	0.78	5.40	0.48	10	250	350	50	50	10	6	8	374	19
29/09/12-D	1.84	0.78	4.86	0.49	10	250	350	50	50	10	6	6	374	19
29/09/12-E	1.55	0.74	4.41	0.47	10	250	350	50	50	10	6	10	374	19
01/10/12-A	1.43	0.76	4.10	0.46	10	250	350	50	50	10	6	7	350	19
01/10/12-B	1.35	0.76	3.82	0.46	10	250	350	50	50	10	6	7	350	19
01/10/12-C	1.25	0.76	3.68	0.44	10	250	350	50	50	10	6	7	374	19
01/10/12-D	1.26	0.76	3.60	0.45	10	250	350	50	50	10	6	7	400	19
02/10/12-B	1.60	0.78	4.46	0.46	10	250	350	50	50	10	6	7	425	19
02/10/12-C	1.46	0.78	3.97	0.47	10	250	350	50	50	10	6	7	450	19
04/10/12-B	0.96	0.76	2.93	0.43	10	250	350	50	50	10	6	7	374	19
04/10/12-C	1.22	0.78	3.56	0.44	10	250	350	50	50	10	6	7	374	19
08/10/12-A	1.17	0.79	3.31	0.44	10	250	350	50	50	10	6	7	374	40
08/10/12-B	1.90	0.78	5.16	0.44	10	250	350	50	50	10	6	7	374	40
26/11/12-A	2.11	0.79	5.86	0.45	10	250	350	50	50	10	6	7	374	40
26/06/13-A	2.83	0.84	7.82	0.43	10	180	350	50	50	10	50	8	375	44
26/06/13-B	2.47	0.84	7.06	0.41	10	180	350	50	50	10	50	8	375	44

Table 8.2: P-I-N devices development (continued)

Sample ID	**Efficiency** *(%)*	**Voc** *(v)*	**FF**	**Jsc** *(mA/cm^2)*	**RF Power** *(W)*	**Temp** *($^\circ C$)*	**Pressure** *(mTorr)*	**SiH4** *(sccm)*	**H2** *(sccm)*	**B2H6 in P** *(sccm)*	**PH3 in N** *(sccm)*	*P (nm)*	**Thickness** *I (nm)*	*N (nm)*
01/07/13-A	1.56	0.78	4.65	0.43	10	210	350	50	50	10	50	8	375	40
01/07/13-B	1.29	0.78	3.95	0.41	10	210	350	50	50	10	50	8	375	40
11/07/13-A	1.86	0.82	5.34	0.42	10	250	350	50	50	10	50	7	374	40
11/07/13-B	1.65	0.82	4.88	0.41	10	250	350	50	50	10	50	7	374	40
15/07/13-A	2.14	0.84	5.83	0.44	10	250	350	50	50	10	50	8	200	32
17/07/13-A	1.08	0.78	3.27	0.42	10/20/10	250	350	50	50	10	50	6	300	40
02/10/13-A	0.13	0.34	1.75	0.24	HWCVD	315	0.38/19/19	3/50/3	0/20/0	1	108	10	361	40
04/10/13-A	0.39	0.38	3.82	0.27	HWCVD	315	0.75/19/19	3/40/3	0/20/0	10	108	10	361	40
11/12/13-A	0.52	0.74	1.97	0.35	10	250	350	50	50	10	50	7	374	40
11/12/13-B	0.60	0.76	2.14	0.37	10	250	350	50	50	10	50	7	374	40
04/02/14-A	1.79	0.79	5.06	0.44	10	250	350	50	50	10	6	7	374	40
04/02/14-B	1.81	0.82	4.86	0.45	10	250	350	50	50	10	6	7	374	40
05/02/14-A	1.63	0.82	4.19	0.47	10	250	350	50	50	10	6	7	374	40
05/02/14-B	2.06	0.82	5.27	0.47	10	250	350	50	50	10	6	7	374	40
11/02/14-A	1.12	0.78	3.26	0.43	10	250	350	50	50	10	6	7	374	40
11/02/14-B	1.60	0.78	4.57	0.44	10	250	350	50	50	10	6	7	374	40
12/02/14-A	1.30	0.82	3.93	0.40	10	250	350	50	50	10	6	7	374	40
07/08/15-B	1.51	0.30	14.05	0.35	10	250	350	50	50	10	6	7	374	40
05/08/15-A	1.80				10	250	350	50	50	10	6	4	374	40
05/08/15-B	1.80				10	250	350	50	50	10	6	4	374	40
09/08/15-A	3.11	0.46	14.48	0.46	10	250	350	50	50	10	6	6	374	40
10/08/15-A	5.23	0.82	10.57	0.60	10	250	350	50	50 (41P)	10	6	10	374	40
10/08/15-B	5.65	0.74	13.05	0.58	10	250	350	50	50 (41P)	10	6	8	374	40
10/08/15-C	5.65	0.70	13.43	0.60	10	250	350	50	50 (41P)	10	6	6	374	40
13/08/15-A	3.57	0.82	8.34	0.52	10	250	350	50	50 (41P)	10	6	7	374	40
13/08/15-B	6.01	0.74	12.53	0.65	10	250	350	50	50 (41P)	10	6	7	374	40
13/08/15-C	4.77	0.82	9.86	0.59	10	250	350	50	50 (39P)	12	6	7	374	40
13/08/15-D	5.53	0.78	10.31	0.56	10	250	350	50	50 (41P)	10	6	7	374	40
13/08/15-E	3.31	0.82	8.24	0.49	10	250	350	50	50 (39P)	12	6	7	374	40

Table 8.3: P-I-N devices development (continued)

Sample ID	**RF power** *(W)*	**Temp** *(°C)*	**Pressure** *(mT)*	**SiH4** *(sccm)*	**H2** *(sccm)*	**Thickness** *(nm)*	**Deposition Rate** *(nm/sec)*	**Photo Conductivity O'** $(S\,cm^{-1})$	**Dark Conductivity O'** $(S\,cm^{-1})$	**Photo / Dark** *Ratio*
11/07/12-i-1	20	250	350	50	50	484	0.54	5.70E-05	1.04E-08	5457
11/07/12-i-2	15	250	350	50	50	387	0.43	3.39E-05	8.89E-09	3814
11/07/12-i-3	10	250	350	50	50	246	0.27	3.79E-05	4.26E-08	888
25/07/12-i-1	10	250	300	50	50	243	0.27	8.45E-05	1.94E-07	436
25/07/12-i-2	10	250	350	50	50	251	0.28	4.58E-04	8.19E-06	56
25/07/12-i-3	10	250	450	50	50	266	0.3	3.69E-04	2.81E-05	13
25/07/12-i-4	10	250	550	50	50	206	0.23	2.19E-03	6.83E-05	32
25/07/12-i-5	10	250	650	50	50	164	0.18	6.73E-04	1.05E-05	64
25/07/12-i-6	15	250	350	50	50	448	0.5	2.41E-04	6.43E-06	37
25/07/12-i-7	20	250	350	50	50	611	0.68	1.21E-04	4.52E-06	27
25/07/12-i-8	25	250	350	50	50	790	0.88	7.90E-05	2.71E-06	29
08/08/12-i-1	10	250	250	50	50	220	0.24	2.10E-03	1.85E-04	11
08/08/12-i-2	10	250	300	50	50	233	0.26	8.72E-04	9.78E-05	9
08/08/12-i-3	10	250	350	50	50	234	0.26	7.99E-04	5.54E-05	14
08/08/12-i-4	10	250	400	50	50	244	0.27	1.29E-03	7.35E-05	18
04/10/12-i-1	10	300	7.5	26	0	550	0.26	3.03E-06	2.39E-07	13
04/10/12-i-2	10	250	350	50	50	550	0.75	5.19E-05	1.43E-08	3642
10/10/12-i-1	10	250	350	50	50	405	0.28	3.26E-05	1.43E-08	2279
10/10/12-i-2	10	250	375	50	50	403	0.28	3.57E-04	1.68E-05	21
10/10/12-i-3	10	250	400	50	50	385	0.27	1.96E-04	1.01E-05	19
10/10/12-i-4	10	250	425	50	50	379	0.26	1.32E-03	4.40E-05	30
10/10/12-i-5	10	250	450	50	50	372	0.26	3.40E-04	3.40E-04	1
10/10/12-i-6	10	250	350	50	50	379	0.26	8.03E-04	5.30E-05	15
18/10/12-i-1	10	250	350	100	50	371	0.26	1.12E-03	2.77E-05	41
18/10/12-i-2	10	250	350	100	50	381	0.26	7.53E-04	3.67E-05	21
18/10/12-i-3	10	250	450	100	50	318	0.22	7.02E-04	2.22E-05	32
18/10/12-i-4	10	250	550	100	50	229	0.16	2.43E-03	3.16E-04	8
31/10/12-i-1	10	300	350	50	0	75	0.25	8.26E-04	4.20E-06	197
31/10/12-i-2	10	300	575	50	0	86	0.29	5.87E-04	5.98E-06	98
31/10/12-i-3	10	300	800	50	0	96	0.32	1.02E-07	4.63E-08	2
31/10/12-i-4	10	300	350	50	0	122	0.41	2.88E-03	4.39E-05	66
31/10/12-i-5	10	300	800	50	0	268	0.89	5.33E-04	1.00E-04	5
31/10/12-i-6	10	300	575	50	0	120	0.4	3.03E-03	4.44E-04	7
27/11/12-i-1	10	250	350	50	50	345	0.29	6.87E-04	5.65E-06	122
27/11/12-i-2	10	250	350	50	100	284	0.24	1.11E-03	1.59E-05	70
27/11/12-i-3	10	250	350	25	100	193	0.16	2.14E-03	2.89E-05	74
27/11/12-i-4	10	250	350	10	100	127	0.11	2.48E-03	6.90E-06	360

Table 8.4: Intrinsic layers development

Sample ID	**RF power** *(W)*	**Temp** *(°C)*	**Pressure** *(mT)*	**SiH4** *(sccm)*	**H2** *(sccm)*	**Thickness** *(nm)*	**Deposition Rate** *(nm/sec)*	**Photo Conductivity O'** *($S\,cm^{-1}$)*	**Dark Conductivity O'** *($S\,cm^{-1}$)*	**Photo / Dark** *Ratio*
21/03/13-i-1	15	250	450	50	50	63	0.21	2.22E-06	4.40E-08	50
21/03/13-i-2	15	250	850	50	50	95	0.32	2.43E-06	3.14E-08	77
21/03/13-i-3	15	250	650	50	50	72	0.24	4.10E-06	5.75E-08	71
21/03/13-i-4	45	250	450	50	50	108	0.36	2.80E-06	4.47E-08	62
21/03/13-i-5	45	250	850	50	50	208	0.69	1.05E-05	7.61E-09	1376
21/03/13-i-6	30	250	650	50	50	97	0.32	7.45E-06	1.40E-08	531
22/03/13-i-1	45	250	650	50	50	77	0.26	4.99E-07	1.45E-08	34
22/03/13-i-2	30	250	450	50	50	95	0.32	8.12E-07	1.24E-08	65
22/03/13-i-3	30	250	850	50	50	150	0.5	9.08E-07	7.63E-09	119
22/03/13-i-4	45	250	650	50	50	132	0.42	1.00E-06	9.25E-09	108
25/04/13-i-1	10	250	300	50	50	153	0.26	4.31E-05	6.17E-08	699
25/04/13-i-2	10	250	350	50	50	155	0.26	2.33E-05	3.83E-08	608
25/04/13-i-3	15	250	350	50	50	248	0.41	1.82E-05	5.57E-08	327
25/04/13-i-4	20	250	350	50	50	351	0.59	1.23E-05	9.88E-09	1243
25/04/13-i-5	25	250	350	50	50	471	0.79	7.00E-06	4.83E-09	1449
25/04/13-i-6	30	250	350	50	50	545	0.91	7.57E-06	5.75E-09	1317
25/04/13-i-7	10	250	500	50	50	210	0.35	1.67E-05	9.50E-08	176
25/04/13-i-8	10	250	350	50	50	155	0.26	2.11E-05	3.19E-08	663
25/04/13-i-9	15	250	350	50	50	248	0.41	6.06E-06	1.85E-08	328
25/04/13-i-10	10	250	400	50	50	163	0.27	1.55E-05	3.10E-08	501
25/04/13-i-11	10	250	400	50	50	100	0.17	1.54E-05	3.16E-08	486
25/04/13-i-12	10	250	400	50	50	100	0.17	2.69E-06	6.57E-08	41
25/04/13-i-13	10	250	400	50	50	100	0.17	4.48E-06	3.57E-08	125
25/04/13-i-14	10	250	350	50	50	150	0.25	1.58E-05	2.67E-08	592
25/04/13-i-15	10	250	350	50	50	100	0.17	1.25E-05	2.58E-08	485
26/06/13-i-1	10	180	350	50	50	241	0.27	1.19E-06	9.04E-09	132
01/07/13-i-1	10	210	350	50	50	227	0.25	7.31E-06	3.81E-08	192
17/07/13-i-1	20	250	350	50	50	520	0.58	4.17E-06	2.38E-08	175
17/07/13-i-2	20	250	350	50	50	521	0.58	4.61E-06	7.31E-09	630
07/08/13-i-1	HWCVD	317	5.5	10	0	146	0.24	1.32E-06	1.12E-07	12
07/08/13-i-2	HWCVD	317	17	30	0	378	0.63	1.66E-06	1.56E-08	107
07/08/13-i-3	HWCVD	317	47	30	0	391	0.65	2.12E-06	4.66E-08	45
13/08/13-i-1	HWCVD	317	24	40	20	530	0.88	4.38E-05	1.45E-08	3016
13/08/13-i-2	HWCVD	317	30	40	40	536	0.89	6.45E-06	1.04E-08	621
01/10/13-i-1	HWCVD	315	18	40	30	502	0.84	4.25E-06	1.78E-08	239

Table 8.5: Intrinsic layers development (continued)

Sample ID	**RF power** *(W)*	**Temp** *(°C)*	**Pressure** *(mT)*	**SiH4** *(sccm)*	**H2** *(sccm)*	**Thickness** *(nm)*	**Deposition Rate** *(nm/sec)*	**Photo Conductivity O'** *($S\,cm^{-1}$)*	**Dark Conductivity O'** *($S\,cm^{-1}$)*	**Photo / Dark** *Ratio*
01/10/13-i-2	HWCVD	315	27	40	30	546	0.91	2.98E-06	4.47E-09	667
01/10/13-i-3	HWCVD	315	19	40	20	517	0.86	2.84E-06	5.01E-09	568
06/03/15-i-1	10	250	350	50	50	375	0.26	1.45E-04	5.83E-08	2490
09/03/15-i-1	10	250	350	50	50	375	0.26	3.65E-05	2.35E-08	1553
09/03/15-i-2	10	250	350	50	50	375	0.26	2.55E-05	1.79E-08	1420
20/03/15-i-1	10	250	350	50	50	375	0.26	2.54E-05	3.02E-08	841
20/03/15-i-2	10	250	350	50	50	375	0.26	2.63E-05	1.05E-08	2490
15/08/15-i-1	10	250	350	50	50	375	0.26	4.68E-05	3.87E-09	12076
15/08/15-i-2	10	250	350	50	50	375	0.26	6.57E-05	4.93E-09	13325

Table 8.6: Intrinsic layers development (continued)

Sample ID	**RF power** *(W)*	**Temp** *(°C)*	**Pressure** *(mT)*	**SiH4** *(sccm)*	**H2** *(sccm)*	**B2H6** *(sccm)*	**PH3** *(sccm)*	**Thickness** *(nm)*	**Photo Conductivity O'** *($S\,cm^{-1}$)*	**Dark Conductivity O'** *($S\,cm^{-1}$)*	**Photo / Dark** *Ratio*
20-03-13-P-1	15	250	450	50	50	10	0	10	2.89E-04	1.09E-04	0
20-03-13-P-2	15	250	850	50	50	10	0	10	2.15E-04	2.07E-04	1
20-03-13-P-3	15	250	650	50	50	10	0	10	3.58E-04	1.44E-04	0
26-06-13-P-1	10	180	350	50	50	10	0	16	4.05E-06	1.42E-06	3
26-06-13-N-1	10	180	350	5	5	0	6	44	6.67E-04	2.21E-04	3
01-07-13-P-1	10	210	350	50	50	10	0	19	6.51E-05	8.04E-05	1
01-07-13-N-1	10	210	350	5	5	0	6	42	1.27E-03	9.93E-05	13
15-07-13-P-1	10	250	350		50	10	0	11	7.32E-06	2.01E-06	4
15-07-13-N-1	10	250	350	5	5	0	50	14	4.40E-07	3.56E-07	1
02-10-13-P-1	10	315	0.38	3	0	1	0	20	2.35E-06	2.28E-06	1

Table 8.7: Doped layers development

References

[1] L. J. Crudgington, M. A. Rind, D. N. R. Payne, and D. M. Bagnall, "The Effects of Varied Deposition Conditions, Including the Use of Argon, on Thin-Film Silicon Solar Cells Prepared Using PECVD," *Molecular Crystals and Liquid Crystals*, no. April 15, 2014.

[2] D. Goodkind, "The World Population at 7 Billion," *United States Census Bureau*, 2011.

[3] The World Energy Outlook, "WEO 2014 Electricity Database," tech. rep., The World Energy Outlook, 2014.

[4] K. Harijan, M. A. Uqaili, and U. K. Mirza, "Assessment of Solar PV Power Generation Potential in Pakistan," *Journal of Clean Energy Technologies*, vol. 3, no. 1, pp. 54–56, 2015.

[5] G. Gottschick, "Trail-blazing Power Plant Technology," 2011.

[6] BP, "BP Statistical Review of World Energy," tech. rep., 2015.

[7] T. J. Crone and M. Tolstoy, "Magnitude of the 2010 Gulf of Mexico oil leak.," *Science (New York, N.Y.)*, vol. 330, no. 6004, p. 634, 2010.

[8] B. Tufft, "Costa Rica goes 75 days powering itself using only renewable energy," *The Independent*, Mar 2015.

[9] C. Breyer, D. Bogdanov, K. Komoto, T. Ehara, J. Song, and N. Enebish, "North-East Asian Super Grid: Renewable energy mix and economics," *Japanese Journal of Applied Physics*, vol. 54, no. 8S1, p. 08KJ01, 2015.

[10] A. Nelsen, "New energy storage plant could 'revolutionise' renewable sector," *The Guardian*, Apr 2015.

[11] Thomson Reuters, "Europe Brent Spot Price FOB," tech. rep., 2015.

[12] A. Vaughan, "Global Carbon Dioxide Levels Break 400ppm Milestone," *The Guardian*, May 2015.

[13] P. Tans, "Trends in Atmospheric Carbon Dioxide," tech. rep., NOAA/ESRL, 2015.

[14] K. Pearson, "Kerosene : Still a burning issue in Africa," *Mosaique*, no. October, pp. 1–6, 2012.

[15] C. Mcglade and P. Ekins, "The geographical distribution of fossil fuels unused when limiting global warming to 2C," *Nature*, vol. 517, no. 7533, pp. 187 – 190, 2014.

[16] J. M. Pearce, "Photovoltaics - A path to sustainable futures," *Futures*, vol. 34, no. 7, pp. 663–674, 2002.

[17] A. B. Mouchot, *(La) Chaleur solaire et ses applications industrielles.* Gauthier-Villars, 1869.

[18] Construction Review Online, "Bukina Faso to install US$50m solar photovoltaic plant," 2014.

[19] Fraunhofer Institute for Solar Energy Systems ISE, "Photovoltaics Report," tech. rep., Fraunhofer Institute for Solar Energy Systems ISE, 2015.

[20] S. A. Kalogirou, *Solar Energy Engineering.* 2009.

[21] S. Dietrich, M. Sander, M. Pander, and M. Ebert, "Interdependency of mechanical failure rate of encapsulated solar cells and module design parameters," p. 84720P, Oct 2012.

[22] M. Fonrodona, S. Santos, C. Mata, M. Vetter, and J. Andreu, "Performance and productivity improvements in very large area amorphous silicon modules," *25th European Photovoltaic Solar Energy Conference (25th PVSEC)*, vol. 2, no. September, pp. 7–10, 2010.

[23] J. Yang, a. Banerjee, and S. Guha, "An Amorphous Silicon Alloy Triple-Junction Solar Cell with 14.6% Initial and 13.0% Stable Efficiencies," *MRS Proceedings*, vol. 467, no. 1997, pp. 13–16, 1997.

[24] M. Liu, M. B. Johnston, and H. J. Snaith, "Efficient planar heterojunction perovskite solar cells by vapour deposition.," *Nature*, vol. 501, no. 7467, pp. 395–8, 2013.

[25] M. Grätzel, "Dye-sensitized solar cells," *Journal of Photochemistry and Photobiology C: Photochemistry Reviews*, vol. 4, no. 2, pp. 145–153, 2003.

[26] G. Li, R. Zhu, and Y. Yang, "Polymer solar cells," *Nature Photonics*, vol. 6, no. 3, pp. 153–161, 2012.

[27] J. Hulme, A. Beaumont, and C. Summers, "Report 3 : Metered fuel consumption - Including annex on high energy users," Tech. Rep. 286734, 2013.

[28] Perez-SUNY/NREL, "Average Annual GHI." 2007.

[29] A. E. Becquerel, "Memoire sur les effects d'electriques produits sous l'influence des rayons solaires," *Annalen der Physick und Chemie*, vol. 54, pp. 35–42, 1841.

[30] W. Smith, "Effect of Light on Selenium During the Passage of An Electric Current*," *Nature*, vol. 7, pp. 303–303, Feb 1873.

[31] W. G. Adams and R. E. Day, "The Action of Light on Selenium," *Proceedings of the Royal Society, London*, vol. A25, p. 113, 1877.

[32] C. E. Fritts, "On a New Form of Selenium Photocell," *American J. of Science*, vol. 26, p. 465, 1883.

[33] A. Einstein, "Über einen die Erzeugung und Verwandlung des Lichtes betreffenden heuristischen Gesichtspunkt," *Annalen der Physik*, vol. 14, no. S1, pp. 164–181, 2005.

[34] P. E. Tomaszewski, "Jan Czochralskifather of the Czochralski method," 2002.

[35] R. S. Ohl, "Light-Sensitive Electric Device," *U.S. Patent*, vol. 2, pp. 402,602, 1941.

[36] D. M. Chapin, C. S. Fuller, and G. L. Pearson, "A New Silicon P-N Junction Photocell for Converting Solar Radiation into Electrical Power," *Journal of Applied Physics*, vol. 25, pp. 676–677, 1954.

[37] A. Luque and S. Hegedus, *Handbook of Photovoltaic Science and Engineering*. Wiley, 2011.

[38] T. Markvart and L. Castañer, "IIa-1 - Principles of Solar Cell Operation," in *Practical Handbook of Photovoltaics* (T. Markvart and L. Castañer, eds.), pp. 71–93, Amsterdam: Elsevier Science, 2003.

[39] R. A. Sinton and A. Cuevas, "Contactless determination of currentvoltage characteristics and minority carrier lifetimes in semiconductors from quasisteadystate photoconductance data," *Applied Physics Letters*, vol. 69, no. 17, 1996.

[40] K. Misiakos and D. Tsamakis, "Accurate measurements of the silicon intrinsic carrier density from 78 to 340 K," *Journal of Applied Physics*, vol. 74, p. 3293, 1993.

[41] P. A. Lynn, *Electricity from Sunlight*. Chichester, UK: John Wiley & Sons, Ltd, Apr 2010.

[42] B. Averill and P. Eldredge, *General Chemistry: Principles, Patterns, and Applications*. 2011.

[43] A. R. Moore, "Electron and hole drift mobility in amorphous silicon," *Applied Physics Letters*, vol. 31, no. 11, 1977.

[44] M. A. Green and M. J. Keevers, "Optical properties of intrinsic silicon at 300 K," *Progress in Photovoltaics: Research and Applications*, vol. 3, no. 3, pp. 189–192, 1995.

[45] P. ASTM International, West Conshohocken, "Standard Tables for Reference Solar Spectral Irradiances: Direct Normal and Hemispherical on 37 degree Tilted Surface," tech. rep., ASTM International, West Conshohocken, PA,, 2012.

[46] J. R. Chelikowsky and M. L. Cohen, "Electronic structure of silicon," *Physical Review B*, vol. 10, pp. 5095–5107, Dec 1974.

[47] Argonne National Laboratory (Advanced Photon Source), "Lattice Constants," 2009.

[48] C. Jennings, "PV module performance at PG&E," in *Conference Record of the Twentieth IEEE Photovoltaic Specialists Conference*, pp. 1225–1229, IEEE, 1988.

[49] M. A. Green, "The path to 25% silicon solar cell efficiency: History of silicon cell evolution," *Progress in Photovoltaics: Research and Applications*, vol. 17, no. 3, pp. 183–189, 2009.

[50] J. Zhao, A. Wang, and M. A. Green, "24.5% Efficiency silicon PERT cells on MCZ substrates and 24.7% efficiency PERL cells on FZ substrates," *Progress in Photovoltaics: Research and Applications*, vol. 7, no. 6, pp. 471–474, 1999.

[51] D. Jordan and J. P. Nagle, "Buried contact concentrator solar cells," *Progress in Photovoltaics: Research and Applications*, vol. 2, pp. 171–176, 1994.

[52] S. Mehta, "PV Technology and Cost Outlook, 2013-2017," tech. rep., GTM Research, Jun 2013.

[53] D. L. Staebler and C. R. Wronski, "Reversible conductivity changes in discharge produced amorphous Si," *Applied Physics Letters*, vol. 31, no. 4, 1977.

[54] D. L. Staebler and C. R. Wronski, "Optically induced conductivity changes in discharge produced hydrogenated amorphous silicon," *Journal of Applied Physics*, vol. 51, no. 6, 1980.

[55] D. Han, "Microscopic Mechanism of the Staebler-Wronski Effect in a-Si Films and High-Efficiency Solar Cells: Final Subcontract Report, 1 October 2001–30 September 2004," tech. rep., National Renewable Energy Laboratory (NREL), Golden, CO, May 2005.

[56] V. Augelli, R. Murri, and L. Schiavulli, "The density of states in the mobility gap of amorphous-silicon films computed by a new analytical method," *Il Nuovo Cimento D*, vol. 10, no. 3, pp. 237–246, 1988.

[57] H. Maurus, M. Schmid, B. Blersch, P. Lechner, and H. Schade, "PV for buildings: Benefits and experiences with amorphous silicon in BIPV applications," *Refocus*, vol. 5, no. 6, pp. 22–27, 2004.

[58] H. F. Sterling and R. C. G. Swann, "Chemical vapour deposition promoted by r.f. discharge," *Solid-State Electronics*, vol. 8, no. 8, pp. 653–654, 1965.

[59] R. C. Chittick, J. H. Alexander, and H. F. Sterling, "The Preparation and Properties of Amorphous Silicon," *Journal of The Electrochemical Society*, vol. 116, no. 1, pp. 77–81, 1969.

[60] P. L. Comber and W. Spear, "Electronic transport in amorphous silicon films," *Physical Review Letters*, vol. 25, no. 8, pp. 1968 – 1970, 1970.

[61] R. J. Loveland, W. E. Spear, and A. Al-Sharbaty, "Photoconductivity and absorption in amorphous Si," *Journal of Non-Crystalline Solids*, vol. 13, no. 1, pp. 55–68, 1973.

[62] W. E. Spear and P. G. L. Comber, "Substitutional doping of amorphous silicon," *Solid State Communications*, vol. 17, no. 9, pp. 1193–1196, 1975.

[63] W. E. Spear, P. G. Le Comber, S. Kinmond, and M. H. Brodsky, "Amorphous silicon p-n junction," *Applied Physics Letters*, vol. 28, no. 2, pp. 105–107, 1976.

[64] D. E. Carlson and C. R. Wronski, "Amorphous silicon solar cell," *Applied Physics Letters*, vol. 28, no. 11, pp. 671–673, 1976.

[65] P. Alpuim, V. Chu, and J. P. Conde, "Amorphous and microcrystalline silicon films grown at low temperatures by radio-frequency and hot-wire chemical vapor deposition," *Journal of Applied Physics*, vol. 86, no. 7, pp. 3812–3821, 1999.

[66] E. Wesoff, "The End of Oerlikons Amorphous Silicon Solar Saga," jan 2014.

[67] M. Vetter, J. P. Borrajo, C. Mata, J. Andreu, and T.-s. G. S. A, "Progress In The Fabrication Of Amorphous Silicon Photovoltaic Modules On Very Large 2,60m X 2,20m Glass Substrates," *24th European Photovoltaic Solar Energy Conference*, no. September, pp. 2408–2411, 2009.

[68] M. I. Kabir, S. a. Shahahmadi, V. Lim, S. Zaidi, K. Sopian, and N. Amin, "Amorphous silicon single-junction thin-film solar cell exceeding 10 % efficiency by design optimization," *International Journal of Photoenergy*, 2012.

[69] D. J. You, S. H. Kim, H. Lee, J.-W. Chung, S.-T. Hwang, Y. H. Heo, S. Lee, and H.-M. Lee, "Recent progress of high efficiency Si thin-film solar cells in large area," *Progress in Photovoltaics: Research and Applications*, vol. 23, no. 8, pp. 973–988, 2015.

[70] B. Rech and H. Wagner, "Potential of amorphous silicon for solar cells," *Applied Physics A: Materials Science & Processing*, vol. 69, no. 2, pp. 155–167, 1999.

[71] R. Brendel, "Appendix A: Light Trapping," in *Thin-Film Crystalline Silicon Solar Cells*, pp. 181–208, Wiley-VCH Verlag GmbH & Co. KGaA, 2005.

[72] A. R. Parker, "Natural photonic engineers," *Materials Today*, vol. 5, no. 9, pp. 26–31, 2002.

[73] J. D. Joannopoulos, S. G. Johnson, J. N. Winn, and R. D. Meade, *Photonic Crystals: Molding the Flow of Light (Second Edition)*. Princeton University Press, 2011.

[74] H. Kruglyak, "The compact disc as a diffraction grating," *Physics Education*, vol. 26, no. 4, p. 255, 1991.

[75] J. W. Shirley, "An Early Experimental Determination of Snell's Law," *American Journal of Physics*, vol. 19, no. 9, 1951.

[76] S. A. Boden, *Biomimetic nanostructured surfaces for antireflection in photovoltaics*. PhD thesis, University of Southampton, 2009.

[77] C. Hu and R. M. White, *Solar Cells: From Basic to Advanced Systems*. New York: McGraw-Hill, 1983.

[78] Z. C. Holman, M. Filipič, A. Descoeudres, S. De Wolf, F. Smole, M. Topič, and C. Ballif, "Infrared light management in high-efficiency silicon heterojunction and rear-passivated solar cells," *Journal of Applied Physics*, vol. 113, no. 1, 2013.

[79] D. T. Pierce and W. E. Spicer, "Electronic Structure of Amorphous Si from Photoemission and Optical Studies," *Phys. Rev. B*, vol. 5, pp. 3017–3029, Apr 1972.

[80] H. Zimmermann, *Silicon Optoelectronic Integrated Circuits*. Advanced microelectronics, Springer, 2004.

[81] M. Bass, E. W. Van Stryland, D. R. Williams, and W. L. Wolfe, *Handbook of optics*, vol. 2. McGraw-Hill, 2001.

[82] E. Yablonovitch and G. D. Cody, "Intensity enhancement in textured optical sheets for solar cells," *Electron Devices, IEEE Transactions on*, vol. 29, no. 2, pp. 300–305, 1982.

[83] J. Yang, F. Luo, T. S. Kao, X. Li, G. W. Ho, J. Teng, X. Luo, and M. Hong, "Design and fabrication of broadband ultralow reflectivity black Si surfaces by laser micro/nanoprocessing," *Light Sci Appl*, vol. 3, p. 185, Jul 2014.

[84] R. Biswas and C. Xu, "Nano-crystalline silicon solar cell architecture with absorption at the classical 4n2 limit," *Opt. Express*, vol. 19, pp. A664–A672, Jul 2011.

[85] H. R. Stuart and D. G. Hall, "Thermodynamic limit to light trapping in thin planar structures," *J. Opt. Soc. Am. A*, vol. 14, pp. 3001–3008, nov 1997.

[86] D. S. Bhachu, *The Synthesis and Characterisation of Metal Oxide Thin Films*. PhD thesis, University College London, 2013.

[87] D. N. R. Payne, *The characterization and enhancement of light scattering for thin solar cells*. PhD thesis, University of Southampton, 2014.

[88] R. Sesuraj, *Plasmonic mirror for light-trapping in thin film solar cells*. PhD thesis, University of Southampton, 2014.

[89] S. Hanni, D. T. L. Alexander, L. Ding, G. Bugnon, M. Boccard, C. Battaglia, P. Cuony, J. Escarre, G. Parascandolo, S. Nicolay, M. Cantoni, M. Despeisse, F. Meillaud, and C. Ballif, "On the Interplay Between Microstructure and Interfaces in High-Efficiency Microcrystalline Silicon Solar Cells," *IEEE Journal of Photovoltaics*, vol. 3, pp. 11–16, jan 2013.

[90] M. Python, D. Dominé, T. Söderström, F. Meillaud, and C. Ballif, "Microcrystalline silicon solar cells: effect of substrate temperature on cracks and their role in post-oxidation," *Progress in Photovoltaics: Research and Applications*, vol. 18, pp. 491–499, Apr 2010.

[91] S. A. Maier, *Plasmonics: Fundamentals and Applications*. Springer US, 2007.

[92] Y. Wang, E. W. Plummer, and K. Kempa, "Foundations of Plasmonics," *Advances in Physics*, vol. 60, pp. 799–898, Oct 2011.

[93] A. D. McFarland and R. P. Van Duyne, "Single Silver Nanoparticles as Real-Time Optical Sensors with Zeptomole Sensitivity," *Nano Letters*, vol. 3, pp. 1057–1062, Aug 2003.

[94] P. R. West, S. Ishii, G. V. Naik, N. K. Emani, V. M. Shalaev, and A. Boltasseva, "Searching for better plasmonic materials," *Laser & Photonics Reviews*, vol. 4, no. 6, pp. 795–808, 2010.

[95] C. Langhammer, M. Schwind, B. Kasemo, and I. Zoric, "Localized Surface Plasmon Resonances in Aluminum Nanodisks," *Nano Letters*, vol. 8, pp. 1461–1471, May 2008.

[96] G. H. Chan, J. Zhao, E. M. Hicks, G. C. Schatz, and R. P. Van Duyne, "Plasmonic Properties of Copper Nanoparticles Fabricated by Nanosphere Lithography," *Nano Letters*, vol. 7, pp. 1947–1952, Jul 2007.

[97] U. Kreibig and M. Vollmer, *Optical Properties of Metal Clusters*, vol. 25 of *Springer Series in Materials Science*. Berlin, Heidelberg: Springer Berlin Heidelberg, 1995.

[98] H. A. Atwater and A. Polman, "Plasmonics for improved photovoltaic devices.," *Nature Materials*, vol. 9, no. 3, pp. 205–213, 2010.

[99] P. G. Kik and M. L. Brongersma, "Surface plasmon nanophotonics," *Springer Series in Optical Sciences*, vol. 131, pp. 1–9, 2007.

[100] J. Bardeen and D. Pines, "Electron-phonon interaction in metals," *Physical Review*, vol. 99, no. 4, pp. 1140–1150, 1955.

[101] M. Kerker, *The scattering of light, and other electromagnetic radiation.* Physical chemistry, Academic Press, 1969.

[102] H. R. Stuart and D. G. Hall, "Nanoparticle-Enhanced Photodetection," *Opt. Photon. News*, vol. 7, pp. 26 – 27, Dec 1996.

[103] K. Kneipp, Y. Wang, H. Kneipp, L. T. Perelman, I. Itzkan, R. R. Dasari, and M. S. Feld, "Single Molecule Detection Using Surface-Enhanced Raman Scattering (SERS)," *Phys. Rev. Lett.*, vol. 78, pp. 1667–1670, Mar 1997.

[104] K. Li, M. I. Stockman, and D. J. Bergman, "Self-Similar Chain of Metal Nanospheres as an Efficient Nanolens," *Phys. Rev. Lett.*, vol. 91, p. 227402, Nov 2003.

[105] T. Kalkbrenner, M. Ramstein, J. Mlynek, and V. Sandoghdar, "A single gold particle as a probe for apertureless scanning near-field optical microscopy," *Journal of Microscopy*, vol. 202, no. 1, pp. 72–76, 2001.

[106] H. Ditlbacher, J. R. Krenn, G. Schider, A. Leitner, and F. R. Aussenegg, "Two-dimensional optics with surface plasmon polaritons," *Applied Physics Letters*, vol. 81, no. 10, 2002.

[107] K. L. Kelly, E. Coronado, L. L. Zhao, and G. C. Schatz, "The Optical Properties of Metal Nanoparticles: The Influence of Size, Shape, and Dielectric Environment," *The Journal of Physical Chemistry B*, vol. 107, pp. 668–677, Jan 2003.

[108] D. M. Schaadt, B. Feng, and E. T. Yu, "Enhanced semiconductor optical absorption via surface plasmon excitation in metal nanoparticles," *Applied Physics Letters*, vol. 86, no. 6, 2005.

[109] D. Derkacs, S. H. Lim, P. Matheu, W. Mar, and E. T. Yu, "Improved performance of amorphous silicon solar cells via scattering from surface plasmon polaritons in nearby metallic nanoparticles," *Applied Physics Letters*, vol. 89, no. 9, 2006.

[110] S. Pillai, K. R. Catchpole, T. Trupke, and M. A. Green, "Surface plasmon enhanced silicon solar cells," *Journal of Applied Physics*, vol. 101, no. 9, 2007.

[111] S. Pillai, K. R. Catchpole, T. Trupke, G. Zhang, J. Zhao, and M. A. Green, "Enhanced emission from Si-based light-emitting diodes using surface plasmons," *Applied Physics Letters*, vol. 88, no. 16, 2006.

[112] K. R. Catchpole and A. Polman, "Design principles for particle plasmon enhanced solar cells," *Applied Physics Letters*, vol. 93, no. 19, 2008.

[113] K. R. Catchpole and A. Polman, "Plasmonic solar cells," *Opt. Express*, vol. 16, pp. 21793–21800, Dec 2008.

[114] F. J. Beck, A. Polman, and K. R. Catchpole, "Tunable light trapping for solar cells using localized surface plasmons," *Journal of Applied Physics*, vol. 105, no. 11, 2009.

[115] V. E. Ferry, M. A. Verschuuren, H. B. T. Li, E. Verhagen, R. J. Walters, R. E. I. Schropp, H. A. Atwater, and A. Polman, "Light trapping in ultrathin plasmonic solar cells," *Opt. Express*, vol. 18, pp. A237—-A245, Jun 2010.

[116] A. Centeno, J. Breeze, B. Ahmed, H. Reehal, and N. Alford, "Scattering of light into silicon by spherical and hemispherical silver nanoparticles," *Opt. Lett.*, vol. 35, pp. 76–78, Jan 2010.

[117] H. Tan, R. Santbergen, A. H. M. Smets, and M. Zeman, "Plasmonic Light Trapping in Thin-film Silicon Solar Cells with Improved Self-Assembled Silver Nanoparticles," *Nano Letters*, vol. 12, pp. 4070–4076, Aug 2012.

[118] M. Optimization, S. Zhou, Q. Li, S. Townsend, Y. M. Xie, and X. Huang, "Design of Novel Nanoparticles for Thin-film Solar Cells," *10th World Congress on Structural and Multidisciplinary Optimization*, pp. 1–9, 2013.

[119] B. J. Wiley, S. H. Im, Z.-Y. Li, J. McLellan, A. Siekkinen, and Y. Xia, "Maneuvering the Surface Plasmon Resonance of Silver Nanostructures through Shape-Controlled Synthesis," *The Journal of Physical Chemistry B*, vol. 110, pp. 15666–15675, Aug 2006.

[120] A. Basch, F. J. Beck, T. Söderström, S. Varlamov, and K. R. Catchpole, "Combined plasmonic and dielectric rear reflectors for enhanced photocurrent in solar cells," *Applied Physics Letters*, vol. 100, no. 24, pp. –, 2012.

[121] J. D. Winans, C. Hungerford, K. Shome, L. J. Rothberg, and P. M. Fauchet, "Plasmonic effects in ultrathin amorphous silicon solar cells: performance improvements with Ag nanoparticles on the front, the back, and both," *Opt. Express*, vol. 23, pp. A92 – A105, Feb 2015.

[122] W. G. J. H. M. van Sark, L. Korte, and F. Roca, eds., *Physics and Technology of Amorphous-Crystalline Heterostructure Silicon Solar Cells*. Engineering Materials, Berlin, Heidelberg: Springer Berlin Heidelberg, 2012.

[123] W. Lodders, "Powder formation in silane plasmas," *Philips Electronics*, vol. Nat. Lab., 1997.

[124] H. S. Nalwa, *Handbook of Surfaces and Interfaces of Materials, Five-Volume Set.* Elsevier Science, 2001.

[125] O. D. Clark, *Thin film amorphous silicon cells by inductive PECVD, with a view towards flexible substrates.* PhD thesis, University of Southampton, 2009.

[126] R. E. Schropp, "Hot Wire Chemical Vapor Deposition: Recent Progress, Present State of the Art and Competitive Opportunities," in *ECS Transactions*, pp. 3–14, ECS, 2009.

[127] C. Sotomayor Torres, S. Zankovych, J. Seekamp, A. Kam, C. Clavijo Cedeño, T. Hoffmann, J. Ahopelto, F. Reuther, K. Pfeiffer, G. Bleidiessel, G. Gruetzner, M. Maximov, and B. Heidari, "Nanoimprint lithography: an alternative nanofabrication approach," *Materials Science and Engineering: C*, vol. 23, pp. 23–31, Jan 2003.

[128] T. Yagi, Y. Uraoka, and T. Fuyuki, "Ray-trace simulation of light trapping in silicon solar cell with texture structures," *Solar Energy Materials and Solar Cells*, vol. 90, no. 16, pp. 2647–2656, 2006.

[129] H. Horvath, "Gustav Mie and the scattering and absorption of light by particles: Historic developments and basics," *Journal of Quantitative Spectroscopy and Radiative Transfer*, vol. 110, no. 11, pp. 787–799, 2009.

[130] R. J. Martin, "Mie Scattering Formulae for Non-spherical Particles," *Journal of Modern Optics*, vol. 40, pp. 2467–2494, Dec 1993.

[131] K. Yee, "Numerical solution of initial boundary value problems involving Maxwell's equations in isotropic media," *Antennas and Propagation, IEEE Transactions on*, vol. 14, no. 3, pp. 302–307, 1966.

[132] F. Dominec, "FDTD Yee Grid 2D-3D," *CC BY-SA 4.0 (http://creativecommons.org/licenses/by-sa/4.0)], via Wikimedia Commons*, 2015.

[133] Lumerical Solutions Inc, "FDTD Solutions," 2015.

[134] Lumerical Solutions Inc, "Convergence testing for the FDTD solver," 2015.